Investigation of Hidden Multipolar Spin Order in Frustrated Magnets Using Interpretable Machine Learning Techniques

Jonas Franz Greitemann

SIGILL: UNIVERSITAT: LUDOVIC: MAXIM:

München, 2019

Investigation of Hidden Multipolar Spin Order in Frustrated Magnets Using Interpretable Machine Learning Techniques

Dissertation
an der Fakultät für Physik
der Ludwig-Maximilians-Universität München

vorgelegt von

Jonas Franz Greitemann
aus Arnsberg

München, den 22. August 2019

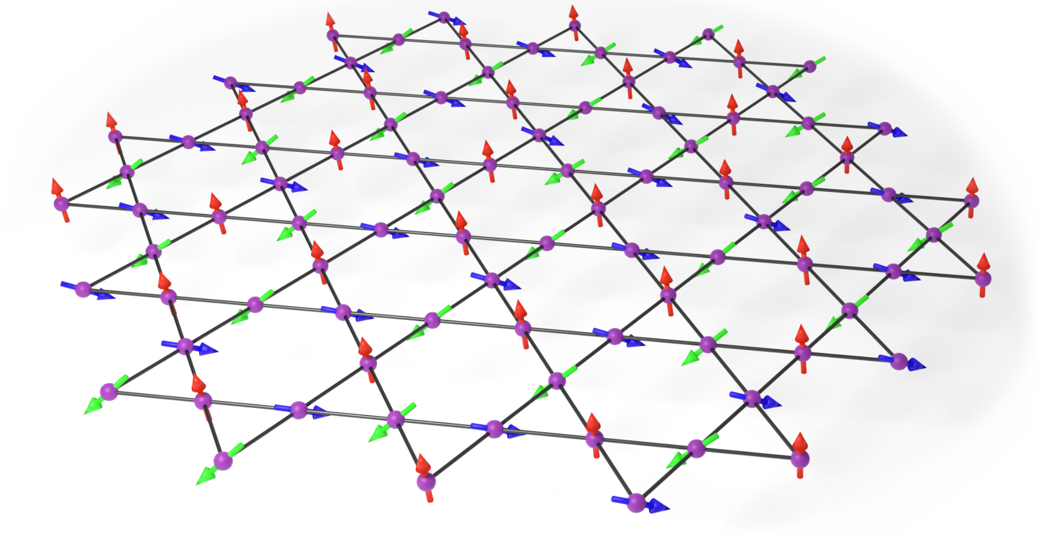

Erstgutachter: Prof. Dr. Lode Pollet
Zweitgutachter: Prof. Dr. Matthias Punk
Datum der mündlichen Prüfung: 15. Oktober 2019

Kurzfassung

Frustration führt zu einer Fülle komplexer Phänomene, von denen die herausragendsten Spinflüssigkeiten sind, sowohl klassische – wie beispielsweise die Spin-Eis-Phase, die experimentell in den Oxiden seltener Erden auf dem Pyrochlor-Gitter realisiert wurde – und ihre schwerer fassbaren quantenmechanischen Gegenstücke. Bei niedrigen Temperaturen können klassische frustrierte Spinsysteme obgleich der extensiven Entartung des Grundzustandes aufgrund des Phänomens der „Ordnung durch Unordnung" dennoch Ordnungen ausbilden. Diese sind oft multipolarer Natur und entziehen sich herkömmlichen Messgrößen. Die Identifikation und Charakterisierung solcher „verborgener" Ordnungen ist daher eine herausfordernde Aufgabe.

In dieser Arbeit wird ein Verfahren für das unvoreingenommene und automatisierte maschinelle Lernen der Phasendiagramme klassischer frustrierter Spinmodelle eingeführt. Die Interpretierbarkeit der resultierenden Klassifikatoren war für das Design der Methode ausschlaggebend. Sie erlaubt den Rückschluss sowohl auf die Ordnungsparametertensoren der symmetriebrechenden Phasen als auch auf die Nebenbedingungen, die für klassische Spinflüssigkeiten charakteristisch sind und auf deren emergente Eichstruktur hindeuten. Darüber hinaus wird eine hierarchische Beziehung zwischen den verschiedenen Phasen gemäß dem Grade ihrer jeweiligen Unordnung hergestellt.

Das Verfahren wird auf drei verschiedene Modelle angewendet und Spin-Konfigurationen werden jeweils aus klassischen Monte-Carlo-Simulationen dieser gewonnen. Ein Eichmodell dient dazu, die Wechselwirkungen zwischen den Mesogenen verallgemeinerter nematischer Flüssigkristalle nachzuahmen. Diese können beliebige Punktgruppensymmetrien besitzen, was zu Benchmark-Modellen mit einer Niedertemperaturphase führt, die die O(3)-Spinsymmetrie entsprechend herunterbricht. Darüber hinaus werden zwei frustrierte Spinmodelle betrachtet. Der historisch wichtige Fall des Heisenberg-Modells auf dem Kagome-Gitter führt zu einer verborgenen trigonalen Ordnung, die eine Beschreibung in Form von zwei Tensoren unterschiedlichen Ranges erforderlich macht; die Maschine ist in der Lage, beide zu finden. Währenddessen rekonstruiert die Maschine für das XXZ-Modell auf dem Pyrochlor-Gitter das komplexe Phasendiagramm, das erst vor Kurzem ausgearbeitet wurde, und identifiziert die spin-nematische Phase sowie drei verschiedene Arten klassischer Spinflüssigkeiten, einschließlich ihrer Übergänge, korrekt.

Die Methode hat das Potenzial, die Charakterisierung von Spinmodellen frustrierter Magnete zu beschleunigen. Sie kann den gesamten Parameterraum auf einmal untersuchen und somit dazu beitragen, interessante Bereiche zu identifizieren. Dies bereitet den Weg für die Suche nach neuen Ordnungen und Spinflüssigkeiten.

Abstract

Frustration gives rise to a plethora of intricate phenomena, the most salient of which are spin liquids, both classical ones—such as the spin-ice phase which has been realized experimentally in rare-earth oxide pyrochlore materials—and their more elusive quantum counterparts. At low temperatures, classical frustrated spin systems may still order, despite their extensive ground-state degeneracy, due to the order-by-disorder phenomenon. The resulting orders are often of a multipolar type which defies conventional probes. Identifying and characterizing such "hidden" orders is thus a challenging endeavor.

This thesis introduces a machine-learning framework for studying the phase diagram of classical frustrated spin models in an unbiased and automated way. The interpretability of the resulting classification was of paramount importance in the design of the method. It allows for the inference of both the order parameter tensors of the phases with broken symmetries as well as the constraints which are characteristic of classical spin liquids and signal their emergent gauge structure. On top of that, it establishes a hierarchical relationship among the various phases according to their degree of disorder.

The framework is applied to three different models and spin configurations are harvested from classical Monte Carlo simulations of those. A gauge model is used to mimic the interactions between the mesogens of generalized nematics. These may possess arbitrary point group symmetry, resulting in benchmark models with a low-temperature phase that breaks the O(3) spin symmetry accordingly. In addition, two frustrated spin models are considered. The historically important case of the Heisenberg model on the kagome lattice gives rise to hidden triatic order which requires a description in terms of two tensors of different ranks; the machine is capable of finding both. Meanwhile, for the XXZ model on the pyrochlore lattice, the machine reconstructs the complex phase diagram which was only recently obtained and correctly identifies the spin nematic phase as well as three distinct types of classical spin liquids, including their crossovers.

The method has the potential to accelerate the characterization of model Hamiltonians of frustrated magnets. It can scrutinize the whole parameter space at once and may thus help to identify interesting regimes, paving the way for the search of new orders and spin liquids.

Acknowledgements

My utmost gratitude goes out to my advisor, **Lode Pollet**, who supported me in countless ways, gave me the freedom to pursue my work without pressure, and whose door was always open. I especially appreciate your flexibility and availability during “crunch time”, in spite of the fact that—being a new father—your life is stressful enough even without us sending you drafts at the last minute.

I thank **Matthias Punk** who took on the unenviable task of reading this whole thesis as well as the other members of my examination board, **Thomas Kuhr**, **Tim Liedl**, **Thomas Birner**, and **Ilka Brunner**, for their time and their positive responses to my inquiries.

I am deeply indebted to my colleague **Ke Liu** who envisioned the project from which this thesis resulted and whose expertise in group theory never ceases to amaze me. You remained calm and focused when discussions got heated and guided me through the intricacies and politics surrounding the study of spin liquids. I also appreciate your help proofreading this thesis, down to the final hours.

I thank **Nic Shannon**, **Ludo Jaubert**, and **Han Yan** for the pleasant collaboration on the XXZ pyrochlore project. Nic’s frequent visits, especially his input during the finalisation of the draft, were invaluable. Ludo provided the Monte Carlo data and swiftly came through on our many requests for more samples. You were also a most pleasant guest during your visit to LMU.

Proofreading help by **Peter Vander Griend** and **Fabian Bindel** is also gratefully acknowledged. I thank Peter for keeping me from excessive shoehorning and Fabian for our frequent discussions on the fine points of typography. I would like to thank **Stefan Wittlinger** for proofreading as well and also for rounding up the Mensa gang almost every day.

Everyone on the Schollwöck/von Delft corridor—postdocs, grad students, and undergrads; past and present: you made for very pleasant colleagues. I especially thank everyone who joined in with the Mensa group. Our conversations on physics, politics, and otherwise made up for a mediocre culinary experience.

The value of **Cordula Weber**’s administrative support cannot be overstated. You were a huge help in navigating the bureaucracy of LMU, making sure travel expenses were correctly reimbursed down to the bike kilometer, contracts extended on time, and time sheets filled out with millisecond-accuracy. Thank you!

My gratitude extends also to those who influenced my scientific journey prior to moving to Munich. In particular, **Stefan Wessel** who supervised my Bachelor and Master theses and who encouraged me to apply to Lode. Furthermore, everyone who supported me along the way, especially those who facilitated my scholarship from the Studienstiftung.

Finally, I want to express my heartfelt appreciation to my family, especially Klaus, but in particular to my parents who supported me not just throughout the PhD, but always. You have accepted me for who I am without hesitation, even if that might not always have been easy. This thesis is dedicated to you.

Publications

This work is based on the following publications and preprints which are partially reprinted.

Generic first-order phase transitions between isotropic and orientational phases with polyhedral symmetries

Ke Liu, Jonas Greitemann, and Lode Pollet

Phys. Rev. E **97**, 012706 (2018) [1]

Polyhedral nematics are examples of exotic orientational phases that possess a complex internal symmetry, representing highly nontrivial ways of rotational symmetry breaking, and are subject to current experimental pursuits in colloidal and molecular systems. The classification of these phases has been known for a long time; however, their transitions to the disordered isotropic liquid phase remain largely unexplored, except for a few symmetries. In this work, we utilize a recently introduced non-Abelian gauge theory to explore the nature of the underlying nematic-isotropic transition for all three-dimensional polyhedral nematics. The gauge theory can readily be applied to nematic phases with an arbitrary point-group symmetry, including those where traditional Landau methods and the associated lattice models may become too involved to implement owing to a prohibitive order-parameter tensor of high rank or (the absence of) mirror symmetries. By means of exhaustive Monte Carlo simulations, we find that the nematic-isotropic transition is generically first-order for all polyhedral symmetries. Moreover, we show that this universal result is fully consistent with our expectation from a renormalization group approach, as well as with other lattice models for symmetries already studied in the literature. We argue that extreme fine tuning is required to promote those transitions to second-order ones. We also comment on the nature of phase transitions breaking the O(3) symmetry in general cases.

Probing hidden spin order with interpretable machine learning

Jonas Greitemann, Ke Liu, and Lode Pollet

Phys. Rev. B **99**, 060404(R) (2019) [2]

The search of unconventional magnetic and nonmagnetic states is a major topic in the study of frustrated magnetism. Canonical examples of those states include various spin liquids and spin nematics. However, discerning their existence and the correct characterization is usually challenging. Here we introduce a machine-learning protocol that can identify general nematic order and their order parameter from seemingly featureless spin configurations, thus providing comprehensive insight on the presence or absence of hidden orders. We demonstrate the capabilities of our method by extracting the analytical form of nematic order parameter tensors up to rank 6. This may prove useful in the search for novel spin states and for ruling out spurious spin liquid candidates.

Learning multiple order parameters with interpretable machines

Ke Liu, Jonas Greitemann, and Lode Pollet

Phys. Rev. B **99**, 104410 (2019) [3]

Machine-learning techniques are evolving into a subsidiary tool for studying phase transitions in many-body systems. However, most studies are tied to situations involving only one phase transition and one order parameter. Systems that accommodate multiple phases of coexisting and competing orders, which are common in condensed matter physics, remain largely unexplored from a machine-learning perspective. In this paper, we investigate multiclassification of phases using support vector machines (SVMs) and apply a recently introduced kernel method for detecting hidden spin and orbital orders to learn multiple phases and their analytical order parameters. Our focus is on multipolar orders and their tensorial order parameters whose identification is difficult with traditional methods. The importance of interpretability is emphasized for physical applications of multiclassification. Furthermore, we discuss an intrinsic parameter of SVM, the bias, which allows for a special interpretation in the classification of phases, and its utility in diagnosing the existence of phase transitions. We show that it can be exploited as an efficient way to explore the topology of unknown phase diagrams where the supervision is entirely delegated to the machine.

Identification of emergent constraints and hidden order in frustrated magnets using tensorial kernel methods of machine learning

Jonas Greitemann, Ke Liu, Ludovic D. C. Jaubert, Han Yan, Nic Shannon, and Lode Pollet

Preprint (2019), arXiV:1907.12322 [4]

Machine-learning techniques have proved successful in identifying ordered phases of matter. However, it remains an open question how far they can contribute to the understanding of phases without broken symmetry, such as spin liquids. Here we demonstrate how a machine learning approach can automatically learn the intricate phase diagram of a classical frustrated spin model. The method we employ is a support vector machine equipped with a tensorial kernel and a spectral graph analysis which admits its applicability in an effectively unsupervised context. Thanks to the interpretability of the machine we are able to infer, in closed form, both order parameter tensors of phases with broken symmetry, and the local constraints which signal an emergent gauge structure, and so characterize classical spin liquids. The method is applied to the classical XXZ model on the pyrochlore lattice where it distinguishes—among others—between a hidden biaxial spin nematic phase and several different classical spin liquids. The results are in full agreement with a previous analysis by Taillefumier *et al.*, but go further by providing a systematic hierarchy between disordered regimes, and establishing the physical relevance of the susceptibilities associated with the local constraints. Our work paves the way for the search of new orders and spin liquids in generic frustrated magnets.

To my parents,

Thomas and Monika

Contents

List of Symbols

$\mathcal{X}$	space of input data; raw spin configurations
d	dimension of input data, $\mathcal{X} \subseteq \mathbb{R}^d$
$\mathbf{x}$	input data, $\mathbf{x} \in \mathcal{X}$; spin configuration
$\mathbf{x}^{(k)}$	k-th training data sample; possibly a support vector
$y^{(k)}$	label corresponding to $\mathbf{x}^{(k)}$
λ_k	coefficient with which training sample $\mathbf{x}^{(k)}$ contributes to the decision function, nonzero for support vectors
$d(\mathbf{x})$	SVM decision function, $d : \mathcal{X} \to \mathbb{R}$
$\mathbf{w}$	hyperplane normal in linear SVM, superseded by coefficient matrix when using the quadratic kernel
K	kernel function, $K : \mathcal{X} \times \mathcal{X} \to \mathbb{R}$
$\mathcal{F}$	high-dimensional feature space where training data become linearly separable, implied by kernel function through Mercer's theorem
$\boldsymbol{\varphi}$	(implicit) *Mercer* mapping to feature space, $\boldsymbol{\varphi} : \mathcal{X} \to \mathcal{F}$
$\mathcal{M}$	space of monomials in TK-SVM
$\boldsymbol{\phi}$	monomial mapping in TK-SVM, $\boldsymbol{\phi} : \mathcal{X} \to \mathcal{M}$; vector of monomials obtained through invocation of the aforementioned mapping on an omitted implicit spin configuration, $\boldsymbol{\phi} = \boldsymbol{\phi}(\mathbf{x}) \in \mathcal{M}$
$\lVert A \rVert_F^2$	Frobenius norm (squared), $\sum_{ij} \lvert A_{ij} \rvert^2$
L	linear system size
D	spatial system dimension
i	lattice site index, $i = 1, \ldots, L^D$
I	cluster index
r	number of spins per cluster
α	index identifying sublattice spin within the cluster ($\alpha = 1, \ldots, r$); color index in case of gauge model ($\alpha = \mathrm{l}, \mathrm{m}, \mathrm{n}$)
a	spatial component index ($a = x, y, z$)
n	tensor rank; degree of monomial mapping
μ, ν	multi-index combining sublattice and component indices for each spin component in a monomial, $\mu = (\alpha_1, \ldots, \alpha_n; a_1, \ldots, a_n)$, enumerates monomials ϕ_μ in feature vector $\boldsymbol{\phi} \in \mathcal{M}$
$C_{\mu\nu}$	coefficient matrix in TK-SVM
$\langle \ldots \rangle_{\mathrm{cl}}$	cluster average
$\langle \ldots \rangle_{\mathrm{diso}}$	disorder average

1

Introduction

A brief history of machine learning

In March 2016, Google's subsidiary DeepMind made worldwide headline news [5] when its *AlphaGo* [6] became the first computer program to defeat a professional (9-dan) human player without handicaps in a series of five games of the board game Go, beating Lee Sedol four to one. Since then, its successor *AlphaZero* [7] has established itself firmly as the world's top Go player, both compared to humans and the original *AlphaGo* which it declassed in a flawless 100–0 victory. Unlike *AlphaGo*, *AlphaZero* was not taught by observing human gameplay and without access to opening books or endgame tables. Rather, it is self-taught, learning exclusively from simulated gameplay against itself. Further, it was not specifically designed for the purpose of playing Go, but also mastered shogi and chess. The super-human performance of *AlphaGo* and *AlphaZero* marks one of the most prominent successes of "deep learning", which heralded the latest resurgence of machine learning and brought artificial intelligence (AI) yet again into public consciousness.

It is worth noting, however, that the idea behind artificial neural networks (ANNs) was pioneered as early as the 1940s [8] and the development of the perceptron in 1957 [9] drew significant media coverage and sparked people's imagination [10]. When it became apparent that the field could not live up to its grandiose early promises, funding was cut and the field entered the first "AI winter" in the early 70s.

At the same time, backpropagation, the algorithm to train today's deep ANNs by updating the connections between neurons via the chain rule, was developed and implemented [11] but failed to gain traction in a contracting field until it was rediscovered and popularized in the 80s [12]. Finally, with the addition of the convolutional neural network (CNN) architecture which incorporated translation invariance in the late 80s [13], all the crucial techniques to build a modern machine learning algorithm were in place by 1990. Despite these early developments on the methods front, ANNs still failed to deliver on their promises and could only tackle simple tasks whereas training consumed considerable computational resources and was limited to rather shallow networks.

On the other hand, by the late 80s, artificial intelligence saw widespread adoption in commercial applications in the form of expert systems. This kind of knowledge-based intelligence makes decisions using simple if-then-else rules and would not be considered machine learning by today's standards as it lacks the ability to learn by itself. As the complexity of applications grew, in part fueled by the emerging world wide web, expert systems failed to scale accordingly and AI fell out of favor again, ushering in a second AI winter in the early 90s.

Toward the end of the millennium, kernel methods brought about a paradigm shift from knowledge-based to data-driven intelligence. Support vector machines (SVMs) [14] and kernel principal component analysis (kPCA) [15] allow for the capture of nonlinear features through the use of appropriate kernel functions and could be trained from existing data. Both of these methods are discussed in Sec. 4.1. What set kernel methods apart from ANNs was their immediate successful applicability. Notably, the MNIST database of handwritten digits [16] which was harvested from forms filled by employees of the U.S. Census Bureau, as well as high-school students, commonly serves as a benchmark of machine learning. Using an SVM, LeCun *et al.*

achieved test error rates below one percent [17]. At the same time, random decision forests [18], another data-driven learning scheme, were developed. The practical applicability of these methods spurred their almost instantaneous adoption and the field once again emerged from its winter.

Another influential dataset for image classification is ImageNet which was first released in 2009. It consists of an ever-growing number (upwards of 14 million) of captioned images depicting everyday objects from tens of thousands of categories, a subset of which is used in a yearly competition. The winning entry of the 2012 edition of the competition, *AlexNet* [19], employed a deep CNN architecture and fared significantly better than the runner up that year. Strikingly, the network was very similar to those proposed in the late 80s. Its success was not necessarily brought on by algorithmic innovation, but by an efficient implementation that made use of the hardware innovation that sustained the exponential speedup of computer hardware in the preceding decades. It also exploited the extreme level of parallelism that graphical processing units (GPUs) offer which has since become the norm in the field. Indeed, *AlphaGo* and *AlphaZero* run on tailor-made tensor processing units (TPUs), and cores specifically designed for “AI applications” are featured (and marketed) on today’s phones.

It has to be concluded that the “deep learning revolution” which we have seen in this decade was rendered possible by the almost million-fold speedup of computers since the original development of the methods in the late 80s. As a consequence, more complex networks with a larger number of neurons became feasible, surpassing the complexity that is required for the emergence of “intelligence”. In particular, the previously unseen success of ANNs is commonly attributed to the added depth, *i.e.* the use of multilayered ANN architectures, trained by backpropagation. Some research into the relevance of depth has been conducted, relating individual layers to successive levels of coarse graining in image recognition [20] or, more abstractly, to stages of compositional or hierarchical generative physical processes from which the training data originate [21]. In other areas, particularly in the application to the many-body problem, the evidence for a superior performance of deep networks has been more conflicted [22–25].

In summary, the field of machine learning underwent a series of “hype cycles”, fostering grossly inflated expectations inspired by singular breakthroughs and flowery language, followed by a failure to live up to them, general disillusionment, and loss of funding. Whereas this pattern is familiar to many areas of human innovation, machine learning has ironically proven itself particularly resistant to learning, repeating the cycle many times. On the other hand, ever since machine learning began delivering workable solutions to real-world problems, it has become indispensable, and it is unlikely that we will see another AI winter with near-complete withdrawal of funding. Furthermore, deep learning is finally reaping the benefits of decades of early research into ANNs. These early years were marked by the struggle between connectionism as embodied by ANNs and the primitive, computational AI that drove the initial popularity of expert systems. In light of the fact that connectionism has prevailed by surpassing more traditional algorithms in most areas, it can be expected that deep neural networks are here to stay in the long term. To a lesser extent, however, the enthusiasm that marked the early years of this decade is already wavering as it becomes increasingly obvious that solutions to challenging problems such as self-driving cars or general AI are still many years away.

Machine learning in condensed matter physics

Compared to the long pursuit of machine learning in computer science, one might be inclined to believe that the adoption of these tools within physics is a relatively recent phenomenon in spite of their having been available for some time. For example, the schemes developed in this thesis are based on kernel methods which reached algorithmic maturity some fifteen years ago, yet their application to phase classification in physics was pioneered only in 2017 [26]. In general, 2017 can be considered the year where machine learning saw wide adoption by physicists. This can be traced back to the successes of deep learning since 2012 which was visible cross-disciplinarily and exposed researchers to these ideas for the first time. In particular, the seminal paper by Carleo and Troyer [24] spurred interest in the applicability of neural networks to the many-body problem. The ensuing "ML hype" prompted physicists to also look into the utility of further established algorithms to physical problems. An overview of the progress made so far in this context is given in the beginning of Ch. 4.

In spite of this, the observation that machine learning is relatively new to physics is arguably inaccurate. In fact, many-body physics especially has always employed numerical methods to scrutinize emergent behavior. Some of the alleged breakthroughs may rather be seen as conforming to the framework of established methods such as variational Monte Carlo, both in spirit and in terms of the algorithms used for the optimization [24, supplementary materials; 27; 28]. Likewise, it has been shown that certain (shallow) neural network architectures are related to tensor network states [29, 30] which predate the rise of machine learning in physics. Indeed, matrix product states (MPS) and the algorithms in their sphere of influence can easily be considered machine learning, but historically developed separately. Ideas from these fields (*e.g.* an understanding of the ability to capture the physics of a system based on the area law of its entanglement entropy [31]) and statistical physics more generally (*e.g.* renormalization groups and coarse graining) therefore also make their way back into ML research.

A major obstacle towards establishing ML techniques as a tool in the study of condensed matter systems, which may ultimately be used to gain knowledge, is posed by their common lack of interpretability. Unlike in many of the industry-proven applications of ML, it is insufficient to merely recognize or classify a certain physical state, but inevitably the follow-up question arises *how* this state differs from another one. In this context, most ML methods can be placed on a spectrum based on a tradeoff between expressibility and interpretability. For example, ANNs are popular specifically because they are extremely versatile and efficiently express highly-dimensional nonlinear functions, a property that is amplified by an increase in depth. However, understanding the physical principle which they exploit along the way is very difficult. This aspect, too, is exacerbated by depth (*cf.* the discussion in Sec. 4.2).

In contrast, kernel methods are less flexible and their successful applicability relies on the choice of a suitably engineered kernel function. On the upside, they can be fully interpretable (although that too depends on the choice of the kernel). Hence, it is essential to choose one's battles wisely by taking to an arena which both poses a wide array of challenging problems but also fits into the framework dictated by the kernel. As part of the premise of this thesis, one such arena is identified in the classification of phases in frustrated magnets.

Spin liquids in frustrated magnets

Frustration is ubiquitous in nature. So much so that the properties of water, including its unusually high melting and boiling points, its large heat capacity, latent heat, and anomalous density curve—all crucial for the development of life as we know it—are all consequences of frustration.

It is well known that the hydrogen atoms in H_2O span an angle of about 104°, slightly less than the 109° corresponding to the unperturbed tetrahedral coordination of hybridized sp^3 orbitals of the central oxygen atom. This leads to a nonvanishing dipolar moment due to the partial charges induced by the larger electronegativity of oxygen as compared to hydrogen. In water ice (specifically the ice I_h phase formed under terrestrial conditions), the molecules are arranged in a lattice with close to tetrahedral bond angles as well. Due to the partial charges, it is energetically favorable for exactly one hydrogen to sit between any neighboring oxygen atoms, being covalently bound to one of them and forming a weak "hydrogen" bond with the other. The orientation of the water molecules in the lattice is then determined by the Bernal-Fowler "ice rules" [32] which state that each molecule should be faced by the hydrogen atoms of two of its neighbors and the oxygen sides of the other two. An example of a configuration respecting these ice rules is shown in Fig. 1.1(a).

The ice rules do not uniquely determine the ground-state configuration of water ice. Rather, the number of compatible configurations, *i.e.* the degeneracy of the ground state, grows exponentially with system size. This then gives rise to an extensive contribution to the residual entropy which was famously estimated by Pauling as $S_0/n = \ln(3/2)R \approx 3.4\,\mathrm{J/(mol\,K)}$ [35]. The extensive residual entropy consequently affects the thermodynamics of bulk properties and leads to the above anomalies associated with water. An exponential ground-state degeneracy is one of the hallmarks of frustrated systems. Somewhat sloppily, it is more commonly referred to as an extensive ground state degeneracy (exGSD) because it gives rise to an extensive residual entropy.

An analogous situation is realized in a class of magnetic systems which—for this reason—are known as spin ices. Experimental realizations of spin ices have been discovered in the rare-earth oxide materials $Ho_2Ti_2O_7$ [33] and $Dy_2Ti_2O_7$ [34, 36]. In these compounds, only the rare-earth ions (Ho^{3+} and Dy^{3+}) are magnetic. These form a pyrochlore lattice, a network of corner-sharing tetrahedra; its geometry is depicted in Fig. 1.1(b). Due to a strong crystal-field anisotropy along the $\langle 111 \rangle$ axis (see Sec. 2.1.2), the magnetic moments behave as Ising spins. The energy of such a configuration is then minimized (*cf.* Sec. 2.1) if within each of the tedrahedra, two of the spins point inwards, while the other two point outwards. This "two-in-two-out" rule is the spin-ice analogue of the ice rules in water. Indeed, Fig. 1.1(b) depicts a configuration obeying the two-in-two-out rule which is equivalent to the water ice configuration in Fig. 1.1(a) by having the spins in the former point towards the location of each of the hydrogen atoms in the latter. The residual entropy of $Dy_2Ti_2O_7$ has been found from its heat capacity to be consistent with that of water ice I_h and Pauling's estimate [37].

The fluctuations permitted by the spin-ice rule may also be understood by analogy to magnetostatics. By identifying the spins $\mathbf{S}_i$ at positions $\mathbf{r}_i$ in the lattice with the local strength of an artificial magnetic field $\mathbf{B}(\mathbf{r}_i) = \mathbf{S}_i$, the spin-ice rule can be summarized in a generalize Gauss' law, $\nabla \cdot \mathbf{B} = 0$ [38]. Hence, two magnetic "field lines" enter into each lattice tetrahedron and

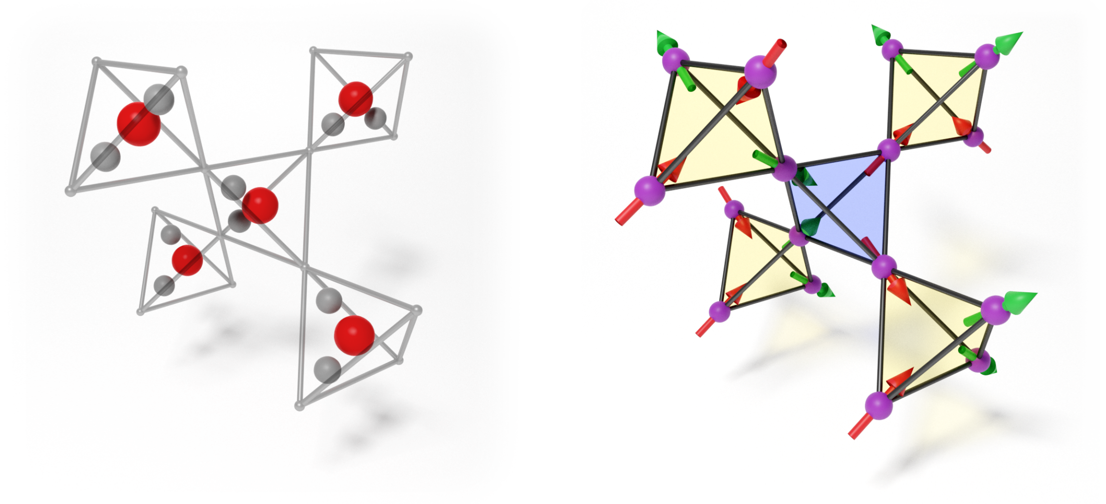

(a) Water ice: each oxygen is covalently bound to two hydrogens and exactly one hydrogen sits between any two neighboring oxygens.

(b) Spin ice: for each tetrahedral cluster, two spins are pointing inwards and two are pointing outwards.

Figure 1.1: Two physical systems obeying the "ice rules": water ice and spin ice. The spin ice is realized in rare-earth oxide pyrochlore materials $Ho_2Ti_2O_7$ [33] and $Dy_2Ti_2O_7$ [34] with Ising spins along the $\langle 111 \rangle$ direction connecting the centers of corner-sharing tetrahedra. In water ice (I_h), the molecules are, too, positioned in an almost tetrahedral coordination. The same pyrochlore lattice is superimposed in panel (a) to reflect that, with the oxygen atoms inscribed into the tetrahedra, even though ice I_h crystallizes in a slightly different lattice geometry. Both panels depict equivalent configurations, *i.e.* the hydrogen atoms in panel (a) are displaced from the sites of the pyrochlore lattice in the direction indicated by the spins on those sites in panel (b).

likewise two also exit it. After coarse graining, this immediately implies that the correlations between magnetic fields a distance $\mathbf{r}$ apart take on a dipolar form [39–41],

$$\langle \mathbf{B}(\mathbf{0}) \otimes \mathbf{B}(\mathbf{r}) \rangle \sim \frac{\mathbf{r}^{\otimes 2} - \|\mathbf{r}\|^2 \mathbb{1}/3}{\|\mathbf{r}\|^5}, \tag{1.1}$$

and thus decays as $1/\|\mathbf{r}\|^3$ at large distances. Power-law correlations like this are unusual away from critical regimes. They manifest themselves as sharp features called "pinch points" in the spin structure factor and have been observed in neutron scattering experiments on $Ho_2Ti_2O_7$ [42].

Violations of the spin-ice rule lead to defects for which $\nabla \cdot \mathbf{B}$ takes on a nonvanishing value which may be interpreted as a magnetic "charge" density. Excitations above the ground state manifold thus correspond to the creation of a pair of magnetic monopoles of opposite charge at which a magnetic field line—in this context referred to as a Dirac string—originates and terminates, respectively [38, 43, 44]. Once created, the monopoles can move away from each other at no additional energy cost. They thus constitute fractionalized excitations and the energy associated with each monopole is half that of a single spin flip [45]. Since the spins carry a magnetic moment, these monopoles exert a magnetostatic Coulomb interaction onto each other. This is weak compared to the electrostatic force but its signature was nonetheless first measured in diffuse neutron scattering experiments on $Dy_2Ti_2O_7$ in 2009 [46]. The ensuing onslaught of experiments has focussed primarily on the dynamics of monopoles both in classical [47] and quantum [48] spin ices. Monopoles have also been observed in artificial spin ice realized in lithographically fabricated magnetic nanodevices [49].

Spin ices are the posterchild of a class of correlated spin states, nowadays collectively known as classical spin liquids (CSLs). More traditionally, these have also been called correlated or cooperative paramagnets as they crucially do not exhibit long-range order, but rather strong algebraically decaying correlations. As in the case of spin ice, these originate from fluctuations within an extensive ground-state manifold which is characterized by local constraints such as the spin-ice rule. The constraints in turn signal the emergence of a gauge theoretical structure, complete with monopole-like fractionalized excitations.

At low enough temperatures, even fluctuations within the ground-state manifold eventually slow down and the CSL may freeze out of equilibrium. For example, in spin ice, at the very least hexagonal rings of six spins can cooperatively flip at once while remaining in the ground state. The ever-smaller tunneling probabilities for such *zero modes* hence cause the spins to freeze into an amorphous glassy state; in $Dy_2Ti_2O_7$ this reportedly happens below $T_f = 0.5\,\mathrm{K}$ [50]. Other types of CSLs may instead enter into an ordered phase below a transition temperature T_c (see "Hidden order" below for a possible mechanism). Either way, the relevant temperatures are expected to lie significantly below the scale set by the Curie-Weiss temperature $|\Theta_{\mathrm{CW}}|$ which provides a rough estimate for the ordering temperature in unfrustrated systems. Θ_{CW} can be determined from the asymptotic high-temperature behavior of the magnetic susceptibility, $\chi^{-1} \sim (T - \Theta_{\mathrm{CW}})$. The frustration-induced CSL behavior thus takes hold in the regime $T_c < T < |\Theta_{\mathrm{CW}}|$ and its extent is commonly quantified by the frustration parameter $f = |\Theta_{\mathrm{CW}}|/T_c$ (or $f = |\Theta_{\mathrm{CW}}|/T_f$ in case of freezing). While $f \sim 5$ may otherwise still occur, frustration can easily result in $f \gg 100$ [51].

Materials with small atomic spins might, however, display an entirely different behavior at the lowest temperatures: quantum fluctuations due to a nonvanishing zero-point energy may allow for the formation of a quantum spin liquid (QSL) which persists down to $T = 0$, corresponding to $f = \infty$.

The energy between any two antiferromagnetically coupled spins is locally minimized by a singlet. One may naively assume that the ground state thus consists of a product of such valence bond singlets, periodically tiled over the bonds of the lattice. Such a valence bond solid (VBS) has a vanishing total spin and is hence nonmagnetic, yet by choosing a specific dimer covering, it breaks lattice symmetries. Anderson proposed that a system might rather form a superposition of all possible dimer coverings of spins into valence bonds on the lattice [52–54], thereby retaining the lattice symmetry. In the language of quantum chemistry, such a state would exhibit valence bonds which constantly fluctuate amongst each other, but do so in a phase-coherent (highly entangled) way, thus coining the name resonating valence bond (RVB) state.

The RVB state is the archetype of QSLs, but a superposition of dimer coverings is not the only possible microscopic realization of a QSL state and a consensus on the defining characteristics of a QSL was not reached until recently (and even that is debateable). Quite generally, however, a "true" QSL would be expected to host fractionalized excitations [51, 55]. This makes them attractive for quantum computation as it allows for the development of topological error correction codes, as exemplified by Kitaev's toric code [56, 57]. Unfortunately, as of yet, not a single QSL has been experimentally identified in an unambiguous way, despite tremendous effort over the past decade. Extensive reviews of the state of the art of experiments into both CSLs and QSL candidates are provided in Refs. 55 and 58.

Hidden order

The experimental identification of spin liquids, both classical and quantum, typically has to resort to a negative definition, *i.e.* ruling out the presence of any symmetry-breaking order, in lieu of experimentally accessible genuine spin-liquid characteristics. This is further complicated by the fact that such orders in frustrated lattice geometries may too elude common experimental probes as they do not give rise to a macroscopically observable magnetization. For this reason, they are referred to as "hidden" orders [59–64].

Indeed, even in Monte Carlo simulations of classical spin models where one has access to the full microscopic spin configuration, identifying the presence of hidden orders remains a highly nontrivial task. This is due to their multipolar nature: in contrast to dipolar orders whose symmetry-breaking is characterized by a nonvanishing vector-like (rank-1) order parameter such as the (staggered) magnetization in the case of (anti)ferromagnetism, frustrated lattice geometries may favor orders which only break part of the full spin-rotational symmetry while staying disordered with respect to the remaining symmetry, giving rise to order parameter tensors of higher rank such as matrices (quadrupolar order) or third-rank tensors (octupolar order). Examples can be found in spin nematic orders [65–76]. Conventional numeric probes then often suffer the same fate as their experimental counterparts and one has to resort to (weak) signatures in thermodynamic properties such as the heat capacity to pin down the presence of a phase transition. Even then, this does not yield any insight into the nature of the tentative phase.

It may seem paradoxical at first that a spin system whose ground state manifold is defined by constraints, which in and of themselves do not break any symmetries, would develop an ordered phase at low temperatures. One mechanism to facilitate symmetry-breaking in classical systems was first described by Villain *et al.* [77]. While by definition all ground states have the same energy, some of them may be entropically selected for their lower free energy. This is the case when a certain subset of ground state configurations admits thermal fluctuations into a vast region of phase space surrounding these ground states at small energy expenditure by means of soft modes[1]. The phenomenon was coined *order-by-disorder* [39] and famously accounts–among other cases [78]—for the selection of coplanar spin order in the Heisenberg antiferromagnet on the kagome lattice which was postulated by Chalker *et al.* in 1992 [79].

---

[1] The term "soft mode" usually refers to any kind of gapless mode, including those with linearly vanishing dispersions; here, modes need to be even "softer", with at-most quadratic dispersion, to fluctuate appreciably down to the low temperatures required for order to emerge.

However, his initial description in terms of a quadrupolar order parameter was later recognized as incomplete and rather called for an additional octupolar order parameter [80–82]. Details are provided in Sec. 2.1.1.

Generalized nematics

Quadrupolar moments also describe the well-known nematic order in liquid crystals. Liquid crystals are (typically) composed of rod-like molecules, or *mesogens* which, below a certain critical temperature, undergo a phase transition where they attain long-ranged orientational order, all the while maintaining fluidity, *i.e.* positional disorder.

In the language of symmetry-breaking, they spontaneously break the orientational O(3) symmetry down to a nontrivial subgroup. Most commonly, uniaxial nematics where the mesogens align along a common axis given by a *director* **D** of unit length while retaining rotational invariance in the plane normal to **D**, corresponding to the infinite dihedral symmetry group $D_{\infty h}$. However, **D** is not the order parameter of the transition as both **D** and −**D** would refer to the same kind of order. In order to capture this additional invariance, one has to promote the vector (rank-1 tensor) **D** to a matrix (rank-2 tensor),

$$\mathbf{Q} = \mathbf{D} \otimes \mathbf{D} - \frac{1}{3}\mathbb{1}, \qquad Q_{ab} = D_a D_b - \frac{1}{3}\delta_{ab}, \tag{1.2}$$

where $a, b = x, y, z$ are the spatial component indices. The additional term $-\mathbb{1}/3$ is conventionally included to render **Q** traceless. One can then construct a Landau theory from this quadrupolar order parameter **Q** and derive a scalar order parameter $q = \sqrt{\operatorname{Tr} \mathbf{Q}^2}$.

O(3) can in fact spontaneously break down to arbitrary 3D point groups [83, 84], giving rise to order parameters given by tensors of different ranks. For instance, the $D_{\infty h}$ symmetry in the above example can further break to smaller subgroups by developing order in the perpendicular plane. For example, a D_{2h} nematic (with the point group symmetry of an irregular orthogonal parallelepiped) is described by a different quadrupolar order parameter matrix (see Sec. 6.2.1) while a D_{3h} nematic (with the point group symmetry of a uniform triangular prism) requires a description in terms of a rank-3 octupolar order parameter tensor (see Sec. 6.2.2).

These generalized nematics thus give rise to a variety of multipolar orders. The smallest symmetry which O(3) can thus be broken down to is naturally given by the point group symmetry of the mesogen. Depending on the details of the system, this may either happen in a single transition from isotropic disorder, or in a succession of two or more phase transitions at successively lower temperatures, each breaking the symmetry to an ever-smaller subgroup. In Sec. 2.2, a gauge model is introduced which allows for the systematic study of various multipolar orders by restricting the gauge field mediating the interaction to representations of arbitrary point groups, thereby mimicing the interaction between mesogens of corresponding point group symmetry.

Unfortunately, only very few experimental realizations of the more exotic nematics exist. One of them is found in liquid crystals formed by viruses in aqueous solution. Aside from filamentous plant viruses which have been shown to exhibit uniaxial order in X-ray diffraction experiments [85], many animal viruses, such as adenoviruses or the polio virus, possess a nonchiral icosahedral (I_h) symmetry[2] and readily form colloidal liquid crystals [86]. This has reached the point where genetic modification of viruses is considered as a way to engineer nanoscopic mesogens for liquid crystals with superior optical properties.

Though, while possibly interesting in their own right, unconventional generalized nematics—and the gauge model simulating their dynamics—primarily serve as a vehicle to explore a wide array of different multipolar orders in a controlled way, whereas here the physical motivation for doing so is primarily derived from the (potential) emergent realization of the same kinds of multipolar orders in frustrated spin systems.

Premise of this thesis

The study of frustrated magnets, particularly the quest for spin liquids—both classical and quantum—remains an active field of research in both theory and experiment. While QSLs have proved more elusive, the occurrence and stability of CSLs, especially as compared to spin nematic phases, is far from understood. Advances in experimental techniques over the past decade have accelerated the pace of the synthesis and charaterization of new materials to the point where it has become a matter of months, not years. Meanwhile the process of piecing together the phase diagram of each new model remains a laborious and manual process which heavily depends on the ingenuity and intuition of individual researchers, rendering it a serious bottleneck.

Devising a machine learning scheme to aid this process, inspired by the recent sprawl of activity, thus seemed like a worthwhile endeavor. However, merely recognizing different phases in frustrated models—while useful—would not have sufficed; rather, a highly interpretable machine is in demand which allows for the reconstruction of the physical order parameter. For this reason, we turned to kernel methods. In Ch. 5, the *tensorial kernel* (TK) is proposed. As the name suggests, its functional form was chosen to be capable of expressing tensorial order parameters like those characteristic of multipolar order, while not imposing any further restrictions other than locality. Its design thus does not require the problem to be already “solved”, but covers the realm of multipolar tensor order parameters exhaustively. For the majority of the thesis, it is combined with a support vector machine, jointly referred to as TK-SVM.

In the final part III, the TK is applied to the infamous case of the aforementioned Heisenberg model on the kagome lattice as well as the XXZ model on the pyrochlore lattice which features a diverse phase diagram, including a spin nematic phase and three types of CSLs [87, 88]. Both of these are introduced more closely in Ch. 2. Indeed, the order parameter tensors of both the spin nematic phase in the case of the XXZ pyrochlore model and the *complete* characterization of the hidden order in the kagome model have been identified by TK-SVM.

Serendipitously, while the original design of the TK was aimed at expressing multipolar order, it turned out to be also capable of expressing the emergent constraints which characterize the ground-state manifold of CSLs and underpin their gauge-theoretical description. In that regard, the method went above and beyond expectations and reconstructed the phase diagram of the XXZ pyrochlore model, including the location of the crossover regimes between different types of CSLs, with little human guidance.

---

[2] The corresponding nematic order is parametrized by a tensor of no less than sixth rank [83], see Eq. (6.15). The icosahedral point group I_h is not to be confused with the ice phase designation I_h (“one hexagonal”).

In the part II leading up to these applications, the toolbox necessary to interpret the classifiers learned by TK-SVM is assembled. A gauge model of generalized nematics (introduced in Sec. 2.2) serves as a testbed to probe a variety of different multipolar orders of high tensor ranks. The tools to extract and infer these order parameter tensors are developed, tried, and tested in a various challenging setups, ranging from the simultaneous occurrence of separate order parameters to the inference of the rank-6 order parameter tensor of an icosahedral nematic. It will also become apparent how TK-SVM, which is technically a supervised classification scheme, can be used in an semantically unsupervised context which is the basis for the unbiased construction of phase diagrams.

2

Models

The purpose of this chapter is to introduce the microscopical models which will be used throughout this thesis and to review some aspects of their physics.

During the development of the machinery for learning order parameter tensors, it is beneficial to scrutinize a system that is known to exhibit a certain multipolar order reliably, is accessible to numerical methods, specifically Monte Carlo, and offers a large variety of distinct nontrivial multipolar orders with tensor descriptions of different ranks. In Sec. 2.2, a gauge model is introduced which can mimic the interaction of nematic mesogens of arbitrary point group symmetries. By choosing a particular point group, the system develops a phase transition into an ordered phase which breaks the O(3) symmetry accordingly. Though somewhat artificial, the gauge model fulfills all of the above requirements which makes it the ideal "guinea pig" model.

In the final part of this thesis, the machinery is subsequently employed to investigate hidden multipolar orders—and nontrivial constraints—which emerge from geometrical frustration. The relevant Hamiltonians and lattice geometries are introduced here first in the ensuing section.

2.1 Frustrated spin models

From the Hubbard model to the Heisenberg model

Much of the attention in the field of condensed matter has been drawn to the analysis of the Hubbard model in the decades that passed since its inception [89]. Derived as an approximate model for itinerant d- and f-electrons in transition metals, its Hamiltonian is comprised of a kinetic term and an on-site Coulomb repulsion,

$$H_{\text{Hubbard}} = -\sum_{ij,s} t_{ij} c^{\dagger}_{is} c_{js} + U \sum_{i} n_{i\uparrow} n_{i\downarrow}, \tag{2.1}$$

where $c^{(\dagger)}_{is}$ are annihilation (creation) operators for Wannier states of electrons with spin $s = \uparrow, \downarrow$ which are localized at lattice site i, obeying fermionic statistics, $\left\{c_{is}, c^{\dagger}_{js'}\right\} = \delta_{ij}\delta_{ss'}$, and $n_{is} = c^{\dagger}_{is} c_{is}$. The tunneling amplitudes $t_{ij} = t^{*}_{ji}$ for "hopping" processes between sites i and j are obtained through a tight-binding approximation and oftentimes restricted to nearest neighbors. The Coulomb interaction between electrons on different sites is screened and becomes thus short-ranged. It is renormalized into an energy U that penalizes double occupations of the same lattice site only.

In the limit of large on-site interaction, $U \gg |t_{ij}|$, and below half filling, double occupations are suppressed and the kinetic term can be considered as a perturbation. The Hamiltonian may then be projected into the subspace of at most singly-occupied sites ($n_i = n_{i\uparrow} + n_{i\downarrow} \leq 1$) by means of the projector $P_s = \prod_i \left(1 - \frac{1}{2} n_i (n_i - 1)\right)$ resulting in the t-J model [90],

$$H_{t\text{-}J} = P_s \left[-\sum_{ij,s} t_{ij} c^{\dagger}_{is} c_{js} + \frac{1}{2} \sum_{ij} J_{ij} \left(\mathbf{S}_i \cdot \mathbf{S}_j - \frac{n_i n_j}{4} \right) \right] P_s, \tag{2.2}$$

where the spin operators (with $\|\mathbf{S}_i\|^2 = S(S+1)$ and $S = 1/2$) are related to the electronic ones by

$$\mathbf{S}_i = \frac{1}{2} \sum_{ss'} c^{\dagger}_{is} \boldsymbol{\sigma}_{ss'} c_{is'}, \tag{2.3}$$

and $J_{ij} = 4|t_{ij}|^2/U$ is the exchange coupling, corresponding to second-order processes where electrons of opposite spins are exchanged between lattice sites. An additional second-order hopping process between two sites via a third is omitted here. Its effect is usually considered to be small, but can become significant on bipartite lattices away from half filling where it facilitates electronic transport within the same sublattice without disturbing the antiferromagnetic order [90].

At half filling, *i.e.* when every lattice site is occupied by exactly one electron, $n_i = 1$, any single hopping process would result in a double occupation. The kinetic term is, hence, annihilated by the projectors P_s. The term $n_i n_j = 1$ is a trivial constant. Thus at half filling, the t-J model reduces to the Heisenberg model:

$$H_{\text{Heisenberg}} = \frac{1}{2} \sum_{i,j} J_{ij}\, \mathbf{S}_i \cdot \mathbf{S}_j. \tag{2.4}$$

This is often further simplified by assuming equal exchange couplings between nearest neighbors only,

$$H_{\text{Heisenberg}} = J \sum_{\langle i,j \rangle} \mathbf{S}_i \cdot \mathbf{S}_j, \tag{2.5}$$

where $\langle i,j \rangle$ denotes summation over bonds between neighboring sites i and j.

The half-filled Hubbard model indeed undergoes a transition from a metallic phase at low U to an insulator. Materials realizing such a Mott insulator are attractive targets in the search for QSLs, however as of yet, none has shown experimental signatures revealing it as an unambiguous QSL [51].

Classical magnetic models

The Heisenberg Hamiltonian (2.5) formally also describes many compounds where the atomic spin of the magnetic ions has a quantum number $S > 1/2$. The limit $S \longrightarrow \infty$ corresponds to the classical case. The spin operators $\mathbf{S}_i$ may then be replaced by classical moments $\mathbf{S}_i \in \mathbb{R}^3$ of unit length, $\|\mathbf{S}_i\| = 1$.

The physics exhibited by the Heisenberg Hamiltonian (2.5) with antiferromagnetic coupling $J > 0$ crucially depends on the geometry of the lattice. On bipartite lattices, such as the square or honeycomb lattice, spins on either sublattice align themselves in opposite directions, the so-called Néel state. This order is parametrized by the staggered magnetization, the sum over all spins with a sign alternating between sublattices, which is itself a vector order parameter. The Néel state—just like the ferromagnetic state for $J < 0$—thus breaks the O(3) symmetry of the Hamiltonian down to O(2) and its ground state degeneracy thus reflects the remaining

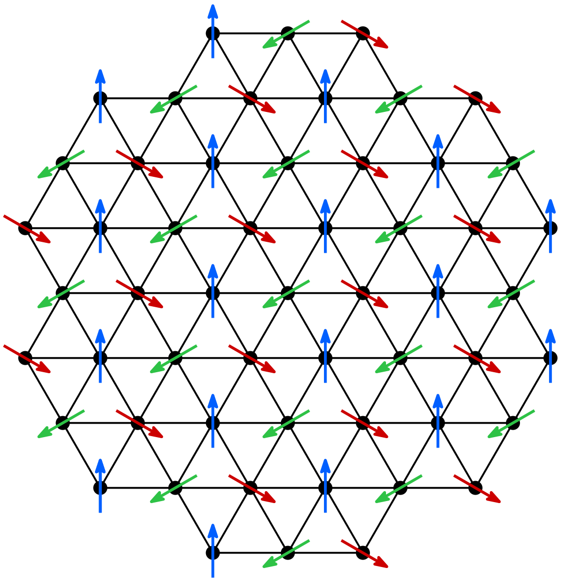

Figure 2.1: The triangular lattice in its $\sqrt{3}\times\sqrt{3}$ ground state. Its name is derived from the fact that the lattice decomposes into three triangular sublattices with a lattice constant that is a factor $\sqrt{3}$ larger than that of the original lattice. Within each triangular plaquette of the original lattice, the spins sum to zero.

global $\mathrm{O}(3)/\mathrm{O}(2) = S^2$ symmetry; it is however not extensive. The Néel state is thus trivially unfrustrated as the energy of each bond can be minimized individually.

In frustrated lattice geometries, this is no longer possible. In some, the ground state manifold is more easily found by rewriting the Hamiltonian (2.5) as a sum over plaquettes. As an example, consider the triangular lattice depicted in Fig. 2.1 which can be written as a sum over all triangles,

$$H_{\mathrm{trig}} = \frac{J}{2}\sum_{\triangle}\sum_{\langle i,j\rangle\in\triangle}\mathbf{S}_i\cdot\mathbf{S}_j = \frac{J}{4}\sum_{\triangle}\left(\left\|\sum_{i\in\triangle}\mathbf{S}_i\right\|^2 - 3\right), \tag{2.6}$$

where the outer sum runs over both up and down triangles (incurring a factor $1/2$ to compensate for the fact that each bond is shared between two triangles), $\langle i,j\rangle\in\triangle$ denotes summation over the three bonds between sites i and j in each triangle, and $i\in\triangle$ runs over the three sites in each triangle.

Thus, a spin configuration for which the total sum on each triangle vanishes,

$$\sum_{i\in\triangle}\mathbf{S}_i = 0, \tag{2.7}$$

is a ground state, should such a configuration exist. Indeed, this is the case for the "$\sqrt{3}\times\sqrt{3}$" state which is also shown in Fig. 2.1. To find its degeneracy, it is instructive to approach the problem constructively. On an empty lattice, one is free to choose the first spin isotropically.

Because of the constraint (2.7), the three spins in any plaquette must be at angles of 120° with one another and lie in the same plane. Once this plane has been chosen (which coincides with the plane of the lattice in Fig. 2.1 for illustrative purposes, but this is arbitrary), the directions of the other two spins on the triangle are determined and one can only fix the chirality of the state by choosing which of the two directions is assigned to which site. Since two spins are shared between adjacent triangles and two spins uniquely determine the third, once the first triangle is fixed, so are all of its neighbors, and so are theirs.... One can thus expand from the central triangle outwards in concentric circles without ever encountering a contradiction. Hence, up to the initial choice of the chirality (and the common plane), the $\sqrt{3} \times \sqrt{3}$-state is unique and, in particular, does not exhibit an extensive ground-state degeneracy (exGSD).

As illustrated in the introduction for the example of water and spin ice, an exGSD gives rise to interesting phenomena such as exotic excitations in CSLs which are generally associated with frustration [91, 92]. However, even though the triangular lattice is often the go-to model of a frustrated system to illustrate that not all bonds can be minimized individually, the Heisenberg model on a triangular lattice is itself not frustrated in the more narrow sense that it does not exhibit an exGSD and hence fluctuations are suppressed at low temperature. In contrast, the Ising model is genuinely frustrated on a triangular lattice as it does exhibit an exGSD [93].

Counting constraints

Moessner and Chalker revived a counting argument first put forth by Maxwell [94] and applied it in the context of magnetism to find the number of independent ground-state degrees of freedom G [69, 95]. In a system with N three-component classical spins, a general spin configuration is fully determined by $F = 2N$ degrees of freedom (two angles per spin). If these are subject to K independent constraints in the ground state, $G = F - K$ degrees of freedom are left. An estimate for K can be obtained by assuming that each plaquette imposes a vector constraint akin to Eq. (2.7). In that case, $K = 3N_{\text{plq.}}$ where the ratio between the number of plaquettes, $N_{\text{plq.}}$, and the total number of spins is given by $N_{\text{plq.}}/N = m/r$ with r, the number of spins in each plaquette, and m, the number of plaquettes each spin takes part in. One thus obtains an estimate for the ground-state degrees of freedom given by

$$G_{\text{plq.}} = 2N - 3N_{\text{plq.}} = \left(2 - 3\frac{m}{r}\right) N. \tag{2.8}$$

In practice, $G_{\text{plq.}}$ is a lower bound for the true G since not all of the constraints are independent and K is thus overestimated. Indeed, in the above explicit construction of the $\sqrt{3} \times \sqrt{3}$ ground state on the triangular lattice ($m = 6$, $r = 3$), occasionally one would encounter triangles whose spins were already fully determined by two neighboring triangles, thus rendering their constraint redundant. Accordingly, $G_{\text{plq.}} = -4N < 0$ underestimates the true $G/N \longrightarrow 0^+$ as $N \longrightarrow \infty$.

Despite its limitations, Eq. (2.8) gives an indication that lattices with corner-sharing geometries ($m = 2$) are particularly susceptible to exGSD. For the pyrochlore lattice, a network of corner-sharing tetrahedra ($r = 4$, see Fig. 1.1), $G_{\text{plq.}}/N = 1/2 > 0$ indicates a continuous exGSD. Indeed, a more careful analysis shows that corrections to this estimate are at most subextensive, $G/G_{\text{plq.}} \to 1$ as $N \to \infty$ [69]. Consequently, the pyrochlore Heisenberg model exhibits CSL behavior down to the lowest temperatures accessible by Monte Carlo, as will be seen in Ch. 8. An interesting marginal case is obtained for the Heisenberg model on the kagome lattice of corner-sharing triangles ($m = 2$, $r = 3$, see Fig. 2.2) for which $G_{\text{plq.}} = 0$. However, in a subset of ground-state configurations, some of the constraints on the plaquettes are in fact linearly dependent which results in $G/N \to 1/9$ upon careful analysis [39]. Hence, this subset contributes extensively to the residual entropy.

In the following subsection, the kagome Heisenberg model is examined more closely, including the characterization of the resulting order. Afterwards, anisotropic generalizations of the Heisenberg model on the pyrochlore lattice are introduced, in particular the XXZ model. Both of these models are subject to an elaborate discussion using TK-SVM in part III of this thesis.

2.1.1 Heisenberg model on the kagome lattice

The Heisenberg Hamiltonian on the kagome lattice can be rewritten as a sum over triangular plaquettes in much the same way as on the triangular lattice in Eq. (2.6). Unlike thereon, each bond is however part of exactly one triangle, so the resulting Hamiltonian formally differs from H_{trig} by a factor of two. Consequently, the same local constraint, Eq. (2.7), applies to its ground-state manifold. This again implies that, within each triangular plaquette, the spins lie in a common plane, spanning angles of 120° with each other.

This is however where the similarity with the triangular lattice ends. Because adjacent triangles on the kagome lattice only share a single spin, their local planes do not need to coincide; rather, they may intersect on a line determined by the shared spin. Following a similar constructive approach for building up a ground state as for the triangular case, starting from a single triangle, each consecutive adjacent triangle that is added allows for the choice of one angle. However, as triangles start to close loops around the hexagonal plaquettes, their planes are not necessarily compatible. Hence, not all of the aforementioned angles can in fact be chosen freely, but are subject to intricate constraints themselves. The exact degeneracy of the ground state is not known. Still, *nonplanar* solutions do exist for which the local plane of the triangles is different and becomes independent for triangles at large distances. This is to be contrasted with the triangular lattice, where the constraint implies a *coplanar* order where all triangles share the same plane, even at (quasi-)long range, thus breaking the O(3) spin-rotational symmetry.

Nonetheless, Chalker *et al.* suggested in 1992 that the kagome-Heisenberg model may still order at low temperatures in a coplanar fashion [79], governed by the order-by-disorder mechanism [77], the rationale being that coplanar configurations give rise to an entire branch of soft modes which they subjected to a harmonic analysis. Meanwhile, nonplanar configurations, which can be generated from coplanar ones by introducing line defects at no energy cost (zero modes), are more irregular and thus cannot host similar long-wave-length excitations. For this reason, coplanar states were conjectured to be entropically selected at low temperatures.

Chalker *et al.* likened the selection of a common plane to the formation of a spin nematic

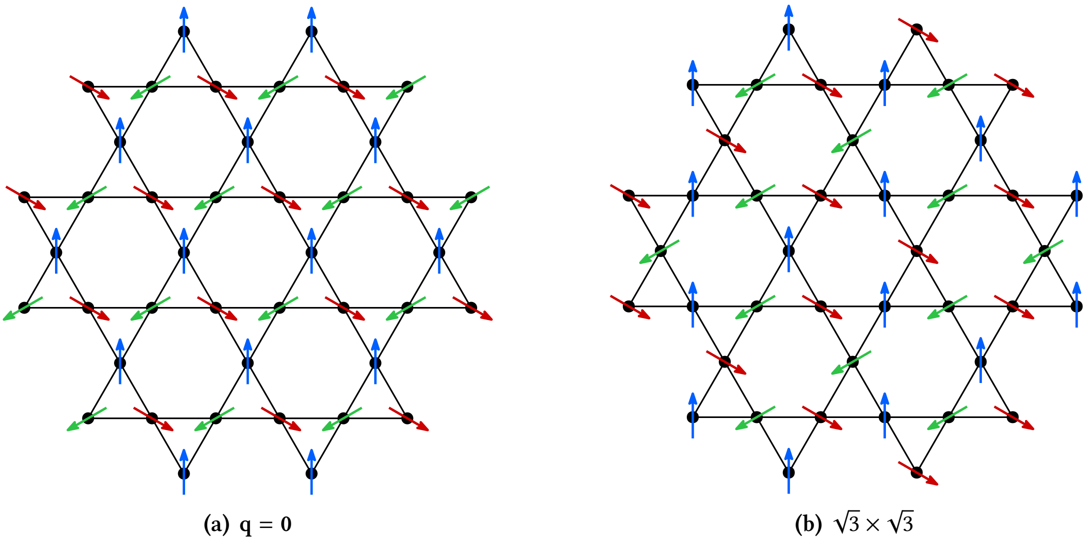
(a) $\mathbf{q} = \mathbf{0}$ (b) $\sqrt{3} \times \sqrt{3}$

Figure 2.2: Periodic coplanar ground states of the kagome-Heisenberg model.

phase. To verify its existence numerically, they introduced a director

$$\boldsymbol{\kappa}^{\triangle} = \frac{2}{3\sqrt{3}}\left(\mathbf{S}_1 \times \mathbf{S}_2 + \mathbf{S}_2 \times \mathbf{S}_3 + \mathbf{S}_3 \times \mathbf{S}_1\right), \tag{2.9}$$

which is normal to the local plane span by the three spins on any given triangular plaquette, $\mathbf{S}_1, \mathbf{S}_2, \mathbf{S}_3$. They preceded to construct a quadrupolar order parameter,

$$Q_{ab}^{(\kappa)} = \frac{1}{N_{\triangle}} \sum_{\triangle} \left(\kappa_a^{\triangle} \kappa_b^{\triangle} - \frac{1}{3} \left\| \boldsymbol{\kappa}^{\triangle} \right\|^2 \delta_{ab} \right), \tag{2.10}$$

and monitored the behavior of the corresponding quadrupolar correlations between neighboring and next-nearest-neighboring triangles in a Monte Carlo simulation. The temperatures they could reach were however insufficient to observe the transition; still, the correlations were seen to become stronger with lower temperature, consistent with quasi-long-range[1] order at either $T \longrightarrow 0$ or at small but finite temperature.

Subsequent Monte Carlo studies indeed suggested the presence of a finite-temperature transition into an ordered coplanar state. In Ref. 97, temperatures of $T = 0.005J$ were reached and the onset of quadrupolar nematic order was observed. In hindsight, this was quite close to the actual transition temperature of $T_K = 0.004J$ [82] which is also observed in Ch. 9. Some disagreement arose as to whether an even smaller subset of coplanar states would be selected. Out of the extensively many coplanar states, two chiral states stand out as they are the only ones to be described by a single wave vector: the $\mathbf{q} = \mathbf{0}$ state where each upwards or downwards

---

[1] Because of the Mermin-Wagner theorem [96], true long-range order is not supported by the two-dimensional kagome-Heisenberg model. Rather, the alledged transition is akin to the *Berezinskii-Kosterlitz-Thouless*-type [81, 82], giving rise to algebraically decaying correlations ("quasi-long-range" order).

pointing triangle features the same spin pattern [Fig. 2.2(a)] and the $\sqrt{3}\times\sqrt{3}$ state, corresponding to $\mathbf{q} = (\frac{4\pi}{3}, 0)$, for which the three spin sublattices themselves form kagome lattices with a lattice constant enlarged by a factor of $\sqrt{3}$ as compared to the original lattice [Fig. 2.2(b)]. The $\sqrt{3}\times\sqrt{3}$ state was conjectured to be selected in the ordered phase. However, this was consequently falsified by mapping the coplanar states to a three-state Potts model which can be simulated to much lower temperatures thanks to a loop update scheme and the model was found to relax back into a nonchiral state from either $\mathbf{q} = \mathbf{0}$ or $\sqrt{3}\times\sqrt{3}$ [98].

The selected ordered state thus still fluctuates among all coplanar states at $T < T_K$. Its description in terms of a quadrupolar order parameter, Eq. (2.10), or its equivalent single-spin form which breaks the same symmetry,

$$Q_{ab} = \frac{1}{N}\sum_i \left(S_{i,a}S_{i,b} - \frac{1}{3}\delta_{ab}\right) \tag{2.11}$$

is—however—incomplete as it would admit spins to rotate freely within the plane, corresponding to the $D_{\infty h}$ symmetry captured by $\mathbf{Q}$. This is not what Chalker *et al.* had in mind, stating that the coplanar state "is highly constrained, in the sense that only three distinct spin orientations occur, but the subset as a whole retains a large degeneracy" [79]. The correct *triatic* symmetry of the coplanar state is thus given by D_{3h} which was first realized by the authors of Ref. 80 who also proposed a rank-3 description to supplement the quadrupolar one. The correct order parameter set was eventually obtained in 2008 by Zhitomirsky [82], consisting of the octupolar triatic tensor,

$$T_{abc} = \frac{1}{N}\sum_i \left(S_{i,a}S_{i,b}S_{i,c} - \frac{1}{5}S_{i,a}\delta_{bc} - \frac{1}{5}S_{i,b}\delta_{ca} - \frac{1}{5}S_{i,c}\delta_{ab}\right), \tag{2.12}$$

as the primary order parameter and the quadrupolar tensor, Eq. (2.11), as the secondary order parameter. He also demonstrated how these may be used to construct the corresponding Landau theory.

Early on, experimental efforts into kagome systems focused almost exclusively on the compound $\mathrm{SrCr}_{8-x}\mathrm{Ga}_{4+x}\mathrm{O}_{19}$ (SCGO) in which the magnetic Cr^{3+} ions ($S = 3/2$) form layers of kagome lattices. SCGO was found to exhibit strong frustration as it did not order down to helium temperatures ($T = 4.2\,\mathrm{K}$), despite its Curie-Weiss temperature of $\Theta_{\mathrm{CW}} = 515\,\mathrm{K}$ [99]. It was however found to freeze into a spin glass below $T_f = 3.3\,\mathrm{K}$ [100] rather than order into a coplanar state and it has been argued that the order-by-disorder effect may break down due to defects which destabilize soft modes [101–103]. In present-day alternatives however, such as $\mathrm{Y}_{0.5}\mathrm{Ca}_{0.5}\mathrm{BaCo}_4\mathrm{O}_7$ ($S = 3/2$) [104] and deuteronium jarosite $(\mathrm{D}_3\mathrm{O})\mathrm{Fe}_3(\mathrm{SO}_4)_2(\mathrm{OD})_6$ ($S = 5/2$) [105], properties of the coplanar phase have been observed in agreement with Monte Carlo simulations. These materials thus seem to realize the classical nearest-neighbor Heisenberg model on the kagome lattice quite well.

2.1.2 Anisotropy on the pyrochlore lattice

As has been previously argued on the basis of the Maxwellian counting argument, Eq. (2.8), the ground state of the Heisenberg Hamiltonian (2.5), on the pyrochlore lattice is extensively underconstrained and the model continues to exhibit CSL behavior down to the lowest accessible temperatures.

A more varied phase diagram is obtained when the extensive ground-state degeneracy is partially lifted by a modification of the exchange interaction. In particular, due to spin-orbit coupling, the geometry of the pyrochlore lattice may induce a uniaxial anisotropy in the exchange interaction along the local ⟨111⟩ axis connecting the centers of the adjacent tetrahedra. By choosing a local coordinate system[2] attached to each sublattice, such that the local z direction aligns with the ⟨111⟩ axis, the resulting Hamiltonian takes the form of the XXZ model,

$$H_{\mathrm{XXZ}} = \sum_{\langle i,j\rangle} \left[J_{zz} S_{i,z} S_{j,z} - J_{\pm} \left(S_i^+ S_j^- + S_i^- S_j^+ \right) \right], \tag{2.13}$$

where $S_j^{\pm} \coloneqq S_{j,x} \pm i S_{j,y}$ has been introduced[3]. This model has recently been investigated and a rich phase diagram was reported [87, 106], including a spin nematic phase and a wide array of CSLs, characterized by different local constraints. These findings are reproduced in Ch. 8 within the machine learning framework developed in this thesis.

Likewise, the exchange interaction may attain an antisymmetric component in the form of the Dzyaloshinsky-Moriya interaction [107, 108] as a result of spin-orbit coupling,

$$H_{\mathrm{DM}} = \sum_{\langle i,j\rangle} \mathbf{D}_{ij} \cdot \left(\mathbf{S}_i \times \mathbf{S}_j \right). \tag{2.14}$$

This term favors spin canting and gives rise to complex magnetic structures, called skyrmions which are of particular interest in spintronics applications.

Both of these modifications are encompassed by a generalized exchange Hamiltonian,

$$H_{\mathrm{aniso.}} = H_{\mathrm{XXZ}} + H_{\mathrm{DM}} = \sum_{\langle i,j\rangle} \mathbf{S}_i \cdot \mathbf{J} \mathbf{S}_j, \qquad \mathbf{J} = \begin{bmatrix} -2J_{\pm} & D & 0 \\ -D & -2J_{\pm} & 0 \\ 0 & 0 & J_{zz} \end{bmatrix} \tag{2.15}$$

where the exchange coupling J in Eq. (2.5) is replaced by an exchange tensor $\mathbf{J}$. The above form of $\mathbf{J}$ assumes that $\mathbf{D}_{ij} = (0, 0, D)$. In the next chapter, Monte Carlo update schemes based on this general form (2.15) will be presented. The remainder of this thesis will not further study the effects of H_{DM}.

---

[2] In a global coordinate frame where the four sublattice spins occupy the positions $\mathbf{r}_i, i = 0, 1, 2, 3$, the axes $\{\mathbf{x}_i, \mathbf{y}_i, \mathbf{z}_i\}$ in the local frame are given by:

$$\begin{array}{llll}
\mathbf{r}_0 = \frac{a}{8}(+1, +1, +1), & \mathbf{x}_0 = \frac{1}{\sqrt{6}}(-2, +1, +1), & \mathbf{y}_0 = \frac{1}{\sqrt{2}}(0, -1, +1), & \mathbf{z}_0 = \frac{1}{\sqrt{3}}(+1, +1, +1), \\
\mathbf{r}_1 = \frac{a}{8}(+1, -1, -1), & \mathbf{x}_1 = \frac{1}{\sqrt{6}}(-2, -1, -1), & \mathbf{y}_1 = \frac{1}{\sqrt{2}}(0, +1, -1), & \mathbf{z}_1 = \frac{1}{\sqrt{3}}(+1, -1, -1), \\
\mathbf{r}_2 = \frac{a}{8}(-1, +1, -1), & \mathbf{x}_2 = \frac{1}{\sqrt{6}}(+2, +1, -1), & \mathbf{y}_2 = \frac{1}{\sqrt{2}}(0, -1, -1), & \mathbf{z}_2 = \frac{1}{\sqrt{3}}(-1, +1, -1), \\
\mathbf{r}_3 = \frac{a}{8}(-1, -1, +1), & \mathbf{x}_3 = \frac{1}{\sqrt{6}}(+2, -1, +1), & \mathbf{y}_3 = \frac{1}{\sqrt{2}}(0, +1, +1), & \mathbf{z}_3 = \frac{1}{\sqrt{3}}(-1, -1, +1).
\end{array}$$

where a is the length of the traditional cubic unit cell made of 16 sites.

[3] This notation has been chosen in alignment to the one used in Ref. 87. $S_j^{\pm}$ alludes to the ladder operators in the quantum version of Eq. (2.13), yet the model simulated and scrutinized in Ch. 8 is entirely classical. In less suggestive terms, $J_{xx} = J_{yy} = -2J_{\pm}$.

In real materials, the pyrochlore lattice is commonly realized by magnetic ions within an otherwise nonmagnetic crystal. Examples include the spin-ice materials $Ho_2Ti_2O_7$ ($S = 8$) and $Dy_2Ti_2O_7$ ($S = 15/2$) discussed in the introduction where the rare-earth ions Ho^{3+} ($S = 8$) and Dy^{3+} ($S = 15/2$) form the pyrochlore lattice. Crystal-field effects may then induce a single-ion anisotropy

$$H_{\text{cf.}} = -A \sum_i \left(\mathbf{S}_i \cdot \mathbf{n}_i\right)^2, \tag{2.16}$$

where $\mathbf{n}_i$ is the local easy ($A > 0$) or hard ($A < 0$) axis. In the case of $Ho_2Ti_2O_7$, the easy-axis anisotropy is on the order of $A \sim 50\,\mathrm{K}$ along the $\langle 111 \rangle$ (local z) axis whereas the exchange interaction is on the order of $1\,\mathrm{K}$ [33]. Thus, the low-temperature physics is predominantly governed by the $|m_S = \pm 8\rangle$ doublet, hence resulting in an effective Ising-like model.

2.2 Gauge model of generalized nematics

As motivated in the introduction, generalized nematics with polyhedral mesogens can serve as a testbed for the detection and realization of multipolar orders. To this end, a lattice gauge model is employed [83]. On each site of a cubic lattice, a triad of three orthogonal "spins", $\{\mathrm{S}^{\mathrm{l}}, \mathrm{S}^{\mathrm{m}}, \mathrm{S}^{\mathrm{n}}\}$ with $\mathrm{S}^\alpha \times \mathrm{S}^\beta = \pm\varepsilon_{\alpha\beta\gamma}\mathrm{S}^\gamma$, fully determines the orientation (and chirality) of a mesogen. $\alpha, \beta, \gamma = \mathrm{l}, \mathrm{m}, \mathrm{n}$ are referred to as "color indices". The classical Hamiltonian is then given by

$$H = \sum_{\langle i,j \rangle} \sum_{\alpha,\beta,\gamma} \sum_{a,b} J_{ab}^{\alpha\beta} S_{i,a}^{\alpha} U_{ij}^{\beta\gamma} S_{j,b}^{\gamma}, \tag{2.17}$$

where the interaction between mesogens on nearest-neighboring sites is mediated through additional fields $U_{ij} \in G \subset \mathrm{O}(3)$ which live on the bonds. G is the intended point group of the mesogens. These fields are in fact gauge fields, as the Hamiltonian (2.17) possesses a local point-group symmetry (Einstein summation implied),

$$\begin{aligned} S_{i,a}^{\alpha} &\mapsto \Lambda_i^{\alpha\alpha'} S_{i,a}^{\alpha'}, && \qquad (2.18)\\ U_{ij}^{\alpha\beta} &\mapsto \Lambda_i^{\alpha\alpha'} U_{ij}^{\alpha'\beta'} \Lambda_j^{\beta'\beta}, && \forall\, \Lambda_i, \Lambda_j \in G, \qquad (2.19) \end{aligned}$$

in addition to a global O(3) symmetry,

$$S_{i,a}^{\alpha} \mapsto S_{i,a'}^{\alpha} \Omega_{a'a}, \qquad \forall\, \Omega \in \mathrm{O}(3). \tag{2.20}$$

Since it is impossible to spontaneously break a gauge symmetry [109], the Hamiltonian (2.17) eventually orders into a state which breaks O(3) down to G, possibly through one or more intermediate phases with symmetry G' such that $G \subset G' \subset \mathrm{O}(3)$ [110]. The ground-state manifold is hence given by $\mathrm{O}(3)/G$. The phase transitions between these phases have been found to be generically of first order, except in special cases where fine-tuning of the interaction coupling can give second order transitions [1].

For example, when $G = \mathrm{O}(2)$, the gauge theory recovers the Heisenberg model with general exchange interaction, Eq. (2.15), while for $G = D_{\infty h}$ it reduces to the Lebwohl-Lasher model [111, 112],

$$H_{\mathrm{LL}} = \sum_{\langle i,j \rangle} J'_{ab} \left(S^{\mathrm{n}}_{i,a} S^{\mathrm{n}}_{j,b} \right)^2 . \tag{2.21}$$

A mathematical derivation of these limits is provided in Ref. 84.

In the course of this thesis, the gauge model (2.17) will be used to produce spin configurations for a number of different choices of G. In Sec. 6.1 and Sec. 6.2.1, a uniaxial ($G = D_{\infty h}$) and biaxial ($G = D_{2h}$) nematic are simulated, respectively, both of which give rise to different quadrupolar orders. In Sec. 6.2.2, a different biaxial nematic with $G = D_{3h}$ presents a case where two order parameters, a quadrupolar uniaxial one and an octupolar (rank 3) biaxial one, appear in unison. In Sec. 6.3, several even larger point groups are considered which give rise to multipolar order with high-rank order parameters; specifically $G = T_d$ (rank 3), $G = O_h$ and $G = T_h$ (rank 4), and $G = I_h$ (rank 6). A systematic abstract classification of these has only been achieved recently [84, 113, 114].

For the purpose of machine-learning these order parameters, raw configurations are sampled from the Monte Carlo simulation of Eq. (2.17) and fed to the tensorial kernel (see Ch. 5). The three “spins” defining the local triad are thus treated as separate spins in a spin cluster. Their Greek color index takes the place of the sublattice index.

Part I

Methods

3

Classical Monte Carlo

In this chapter, the Monte Carlo method is introduced. Particular attention will be paid to the update schemes suitable for simulating frustrated classical spin systems, and specifically the (generalized) Heisenberg Hamiltonian, Eq. (2.15). Snapshots of the spin configuration as obtained from the Monte Carlo simulation are used to train the machine-learning algorithm in the subsequent chapters.

Henceforth, we shall denote by $\mathcal{X} = \{\mathbf{x}_i \mid i \in I\}$ the space of classical microscopic configuration of the system under investigation. In lattice systems, it is given by the Cartesian product of the local states on each lattice site, $\mathcal{X} = \mathcal{X}_{\text{site}}^N$, N being the number of lattice sites. For example, $\mathcal{X}_{\text{site}} = \mathbb{Z}_q$ for the q-states Potts model, $\mathcal{X}_{\text{site}} = S^1$ for the XY model, and $\mathcal{X}_{\text{site}} = S^2$ for the Heisenberg model.

$\mathcal{X}$ is a finite set only for systems with discrete degrees of freedom, in which case we denote by N_C the total number of configurations[1]. In the Potts model, $N_C = q^N$ exemplifies the exponential growth of the configuration space. This “curse of dimensionality” prohibits the use of direct summation over all states to calculate the partition function or thermal expectation values.

Monte Carlo methods overcome this “curse” by sampling a sparse and finite subset of N_{MC} configurations, enumerated by index set $J \subset I$,

$$\langle A \rangle = \sum_{i \in \mathcal{I}} P(\mathbf{x}_i) A(\mathbf{x}_i) \approx \frac{1}{N_{\text{MC}}} \sum_{j \in \mathcal{J}} A(\mathbf{x}_j) = \langle A \rangle_{\text{MC}}\,, \tag{3.1}$$

where configurations $\mathbf{x}_j$ are drawn according to their canonical distribution function,

$$P(\mathbf{x}) = e^{-\beta E(\mathbf{x})}/Z, \qquad\qquad Z = \sum_{i \in \mathcal{I}} e^{-\beta E(\mathbf{x}_i)}, \tag{3.2}$$

where $\beta = 1/(k_B T)$ is the inverse temperature at which the system is simulated. Doing so allows for an efficient approximation of the true thermal expectation value, as configurations are more likely to be included the more likely they are to be visited by the physical system in the course of its time evolution, a fact that is known as importance sampling. The error of this approximation systematically vanishes as $1/\sqrt{N_{\text{MC}}}$, independent of the dimension of the configurations. The efficiency of Monte Carlo methods then relies on the algorithmic generation of random P-distributed configurations which will concern us for the remainder of this chapter.

Monte Carlo techniques are also widely applied to study quantum systems where the state space is even larger owing to the growth of dimensionality of the local Hilbert space with the number of basis states. In many quantum Monte Carlo (QMC) schemes, this is resolved by mapping the D-dimensional quantum system to a $(D+1)$-dimensional classical system where the configurations are again restricted to a set of basis states that is closed under the update

---

[1] The discrete case will be assumed here for simplicity, but the discussion carries over to the continuous case where $\mathcal{X}$ is uncountably infinite and summation over i has to be replaced by integration over continuous variables.

scheme. Other quantum Monte Carlo schemes such as variational Monte Carlo or diagrammatic Monte Carlo take a more abstract view but ultimately arrive at a multidimensional integration problem that is again tackled by importance sampling. Unlike in the classical case, the configuration probabilities are no longer given by the (positive) Boltzmann weights, Eq. (3.2), and may no longer be positive, resulting in the infamous sign problem. The naive remedy in such a scenario of sampling $\langle \mathrm{sgn}(P)A\rangle / \langle \mathrm{sgn}(P)\rangle$ according to $|P(\mathbf{x}_i)|$ results in exponentially large errors due to the vanishing expectation value of the sign, rendering QMC infeasible for some systems.

The presence of a sign problem depends on the employed QMC scheme but frustrated lattice geometries are notorious for introducing sign problems. This is one reason for limiting the scope of the discussion of machine learning techniques for phase classification in this thesis to classical models. Another lies in the fact that QMC configurations in many schemes incorporate the quantumness by adding an imaginary time-like dimension to capture dynamic correlations within the quantum state. It is not readily apparent how to properly isolate the relevant features from such QMC configurations and remains subject to further investigation.

3.1 Markov chain Monte Carlo

Generating independent random configurations from scratch according to the thermal distribution $P(\mathbf{x})$ is in general not possible efficiently. Instead, a stochastic process is employed which, starting from some initial configuration $\mathbf{x}_{i(0)}$, takes the system through a series of N_{MC} updates,

$$\mathbf{x}_{i(0)} \longrightarrow \mathbf{x}_{i(1)} \longrightarrow \cdots \longrightarrow \mathbf{x}_{i(N_{\mathrm{MC}})}. \tag{3.3}$$

At each update step, the current configuration $\mathbf{x}_{i(n)}$ transitions to the next one with probabilities $P(\{\mathbf{x}_{i(k)}\}_{k=0}^{n} \longrightarrow \mathbf{x}_{i(n+1)})$ which are engineered to achieve the desired target distribution. Whereas these transition probabilities could in principle depend on the entire history of the system, the most simple choice employs a Markov process in which the transition probabilities in each update step depend only on the current configuration, $P(\mathbf{x}_{i(n)} \longrightarrow \mathbf{x}_{i(n+1)})$. In such a situation, the stochastic process is referred to as a Markov chain and its application to traverse the configuration space of a Monte Carlo simulation is known as Markov chain Monte Carlo (MCMC).

Given an ensemble of configurations which at one point in time are distributed according to some $P(\mathbf{x})$, the resultant distribution, $P'(\mathbf{x})$, after carrying out one Markovian update step is given by the master equation,

$$P'(\mathbf{x}) = P(\mathbf{x}) + \sum_{j} \left[P(\mathbf{x}_j)P(\mathbf{x}_j \longrightarrow \mathbf{x}) - P(\mathbf{x})P(\mathbf{x} \longrightarrow \mathbf{x}_j) \right], \tag{3.4}$$

where the two terms in the sum track the influx to and the efflux from the current configuration, respectively. In the MCMC setting, one seeks to sample configurations according to a stationary thermal distribution, meaning that the transition probabilities must satisfy the fixed point condition of the master equation, given that the system is already thermalized. Thus, the total influx and efflux must cancel for each configuration. A sufficient (albeit not necessary) condition to ensure this is given by detailed balance,

$$P(\mathbf{x}_i)P(\mathbf{x}_i \longrightarrow \mathbf{x}_j) = P(\mathbf{x}_j)P(\mathbf{x}_j \longrightarrow \mathbf{x}_i) \qquad \forall\, i \neq j, \tag{3.5}$$

where each possible update step is individually balanced with its reverse.

To ensure detailed balance algorithmically, the transition probabilities factorize into the probability distribution for proposing an update to configuration $\mathbf{x}_j$, given the current configuration $\mathbf{x}_i$, and a subsequent acceptance probability which decides if the update to $\mathbf{x}_j$ is indeed carried out, or if the system remains in $\mathbf{x}_i$,

$$P(\mathbf{x}_i \longrightarrow \mathbf{x}_j) = P_{\text{proposal}}(\mathbf{x}_i \longrightarrow \mathbf{x}_j) \times P_{\text{accept}}(\mathbf{x}_i \longrightarrow \mathbf{x}_j). \tag{3.6}$$

While the former is determined by the algorithmic generation of tentative updates, the latter is then chosen to satisfy detailed balance. In general, it is desirable to absorb as much of the total transition probability in the proposal step to keep the acceptance probability close to unity.

In addition to observing detailed balance, the update scheme must also ensure that the entire configuration space is reachable through a finite number of updates, a requirement which, alluding to the eponymous concept from statistical mechanics, is known as ergodicity. The master equation (3.4) may also be cast in matrix form, $P' = TP$, with the transition matrix $T_{ij} = P(\mathbf{x}_j \longrightarrow \mathbf{x}_i) \geq 0$. T is obviously a row-stochastic matrix[2]; additionally, for an ergodic Markov process, T is seen to be primitive[3]. The Perron-Frobenius theorem then states that T has a nondegenerate eigenvalue 1 whose corresponding eigenvector P is positive ($P(\mathbf{x}_i) > 0\ \forall\, i$), representing the desired fixed-point (thermal) distribution, $P = TP$. All other eigenvalues are strictly less than one in modulus, meaning that the system will converge to the thermal distribution from any initial configuration [115]. The characteristic time scale of this thermalization is given by the eigenvalue with the second largest absolute value. In practice, this is not accessible analytically and one resorts to heuristic arguments to allow for a sufficiently long thermalization phase before commencing the measurement phase.

During the measurement phase, after each (MC) update step, the relevant observables are calculated with respect to the current configuration and accumulated in some way. Since Markovian updates will typically alter the configuration only locally or on a finite-size cluster, such that the update can be proposed and the energy difference evaluated in constant complexity, the updated configuration is not entirely decorrelated from its predecessors. These autocorrelations decay exponentially with a characteristic "time" scale (measured in MC update steps), dubbed autocorrelation time. Thus, a naive estimate of the error on the mean value, σ_{naive}, is bound to underestimate the true statistical error. By averaging the measurements within a hierarchy of successively larger bins and considering the sample variance of these bin averages, autocorrelations among bins vanish as the bin size exceeds the autocorrelation time. Given enough statistics, the error obtained at sufficiently high binning levels will eventually saturate to the "true" error, σ_{true}. An estimate for the (integrated) autocorrelation time may be obtained as $\tau = \sigma^2_{\text{true}}/(2\sigma^2_{\text{naive}})$ [116]. More sophisticated error estimates, especially for estimating the error bars on derived quantities, may be obtained through the jackknife and bootstrap resampling methods, but these require access to the full time series.

---

[2] T is row-stochastic, iff $0 \leq T_{ij} \leq 1\ \forall\, i, j$, $\sum_j T_{ij} = 1\ \forall\, i$.

[3] T is *primitive*, iff $\forall\, i, j\ \exists\, m \in \mathbb{N}$, such that $(T^m)_{ij} > 0$ (Frobenius test).

3.2 Single spin updates

In single spin updates, one randomly picks a lattice site k and proposes an update of spin $\mathbf{S}_k$ to $\mathbf{S}'_k$. The random choice of the lattice site incurs a factor of $1/N$ in the proposal probability which however cancels in the detailed balance equation. A couple of different options are feasible for the specific choice and subsequent acceptance of $\mathbf{S}_k$ which are presented below. Conventionally, N such single spin updates are executed in sequence and together constitute one MC step, to account for the extensiveness of the configuration, *i.e.* to give every spin the chance of being updated on average once per MC step.

Generally speaking, single spin updates change the spin configuration only locally which both makes them very versatile and leads to slow thermalization and long autocorrelation times, especially near phase transitions ("critical slowing-down") or in frustrated or disordered systems with a nontrivial ground state degeneracy at low temperature. Alternatives to single spin updates have been developed in the course of the past decades. Cluster updates such as the Swendsen-Wang algorithm [117] and the Wolff algorithm [118] combat critical slowing-down but accommodate only a limited range of models and fail to produce efficient dynamics in frustrated antiferromagnets. More recently, worm algorithms on the dual lattice have been developed [119] and applied to frustrated Ising antiferromagnets [120, 121]. However, no such cluster update exists to date that can tackle continuous degrees of freedom (XY, O(2); or Heisenberg, O(3), spins) on frustrated lattices. In its absence, single spin updates remain the only recourse to achieve an ergodic update scheme.

A number of remedies exist to facilitate single spin updates: microcanonical updates which propose updates between configurations with the same energy and will, hence, be always accepted, allowing for the traversal of frustrated ground state manifolds; and parallel tempering which alleviates the above issues by performing a random walk through parameter space, allowing individual simulations to fight their way out of challenging parameter regimes, only to reenter them again later. Both of these are discussed in the forthcoming sections, whereas neither is ergodic on its own but meant to supplement the single spin update, nor can it fully overcome the shortcomings of the latter.

3.2.1 Metropolis-Hastings algorithm

Once a random lattice site k has been picked, one may replace the old spin $\mathbf{S}_k$ by a new spin $\mathbf{S}'_k$, sampled isotropically from the unit sphere. Thus, the reverse update will be proposed with an equal probability and the proposal probabilities in the detailed balance equation cancel, resulting in a ratio of the acceptance probabilities which is determined purely by the energy difference due to the spin update,

$$\frac{P_{\text{accept}}(\mathbf{x}_i \longrightarrow \mathbf{x}_j)}{P_{\text{accept}}(\mathbf{x}_j \longrightarrow \mathbf{x}_i)} = \frac{P(\mathbf{x}_j)}{P(\mathbf{x}_i)} = e^{-\beta[E(\mathbf{x}_j)-E(\mathbf{x}_i)]} =: R_{ij} > 0. \tag{3.7}$$

The Metropolis solution [122] satisfies the above equation by choosing $P_{\text{accept}}(\mathbf{x}_i \longrightarrow \mathbf{x}_j) =$

$\min\left\{1, R_{ij}\right\}$, *i.e.* by accepting the update always (if $R_{ij} > 1$), or with probability $R_{ij} < 1$,

$$\frac{P_{\text{accept}}(\mathbf{x}_i \longrightarrow \mathbf{x}_j)}{P_{\text{accept}}(\mathbf{x}_j \longrightarrow \mathbf{x}_i)} = \frac{\min\left\{1, R_{ij}\right\}}{\min\left\{1, R_{ji}\right\}} = \frac{\min\left\{1, R_{ij}\right\}}{\min\left\{1, R_{ij}^{-1}\right\}} = R_{ij}, \tag{3.8}$$

as either $R_{ij} \le 1$ or $R_{ij}^{-1} \le 1$.

In the case of the (anisotropic) nearest-neighbor Heisenberg model, the Hamiltonian, Eq. (2.15), can be rewritten to single out the spin at site k,

$$H = \sum_{\substack{\langle i,j\rangle \\ i,j\neq k}} \mathrm{S}_i \cdot \mathbf{J}\, \mathrm{S}_j + \sum_{\substack{j \\ \text{n.n. of } k}} \mathrm{S}_k \cdot \mathbf{J}\, \mathrm{S}_j = H_k^{\text{rest}} + \mathrm{S}_k \cdot \mathbf{M}_k, \qquad \mathbf{M}_k = \mathbf{J} \sum_{\substack{j \\ \text{n.n. of } k}} \mathrm{S}_j, \tag{3.9}$$

such that the energy difference is merely given by the scalar product between the change of the spin at the selected site and the intrinsic magnetic field $\mathbf{M}_k$ it feels,

$$E(\{\mathrm{S}_1, \ldots, \mathrm{S}'_k, \ldots, \mathrm{S}_N\}) - E(\{\mathrm{S}_1, \ldots, \mathrm{S}_k, \ldots, \mathrm{S}_N\}) = (\mathrm{S}'_k - \mathrm{S}_k) \cdot \mathbf{M}_k. \tag{3.10}$$

The resulting transition probabilities hence read:

$$P(\{\ldots \mathrm{S}_k \ldots\} \longrightarrow \{\ldots \mathrm{S}'_k \ldots\}) = \frac{1}{N} \frac{\mathrm{d}\Omega_k}{4\pi} \times \min\left\{1, e^{-\beta(\mathrm{S}'_k - \mathrm{S}_k)\cdot \mathbf{M}_k}\right\}. \tag{3.11}$$

At low temperatures, the energy difference may be too large to allow for sufficiently high acceptance rates. To a certain point, this can be avoided by restricting the proposal of the updated spin S'_k to a cone around the original spin S_k of aperture $2\theta_0$. As long as the aperture angle is keep constant, detailed balance is preserved. Since $\|\mathrm{S}'_k - \mathrm{S}_k\| = 2\sin(\theta/2)$, a sufficiently narrow cone will boost acceptance rates. This may be particularly beneficial to capture low temperature classical spin wave excitations but will generally not help with frustrated ground states.

Algorithm 1: Cone-restricted Metropolis update for the (anisotropic) Heisenberg model

```
repeat $N$ times
    $k \longleftarrow$ UniformInteger$[1, N]$
    $\mathbf{M} \longleftarrow \mathbf{J} \sum_j \mathbf{S}_j$    // $j$ runs over nearest neighbors of $k$
    $\varphi \longleftarrow$ Uniform$[0, 2\pi]$
    $\cos\theta \longleftarrow$ Uniform$[\cos\theta_0, 1]$
    $\mathbf{S}'_k \longleftarrow \begin{bmatrix} \sqrt{1-\cos^2\theta}\cos\varphi \\ \sqrt{1-\cos^2\theta}\sin\varphi \\ \cos\theta \end{bmatrix}$
    $\mathbf{S}'_k \longleftarrow \mathbf{R}\mathbf{S}_k$    where  $\mathbf{R} = \begin{bmatrix} S_{k,x}S_{k,z}/\sqrt{1-S_{k,z}^2} & -S_{k,y}/\sqrt{1-S_{k,z}^2} & S_{k,x} \\ S_{k,y}S_{k,z}/\sqrt{1-S_{k,z}^2} & S_{k,x}/\sqrt{1-S_{k,z}^2} & S_{k,y} \\ -S_{k,y}/\sqrt{1-S_{k,z}^2} & 0 & S_{k,z} \end{bmatrix}$
    $\Delta E \longleftarrow (\mathbf{S}'_k - \mathbf{S}_k) \cdot \mathbf{M}$
    if $\Delta E < 0$ or Uniform$[0, 1] < e^{-\beta\Delta E}$ then
        $\mathbf{S}_k \longleftarrow \mathbf{S}'_k / ||\mathbf{S}'_k||$    // renormalize to avoid error aggregation
```

3.2.2 Heat-bath algorithm

The heat-bath algorithm constitutes yet another solution to the detailed balance equation. Whereas the Metropolis transition probability only depended on the energy difference between the current and updated configurations, the heat-bath transition probability is independent of the former and accepts transitions to the updated configuration $\mathbf{x}_j$ with a probability proportional to $P(\mathbf{x}_j)$,

$$P_{\text{accept}}(\mathbf{x}_i \to \mathbf{x}_j) = \frac{P(\mathbf{x}_j)}{\sum_l P(\mathbf{x}_l)}, \tag{3.12}$$

where l sums over the set of all resultant configurations $\mathbf{x}_l$ that is closed under the proposed update in order to ensure the normalization of the acceptance probabilities,

$$\sum_l P(\mathbf{x}_i \to \mathbf{x}_l) = 1 \qquad \forall\, i. \tag{3.13}$$

In general, the heat-bath algorithm can only be applied to systems with discrete degrees of freedom, such as the q-state Potts model (and its $q = 2$ special case, the Ising model) where the sum in the denominator runs over the q possible states and updates to each of the q states are proposed with equal probability.

For systems with continuous degrees of freedom, a heat-bath algorithm can be devised only in special cases. Fortunately, for the (anisotropic) Heisenberg model this is indeed possible. In order to preserve the normalization of the transition probabilities, one considers the integral,

$$\int \mathrm{d}\Omega_k\, e^{-\beta E} = e^{-\beta E_k^{\text{rest}}} \int \mathrm{d}\Omega_k\, e^{-\beta \mathbf{S}_k \cdot \mathbf{M}_k} = e^{-\beta E_k^{\text{rest}}}\, 2\pi \int_{-1}^{1} \mathrm{d}\cos\theta\, e^{-\beta \|\mathbf{M}_k\| \cos\theta} \tag{3.14}$$

$$= e^{-\beta E_k^{\text{rest}}} \frac{4\pi}{\beta \|\mathbf{M}_k\|} \sinh(\beta \|\mathbf{M}_k\|). \tag{3.15}$$

Hence, the following heat-bath expression for the transition probabilities formally satisfies detailed balance:

$$P(\{\dots \mathbf{S}_k \dots\} \to \{\dots \mathbf{S}'_k \dots\}) = \frac{1}{N} \frac{e^{-\beta E(\{\dots \mathbf{S}'_k \dots\})}\, \mathrm{d}\Omega'_k}{\int \mathrm{d}\Omega''_k\, e^{-\beta E(\{\dots \mathbf{S}''_k \dots\})}} \tag{3.16}$$

$$= \frac{\mathrm{d}\Omega'_k}{4\pi N} \times \frac{\beta \|\mathbf{M}_k\|\, e^{-\beta \mathbf{S}'_k \cdot \mathbf{M}_k}}{\sinh(\beta \|\mathbf{M}_k\|)}. \tag{3.17}$$

One may be tempted to view this as the product of the proposal probability for choosing a random site and proposing an updated spin isotropically, multiplied by a subsequent acceptance probability. However, the latter is not guaranteed to be smaller than one for all temperatures, owing to its origin in a probability *density*. This is why the heat-bath algorithm is not readily generalized to continuous degrees of freedom.

Rather than drawing $\mathbf{S}'_k$ isotropically, one can instead view the whole of Eq. (3.17) as the proposal probability (density) according to which $\mathbf{S}'_k$ is generated. To that end, one writes

$$P(\{\dots \mathbf{S}_k \dots\} \to \{\dots \mathbf{S}'_k \dots\}) = \frac{1}{N} \frac{\mathrm{d}\varphi}{2\pi} f_{\beta \|\mathbf{M}_k\|}(\cos\theta)\, \mathrm{d}\cos\theta, \qquad f_\alpha(z) = \frac{\alpha\, e^{-\alpha z}}{e^{\alpha} - e^{-\alpha}}, \tag{3.18}$$

finds the cumulative density, $F_\alpha(z) = (e^{\alpha} - e^{-\alpha z})/(e^{\alpha} - e^{-\alpha})$, and generates values of $\cos\theta$ accordingly. Since θ is the angle between the updated spin $\mathbf{S}'_k$ and its local magnetic field $\mathbf{M}_k$, one needs to ensure the resulting spin is properly rotated. This can be done in a similar way as in the cone-restricted Metropolis update, however this time relative to $\mathbf{M}_k$, rather than $\mathbf{S}_k$.

The heat-bath algorithm is widely adopted in the field of lattice gauge theories where it was originally developed [123]. It performs generally better than the Metropolis algorithm[4], especially at low temperatures [124]. The version outlined above for the Heisenberg model eliminates the need for a subsequent acceptance step. Further, it does away with the cone aperture tuning parameter since the polar angle θ is already sampled from the optimal distribution. Its superior performance has been verified numerically and it was thus adopted in place of the Metropolis update for the numerical work in part III of this thesis.

---

[4] A known exception to this rule is, in fact, the Ising model for which the Metropolis algorithm performs slightly better at criticality.

Algorithm 2: Heat-bath update for the (anisotropic) Heisenberg model

```
repeat $N$ times
    $k \longleftarrow$ UniformInteger$[1, N]$
    $\mathbf{M} \longleftarrow \mathbf{J} \sum_j \mathrm{S}_j$                    // $j$ runs over nearest neighbors of $k$
    $\varphi \longleftarrow$ Uniform$[0, 2\pi]$
    $u \longleftarrow$ Uniform$[-1, 1]$
    $\cos\theta \longleftarrow -1 - \frac{1}{\beta \|\mathbf{M}\|} \ln\left[1 - u\left(1 - e^{-2\beta\|\mathbf{M}\|}\right)\right]$
    $\mathrm{S}_k \longleftarrow \begin{bmatrix} \sqrt{1-\cos^2\theta}\cos\varphi \\ \sqrt{1-\cos^2\theta}\sin\varphi \\ \cos\theta \end{bmatrix}$
    $\mathrm{S}_k \longleftarrow \mathbf{R}\mathrm{S}_k \quad \textit{where} \quad \mathbf{R} = \begin{bmatrix} M_x M_z/\|\mathbf{M}\| M_\perp & -M_y/M_\perp & M_x/\|\mathbf{M}\| \\ M_y M_z/\|\mathbf{M}\| M_\perp & M_x/M_\perp & M_y/\|\mathbf{M}\| \\ -M_y/M_\perp & 0 & M_z/\|\mathbf{M}\| \end{bmatrix},$
        $M_\perp = \sqrt{\|\mathbf{M}\|^2 - M_z^2}$
```

3.3 Microcanonical updates

3.3.1 Global O(3) symmetry

In cases where the Hamiltonian possesses a global symmetry Ω, it can be beneficial to include an update that transforms the system's state accordingly by some $\boldsymbol{\omega} \in \Omega$. Hence, the proposed update is microcanonical and can always be accepted so long as $\boldsymbol{\omega}$ and $\boldsymbol{\omega}^{-1}$ are proposed with equal probability. In the case of the isotropic Heisenberg model, $\Omega = \mathrm{O}(3)$ admits for global rotoreflections in spin space. Uniform proper rotations matrices [SO(3)] are readily generated by choosing the Euler angles (α, β, γ) uniformly. Reflections may be incorporated by flipping the sign of one column conditional on a coin toss. Since the random rotoreflection matrix only needs to be set up once per update, this update is fairly cheap and trivially vectorizable.

Algorithm 3: Global O(3) rotoreflection update

```
$\alpha \longleftarrow \texttt{Uniform}[0, 2\pi]$
$\beta \longleftarrow \texttt{Uniform}[0, 2\pi]$
$\gamma \longleftarrow \texttt{Uniform}[0, 2\pi]$
$\boldsymbol{\omega} \longleftarrow \begin{bmatrix} \cos\alpha\cos\gamma - \sin\alpha\sin\beta\sin\gamma & -\sin\alpha\cos\beta & -\cos\alpha\sin\gamma - \sin\alpha\sin\beta\cos\gamma \\ \cos\alpha\sin\beta\sin\gamma + \sin\alpha\cos\gamma & \cos\alpha\cos\beta & \cos\alpha\sin\beta\cos\gamma - \sin\alpha\sin\gamma \\ \cos\beta\sin\gamma & -\sin\beta & \cos\beta\cos\gamma \end{bmatrix}$
if UniformBool then                                        // coin toss
    $\boldsymbol{\omega} \longleftarrow \begin{bmatrix} -1 & 0 & 0 \\ 0 & 1 & 0 \\ 0 & 0 & 1 \end{bmatrix} \boldsymbol{\omega}$
foreach lattice site $k = 1, \dots, N$ do
    $\mathrm{S}_k \longleftarrow \boldsymbol{\omega}\mathrm{S}_k$
```

The same symmetry is also present in the gauge model, *cf.* Eq. (2.20). In cases where this symmetry is explicitly broken by the Hamiltonian, one may resort to a subgroup; *e.g.* the XXZ Heisenberg model retains a global $D_{\infty h} = \mathrm{O}(2) \times Z_2$ symmetry.

Whether or not this update can provide an reduction in autocorrelation times ultimately depends on the observable. Neither does it provide any utility in navigating the intricate low-energy landscape of frustrated systems, nor is there any benefit to combating critical slowing-down. Physically relevant observables will also often explicitly obey the same symmetry, such that their measurements are not affected by the update and, hence, their autocorrelation times will not change. For these reasons, global rotations are often not included in the update scheme.

In particular, this is the case for the scalar order parameter, whereas the underlying tensorial order parameter transforms according to the rotoreflection $\boldsymbol{\omega}$, *i.e.* each of its indices is contracted with one instance of $\boldsymbol{\omega}$. For the sake of machine learning of order parameters, the symmetry Ω may or may not be respected by the machine's design. For the TK-SVM method that will be introduced in Ch. 5, this is not the case and, hence, the machine will have to learn the symmetry from the training data. Thus, the global O(3) update is indeed essential to obtain independent training data.

3.3.2 Overrelaxation

Like the heat-bath algorithm, the overrelaxation update was originally developed in the context of lattice gauge theories [125, 126], building on ideas stemming from the numerical solution of systems of linear equations. The underlying idea is to propose an updated configuration that is located on (approximately) the same isoline in the energy landscape around a local minimum. That is, rather than relaxing the configuration into the local energy minimum (a move that is always accepted in the Metropolis scheme, but difficult to reverse), the system is *over*relaxed to a configuration opposite the local minimum. As long as the energy remains comparable, the update would still have a high acceptance probability while not maneuvering the system into a configuration that is difficult to escape from. Hence, overrelaxation is particularly useful in reducing autocorrelation times in frustrated systems whose ground state is highly degenerate.

In the case of continuous spin systems such as the (anisotropic) Heisenberg model, it is possible to formulate a microcanonical overrelaxation update exactly, voiding the need for a subsequent acceptance step. To this end, once again a single spin $\mathbf{S}_k$ is considered and updated such that the scalar product with its local magnetic field, $\mathbf{S}_k \cdot \mathbf{M}_k$, and by extension the energy, is left invariant. Any such choice would be valid, but best results are achieved when mirroring $\mathbf{S}_k$ on $\mathbf{M}_k$.

Since this update is deterministic, one can avoid the use of random numbers entirely by executing it sequentially for all spins, though it has to be noted that each updated spin affects the local magnetic field felt by its neighbors. For this reason, the overrelaxation update is tricky to vectorize on frustrated lattices; on bipartite lattices, both sublattices may again be updated sequentially but within each sublattice, the update can be vectorized. Regardless, when used in conjunction with the other update schemes, the overrelaxation update is not performance-critical.

Algorithm 4: Overrelaxation update for the (anisotropic) Heisenberg model

```
foreach lattice site $k = 1, \ldots, N$ do
    $\mathbf{M} \longleftarrow \mathbf{J} \sum_j \mathbf{S}_j$        /* $j$ runs over nearest neighbors of $k$ */
    $\mathbf{S}_k \longleftarrow \frac{2\,\mathbf{S}_k \cdot \mathbf{M}}{||\mathbf{M}||^2} \mathbf{M} - \mathbf{S}_k$
```

3.4 Parallel tempering

The parallel tempering (PT) update [127] works in an extended configuration space as it operates on an ensemble of (spin) configurations at a number of different temperatures. For each temperature, an otherwise independent Monte Carlo configuration is simulated using, for example, the updates presented in the previous sections. These replicas typically run as parallel processes or threads, possibly also on separate nodes of a distributed compute cluster.

As part of the regular update sequence, the parallel tempering update proposes a swap of the configurations of two replicas at different temperatures. Thus, this update constitutes a point of synchronization and communication between otherwise ("embarrassingly") parallel simulations. To be concrete, consider that a pair of replicas at temperatures T_1 and T_2 is picked at random. Prior to the update, let the configuration of the first one be $\mathbf{x}_i$ and that of the second one $\mathbf{x}_j$. The swap of the configurations $\mathbf{x}_i$ and $\mathbf{x}_j$ can then be accepted according to the Metropolis probability. Since the PT update is its own reverse, the proposal probabilities for the update cancel in the detailed balance equation, yielding

$$P_{\text{accept}}((\mathbf{x}_i, \mathbf{x}_j) \longrightarrow (\mathbf{x}_j, \mathbf{x}_i)) = \max\left\{1, \frac{P((\mathbf{x}_j, \mathbf{x}_i))}{P((\mathbf{x}_i, \mathbf{x}_j))}\right\}, \tag{3.19}$$

where the Metropolis ratio is given by

$$\frac{P((\mathbf{x}_j, \mathbf{x}_i))}{P((\mathbf{x}_i, \mathbf{x}_j))} = \frac{e^{-\beta_1 E(\mathbf{x}_j)} e^{-\beta_2 E(\mathbf{x}_i)}}{e^{-\beta_1 E(\mathbf{x}_i)} e^{-\beta_2 E(\mathbf{x}_j)}} = \exp\left[-(\beta_2 - \beta_1)(E(\mathbf{x}_i) - E(\mathbf{x}_j))\right]. \tag{3.20}$$

In order to maximize the acceptance, only swaps between adjacent temperatures are proposed.

Rather than swapping configurations, the replicas may simply swap temperatures and keep their configuration. The PT update thus only requires minimal communication between replicas: each only has to evaluate $(\beta' - \beta)E(\mathbf{x})$ where β' is the inverse temperature of its update partner. The replicas are thus seen to perform a random walk in temperature. Hence, the benefit of PT toward curing excessively long autocorrelation times at low temperatures comes about by allowing a MC configuration that is "stuck" in a local energy minimum to escape it after heating up to a higher temperature and subsequently anneal back to lower temperatures, reaching a different local minimum. In this way, PT serves a similar role as simulated annealing (which may additionally be used during the thermalization phase), but does so in a way that dynamically adjusts the temperature over the course of the entire simulation, all the while preserving detailed balance such that one does not need to allow for any additional thermalization phases after each swap. It is therefore particularly useful in frustrated systems which have a highly degenerate ground state.

The choice of the (fixed) temperatures at which the replicas run is crucial to the utility of PT. On the one hand, the temperatures should span a range that includes both the physically interesting low temperatures and high enough temperatures to escape local minima. On the other hand, if the temperatures are spaced too far apart from each other, the acceptance rate of swaps will decay exponentially. Counterintuitively, using too many temperatures in total will not only be expensive but also detrimental to the overall performance: the benefit arising from high acceptance rates will be offset by the larger extent of the configuration space. The relevant quantity to gauge the performance of the PT update is thus not given by the acceptance rate, but rather by the turnaround time, *i.e.* the time it takes a single replica to diffuse from the lowest temperature to the highest and back to the lowest. An automatic scheme has been proposed to optimize the distribution of the temperatures with respect to the turnaround time [128]. Doing so can be especially helpful around phase transitions where it results in a higher concentration of temperature in the vicinity of the critical point where the sudden change in energy might otherwise inhibit acceptance rates. In the case of the frustrated systems investigated in this thesis, particularly for the kagome antiferromagnet studied in Ch. 9, it was found that near-ideal results were obtained when adopting a logarithmic temperature grid, negating the need to implement the elaborate automatic scheme.

PT can also be applied more generally. Rather than swapping configurations between replicas of different temperatures, other parameters of the system may be varied, *e.g.* coupling constants. In those cases, the energy function itself depends on the parameter that is being swapped. This also applies to quantum Monte Carlo simulations where more generally, the ratio between the weights of the current configuration given the two different values of the PT parameter needs to be evaluated. This flexibility renders PT a versatile update scheme. Its implementation comes at the cost of additional overhead both at runtime (due to the necessity of interprocess communication and synchronization) and in terms of implementation (as it defies the otherwise "embarrassingly parallel" nature of Monte Carlo codes), but can be applied subsequently to arbitrary Monte Carlo schemes. A generic implementation of PT for the ALPSCore library has been developed as part of the source codes supporting this thesis.

4

Machine learning states of matter

Machine learning methods, generally speaking, aim to infer a predictive statistical model from a set of representative training data $\left\{\mathbf{x}^{(k)} \in \mathcal{X} \,|\, k = 1, \ldots, N_s\right\}$. $\mathcal{X}$ is the space from which the data are sampled. For the sake of this thesis and in other works which study classical spin systems [23, 26, 129, 130], it is identical to the classical spin configuration space of the Monte Carlo simulation, as introduced in the previous chapter. These raw configurations are the natural choice as they are accessible from the simulation, specify the underlying state fully, and any derived quantities ("features") may be calculated from them.

In quantum systems, the choice of the input data becomes more ambiguous. Dependent upon the goals of the respective project, machine learning schemes based on auxiliary field configurations [131], entanglement spectra [132, 133], Green functions [134], feature extraction through quantum loop topography (QLT) [135, 136], eigenfunctions [137], and momentum-space representations of Hamiltonians [138, 139] have all been devised. More recently, experimental data obtained through quantum state tomography (QST) [140, 141] and single-shot momentum-space density images in cold atom systems [142] were successfully used to train neural networks.

As of yet, no single "killer application" of machine learning within the realm of condensed matter physics has emerged where new results were obtained which had a profound impact on the field. This is certainly not for a lack of effort, though. The activities in this area broadly fall into three loosely connected categories. The first tries to represent the quantum many-body wave function through neural networks such that an efficient representation capturing the relevant correlations is learned, which may then be used to find the ground state. This approach is in spirit similar to the idea behind matrix and tensor network states and some explicit connections have been pointed out [29, 30]. These neural quantum states (NQS) were pioneered in the context of variational Monte Carlo [24] and the possibilities and limitations have since been studied on a variety of systems and for various related architectures [22, 25, 140, 141, 143].

Inspired by the successful application of machine learning to image recognition, the recognition and classification of phases established itself as the second pillar of machine learning in physics. In this context, both kernel methods [26, 144–146] and artificial neural networks [133, 147], in particular convolutional ones [23, 131, 138, 139, 148], have been successfully applied.

Third, machine learning has also been used to devise optimized cluster updates for Monte Carlo simulations using generative sampling [149, 150]. The "self-learning" Monte Carlo scheme, in contrast, tries to achieve the same goal by learning an effective model Hamiltonian which can be updated more efficiently and applying the resulting update to the original model [151–156]. Lastly, artificial neural networks have also been used to solve the ill-posed problem that is inherent to the analytic continuation of imaginary-time correlators to the real-time domain in many quantum Monte Carlo schemes [157].

Sometimes, the training data are supplemented with discrete labels, $\left\{(\mathbf{x}^{(k)}, y^{(k)})\right\}$, corresponding to the particular quantity that one wishes to predict later on for unlabeled testing data. Examples from the domain of physics include labels corresponding to distinct phases or winding numbers [138, 139]. Such supervised learning schemes tend to be easier to train, allow for an optimization with respect to a physically well-defined quantity, and typically make do with less training data compared to unsupervised schemes where the former remain unlabeled.

In contrast, in unsupervised learning, the machine has to infer the labeling by itself which can, in principle, greatly advance the physical understanding, for example in the case of phase classification when confronted with an unknown phase diagram. Unsupervised learning can also be beneficial in situations where the labeling of the data is in principle possible but prohibitively expensive to perform on a large data set, *e.g.* because it requires input by (paid) humans. In those cases, semi-supervised learning, a combination of supervised learning on a small set of labeled data and unsupervised learning on the whole set, can serve to nudge the machine towards the desired labeling while still taking advantage of the large repository of data.

In addition to supervised and unsupervised learning, a third paradigm, reinforcement learning, works fundamentally differently, in that no fixed training data are present *a priori*, but the machine rather learns a policy according to which an agent can take certain actions. The effect of an action on its environment is subsequently evaluated against some supplied cumulative reward (or regret) function. Crucially, suboptimal actions are not immediately corrected but force the machine to learn to counter them. This game-oriented approach is more alien to the physicist's mindset and saw adoption in physics only recently where, among other applications [143, 158, 159], it was used to learn topological error correction codes [160–162].

In the forthcoming section, a technical introduction to two kernel methods is given, one of which, support vector machines (SVMs), falls under the umbrella of supervised learning, while the other, (kernel) principal component analysis (kPCA), is unsupervised. This discussion is framed in the context of a generic machine learning problem. In the next chapter, the introduction of the tensorial kernel will make the connection back to physics and explain how these kernel methods can be used to learn multipolar order in classical spin systems. The remainder of this thesis chiefly applies the tensorial kernel to SVM (TK-SVM), the exception being Sec. 8.4 where its capability in conjunction with kPCA is demonstrated. Nonetheless, while SVM itself is technically a supervised scheme, it will become apparent that it can be used in an unsupervised context by labeling the training data trivially by the parameters they have been sampled at. Ch. 7 discusses how a physically meaningful phase diagram, *i.e.* labeling, can be automatically inferred using a spectral graph analysis.

The final section of this chapter dives deeper into the applications of artificial neural networks specifically. A rudimentary definition of the most important network architectures will be given, but the focus of that section is on their application in condensed matter physics. Since neural networks are more difficult to interpret as compared to kernel methods, an interesting question in this context arises in regard to what physical quantities can actually be learned.

4.1 Kernel methods

4.1.1 Support vector machines

Support vector machines (SVM) provide a means to construct a classifier from N_s training data samples, $(\mathbf{x}^{(k)}, y^{(k)})$, where $\mathbf{x}^{(k)} \in \mathcal{X} \subseteq \mathbb{R}^d$ and $y^{(k)}$ labels the class of the training sample. The

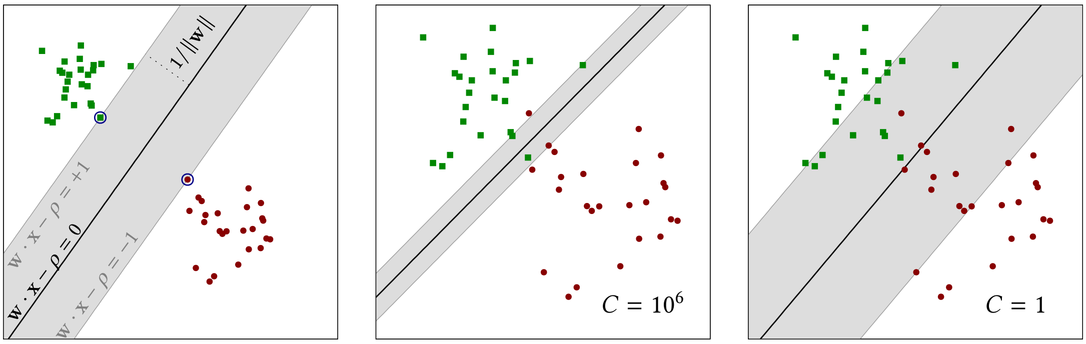

(a) Perfectly separable data with an optimal hard margin;

(b) regularized SVM with a relatively hard margin;

(c) same as (b) but with a softer margin.

Figure 4.1: Illustration of SVM on two-dimensional training data from two classes, green (squares) and red (circles). The decision boundary is indicated by the black line, the margin by the shaded area.

case of binary classification, $y^{(k)} \in \{-1, +1\}$, is considered here first and extensions to the case of more than two classes will be made afterwards.

Definition of the optimization problem

The aim of SVM is to find a hyperplane, dubbed *decision boundary*,

$$\mathbf{w} \cdot \mathbf{x} - \rho = 0, \tag{4.1}$$

defined by parameters $\mathbf{w} \in \mathbb{R}^d$, the normal vector, and *bias* $\rho \in \mathbb{R}$, that separates the data into the two classes, such that

$$y^{(k)} \left(\mathbf{w} \cdot \mathbf{x}^{(k)} - \rho \right) > 0 \qquad \forall \quad k = 1, \ldots, N_s. \tag{4.2}$$

In general, this may not be possible, but if it is, typically infinitely many solutions exist. In order to select the solution that separates the data most clearly, a finite *margin* is imposed which must not contain any of the training data samples, and the width of the margin is sought to be maximal, as shown in Fig. 4.1(a). Formally, the right-hand-side of inequality (4.2) can be replaced by unity, such that the width of the margin is given by $2/\|w\|$. The optimization problem may then be written as

$$\begin{cases} \text{minimize} \quad \frac{1}{2}\|\mathbf{w}\|^2 \quad \text{with respect to} \quad \mathbf{w}, \rho, \\ \text{subject to} \quad y^{(k)} \left(\mathbf{w} \cdot \mathbf{x}^{(k)} - \rho \right) \geq 1 \quad \forall\, k. \end{cases} \tag{4.3}$$

Most of the time, the data may not be perfectly separable and the constraint (4.3) must be relaxed, allowing for incursions into the margin at a cost proportional to $C > 0$ which serves as a regularization parameter:

$$\begin{cases} \text{minimize} & \frac{1}{2}\|\mathbf{w}\|^2 + C\sum_k \xi_k \quad \text{w. r. t.} \quad \mathbf{w}, \rho, \{\xi_k\}, \\ \text{subject to} & y^{(k)}\left(\mathbf{w}\cdot\mathbf{x}^{(k)} - \rho\right) \geq 1 - \xi_k, \;\; \xi_k \geq 0 \;\; \forall\, k \end{cases} \tag{4.4}$$

where $\xi_k, k = 1, \dots, N_s$ are slack variables. $\xi_k > 1$ corresponds to a misclassified sample. The optimization problem (4.4) constitutes a quadratic programming (QP) problem. The slack variables increase the dimensionality of the parameter space by N_s. However, the optimal value of each slack variable is determined by the $d + 1$ original parameters and the coordinates of the corresponding training sample, $\xi_k = h(\mathbf{x}^{(k)}, y^{(k)})$, through the so-called *hinge loss*,

$$h(\mathbf{x}, y) = \max\{0, 1 - y(\mathbf{w}\cdot\mathbf{x} - \rho)\}, \tag{4.5}$$

and, thus, the constraints could be eliminated. Perhaps counterintuitively, it is often beneficial to the solution of convex optimization problems not to eliminate auxiliary variables, but to solve the higher-dimensional optimization problem with additional constraints in favor of a simpler optimization objective [163]. Thus, one solves the constrained optimization problem (4.4) numerically, yet its solution is fully determined by $\mathbf{w}$ and ρ.

Since the training data enter the optimization problem only as inner products in the constraint, the optimal $\mathbf{w}$ will lie in the span of the training data,

$$\mathbf{w} = \sum_k \lambda_k y^{(k)}\mathbf{x}^{(k)}, \tag{4.6}$$

as any additional orthogonal component would be detrimental to the optimization objective. Indeed, only those samples which violate (or touch) the margin incur a nonzero hinge loss and contribute to $\mathbf{w}$ with a nonzero λ_k. These are the support vectors.

Larger values of the regularization parameter C "harden" the margin, making it more narrow and reducing the number of support vectors. This comes at the risk of overfitting noise. In the limit $C \longrightarrow \infty$, the solution to Eq. (4.3) is reproduced. For example, in Fig. 4.1(a) only the two points touching the margin are support vectors. Smaller values of C regularize the problem more strongly, allowing for a wider margin and consequently a higher number of support vectors, but potentially discard faithful information in the training data set. Panels (b) and (c) of Fig. 4.1 illustrate two different regularization for the same noisy data. The optimal choice of C is ultimately problem-specific. In principle, one has to validate the learned model with respect to independent test data for different values of C which can span many orders of magnitude.

There exists however an alternative reparametrization of Eq. (4.4) in terms of a regularization parameter $\nu \in [0, 1)$ which has been shown to impose an upper bound on the fraction of training samples that violate the margin and a lower bound on the fraction of training samples that serve as support vectors [164]. ν-SVM thus admits a more universal interpretation and it was found to simplify the selection of an appropriate regularization. The exact relation between C and ν is rather complicated while it does not further the understanding of the principles of the method and is therefore omitted here. It is important to note, however, that C-SVM and ν-SVM are equivalent regarding their ability to perform data classification. The optimization problem may not have a feasible solution for all values of ν if the training data are unbalanced.

In fact, the maximum feasible value is given by $\nu_{\max} = 2\min(N_s^+, N_s^-)/N_s$ where $N_s^\pm$ are the number of training samples in either class [165].

Equation (4.4) constitutes a quadratic programming (QP) problem having a quadratic optimization objective and linear inequality constraints [163]. QP problems are a subclass of convex optimization problems, a fact that conveys a number of reassuring mathematical properties. In particular, the convergence to the global minimum is guaranteed [163] and QP problems are numerically tractable by standard methods such as sequential minimal optimization (SMO) [166, 167]. The complexity of SMO is somewhat dependent on the nature of the training data. Reference [166] gives an empirical estimate of better than $\mathcal{O}(N_s^{2.2})$ which is roughly in line with the observations made in this work. Note that for the purposes of this thesis, the computational effort was dominated by the generation of independent training data, rather than by the SVM optimization.

Decision function

The decision function

$$d(\mathbf{x}) = \mathbf{w} \cdot \mathbf{x} - \rho \tag{4.7}$$

determines the orientated distance of a test sample $\mathbf{x}$ from the hyperplane and its sign can be used to predict the class label. Plugging Eq. (4.6) into the above allows for the practical calculation of the decision function as a sum over inner products with the support vectors:

$$d(\mathbf{x}) = \sum_k \lambda_k y^{(k)} \mathbf{x}^{(k)} \cdot \mathbf{x} - \rho. \tag{4.8}$$

The solution to the optimization problem is thus entirely given by the optimal parameters $\{\lambda_k\}$ and the bias ρ.

The kernel trick

Often, the data in the original d-dimensional space $\mathcal{X}$ is not expected to be separable by a hyperplane. The solution is to invoke a mapping $\boldsymbol{\varphi} : \mathcal{X} \to \mathcal{F}, \mathbf{x} \mapsto \boldsymbol{\varphi}(\mathbf{x})$ to a higher-dimensional auxiliary feature space $\mathcal{F}$ where the mapped training data become linearly separable. Furthermore, since the decision function and the optimization problem (4.4) involve only inner products in the auxiliary space, the details of the mapping $\boldsymbol{\varphi}$ (and even the dimensionality of the auxiliary space) need not be known as long as one can compute a kernel function K of the original data in the raw feature space, such that

$$K(\mathbf{x}, \mathbf{y}) = \boldsymbol{\varphi}(\mathbf{x}) \cdot \boldsymbol{\varphi}(\mathbf{y}). \tag{4.9}$$

Indeed, Mercer's theorem implies the existence of such a mapping $\boldsymbol{\varphi} : \mathcal{X} \to \mathcal{F}$ to a (possibly infinite-dimensional) auxiliary feature space $\mathcal{F}$ for any kernel function $K : \mathcal{X} \times \mathcal{X} \to \mathbb{R}$ satisfying *Mercer's condition*, *i.e.*, for any square-integrable function g on $\mathcal{X}$, the inequality

$$\iint_{\mathcal{X}\times\mathcal{X}} \mathrm{d}\mathbf{x}\, \mathrm{d}\mathbf{y}\, g(\mathbf{x}) K(\mathbf{x}, \mathbf{y}) g(\mathbf{y}) \geq 0, \tag{4.10}$$

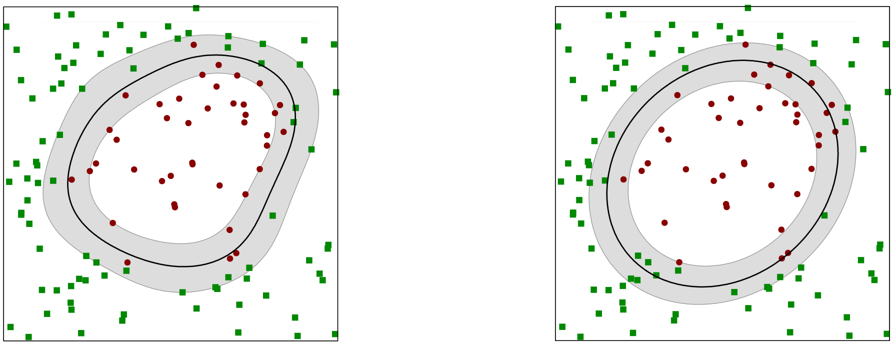

(a) radial basis functions kernel **(b)** quadratic kernel

Figure 4.2: Data which are not linearly separable can be classified using a SVM with an appropriate kernel. The attainable shape of the decision boundary depends on the choice of the kernel; for the quadratic kernel in panel (b) this yields an ellipse.

holds [168].

The decision function is consequently obtained by replacing the inner product in Eq. (4.8) with an evaluation of the kernel function,

$$d(\mathbf{x}) = \sum_k \lambda_k y^{(k)} K(\mathbf{x}^{(k)}, \mathbf{x}) - \rho. \tag{4.11}$$

This is also done in the definition of the optimization problem (4.4), where $\mathbf{w}$ is first replaced by its expansion in terms of support vectors, Eq. (4.6). For example, in the optimization objective, one replaces

$$\|\mathbf{w}\|^2 = \mathbf{w} \cdot \mathbf{w} = \sum_{k,k'} \lambda_k \lambda_{k'} y^{(k)} y^{(k')} \mathbf{x}^{(k)} \cdot \mathbf{x}^{(k')} \to \sum_{k,k'} \lambda_k \lambda_{k'} y^{(k)} y^{(k')} K(\mathbf{x}^{(k)}, \mathbf{x}^{(k')}). \tag{4.12}$$

The kernel trick does not acquit one of choosing the kernel suitably for it to result in an adequate classification. However, coming up with a kernel function is generally more accessible to domain knowledge or physical insight than engineering the feature mapping $\boldsymbol{\varphi}$ explicitly.

An example of this can be seen in the popular choice of a kernel function based on radial basis functions (RBF), such that, $K(\mathbf{x}, \mathbf{y}) = f(\|\mathbf{x} - \mathbf{y}\|)$. Commonly, Gaussian radial basis functions are used,

$$K_{\mathrm{RBF}}(\mathbf{x}, \mathbf{y}) = \exp\left(-\varepsilon \|\mathbf{x} - \mathbf{y}\|^2\right), \tag{4.13}$$

resulting in a decision function that is given by a superposition of Gaussians centered on each of the support vectors. The RBF kernel derives its versatility from the assumption that the notion of locality induced by the metric on $\mathcal{X}$ is meaningful in the problem at hand. Hence, it can accomodate smooth clusters of otherwise arbitrary shape in $\mathcal{X}$. Fig. 4.2(a) illustrates the use of the RBF kernel in two dimensions. The characteristic length scale determining the radius affected by a single data point is given by $1/\varepsilon$. Choosing ε too large leads to overfitting by proposing a decision boundary that wiggles around individual data points, while an excessively small value of ε might brush off legit features. Thus, the choice of the kernel parameter ε in principle has to be crossvalidated in a similar way to the regularization parameter.

Chapter 5 introduces the particular choice of the kernel function that was adopted for the identification of multipolar spin order and it is based on the quadratic kernel,

$$K_{\text{quad}}(\mathbf{x}, \mathbf{y}) = (\mathbf{x} \cdot \mathbf{y})^2. \tag{4.14}$$

In $d = 2$ dimensions, one can see that the quadratic kernel can explicitly be rewritten as an inner product of at least three-dimensional feature vectors,

$$\begin{aligned} K_{\text{quad}}(\mathbf{x}, \mathbf{y}) &= (x_1 y_1 + x_2 y_2)^2 = x_1^2 y_1^2 + 2 x_1 x_2 y_1 y_2 + x_2^2 y_2^2 \\ &= \begin{bmatrix} x_1^2 & \sqrt{2}\, x_1 x_2 & x_2^2 \end{bmatrix} \begin{bmatrix} y_1^2 \\ \sqrt{2}\, y_1 y_2 \\ y_2^2 \end{bmatrix} = \boldsymbol{\varphi}_{\text{quad}}(\mathbf{x}) \cdot \boldsymbol{\varphi}_{\text{quad}}(\mathbf{y}). \end{aligned} \tag{4.15}$$

In general, the minimum feature space mimicked by the quadratic kernel is $d(d+1)/2$-dimensional and would quickly grow prohibitively large if the mapping $\boldsymbol{\varphi}_{\text{quad}}$ was applied explicitly.

Another useful property of the quadratic kernel becomes apparent when reshuffling the order of summations in the kernelized decision function, Eq. (4.11),

$$\begin{aligned} d(\mathbf{x}) &= \sum_k \lambda_k y^{(k)} \left(\mathbf{x}^{(k)} \cdot \mathbf{x}\right)^2 - \rho = \sum_k \lambda_k y^{(k)} \sum_{i,j} x_i^{(k)} x_i x_j^{(k)} x_j - \rho \\ &= \sum_{i,j} \left(\sum_k \alpha_k y^{(k)} x_i^{(k)} x_j^{(k)} \right) x_i x_j - \rho = \sum_{i,j} C_{ij} x_i x_j - \rho, \end{aligned} \tag{4.16}$$

i.e. the summation over the support vectors can be carried out to yield a coefficient matrix $C \in \mathbb{R}^{d \times d}$ which represents an alternative parametrization of the solution to the optimization problem. It reveals that the decision function using the quadratic kernel is, in fact, a quadratic form with respect to the test sample coordinates. Hence, in two dimensions, its isosurfaces are conic sections as illustrated in Fig. 4.2(b). The matrix C can be diagonalized to find their principal axes. In this way, the coefficient matrix admits the extraction of an analytical functional form of the optimal decision boundary. This mechanism is the groundwork for the interpretability of the TK-SVM method exposed in Sec. 6.

The $d(d+1)/2$ independent elements of the symmetric coefficient matrix can also be seen to be identical to the entries of the normal vector $\mathbf{w}$ if the Mercer mapping $\boldsymbol{\varphi}$ was carried out explicitly and a linear SVM was trained on the resulting feature vectors. In practice, often only a small fraction ($\approx \nu$) of training samples is required as support vectors whereas the dimension of the input data, d, may be quite large. In this scenario, the parametrization of the decision function through the support vector weights $\{\lambda_k\}$ is generally more efficient than that through the coefficient matrix, both in terms of space (N_s numbers vs. $d(d+1)/2$ numbers) and evaluation complexity ($O(\nu N_s d)$ vs. $O(d^2)$).

Multiclassification

The extension of SVM to the case where $M > 2$ distinct labels are assigned to the training samples is most effectively accomplished by considering all $M(M-1)/2$ pairs of labels one by one [169], considering only the training samples belonging to either label and solving the binary classification problems individually. This produces $M(M-1)/2$ distinct decision functions. Any training sample that contributes to any decision function by a nonzero λ_k is considered a support vector of the multiclassification problem. Note that depending on the nature of the problem, the share of support vectors contributing to multiple decision functions may be significant, allowing for a space-efficient representation.

When it comes to predicting the label for a test sample, each decision function establishes a precedence of one label over the other. Ideally, these relations are collectively compatible with transitivity and one can unambiguously assign a label. When this is not the case, the approach to reconcile the relations followed by most SVM software packages is to "poll" by giving one vote to each decision function and picking the label that accumulates the majority of votes [170]. This approach is not well suited to situations where the labeling of the training data does not necessarily correspond to the "physical" reality and multiple labels in fact represent the same class, resulting in the vote being split among them. It also fails to recognize situations where the decision function is incapable of distinguishing between two labels but rather overfits noise.

For the purpose of this thesis, the blanket polling scheme is therefore not followed but instead the decision functions are considered individually and may be discarded based on physical insight.

4.1.2 Principal component analysis

Principal component analysis (PCA) is an unsupervised method to identify the most relevant orthogonal "directions" (components) among the set of N_s training samples, $\{\mathbf{x}^{(k)}\}$. This is reminiscent to the principal axis transformation in mechanics where one identifies the orthogonal principal axis of rotation of a rigid body by diagonalizing its inertia tensor. Likewise, in PCA, the sample covariance matrix of the training data is diagonalized.

In this subsection, we will first introduce this basic linear PCA to illustrate the general idea and establish notation. Subsequently, its nonlinear extension will be discussed which once again makes use of the kernel trick which has been introduced previously in the context of SVM (*cf.* Sec. 4.1.1). The particular choice of the quadratic kernel will be revisited and a concept akin to the coefficient matrix in SVM (*cf.* Eq. (4.16)) will be seen to arise.

While (linear) PCA dates back to the early 20th century, the development of its kernelized extension (kPCA) coincided with the heyday of other kernel methods in the late 1990s [15]. The tensorial kernel, which will be introduced in the next chapter, can also be applied to kPCA. A demonstration of this is given in Sec. 8.4.

Linear PCA

The goal of PCA is to identify for each principal component, indexed $j = 1, \dots, N_c$, a set of weights $\mathbf{w}^{(j)} \in \mathbb{R}^d$ which linearly combine the input data $\mathbf{x} \in \mathbb{R}^d$ to find the contribution of that principal component to the makeup of $\mathbf{x}$, dubbed the *score*, $t^{(j)}(\mathbf{x}) = \mathbf{x} \cdot \mathbf{w}^{(j)}$. When collecting all training samples $\mathbf{x}^{(k)} \in \mathbb{R}^d$, $k = 1, \ldots, N_s$, into a single matrix of row vectors, $\mathbf{X} \in \mathbb{R}^{N_s \times d}$, such that $X_{k,i} = x_i^{(k)}$, and likewise the weights of all principal components into a matrix of column vectors, $\mathbf{W} \in \mathbb{R}^{d \times N_c}$, such that $W_{i,j} = w_i^{(j)}$, then

$$\mathbf{T} = \mathbf{X}\mathbf{W} \tag{4.17}$$

is the score matrix $\mathbf{T} \in \mathbb{R}^{N_s \times N_c}$, such that $T_{k,j}$ is the score of sample k with respect to the j-th principal component, $t^{(j)}(\mathbf{x}^{(k)})$. Analogously, once the principal components have been identified based on the training data $\mathbf{X}$, given another set of N_t test samples, $\tilde{\mathbf{X}} \in \mathbb{R}^{N_t \times d}$, one may define their corresponding score matrix $\tilde{\mathbf{T}} = \tilde{\mathbf{X}}\mathbf{W}$ with respect to the same principal components. Since the principal components ought to be orthogonal, $\mathbf{W}$ is an orthogonal matrix, $\mathbf{W}^\top = \mathbf{W}$.

Assuming that the training data are shifted in such a way that their sample average, *i.e.* the columnwise mean of $\mathbf{X}$, vanishes, then the product $\mathbf{X}^\top\mathbf{X}$ is proportional to the sample covariance matrix,

$$\operatorname{cov}(x_i, x_j) = \frac{1}{N_s - 1} \sum_{k=1}^{N_s} \left(x_i^{(k)} - \bar{x}_i\right)\left(x_j^{(k)} - \bar{x}_j\right) = \frac{1}{N_s - 1} \sum_{k=1}^{N_s} \mathbf{X}_{k,i}\mathbf{X}_{k,j} = \frac{(\mathbf{X}^\top\mathbf{X})_{i,j}}{N_s - 1}, \tag{4.18}$$

where $\bar{x}_i = 0$ is the (vanishing) sample mean of the i-th component. In order to find the principal components, the covariance matrix is diagonalized,

$$\mathbf{X}^\top\mathbf{X} = \mathbf{W}\mathbf{\Lambda}\mathbf{W}^\top, \tag{4.19}$$

where $\mathbf{W}$ is indeed orthogonal and $\mathbf{\Lambda}$ is the diagonal matrix holding the nonnegative eigenvalues λ_j, $j = 1, \ldots, N_c$, since $\mathbf{X}^\top\mathbf{X}$ is symmetric. Without loss of generality, λ_k are assumed in descending order and any trailing eigenvalues zero are truncated. Thus, the maximum number of principal components, N_c, is given by the rank of $\mathbf{X}$. In practice, the purpose of PCA is to identify the most relevant components and discard the remaining ones, thus performing a dimensional reduction that retains the most relevant correlations. Intuitively, the relevance of the k-th component is given by the eigenvalue λ_k which is seen to be proportional to the average square of its corresponding score over the training data,

$$\lambda_k = \left(\mathbf{W}^\top\mathbf{X}^\top\mathbf{X}\mathbf{W}\right)_{k,k} = \left(\mathbf{T}^\top\mathbf{T}\right)_{k,k} = \sum_{i=1}^{N_s} \left[t^{(k)}(\mathbf{x}^{(k)})\right]^2. \tag{4.20}$$

Rather than diagonalizing $\mathbf{X}^\top\mathbf{X}$, one can also calculate the singular value decomposition of the data matrix $\mathbf{X}$ itself, rewriting it as

$$\mathbf{X} = \mathbf{U}\mathbf{\Sigma}\mathbf{W}^\top, \tag{4.21}$$

where $\mathbf{\Sigma}$ is the diagonal matrix holding the N_c singular values σ_j and $\mathbf{U} \in \mathbb{R}^{N_s \times N_c}$, $\mathbf{W} \in \mathbb{R}^{d \times N_c}$ are orthogonal. The latter can be seen to be identical to the weight matrix, which was obtained through the eigendecomposition above, by substituting

$$\mathbf{X}^\top\mathbf{X} = \mathbf{W}\mathbf{\Sigma}\mathbf{U}^\top\mathbf{U}\mathbf{\Sigma}\mathbf{W}^\top = \mathbf{W}\mathbf{\Sigma}^2\mathbf{W}^\top \tag{4.22}$$

and identifying $\mathbf{\Lambda} = \Sigma^2$. Again, the absolutes of the singular values can be used to gauge each component's average score, arrange them by relevance, and reduce the dimension of the problem.

Using SVDs to compress (matrix product) wave functions while keeping the most relevant correlations between sites is also the idea behind DMRG. Indeed, variations of this method have numerous applications in science and engineering.

Kernel PCA

In order to extend PCA in a way that allows it to form the principal components from non-linear functions of the training data, one again resorts to the kernel trick, *i.e.* by performing linear PCA in a high-dimensional feature space. Crucially, the Mercer mapping, $\boldsymbol{\varphi}$, to that feature space $\mathcal{F}$ is again only implicitly defined through the kernel function K, calculating the inner product in $\mathcal{F}$, *cf.* Eq. (4.9). Likewise, the number of features, $N_f = \dim \mathcal{F}$, remains undetermined.

To this end, one introduces the feature matrix $\mathbf{F} \in \mathbb{R}^{N_s \times N_f}$ which is—in principle—obtained by mapping the rows of $\mathbf{X}$ through $\boldsymbol{\varphi}$. This is despite the fact that $\mathbf{F}$ cannot actually be calculated. Following the recipe of linear PCA, a fictional SVD, $\mathbf{F} = \mathbf{U}\Sigma\mathbf{W}^\top$, would serve to diagonalize the feature correlation matrix $\mathbf{F}^\top\mathbf{F} = \mathbf{W}\Sigma^2\mathbf{W}^\top$.

While $\mathbf{F}$ and consequently its covariance matrix $\mathbf{F}^\top\mathbf{F}$ remain inaccessible, however, one does have access to the reverse product, dubbed kernel matrix, $\mathbf{K} = \mathbf{F}\mathbf{F}^\top$, as its elements correspond to all $N_s \times N_s$ evaluations of the kernel function among the training data,

$$\mathbf{K}_{k,l} = \left(\mathbf{F}\mathbf{F}^\top\right)_{k,l} = \boldsymbol{\varphi}(\mathbf{x}^{(k)}) \cdot \boldsymbol{\varphi}(\mathbf{x}^{(l)}) = K(\mathbf{x}^{(k)}, \mathbf{x}^{(l)}). \tag{4.23}$$

One caveat to be aware of is that in order for $\mathbf{F}^\top\mathbf{F}$ to represent the covariance matrix with respect to the features, the average of the features over all training samples must again individually vanish, $\frac{1}{N_s}\sum_{k=1}^{N_s} \mathbf{F}_{k,j} = 0$ for all $j = 1, \ldots, N_f$. This property has to be enforced by a shift $\mathbf{F} \mapsto \mathbf{F}' = (\mathbb{1} - \mathbf{1}_{N_s})\mathbf{F}$ where $\mathbf{1}_{N_s}$ is the $N_s \times N_s$ matrix with all elements equal to $1/N_s$. Since, $\mathbf{F}$ is only implicitly defined, this centralization is explicitly carried out on the level of the corresponding kernel matrix:

$$\mathbf{K} \mapsto \mathbf{F}'(\mathbf{F}')^\top = (\mathbb{1} - \mathbf{1}_{N_s})\mathbf{F}\mathbf{F}^\top(\mathbb{1} - \mathbf{1}_{N_s}) \tag{4.24}$$

$$= \mathbf{K} - \mathbf{K}\mathbf{1}_{N_s} - \mathbf{1}_{N_s}\mathbf{K} + \mathbf{1}_{N_s}\mathbf{K}\mathbf{1}_{N_s}. \tag{4.25}$$

Substituting the SVD of $\mathbf{F}$ into the definition of the kernel matrix,

$$\mathbf{K} = \mathbf{F}\mathbf{F}^\top = \mathbf{U}\Sigma\mathbf{W}^\top\mathbf{W}\Sigma\mathbf{U}^\top = \mathbf{U}\Sigma^2\mathbf{U}^\top, \tag{4.26}$$

the orthogonal matrix $\mathbf{U}$ is seen to diagonalize $\mathbf{K}$. Hence, both $\mathbf{U}$ and the (absolute value of) the singular values of $\mathbf{F}$ can actually be calculated by performing an eigenvalue decomposition on the kernel matrix. Meanwhile, the other orthogonal matrix, $\mathbf{W}$, which defined the principal components in linear PCA, remains inaccessible unless the explicit form of $\boldsymbol{\varphi}$ is specified.

This poses the question how one is supposed to calculate the score matrix $\mathbf{T} = \mathbf{F}\mathbf{W}$ while either factor is inaccessible. Fortunately, this turns out to be possible after all by inserting the identity,

$$\mathbf{T} = \mathbf{F}\mathbf{F}^\top \left(\mathbf{F}^\top\right)^{-1} \mathbf{W} = \mathbf{F}\mathbf{F}^\top \left(\mathbf{W}\Sigma\mathbf{U}^\top\right)^{-1} \mathbf{W} = \mathbf{K}\mathbf{U}\Sigma^{-1} = \mathbf{U}\Sigma. \tag{4.27}$$

In order to calculate the scores with respect to further testing data, $\tilde{\mathbf{T}} = \tilde{\mathbf{F}}\mathbf{W}$, the kernel matrix between the test samples and the original training samples needs to be provided, $\tilde{\mathbf{K}} = \tilde{\mathbf{F}}\mathbf{F}^\top$. The above calculation still holds up to the penultimate equality, $\tilde{\mathbf{T}} = \tilde{\mathbf{K}}\mathbf{U}\Sigma^{-1}$. Written in components, the score of j-th principal component for a single test sample $\mathbf{x}$ is given by:

$$t^{(j)}(\mathbf{x}) = \sum_{k=1}^{N_s} K(\mathbf{x}, \mathbf{x}^{(k)})\, \mathbf{U}_{k,j}/\sigma_j. \tag{4.28}$$

Numerically, kPCA thus entails the calculation and diagonalization of the (centralized) $N_s \times N_s$ kernel matrix. Since this matrix is dense, it must therefore be stored in memory. For large training sets, this can quickly become prohibitively expensive. This is to be contrasted with SVM which, using the SMO algorithm, does not require addition matrix storage [166].

Quadratic kernel

Hearkening back to the specific case of the quadratic kernel, Eq. (4.14), one finds that the scoring function of each principal component assumes a quadratic form,

$$t^{(l)}(\mathbf{x}) = \sum_{k=1}^{N_s} K_{\text{quad}}(\mathbf{x}, \mathbf{x}^{(k)})\, \mathbf{U}_{k,l}/\sigma_l = \sum_{k=1}^{N_s} \sum_{i,j=1}^{d} x_i x_i^{(k)} x_j x_j^{(k)} \mathbf{U}_{k,l}/\sigma_l = \sum_{i,j=1}^{d} C_{ij}^{(l)}\, x_i x_j, \tag{4.29}$$

where each principal component l defines a coefficient matrix,

$$C_{ij}^{(l)} = \sum_{k=1}^{N_s} \mathbf{U}_{k,l}/\sigma_l\, x_i^{(k)} x_j^{(k)}. \tag{4.30}$$

Typically, software packages for kPCA do not give the user access to the resulting $\mathbf{U}$ but rather return the scores $\tilde{\mathbf{T}}$ corresponding to test data $\tilde{\mathbf{X}}$. By defining

$$\tilde{\mathbf{X}}^{(1)} \in \mathbb{R}^{d\times d}, \qquad \tilde{\mathbf{X}}^{(1)}_{i,m} = \delta_{im} \qquad \Rightarrow \qquad \tilde{\mathbf{T}}^{(1)}_{i,l} = C_{ii}^{(l)}, \tag{4.31}$$

$$\tilde{\mathbf{X}}^{(2)} \in \mathbb{R}^{d^2\times d}, \qquad \tilde{\mathbf{X}}^{(2)}_{(i,j),m} = \delta_{im} + \delta_{jm} \qquad \Rightarrow \qquad \tilde{\mathbf{T}}^{(2)}_{(i,j),l} = C_{ii}^{(l)} + 2C_{ij}^{(l)} + C_{jj}^{(l)}, \tag{4.32}$$

one may then extract the coefficient matrix through

$$C_{ij}^{(l)} = \frac{1}{2}\left(\tilde{\mathbf{T}}^{(2)}_{(i,j),l} - \tilde{\mathbf{T}}^{(1)}_{i,l} - \tilde{\mathbf{T}}^{(1)}_{j,l}\right). \tag{4.33}$$

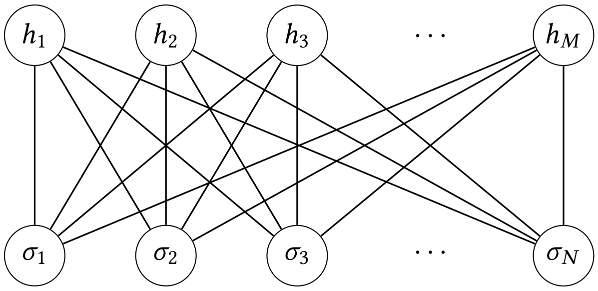

Figure 4.3: Graphical representation of a restricted Boltzmann machine (RBM). Each of the M hidden units (top layer) is exclusively connected to the N visible units (bottom layer) and vice versa.

4.2 Artificial neural networks

An artificial neural network (ANN) is a computational graph in which a weight is associated with each edge. By tuning these weights, the network can be trained to approximate arbitrary functions, given a suitable underlying graph, *i.e.* the network's *architecture*. In analogy with biological neural networks, the vertices of the graph are referred to as *neurons* (or *units*). Unlike in their biological counterparts, the architecture of an ANN, particularly the number of neurons, is typically fixed and learning is achieved solely by strengthening or weakening the connections between neurons, akin to synaptic neuroplasticity.

A simple, yet popular ANN architecture are restricted Boltzmann machines (RBMs). These feature two *layers* of N *visible* units $\{\sigma_i\}$ and M *hidden* units $\{h_j\}$, respectively. The visible layer acts as the input to evaluate the network for a given configuration of visible units. The output is then obtained by contracting the network over all possible configurations of the hidden units and superimposing their exponentials, $\sum_{\{h_j\}} \exp[-\beta E(\{\sigma_i\}, \{h_j\})]$ where $-\beta E$ is the result of the respective contractions. This is reminiscent of the calculation of a partition function by tracing over the Boltzmann weights of all thermodynamic microstates, hence the name. A Boltzmann machine is *restricted* if the network is bipartite, *i.e.* if visible units are exclusively connected to hidden units and vice versa, implying that no intralayer connections exist. Fig. 4.3 illustrates the RBM architecture.

The pioneering application of a RBM to the many-body problem employs it as an *ansatz* for the wave function of a quantum spin-$\frac{1}{2}$ system within the context of variational Monte Carlo (VMC) [24]. Both the visible and hidden degrees of freedom are then treated as binary variables, $\sigma_i, h_j = \pm 1$. The hidden units may then be traced out, yielding a product of hyperbolic cosines:

$$\Psi_M(\{\sigma_i\}, \{a_i, b_j, W_{ij}\}) = \sum_{\{h_j\}} \exp\left[\sum_i a_i\sigma_i + \sum_j b_j h_j + \sum_{ij} W_{ij} h_j \sigma_i\right] \tag{4.34}$$

$$= \exp\left[\sum_i a_i\sigma_i\right] \times \prod_j 2\cosh\left[\sum_i W_{ij}\sigma_i\right], \tag{4.35}$$

where $\{a_i, b_j, W_{ij}\}$ are the weights of visible units, hidden unit, and network connections between them, respectively. To find the ground state, stochastic reconfiguration (SR) [27, 28]

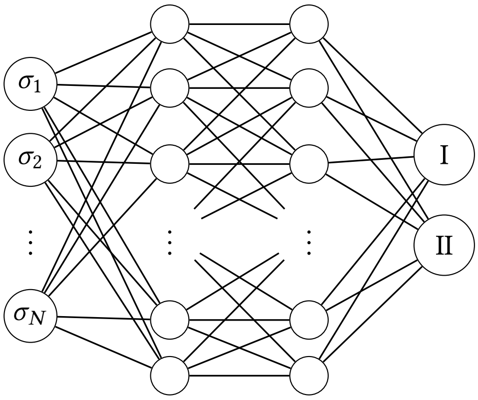

Figure 4.4: A feed-forward neural network with two hidden layers and two output units

was employed to minimize the energy with respect to the RBM trial wave function; more commonly, stochastic gradient descent (SGD) is used.

More so than the optimization algorithm, the architecture plays a crucial role for efficiency of the representation of an ANN. While RBMs have been shown to be universally capable of approximating generic probability distributions [171], this is without regard for the number of hidden units required to do so. Indeed, it has been explicitly shown that a certain class of ground states of gapped Hamiltonians cannot be *efficiently* represented by RBMs, meaning that the number of required hidden units scales faster than polynomially with the inverse energy gap [25]. The same authors show that a deep Boltzmann machine (DBM) which has at least two hidden layers however can do so. On the other hand, DBMs are harder to train compared to RBMs.

While RBMs (and DBMs) parametrize the wave function through a trace over their hidden layer(s), most ANNs rather rely on a feed-forward architecture where the input is successively passed through a number of hidden layers, the last of which is then connected to a (relative small) number of output units (*cf.* Fig. 4.4). In order to introduce nonlinearities, a nonlinear activation function is applied at each layer. The choice of these activation functions (sigmoid, "soft-max", rectified linear units (ReLU)) factors into the design of the network architecture; so does the number of hidden layers, the number of neurons in each layer, the connectivity between layers, and the addition of pooling layers. Within the supervised learning paradigm, feed-forward neural networks (FFNNs) can be efficiently trained using backpropagation [12], an algorithm relying on automatic differentiation (AD) to propagate corrections to the network weights backward through the network using the chain rule.

FFNNs have been successfully applied to parametrize wave functions for VMC using two output units, one for the complex phase and one for the modulus [22]. They have also come to fruition in the context of supervised phase classification [23, 133, 142] where one output unit per phase is used by employing *one-hot* encoding, *i.e.* phases are labeled by the unit vectors with respect to the space spanned by the output neurons. Predictions on unlabeled test data may then be made by choosing the phase corresponding to the output unit with the strongest response.

In unsupervised learning scenarios, FFNNs may still be of use for phase classification. In (variational) autoencoders, a standard FFNN is mirrored such that the former output layer resides in the middle and is subsequently used as input to the mirrored network that reconstructs the original input data based on the *latent variables* in the middle layer. The network may then be trained to minimize the reconstruction error. Since the latent variables are typically far fewer than the input variables, autoencoders thus perform a dimensional reduction. One must not choose too few latent variables for the reconstruction to become impossible. Thus, the latent variables can typically not be related to different phases directly but may be used as features for standard unsupervised methods such as kPCA [146] or t-SNE [172]. Autoencoders may also be viewed as tools for generative modeling by generating random latent variables and decoding physically realistic states from it.

Sometimes, input data are available not in the form of interchangeable independent samples, but as sequential time-series data. Prime examples for applications include both speech and video recognition. Recurrent neural networks (RNNs) are a type of network whose architecture is specifically adapted to time-series data by passing it into successive identical intra-connected layers, each passing their output on to the next one. In the physics domain, RNNs have recently been used to both classify dynamics [173] and to predict the time evolution of a quantum system [174].

The substantial importance of the network architecture and the plenitude of hyperparameters that govern it raise the question: What can an ANN actually learn? The motivation for this question is twofold. On the one hand, in physical applications it is more often than not insufficient to learn a black-box representation that captures a wave function or classifies phases; rather one wishes to characterize the underlying state of matter. On the other hand, one would hope to gain some insight as to why certain architectures succeed where others fail to guide the design of ANNs.

In a similar vein to the properties of RBMs [171], FFNNs have been shown to be universal approximators of L^p functions even with a single hidden layer and for arbitrary bounded nonlinear activation functions, given a sufficient number of hidden units in that layer [175, 176]. However, these mathematical theorems do not provide a bound on the number of hidden units and it is evident in applications that the number of layers, the connectivity among them, and the choice of the activation function all dramatically influence the required number of neurons to achieve a certain level of approximation. Indeed, the class of functions that can be efficiently approximated with a feasible number of neurons in any given architecture is comparably small. In Ref. 21, the authors argue that the reason why deep learning in particular has been successful in problems like image classification or speech recognition lies in the fact that typical data in these problems themselves originate from a small subspace of the entire configuration space. They identify the hierarchical physical process by which these data are generated as the reason why deep networks are suited to retrace the individual steps of the hierarchy one-by-one.

This hierarchical interpretation is also corroborated by insight gained from the analysis of fully trained deep neural networks for image classification. By analyzing the outputs of the intermediate layers of neurons, one observes that different layers are sensitive towards different levels of detail, becoming more coarse the closer a layer is toward the final output layer [20]. Likewise, the analysis of convolutional filter maps has produced similar insight in the Ising and XY models [23]. There, it was seen that the network based its classification scheme on the local magnetization, as well as the extent of domain walls which gives an estimate of the energy. While this is the correct approach for the Ising model, in the XY model only finite-size effects are picked up and the vortex unbinding at the Kosterlitz-Thouless (KT) transition is missed. This was previously noted based on the finite-size scaling of the networks performance alone and it was shown that nontrivial feature engineering is required for the network to learn the KT transition [148, 177].

The example of the XY model illustrates the importance of interpretability when addressing physics problems. A variety of other techniques for "rationalizing" deep neural network predictions have been developed [178]. However, all of these provide a rather qualitative understanding. Interpreting ANNs thus remains a difficult task and it is impossible to obtain quantitative results to extract analytical order parameters in quite the same way as kernel methods permit.

5

Kernel functions for tensorial order

The problem of distinguishing an ordered phase from a disordered one may be viewed as a binary classification problem. The training data consist of microscopic configurations which are labeled as being from the ordered or disordered phase, respectively.

The decision function, which quantifies the distance of a sample from the decision boundary, *i.e.*, the phase transition, serves a similar role to the magnitude of an order parameter. Given a suitable choice of the kernel, the decision function will hence reproduce the true order parameter. This relation was first pointed out by Ponte and Melko in Ref. [26]. There, the authors studied the Ising model and several of its variants using the standard quadratic kernel, which is highly interpretable but only applies to linear orders such as the Ising or XY magnetization. While being useful systems for an early proof-of-concept, such linear orders are not particularly challenging test cases, both in the sense that their physics is well-understood, but also in that the diversity of conceivable linear order parameters is limited and, hence, the machine does not learn anything that is not immediately obvious from symmetry considerations alone.

This chapter is devoted to the introduction of the tensorial kernel (TK) which is capable of capturing general O(N)-breaking orientational orders, with $N \leq 3$. This opens the door to a plethora of intricate tensor order parameters while maintaining the interpretability of the quadratic kernel upon which it is based. Below, the construction of this kernel is reviewed first and comments on its combinatorial complexity, symmetries, and implementation are made. In the last section, an argument is given to support the observation that the bias parameter can be an asset in detecting the presence of phase transitions. The resulting "rule of thumb", summarized in Eq. (5.17), paves the way for a systematic inference of the phase diagram as eludicated in Ch. 7.

5.1 Definition of the tensorial kernel

Without assuming the specific form of a potential multipolar order, there are two basic properties one can exploit to construct our kernel: (i) local order can be defined by a finite number of local fields; (ii) a multipolar order can generally be formulated in terms of tensors (or polynomials) of finite rank (degree) that are invariant under certain point-group transformations [84, 179].

The first point motivates us to partition the spin system into clusters, each containing a finite number of spins, r,

$$\mathbf{x} = \{\mathrm{S}_i\} = \{\mathrm{S}_I^\alpha\} = \{S_{I,a}^\alpha\}, \tag{5.1}$$

where $\mathbf{x} \in \mathcal{X}$ is the configuration vector and $\mathrm{S}_i \in \mathrm{O}(3)$ is the spin at lattice site i. The index $I = 1, \ldots, L^D/r$ enumerates spin clusters and $\alpha = 1, \ldots, r$ identifies spins within a cluster[1],

---

[1] For the purpose of describing configurations in the gauge model introduced in Ch. 2, the $r = 3$ "colored" spins coinhabiting each site define the clusters. Consequently, the notation introduced here is slightly deviated from, in that the cluster index $I = 1, \ldots, L^D$ is synonymous to the site index i.

such that $i = (I, \alpha)$. $a = x, y, z$ runs over the components of each spin. Any local order can, thus, be described by a function f of all the $3r$ spin components within a sufficiently large cluster by means of a lattice average over all clusters,

$$\left\langle f(\{S_a^\alpha\})\right\rangle_{\mathrm{cl}} = \frac{r}{L^D} \sum_I f(\{S_{I,a}^\alpha\}). \tag{5.2}$$

It is useful to incorporate this cluster average into the kernel to reduce the complexity of both the optimization itself and the subsequent analysis by eliminating the scaling with system size. Note that the cluster is not assumed to be the optimal choice to accommodate any given order. The choice of the cluster is guided by information on the lattice geometry or the Hamiltonian. For example, one may use a number of lattice cells as a tentative cluster. If the cluster is chosen to be larger than necessary, one will find a reducible form of the physical order parameter and can likely infer the optimal cluster size.

One can then map the spin components within each cluster to all monomials of degree n, and consequently perform a lattice average over all clusters,

$$\boldsymbol{\phi} : \mathcal{X} \to \mathcal{M}, \quad \mathbf{x} \mapsto \boldsymbol{\phi}(\mathbf{x}) = \{\phi_\mu\} = \left\{\left\langle S_{a_1}^{\alpha_1} \dots S_{a_n}^{\alpha_n}\right\rangle_{\mathrm{cl}}\right\}, \tag{5.3}$$

where index tuple has been introduced to collectively refer to the individual monomials, $\mu = (\alpha_1, \dots, \alpha_n; a_1, \dots, a_n)$. These monomials correspond to the components of the rank-n product tensor of the sublattice spins S^α. Since the sought-after local order parameter tensor must itself obey the tensor transformation properties under global SO(3) transformations, it can be represented as a superposition of such product tensors,

$$\mathbb{O} = \sum_{\boldsymbol{\alpha}} c_{\boldsymbol{\alpha}}\, \mathrm{S}^{\alpha_1} \otimes \mathrm{S}^{\alpha_2} \otimes \dots \otimes \mathrm{S}^{\alpha_n}, \tag{5.4}$$

given that their ranks match. This is a result of the fact that no other vector-like quantities are available as building blocks.

The tensorial kernel (TK) is then defined as

$$K(\mathbf{x}, \mathbf{x}') = \left[\boldsymbol{\phi}(\mathbf{x}) \cdot \boldsymbol{\phi}(\mathbf{x}')\right]^2. \tag{5.5}$$

Formally, it is a quadratic kernel with respect to the monomial feature vector $\boldsymbol{\phi}(\mathbf{x}) \in \mathcal{M}$. With this kernel, the decision function can be expressed as a quadratic form with respect to the monomial features, as seen in Sec. 4.1.1,

$$d(\mathbf{x}) = \sum_k \lambda_k y^{(k)} \left[\boldsymbol{\phi}(\mathbf{x}^{(k)}) \cdot \boldsymbol{\phi}(\mathbf{x})\right]^2 - \rho = \sum_k \lambda_k y^{(k)} \left[\sum_\mu \phi_\mu^{(k)} \phi_\mu\right]^2 - \rho = \sum_{\mu\nu} C_{\mu\nu} \phi_\mu \phi_\nu - \rho, \tag{5.6}$$

$$C_{\mu\nu} = \sum_k \lambda_k y^{(k)} \left\langle S_{a_1}^{\alpha_1} \dots S_{a_n}^{\alpha_n}\right\rangle_{\mathrm{cl}}^{(k)} \left\langle S_{a_1'}^{\alpha_1'} \dots S_{a_n'}^{\alpha_n'}\right\rangle_{\mathrm{cl}}^{(k)}, \tag{5.7}$$

where $C_{\mu\nu}$ is the coefficient matrix that is calculated from the learned support vectors. Its meaning may be illustrated for the simple case where a single magnetic order is present. $C_{\mu\nu}$ then represents a set of contractions between the relevant rank-1 basis tensors, such that the quadratic part of the decision function will realize the squared magnitude of the underlying magnetization up to a linear rescaling. More generally, as has been seen in Ch. 2, the (square of the) scalar order parameter corresponding to the tensor $\mathbb{O}$ is obtained by taking the trace of its square, $\mathrm{Tr}(\mathbb{O} \cdot \mathbb{O})$, *i.e.* it too is quadratic in monomials of the same degree as the rank of $\mathbb{O}$. As a consequence, using the tensorial kernel, the decision function can produce the scalar order parameter which ultimately allows to infer the coordinates $c_{\boldsymbol{\alpha}}$ of the order parameter tensor, Eq. (5.4). This is demonstrated many times over in the next chapter.

In the general case where a phase may possess multiple coexisting orders, including hidden nematic orders, and/or emergent local constraints, $C_{\mu\nu}$ will capture all of them simultaneously. Examples for such a case will be seen in Secs. 6.2.1 and 8.2.

Note that both the rank of the basis tensors and the optimal spin cluster do not need to be known from the start. As the rank of orientational tensors of physical interest is bounded by rank $n_{\mathrm{max}} = 6$ (and even smaller for less symmetric lattices), one can successively apply the mapping $\phi_\mu(\mathbf{x})$ [Eq. (5.3)] for different ranks from $n = 1$ to n_{max}. Thereby, tensorial order at all relevant ranks can be probed. Furthermore, the choice of the spin cluster can be guided by information on the lattice. A reasonable trial cluster consists of a number of lattice unit cells. It is hence possible to capture composite orders, such as bond and plaquette order, as well as orders with multiple finite wave vectors. If the cluster is larger than needed, the TK-SVM will learn a reducible representation of the underlying order parameters and/or constraints where a simplification is usually straightforward.

5.2 Complexity and redundancy of the monomial mapping

In Sec. 4.1.1, it was revealed that a major benefit of the kernel trick lies in the ability to avoid explicitly mapping the input data to the final feature space $\mathcal{F}$, given that its dimension would typically be very large. The tensorial kernel may be viewed as the composition of the monomial mapping with the quadratic kernel in both arguments, $K = K_{\mathrm{quad}} \circ (\boldsymbol{\phi}, \boldsymbol{\phi})$, hence, its implied Mercer mapping $\boldsymbol{\varphi} : \mathcal{X} \to \mathcal{F}$ is the composition $\boldsymbol{\varphi}_{\mathrm{quad}} \circ \boldsymbol{\phi}$ where $\boldsymbol{\varphi}_{\mathrm{quad}} : \mathcal{M} \to \mathcal{F}$ is the Mercer mapping corresponding to the quadratic kernel acting on the monomial features.

However, while the dimension of the input data is extensive in the size of the lattice, $\dim \mathcal{X} = 3L^D$, the dimension of the monomial features is not, due to the cluster average in its definition, but merely depends on the degree of the monomials, n, and the number of spins in the cluster, r. In particular, by eliminating redundant elements, *i.e.* by including the monomial $\langle S_{a_1}^{\alpha_1} S_{a_2}^{\alpha_2} \dots S_{a_n}^{\alpha_n} \rangle_{\mathrm{cl}}$ in $\boldsymbol{\phi}(\mathbf{x})$ if and only if $(\alpha_1, a_1) \leq (\alpha_2, a_2) \leq \cdots \leq (\alpha_n, a_n)$ with some arbitrary ordering imposed on the tuples, the dimension of $\mathcal{M}$ is given by the multiset coefficient

$$\dim \mathcal{M} = \left(\!\!\binom{3r}{n}\!\!\right) = \binom{3r+n-1}{n} = \frac{(3r+n-1)!}{n!(3r-1)!}. \tag{5.8}$$

Table 5.1 explicitly demonstrates the growth of the monomial feature dimension with rank.

Thanks to the removal of redundant monomials, $\dim \mathcal{M}$ is significantly smaller than $\dim \mathcal{X}$ for appreciably large system sizes. Thus, $\boldsymbol{\phi}$ actually *reduces* the dimension of the data and it is therefore prudent to carry it out explicitly in practice, *i.e.* calculate and store the monomial

	Rank n					
	1	2	3	4	5	6
$(3r)^n$	9	81	729	6 561	59 049	531 441
$\left(\!\binom{3r}{n}\!\right)$	9	45	165	495	1 287	3 003

Table 5.1: Dimensions of the monomial feature space $\mathcal{M}$ before (top row) and after (bottom row) eliminating redundant monomials. $r = 3$ spins per cluster have been assumed for illustration, as is the case in the gauge model and kagome test cases.

features and to rely on the kernel trick only for the implicit mapping $\boldsymbol{\varphi}_{\text{quad}}$ which in turn would otherwise inflate the dimension up to $\dim \mathcal{F} = (\dim \mathcal{M} + 1)(\dim \mathcal{M})/2$.

For the interpretation of the coefficient tensor, it was found to be more beneficial to reintroduce redundant monomials to avoid obfuscating the block structure discussed in the following chapter. The multiplicity, *i.e.* the number of equivalent permutations, is given by the multinomial coefficients,

$$m_{(\alpha_1,a_1)\dots(\alpha_n,a_n)} = \binom{n}{k_1, k_2, \dots, k_{3r}} = \frac{n!}{k_1!k_2!\dots k_{3r}!}, \tag{5.9}$$

where $k_1 + k_2 + \cdots + k_{3r} = n$ count the occurrences of each of the $3r$ possible index values. One may include the square roots of the multiplicities in the configuration, *e.g.* at rank 2,

$$\boldsymbol{\phi}(\mathbf{x}) = \left\{ \sqrt{m_{(\alpha_1,a_1),(\alpha_2,a_2)}} \left\langle S_{a_1}^{\alpha_1} S_{a_2}^{\alpha_2} \right\rangle_{\text{cl}} \,\middle|\, (\alpha_1, a_1) \leq (\alpha_2, a_2) \right\}. \tag{5.10}$$

That way, when using the above configuration in conjunction with the quadratic kernel, one learns the same decision function that one would have obtained if all $(3r)^n$ monomials had been considered regardless of their redundancy.

5.3 The bias parameter in phase classification

We will now investigate the role of the bias parameter ρ in the decision function. Serendipitously, the observation was made that the biases learned when applying SVM to phase classification were suspiciously close to unity whenever the correct order parameter was learned. This observation could already be made in the application to the Ising model [26], even though the authors did not realize this and focused exclusively on the coefficient matrix. Crucially, whenever the SVM is trained with samples from the same phase, this criterion is violated which enables us to draw conclusions as to the topology of the phase diagram. We will allude to this *bias criterion* throughout the remainder of this thesis and its usefulness will become apparent as it is applied in practice. In this section, an argument is given to rationalize the bias criterion.

The basic idea can be intuitively summarized as follows. For a fully disordered spin configuration $\tilde{\mathbf{x}}$, the magnitude of the ordering and thereby the first term in the decision function

Eq. (5.6) vanishes, leading to $d(\tilde{\mathbf{x}}) = -\rho$. Consequently, $\rho = -d(\tilde{\mathbf{x}}) = 1$, as (ideally) all disordered configurations $\tilde{\mathbf{x}}$ will fall onto the lower margin boundary. Therefore, one may use the behavior of the bias ρ as an indicator to signify the presence or absence of a phase transition: $\rho = 1$, if the data of either label correspond to the disordered and ordered phase, respectively; $\rho \neq 1$ (with significant violations) if the samples are in fact collected from the same phase or a significant portion of samples is mislabeled.

To support the above proposition, we begin by noting that the first term in SVM's optimization objective, Eq. (4.4), after being kernelized [Eq. (4.12)] with the multipolar kernel, Eq. (5.5), amounts to the Frobenius norm of the coefficient matrix, Eq. (5.7):

$$\begin{aligned} \|\mathbf{w}\|^2 \to & \sum_{k,k'} \lambda_k \lambda_{k'} y^{(k)} y^{(k')} \left(\sum_\mu \phi_\mu^{(k)} \phi_\mu^{(k')} \right)^2 \\ &= \sum_{\mu\nu} \sum_k \lambda_k y^{(k)} \phi_\mu^{(k)} \phi_\nu^{(k)} \sum_{k'} \lambda_{k'} y^{(k')} \phi_\mu^{(k')} \phi_\nu^{(k')} \\ &= \sum_{\mu\nu} C_{\mu\nu}^2 = \|C\|_F^2. \end{aligned} \tag{5.11}$$

As for the second part of the optimization objective, the optimal slack variables will assume a value given by the hinge loss, Eq. (4.5), *i.e.*, they satisfy their constraint by equality, or they are unnecessary and will not incur any penalty to the objective.

The data ϕ_μ may obey some internal constraints (such as the normalization of spin vectors, orthogonality among spins, *etc.*) which allow for freedom in the choice of $C_{\mu\nu}$ and ρ while keeping the decision function invariant. In particular, given some matrix $D_{\mu\nu}$ which produces merely a constant when contracted with *any* valid feature vector $\boldsymbol{\phi}$,

$$\sum_{\mu\nu} D_{\mu\nu} \phi_\mu \phi_\nu = D_0, \tag{5.12}$$

one can transform $C_{\mu\nu} \mapsto C_{\mu\nu} + \epsilon D_{\mu\nu}$ and absorb the additional constant by $\rho \mapsto \rho - \epsilon D_0$ without affecting the values of the decision function. Since only the decision function enters the hinge loss and the inequality constraints, SVM will choose the parameter ϵ freely in a way that minimizes the Frobenius norm $\|C + \epsilon D\|^2$. The solution will thus obey

$$\frac{\mathrm{d}}{\mathrm{d}\epsilon} \sum_{\mu\nu} (C_{\mu\nu} + \epsilon D_{\mu\nu})^2 = 2 \sum_{\mu\nu} (C_{\mu\nu} + \epsilon D_{\mu\nu}) D_{\mu\nu} = 0. \tag{5.13}$$

The coefficient matrix $C_{\mu\nu}$ extracted from SVM already manifests the optimal choice with respect to $D_{\mu\nu}$, thus, $\|C + \epsilon D\|$ is minimal for $\epsilon = 0$ which implies

$$\sum_{\mu\nu} C_{\mu\nu} D_{\mu\nu} = 0. \tag{5.14}$$

One particular choice is given by $\tilde{D}_{\mu\nu} := \left\langle \tilde{\phi}_\mu \tilde{\phi}_\nu \right\rangle_{\text{diso}}$ which denotes an ensemble average over configurations $\tilde{\boldsymbol{\phi}}$ from the disordered phase. The requirement of Eq. (5.12) is in fact fulfilled:

$$\sum_{\mu\nu} \tilde{D}_{\mu\nu} \phi_\mu \phi_\nu = \left\langle (\tilde{\boldsymbol{\phi}} \cdot \boldsymbol{\phi})^2 \right\rangle_{\text{diso}} = \text{const.}, \tag{5.15}$$

as the disorder average amounts to an isotropic integral over the disordered spins $\tilde{\mathrm{S}}$ independently and thus the fixed, arbitrary feature vector $\boldsymbol{\phi}$ can be eliminated from the integrand by a change of variables.

One can now calculate the value of the decision function as it is measured in the disordered phase, *i.e.*, one subjects its argument to the same disorder average,

$$\langle d(\tilde{\mathbf{x}})\rangle_{\text{diso}} = \left\langle \sum_{\mu\nu} C_{\mu\nu}\tilde{\phi}_\mu\tilde{\phi}_\nu - \rho \right\rangle_{\text{diso}} = \sum_{\mu\nu} C_{\mu\nu} \left\langle \tilde{\phi}_\mu\tilde{\phi}_\nu \right\rangle_{\text{diso}} - \rho = \sum_{\mu\nu} C_{\mu\nu}\tilde{D}_{\mu\nu} - \rho = -\rho, \quad (5.16)$$

by virtue of Eq. (5.14). This implies that the decision function assumes a constant value throughout the disordered phase. Indeed, local order parameters are typically zero throughout the disordered phase and pick up finite values as the transition to the ordered phase takes place. One should therefore shift the decision function by ρ to interpret it as an order parameter.

Since deep in the disordered phase, the individual spins are independent, the lattice average in the definition of the feature vector $\tilde{\boldsymbol{\phi}}$ already averages over many disordered spins. Thus, given a sufficiently large system, the statement can be refined to $d(\tilde{\mathbf{x}}) = -\rho$ for spin configurations $\tilde{\mathbf{x}}$ in the disordered phase.

The phase classification problem is distinct from generic classification problems in the sense that all the data from one class, the disordered phase, (on average) trace out an isosurface of the decision function. The decision boundary as well as the “upper” and “lower” margin boundaries are isosurfaces of the decision function too, corresponding to values, of 0, +1, and −1 (*cf.* Sec. 4.1.1). Thus, the “lower” margin boundary will fall onto the disordered samples, *i.e.*, $d(\tilde{\mathbf{x}}) \approx -1$, which implies $\rho = 1$. Conversely, if the disordered samples fall onto the “upper” margin boundary, this will result in $\rho = -1$. In this sense, the bias can also give an indication as to the “orientation” of the phase transition. Given two phases A and B, one may introduce the convention that $\rho(A\,|\,B) = 1$ corresponds to a situation in which A (B) is the disordered (ordered) phase. Consequently, $\rho(B\,|\,A) = -\rho(A\,|\,B)$.

The argument laid out in this section so far assumed a simple scenario where a single symmetry-breaking phase transition takes place between A and B. Based on the intuitive picture above and verified by the empirical study of the gauge model in the next chapter, several extensions can be made:

First, if one phase possesses two or more orders, while a subset of them vanishes when entering the disordered phase and the remaining ones only diminish in magnitude, $|\rho|$ will typically be slightly larger than unity, owing to a contribution from the difference in magnitude of the persevering orders. Such behavior can occur when dealing with vestigial orders and partial symmetry breaking.

Second, if the two sets of samples originate from the same ordered phase and, hence, are characterized in the same way, ρ can dramatically exceed unity, $|\rho| \gg 1$. Nevertheless, in those cases, the sign of ρ retains its physical meaning: A negative $\rho(A\,|\,B)$ indicates that A is relatively deeper in the ordered phase.

Third, ρ can also differ significantly from ±1 but fall into the interval $(-1, 1)$. This may happen when both sample sets originate from nontrivial phases featuring different characteristics. In that case, even though $C_{\mu\nu}$ can capture the characteristics of both phases, the sign of ρ will lose its above interpretation. Namely, the TK-SVM can still identify them as distinct phases, but one cannot interpret their relation in terms of a simple order-disorder transition.

Lastly, this bias criterion is also applicable for crossovers between phases of different cooperative behavior. Rather than learning the order parameter associated with the broken symmetry of a particular phase transition, the decision function will encode the constraint that governs the cooperative behavior of the spins. Note that in this case the "ordered phase" in the above argument is the one which is more constrained, even though the spins are still disordered in the sense that no symmetry is broken. Again, a bias in $(-1, 1)$ is indicative of a situation where no statement on the relative level of disorder can be made, *i.e.* both phases exhibit constraints which are mutually incompatible.

Finally, the behavior of the bias can be summarized by the following rules, which have proved themselves useful in probing phase transitions and crossovers,

$$\rho(A \,|\, B) \begin{cases} \left.\begin{matrix} \gg 1 \\ \ll -1 \end{matrix}\right\} & A, B \text{ in the same phase,} \\ \approx 1 & A \text{ in the disordered phase,} \\ \approx -1 & B \text{ in the disordered phase,} \\ \in (-1, 1) & \text{not directly comparable.} \end{cases} \tag{5.17}$$

In Sec. 8.2.1, they were used to arrive at a "hierarchy of disorder", giving a qualitative idea of the onset of various crossovers and phase transitions, even before those were analyzed in detail.

Part II

Interpreting machine results

6

Extracting order parameter tensors

Equipped with the tools presented in part I of this thesis, one has gained the ability to simulate frustrated spin models and apply the tensorial kernel in conjunction with kernel methods of machine learning to learn a classifier to distinguish multipolar phases from paramagnets. To this end, the combination of the tensorial kernel with support vector machines (TK-SVM) is used predominantly for the remainder of this thesis.

This part is devoted to leveraging the interpretability of the tensorial kernel to extract physical insight from the SVM decision function. This process is twofold: the coefficient matrix can be used to infer the analytical expression of the underlying order parameter tensor, whereas the bias parameter can be exploited to diagnose the presence of a phase transition (or a crossover) in the first place. The focus of this chapter is on the former, but references to the role of the bias parameter will be made throughout. The next chapter is exclusively concerned with the bias parameter and will demonstrate that TK-SVM can be used to obtain the phase diagram in an unbiased way.

The problem that TK-SVM tackles in the process is particularly challenging whenever either the rank of the sought-after order parameter tensor is high or multiple orders occur simultaneously. This chapter addresses both of these scenarios, however, to start things off simple, the case of a single uniaxial nematic is considered first. Throughout part II of this thesis, the gauge model that was introduced in Sec. 2.2 is used for demonstration as it allows for the systematic study of any and all of these cases.

6.1 Learning a single quadrupolar order

In this section, a simple quadrupolar order is taken as an example to illustrate the basic idea of the method. The detection of the order and the decoding of the machine result to extract the order parameter will be discussed.

One can generate spin configurations with an emerging quadrupolar order by working with the gauge symmetry $G = D_{\infty h}$ and an anisotropic coupling where $J_{ab}^{\alpha\beta} = -J\delta_{ab}$ for $\alpha\beta = \mathrm{nn}$ and $J_{ab}^{\alpha\beta} = 0$ for other $\alpha\beta$'s. The resulting model is then equivalent to the Lebwohl-Lasher model in Eq. (2.21) and the S^{l} and S^{m} spins become irrelevant. Thus, to simplify the exposition of our analysis, only the S^{n} spins are taken as input data to train the SVM, yielding the configuration vector $\mathbf{x} = \{\mathrm{S}_i^{\mathrm{n}}\}$. However, as will be discussed in Sec. 6.2.1, including S^{l} and S^{m} spins does not change the result.

The SVM is trained successively with the multipolar kernel for increasing tensor rank, *i.e.* for increasing degrees n of the monomials in the mapping Eq. (5.3). When the rank is not sufficient to capture the order parameter, the SVM overfits the training data. Here, this is the case for rank $n = 1$ which produces an erratic decision function, whereas the order is captured at rank $n = 2$, resulting in a curve.

By calculating the coefficient matrix (*cf.* Sec. 5.1), one can interpret the resulting decision

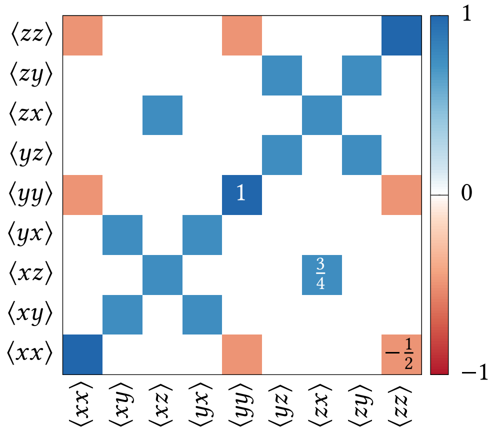

Figure 6.1: Coefficient matrix $C_{\mu\nu} = C_{ab,a'b'}$ for the quadrupolar order with the rank-2 kernel. The pattern can be decomposed according to Eq. (6.2) and leads to the uniaxial nematic tensor Q_{ab}. 28 000 samples have been used for training.

function to access its analytical structure.

$$\begin{aligned} d(\mathbf{x}) &= \sum_{\mu\nu} C_{\mu\nu} \phi_\mu \phi_\nu - \rho \\ &= \sum_{ab} \sum_{a'b'} C_{ab,a'b'} \left\langle S^{\mathrm{n}}_a S^{\mathrm{n}}_b \right\rangle \left\langle S^{\mathrm{n}}_{a'} S^{\mathrm{n}}_{b'} \right\rangle - \rho. \end{aligned} \tag{6.1}$$

The coefficient matrix $C_{ab,a'b'}$ is shown in Fig. 6.1 and encodes the contribution of the individual terms in the sum. It can be readily decomposed into three contractions

$C_{ab,a'b'} = p_1$ 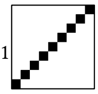 $+ p_2$ 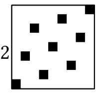 $+ p_3$ 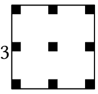 (6.2)

$$= p_1 \delta_{aa'} \delta_{bb'} + p_2 \delta_{ab'} \delta_{ba'} + p_3 \delta_{ab} \delta_{a'b'}, \tag{6.3}$$

where $p_1 = p_2 \approx \frac{3}{4}$ and $p_3 \approx -\frac{1}{2}$ can be read off. The first two contractions are compatible with the form $\|\mathbb{O}\|^2_F = \sum_{ab} \mathbb{O}^2_{ab}$, as they contract indices between two tensors. We shall call them “proper” contractions. The third contraction on the other hand is not, but it only produces a constant $\sum_{ab} \left\langle S^{\mathrm{n}}_a S^{\mathrm{n}}_a \right\rangle \left\langle S^{\mathrm{n}}_b S^{\mathrm{n}}_b \right\rangle = 1$ independent of the configuration vector. This “self-contraction” is an example where an internal constraint of the data (here, the normalization of the spins) allows the SVM to choose the weight p_3 freely in line with its optimization objective, without affecting the ability of the decision function to distinguish the phases, as pointed out in Sec. 5.3.

Substituting Eq. (6.3) back to the decision function, and making use of the properties $\left\langle S^{\mathrm{n}}_a S^{\mathrm{n}}_b \right\rangle = \left\langle S^{\mathrm{n}}_b S^{\mathrm{n}}_a \right\rangle$ and $\|\mathbf{S}^{\mathrm{n}}\| = 1$, one can write the decision function as the (squared) magnitude of a tensor order parameter, up to a linear rescaling:

$$d(\mathbf{x}) = \frac{3}{2} \sum_{ab} \left(\left\langle S^{\mathrm{n}}_a S^{\mathrm{n}}_b \right\rangle - \frac{1}{3} \delta_{ab} \right)^2 - \rho. \tag{6.4}$$

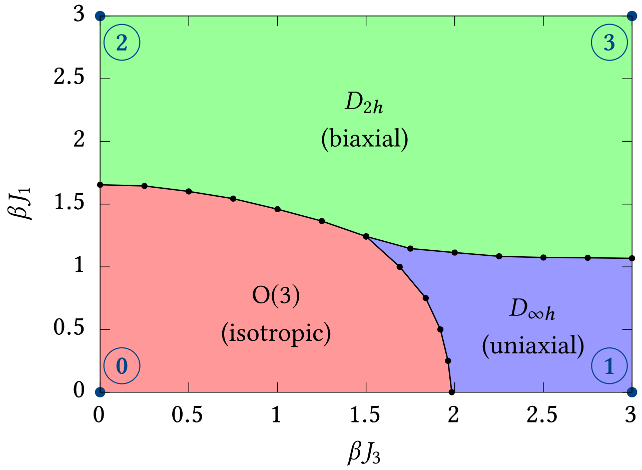

Figure 6.2: The phase diagram for the generalized quadrupolar order (*cf.* Ref. [110]). The points labeled ⓪ through ③ are used to generate training samples.

One identifies the (uniaxial) nematic tensor [180] $Q_{ab} = \left\langle S_a^{\mathrm{n}} S_b^{\mathrm{n}} \right\rangle - \frac{1}{3}\delta_{ab}$. In Fig. 6.13(b), the rescaled decision functions are compared to the true order parameter measured from Monte Carlo simulations.

6.2 Learning multiple orders

If a spin or orbital system of interest develops an order which needs to be characterized by some axial point group, in general, it may require more than one (multipolar) order parameter. For example, a generalized quadrupolar order is defined by two rank-2 tensors. In this section, the ability of our kernel, Eq. (5.5), to detect multiple orders simultaneously is demonstrated. Situations where the orderings occur at the same rank and at different ranks are considered and it is assumed here that the topology of the phase diagram is approximately known. In Sec. 7, a scheme is proposed that yields a phase diagram in lieu of such information.

6.2.1 Multiple tensor order parameters of the same rank

A biaxial order D_{2h} is considered. The training samples are prepared by choosing the gauge symmetry $G = D_{2h}$ and the exchange coupling $J_{ab}^{\mathrm{ll}} = J_{ab}^{\mathrm{mm}} = -J_1\delta_{ab}$, $J_{ab}^{\mathrm{nn}} = -J_3\delta_{ab}$ in Eq. (2.17). The gauge model is then equivalent to the Straley model of generalized quadrupolar orders [181]. J_1 and J_3 are used as tuning parameters for convenience and span the parameter space.

The associated phase diagram is shown in Fig. 6.2. It requires at least two order parameters to characterize the three phases and their transitions. If the two orders are weakly coupled, they will experience (dis-)ordering separately with one of them being irrelevant in the corresponding phase transition. However, if the coupling between them is strong, they may develop ordering in a single phase transition and need to be taken into account simultaneously. This is the case in the transition between the biaxial phase and the isotropic phase.

	$\nu = 0.1$	$\nu = 0.5$
⓪ / ①	1.0017	1.0007
⓪ / ②	1.0013	1.0007
⓪ / ③	1.0010	1.0006
① / ②	0.972	0.9995
① / ③	1.27	1.34
② / ③	8.05	7.50

(a) Labeling samples according to their points in parameter space yields six classifiers. For the last one, $\rho \gg 1$ indicates that ② and ③ belong to the same phase.

	$\nu = 0.1$	$\nu = 0.5$	Fig.
O(3) / $D_{\infty h}$	1.0017	1.0007	6.3
$D_{\infty h}$ / D_{2h}	0.985	1.0004	6.4(a)
O(3) / D_{2h}	1.0011	1.0005	6.4(b)

(b) The data sampled at points ② and ③ are assigned the same label 'D_{2h}'; correspondingly ⓪ is relabeled as 'O(3)', and ① as '$D_{\infty h}$'. In all cases, the biases are close to one, indicating that the labeling indeed represents the phases. The last column refers to the figures showing the (block structure of the) coefficient matrix corresponding to that classifier.

Table 6.1: The values of the bias parameter in learning the phases of the generalized quadrupolar order. Training samples are collected from points ⓪–③ in Fig. 6.2. A total of 25k samples have been used, and results for weak ($\nu = 0.1$) and strong ($\nu = 0.5$) regularization are shown for comparison.

Given the topology of the phase diagram, without knowledge of the exact phase boundary, one can train the SVM with configurations sampled at points deep in each phase. Here, samples at four points, ⓪–③, corresponding to the corners of the phase diagram shown in Fig. 6.2 are taken.

Using the tensorial kernel at rank 2, the multiclassification is performed as described in Sec. 4.1.1 where the samples are assigned $M = 4$ labels corresponding to the points ⓪–③. This yields six classifiers. Their respective biases are tabulated in Table 6.1(a). One can note straight away that the classifier distinguishing points ② and ③ does not correspond to a phase transition as its bias is far away from one. This is consistent with our knowledge that these points are indeed both in the biaxial phase. The bias of the classifier between ① and ③ is also somewhat elevated, so it is not clear that a phase transition takes place. However, after merging the labels ② and ③ and repeating the multiclassification with $M = 3$ distinct labels (which now correspond to the phases), one finds that the bias of the corresponding classifier is closer to one [see Tab. 6.1(b)], affirming that a phase transition is present. The larger deviation from one in this case can be explained by the fact that the uniaxial order is developed in both phases whereas the magnitude of the ordering is larger in the biaxial phase.

One may now proceed with the analysis of the three coefficient matrices obtained from the latter classification with respect to three labels. The nematic order which is now responsible for the isotropic-to-uniaxial transition in the regime of small J_1 in Fig. 6.2 is first revisited. The corresponding $C_{\mu\nu}$ matrix is shown in Fig. 6.3(a). With S^{l} and S^{m} degrees of freedom now included, it contains 81 × 81 elements, defining contractions between $\phi_\mu = \left\langle S^{\alpha_1}_{a_1} S^{\alpha_2}_{a_2} \right\rangle$ and $\phi_\nu = \left\langle S^{\beta_1}_{b_1} S^{\beta_2}_{b_2} \right\rangle$. However, when arranging the index tuples such that color indices are more

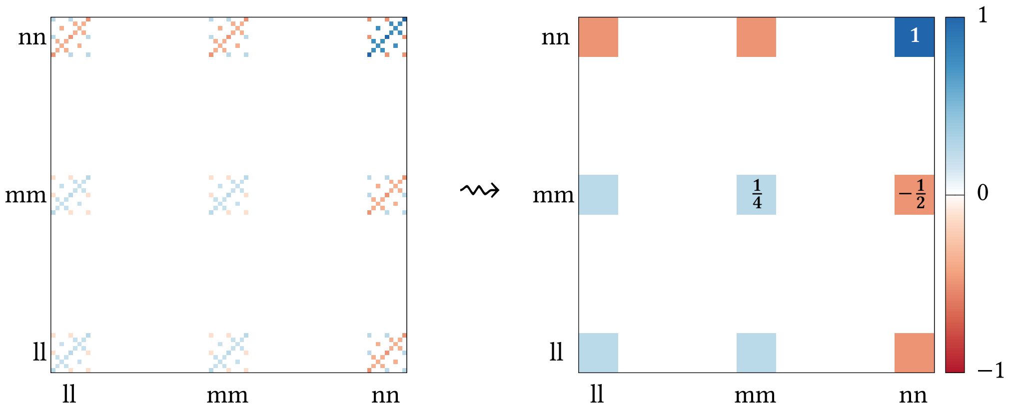

(a) full $C_{\mu\nu}$ **(b)** block structure

Figure 6.3: The coefficient matrix distinguishing the isotropic (O(3)) and uniaxial ($D_{\infty h}$) phase of the generalized quadrupolar order. The left panel displays the full matrix $C_{\mu\nu}$ where the index tuples μ and ν are sorted lexicographically and where the color indices are more significant. The resulting block structure is shown in the right panel. The block weights have been obtained by summing all matrix elements within each block over their component indices and normalizing to the top-right (nn, nn) block. The interpretation leads to an alternative expression of the nematic Q_{ab} tensor, given in Eq. (6.5). The pattern exhibited within each block is identical to Fig. 6.1.

significant than component indices (*i.e.* $\mu = (\alpha_1, \alpha_2; a_1, a_2)$), it can be divided into a 9-by-9 block structure in terms of the color indices $(\alpha_1\alpha_2), (\beta_1\beta_2)$, corresponding to the nine basis tensors in Eq. (5.4). Each block in fact features the same pattern of Fig. 6.1 up to a weight factor. In Sec. 6.1, its relation to the order parameter tensor was explained. In the following analysis, one can ignore the internal pattern of the blocks entirely and instead infer the coordinates of the order parameter tensor in the nine-dimensional tensor space from the relative weight factors of those blocks. The weight of a block may be obtained by a sum over all elements within the block as $\sum_{\mathrm{ab}} C^{\alpha\beta}_{\mathrm{ab}}$, or alternatively by the Frobenius norm as $\sqrt{\sum_{\mathrm{ab}} (C^{\alpha\beta}_{\mathrm{ab}})^2}$. Both definitions have been used and it was verified that they yield the same weights up to a sign. The first definition preserves the sign of the block weights, so it is adopted henceforth. With this definition, normalized to the most pronounced (nn, nn) block in the top-right corner in Fig. 6.3(a), the weights of the (ll, ll) and (mm, mm) blocks turn out to be $\frac{1}{4}$, while those of the (nn, ll) and (nn, mm) blocks are $-\frac{1}{2}$ [see Fig. 6.3(b)]. This gives an order parameter of the form

$$\mathbb{O}_{\mathrm{uni}} = \mathrm{S}^{\mathrm{n}} \otimes \mathrm{S}^{\mathrm{n}} - \frac{1}{2}\mathrm{S}^{\mathrm{m}} \otimes \mathrm{S}^{\mathrm{m}} - \frac{1}{2}\mathrm{S}^{\mathrm{l}} \otimes \mathrm{S}^{\mathrm{l}}. \tag{6.5}$$

Using the relation $\sum_{\alpha=\mathrm{l,m,n}} \mathrm{S}^{\alpha} \otimes \mathrm{S}^{\alpha} = \mathbb{1}$, one recovers the nematic tensor of Eq. (6.4):

$$\mathbb{O}_{\mathrm{uni}} = \frac{3}{2}\left(\mathrm{S}^{\mathrm{n}} \otimes \mathrm{S}^{\mathrm{n}} - \frac{1}{3}\mathbb{1}\right). \tag{6.6}$$

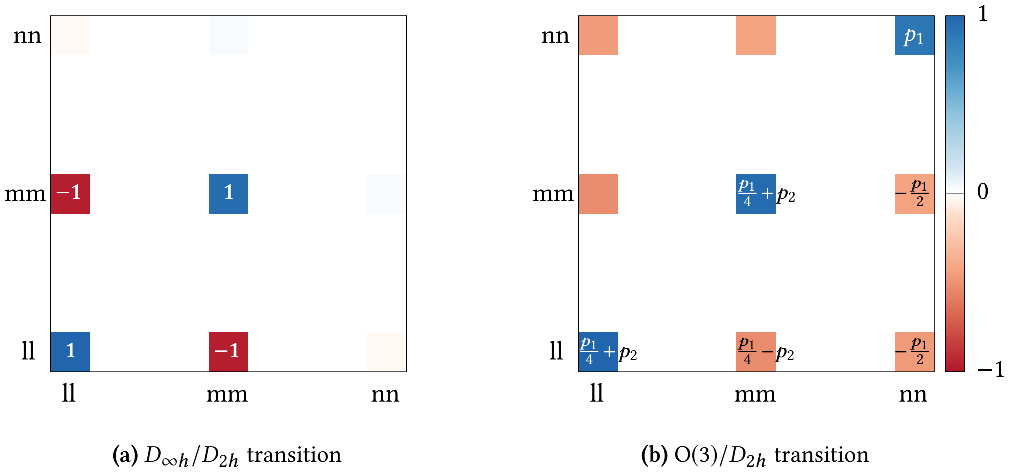

(a) $D_{\infty h}/D_{2h}$ transition

(b) O(3)$/D_{2h}$ transition

Figure 6.4: The block structures of the $C_{\mu\nu}$ matrix of the remaining two decision functions of the generalized quadrupolar order, (a) the uniaxial ($D_{\infty h}$) and biaxial (D_{2h}) phases, and (b) the isotropic [O(3)] and biaxial (D_{2h}) phases. The latter is a superposition of the patterns exhibited by the other two decision functions, shown in Figs. 6.3(b) and 6.4(a). The block weights are not fixed, but rather the coefficients p_1 and p_2 vary with the relative strength of the two orderings.

Thus, to extract the order parameter, it is sufficient to rely on the block structure of $C_{\mu\nu}$, rather than the full matrix. This simplifies the interpretation significantly, especially for learning high-rank (*cf.* Sec. 6.3) and multiple simultaneous orders.

In Fig. 6.4, the block structures of the coefficient matrices for the other two classifications are shown. The direct sum is used to compute the block weights. Figure 6.4(a) is the weight matrix trained with data sampled deep inside the uniaxial and biaxial phases. One immediately realizes a tensor of the form

$$\mathbb{O}_{\text{bi}}^{(D_{2h})} = \mathrm{S}^{\mathrm{l}} \otimes \mathrm{S}^{\mathrm{l}} - \mathrm{S}^{\mathrm{m}} \otimes \mathrm{S}^{\mathrm{m}}, \tag{6.7}$$

which is indeed the biaxial order parameter describing the uniaxial-to-biaxial phase transition [180].

Fig. 6.4(b) is the weight matrix trained with samples from the isotropic and the biaxial phases. It is a superposition of that in Figs. 6.3(b) and 6.4(a), with the weight denoted by p_1 and p_2[1]. Its interpretation then leads to a set of two order parameters, $\{\mathbb{O}_{\text{uni}}, \mathbb{O}_{\text{bi}}^{(D_{2h})}\}$, which is indeed the order parameter set that uniquely defines the D_{2h} biaxial phase.

One finds that the weights of p_1 and p_2 vary as one changes the points in phase diagram from which one samples. This does not come unexpected, as the simulataneous occurrence and the expression of the two orders are protected by symmetry (of their ground-state manifold),

---

[1] Fig. 6.4(b) can also be viewed as a superposition of three order parameters, $\mathrm{S}^{\mathrm{l}} \otimes \mathrm{S}^{\mathrm{l}} - \mathrm{S}^{\mathrm{m}} \otimes \mathrm{S}^{\mathrm{m}}$, $\mathrm{S}^{\mathrm{m}} \otimes \mathrm{S}^{\mathrm{m}} - \mathrm{S}^{\mathrm{n}} \otimes \mathrm{S}^{\mathrm{n}}$, and $\mathrm{S}^{\mathrm{n}} \otimes \mathrm{S}^{\mathrm{n}} - \mathrm{S}^{\mathrm{l}} \otimes \mathrm{S}^{\mathrm{l}}$, where two of them are independent. This is just an equivalent expression of the same ordering.

so their relative ratio depends on the microscopic coupling strengths (the value of J_1 and J_3 in this case).

This further emphasizes the importance of interpretability. In a physical problem, one typically treats different order parameters as individual quantities and measures them separately. However, a machine may combine them into a single numerical classifier. Therefore, a machine trained by samples with certain relative ratios of those order parameters may not be optimal or even misleading when being applied to samples where those ratios vary. In order to make correct predictions, one may need to be able to identify and isolate each order parameter from the machine result. This is, however, not an issue for our kernel method (or in general for an interpretable machine). The occurrence of multiple orders only leads to a *linear* superposition of the pattern of each single order, even though those orders may be strongly coupled.

6.2.2 Multiple tensor order parameters of different ranks

The quadrupolar and octupolar orders in classical kagome antiferromagnets provide examples for spin systems which simultaneously develop multipolar orders of different ranks. Indeed, the quadrupolar order in Eq. (6.6) is compatible with all dihedral symmetries D_n, D_{nh}, D_{nd}, and axial symmetries S_{2n}, C_{nh}. That is, if the ground-state manifold of a spin order cannot be ascertained theoretically, one should not immediately conclude a uniaxial phase after observing a quadrupolar order. This is also true for dipolar (rank-1) orders which are compatible with axial symmetries C_n and C_{nv}, while the Heisenberg and Néel magnetization are just limiting cases for $n \to \infty$, $\mathrm{O}(2) = C_{\infty v}$. Therefore, to correctly characterize a multipolar phase, in principle one needs to identify all relevant orders.

The tensorial kernel handles these situations in a straightforward manner. One simply has to train the SVM with kernels at different ranks n separately. Considering the crystallographic background, it is sufficient to set an upper bound $n \leq 6$. Additional complexity may arise in distinguishing nontrivial high-rank orders from responses which are already captured by order parameters of lower rank. For example, if one was to measure the quadrupolar order parameter $Q_{ab} = S_a S_b - \frac{1}{3}\delta_{ab}$ in a ferromagnetic phase, it would also show a finite response. This quadrupolar order is nevertheless trivial since it is completely captured by a dipolar order, namely, the magnetization. However, this is easily resolved if the machine is interpretable, as is the case for the tensorial kernel. One can extract the analytical expression of the learned order parameters at different ranks, and identify those without lower-rank origin.

To be concrete, take a simultaneous occurrence of quadrupolar and octupolar orders as an example. This can be realized by choosing $G = D_{3h}$ in the gauge theory Eq. (2.17). Analogously to the previous section, the training samples are collected from deep within the ordered D_{3h} phase, the uniaxial $D_{\infty h}$ phase, and the isotropic $\mathrm{O}(3)$ phase.

One then carries out the SVM optimization with kernels of ranks 1 through 6. The biases of the resulting classifiers are tabulated in Table 6.2. One sees that rank 1 is insufficient to capture any order. At rank 2, order parameters describing both the isotropic-to-uniaxial and isotropic-to-biaxial transitions are found, whereas no order parameter describing the uniaxial-to-biaxial transition could be found. The coefficient matrix $C_{\mu\nu}$ is identical to that of Fig. 6.3, indicating a quadrupolar order has been captured. At rank 3, matters are reversed and one captures the uniaxial-to-biaxial transition but not the isotropic-to-uniaxial one. The isotropic-to-biaxial

Rank	$\mathrm{O}(3)/D_{\infty h}$	$D_{\infty h}/D_{3h}$	$\mathrm{O}(3)/D_{3h}$
1	0.134	2.95	2.61
2	1.0019	5.87	1.0018
3	4.10	1.0012	1.0011
4	1.0029	0.617	1.0025
5	0.981	1.0012	1.0011
6	1.0018	1.087	1.0016

Table 6.2: The biases of the three SVM classifiers discerning the isotropic [O(3)], uniaxial ($D_{\infty h}$) and octupolar (D_{3h}) phases. Decision functions are monitored for ranks 1 through 6 of the kernel. As before, $\rho \approx 1$ indicates that an order parameter of that rank could be learned. This is the case for the uniaxial order at ranks 2, 4, 5, and 6, and for the biaxial order at ranks 3, 5, and 6. In both cases, the higher-rank ones are trivial functions of their lowest-rank representation. The transition between the isotropic and biaxial phase in the last column experiences simultaneous uniaxial and biaxial ordering and will thus learn an order parameter for any rank $n \geq 2$.

transition exhibits a coexistence of both the quadrupolar and the rank-3 order parameter. At higher ranks, no new nontrivial order parameters can be found but those that one does find are functions of the lower-rank ones. At rank 4, one essentially learns the square of the quadrupolar order parameter. At ranks 5 and 6, the tensor can be constructed from both of the lower-rank ones. Rather than relying on the bias criterion to determine if an order parameter was found, one may also measure the decision functions and discard them if they exhibit erratic behavior, similarly to how rank 1 was ruled out as an order parameter in Sec. 6.1. This approach leads to the same conclusions.

The coefficient matrix for the rank-3 order is shown in Fig. 6.5(a). For conciseness, the full matrix is omitted and only its block structure is depicted. One infers the contraction of two tensors of the form

$$\mathbb{O}_{\mathrm{bi}}^{(D_{3h})} = \mathrm{S}^{\mathrm{l}} \otimes \mathrm{S}^{\mathrm{l}} \otimes \mathrm{S}^{\mathrm{l}} - \mathrm{S}^{\mathrm{l}} \otimes \mathrm{S}^{\mathrm{m}} \otimes \mathrm{S}^{\mathrm{m}} - \mathrm{S}^{\mathrm{m}} \otimes \mathrm{S}^{\mathrm{l}} \otimes \mathrm{S}^{\mathrm{m}} - \mathrm{S}^{\mathrm{m}} \otimes \mathrm{S}^{\mathrm{m}} \otimes \mathrm{S}^{\mathrm{l}}, \tag{6.8}$$

which is the octupolar order parameter that was also found in classical kagome antiferromagnets [82]. It is a two-spin form of the D_{3h} octupolar order. However, for a coplanar order, the S^{m} spin is arbitrary in the sense that one can always introduce another spin orthogonal to S^{l}. Therefore, the octupolar order may also be defined by the S^{l} spins alone. To obtain the one-spin representation, one simply needs to examine elements inside the (lll, lll) block of the $C_{\mu\nu}$ matrix, shown in Fig. 6.5(b).

This is similar to the discussion of the quadrupolar order in Sec. 6.1, but involves more contractions owing to the higher rank. Still, these contractions and their weight can be readily inferred,

$$\begin{aligned} C^{\mathrm{lll},\mathrm{lll}}_{abc,a'b'c'} = {} & p_1\big(\delta_{aa'}\delta_{bb'}\delta_{cc'} + \text{permutations of } \{a'b'c'\}\big) \\ & + p_0\big(\delta_{aa'}\delta_{bc}\delta_{b'c'} + \text{other self-contractions}\big), \end{aligned} \tag{6.9}$$

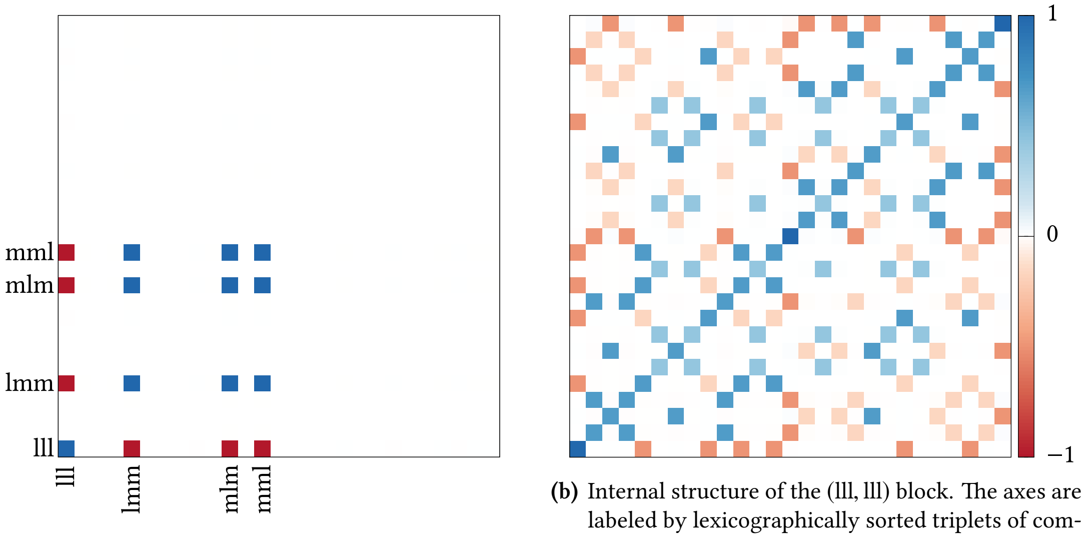

(a) Block structure of the coefficient matrix. The color indices are sorted lexicographically and those of the nonvanishing blocks are explicitly given. The interpretation of this pattern yields the rank-3 octupolar ordering tensor in Eq. (6.8).

(b) Internal structure of the (lll, lll) block. The axes are labeled by lexicographically sorted triplets of component indices (xxx, xxy, ...). This pattern corresponds to the expression Eq. (6.9).

Figure 6.5: Coefficient matrix, $C_{\mu\nu}$, learned by the rank-3 tensorial kernel, distinguishing the biaxial phase (D_{3h}) from the isotropic [O(3)] and the uniaxial phase ($D_{\infty h}$).

where p_1 and p_0 denote the weight of proper and self-contractions, respectively, and a relation $p_1 = -\frac{5}{2}p_0$ is found up to numeric precision.

As $\mathbf{S}^{\mathrm{l}\otimes 3}$ is symmetric, the six proper contractions in Eq. (6.9) are equivalent if one substitutes them to the decision function [as in Eq. (6.4)]. Similarly, the nine self-contractions in this case can also be grouped into three equivalent classes. Thus, Eq. (6.9) can effectively be expressed as

$$C^{\mathrm{lll},\mathrm{lll}}_{abc,a'b'c'} = \delta_{aa'}\delta_{bb'}\delta_{cc'} - \frac{1}{5}\delta_{aa'}\delta_{bc}\delta_{b'c'} - \frac{1}{5}\delta_{ac}\delta_{bb'}\delta_{a'c'} - \frac{1}{5}\delta_{ab}\delta_{a'b'}\delta_{cc'}, \tag{6.10}$$

whose interpretation leads to a tensor given in Eq. (2.12), the one-spin form of the octupolar order given in Ref. 82. See also Sec. 2.1.1 and Eq. (2.12) therein.

6.3 High-rank tensorial orders

In this section, TK-SVM is applied to probe an emergent tetrahedral (T_d), dodecahedral (T_h), octahedral (O_h), and icosahedral (I_h) order. These represent the most complicated multipolar orders, going beyond the quadrupolar ($D_{\infty h}$) and the in-plane octupolar (D_{3h}) order. It is important to emphasize that no prior knowledge about the existence and type of a potential multipolar order is required.

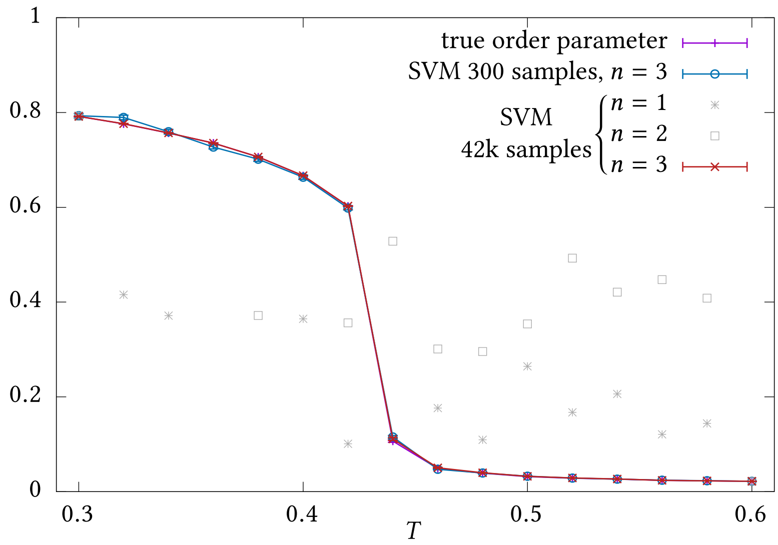

Figure 6.6: The square root of the decision function, $\sqrt{d(\mathbf{x})}$, trained at different ranks for the tetrahedral order. The true order parameter curve is shown for comparison, and $d(\mathbf{x})$ has been rescaled linearly, such that their endpoints match up. Insufficient tensor ranks do not result in a meaningful order parameter.

6.3.1 Rank 3: Tetrahedral order (T_d)

We start with the tetrahedral (T_d) order, training the SVM successively at the lowest ranks. The discriminatory temperature T_{disc} is taken to be the ideal T_c for now (*cf.* Ref. [1]), but situations $T_{\text{disc}} \neq T_c$ will be discussed later.

After training, the decision functions are measured for new testing samples. The results are shown in Fig. 6.6 by plotting $\sqrt{d(\mathbf{x})}$. Clearly, the decision function exhibits only noise for lower ranks $n = 1, 2$, but converges at $n = 3$, indicating that an order is captured at this rank.

One then extracts the order parameter from the corresponding $C_{\mu\nu}$ matrix. At rank 3, the general expression of the tensor $\mathbb{O}$ in Eq. (5.4) involves 27 basis tensors of the form

$$\mathbf{T}^{\alpha_1\alpha_2\alpha_3} = \mathbf{S}^{\alpha_1} \otimes \mathbf{S}^{\alpha_2} \otimes \mathbf{S}^{\alpha_3}. \tag{6.11}$$

As shown in Fig. 6.7(a), these divide $C_{\mu\nu}$ into 27-by-27 blocks, and each block can be identified by their color indices as $[\alpha_1\alpha_2\alpha_3; \alpha_1'\alpha_2'\alpha_3']$. Only blocks with mutually exclusive color indices have nonvanishing entries. From this one can recognize the relevant basis tensors entering the definition of the underlying order parameter. Furthermore, those blocks also exhibit an identical weight, by which the coefficients in $\mathbb{O}$ are also identified. Thus the entire $C_{\mu\nu}$ matrix then corresponds to contracting two tensors,

$$\mathbb{O}^{(T_d)} = \sum_{\alpha_1 \neq \alpha_2 \neq \alpha_3} \mathbf{T}^{\alpha_1\alpha_2\alpha_3} \tag{6.12}$$

which is exactly the tetrahedral order parameter [113]. Consistently, the decision function is related to its norm squared, $d(\mathbf{x}) \sim \|\mathbb{O}^{(T_d)}\|_F^2$, up to linear rescaling.

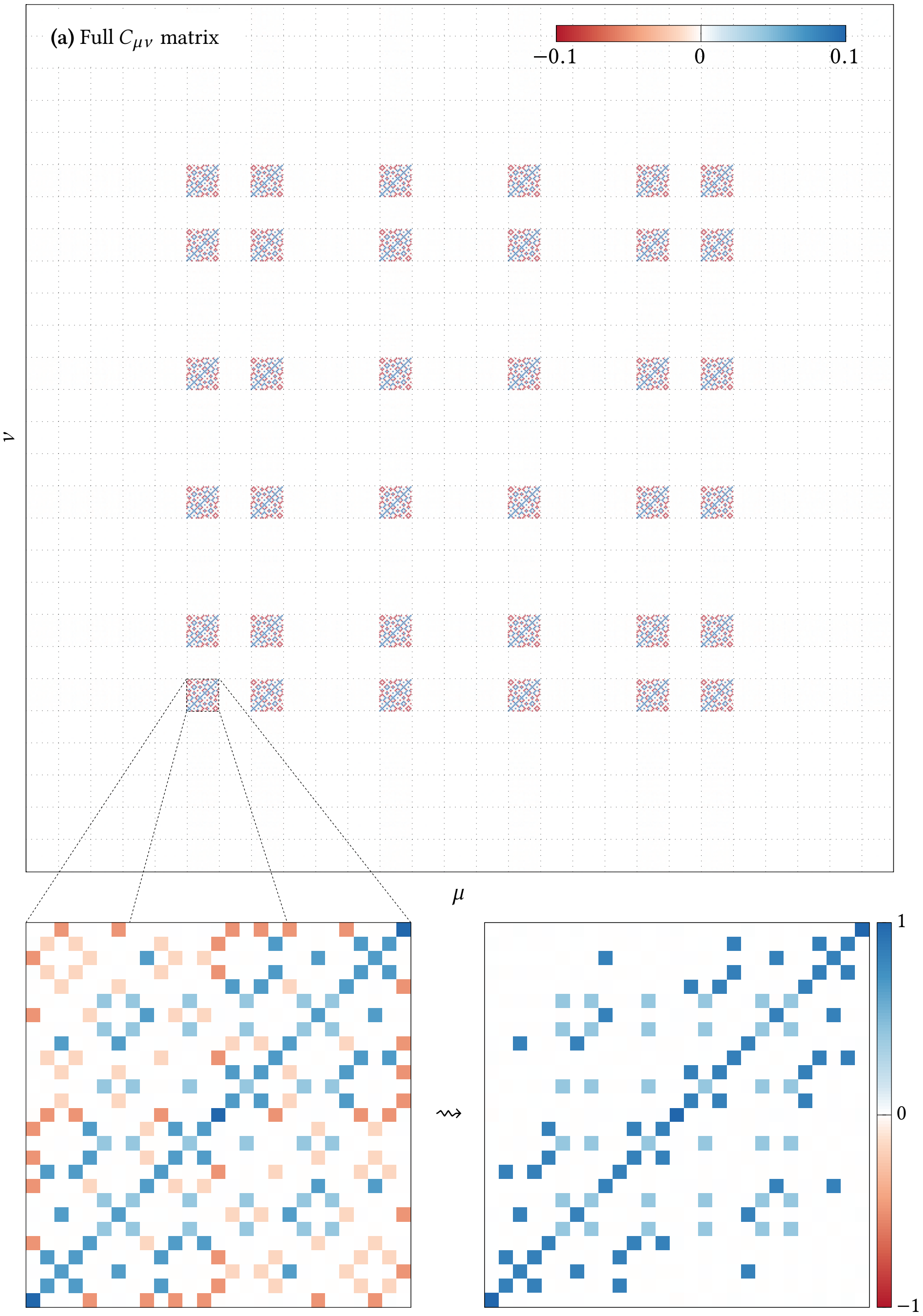

(b) Full lmn; lmn block

(c) Non-trivial contractions

Figure 6.7: The coefficient matrix $C_{\mu\nu}$ for the tetrahedral order learned using the rank-3 kernel. (a) Full $C_{\mu\nu}$ matrix, where the index tuples $\mu, \nu = (\alpha_1, \alpha_2, \alpha_3; a_1, a_2, a_3)$ are lexicographically ordered. Each block is assigned coordinates $[\alpha_1\alpha_2\alpha_3; \alpha_1'\alpha_2'\alpha_3']$. Nontrivial blocks have mutually exclusive color indices. (b) Details of the [lmn; lmn] block, in comparison with (c) where trivial self-contractions have been removed.

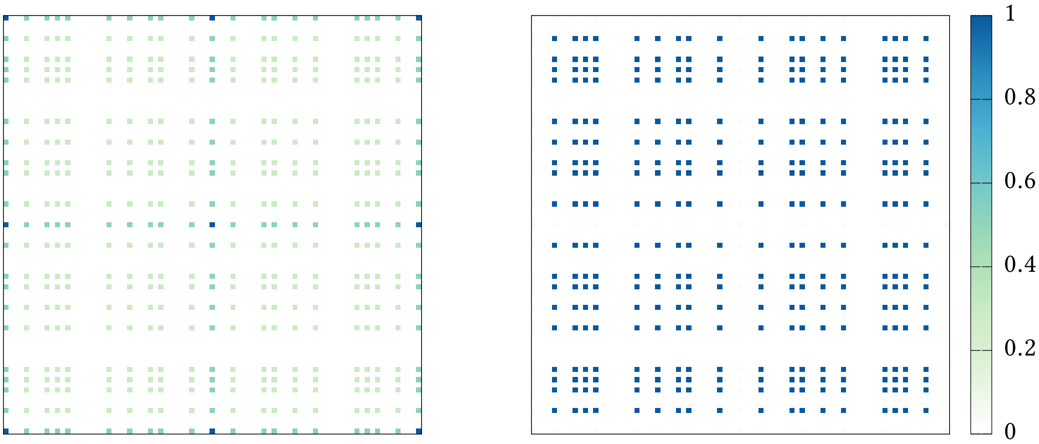

(a) Octahedral O_h **(b)** Dodecahedral T_h

Figure 6.8: Block structure of $C_{\mu\nu}$ for (a) the octahedral and (b) the dodecahedral order, learned using the rank-4 kernel. Each pixel corresponds to a block of $C_{\mu\nu}$, identified by coordinates $[\alpha_1\alpha_2\alpha_3\alpha_4; \alpha'_1\alpha'_2\alpha'_3\alpha'_4]$. The value of each pixel is given by the squared Frobenius norm of the corresponding block.

Zooming into the details of a nontrivial block, *e.g.*, the [lmn; lmn] shown in Fig. 6.7(b), its entries are seen to correspond to all possible contractions of two basis tensors $\mathbf{T}^{\alpha_1\alpha_2\alpha_3}$ and $\mathbf{T}^{\alpha'_1\alpha'_2\alpha'_3}$. These include proper contractions such as $T^{\alpha_1\alpha_2\alpha_3}_{a_1a_2a_3}T^{\alpha'_1\alpha'_2\alpha'_3}_{a_3a_2a_1}$ and self-contractions such as $T^{\alpha_1\alpha_2\alpha_3}_{a_1a_1a_3}T^{\alpha'_1\alpha'_2\alpha'_3}_{a_3a_2a_2}$ which contract at least one pair of indices on the same tensor. The former type is consistent with the Frobenius inner product $\mathrm{Tr}\big(\mathbf{T}^{\alpha_1\alpha_2\alpha_3}\cdot\mathbf{T}^{\alpha'_1\alpha'_2\alpha'_3}\big)$, and has nontrivial contributions to the decision function. In contrast, the self-contractions only contribute a trivial constant to the decision function and can be systematically identified and removed by a least-squares fit, as shown in Fig. 6.7(c).

The key insight here is that, if a multipolar order is detected, its order parameter can be inferred from the "coordinates" of nontrivial blocks and their relative weights, regardless of the details within each block. Hence, the interpretation of $C_{\mu\nu}$ is rather straightforward.

6.3.2 Rank 4: Octahedral (O_h) and dodecahedral (T_h) order

This analysis based on the block structure also holds true for the more complicated orders. In Fig. 6.8, the block structures of $C_{\mu\nu}$ capturing the octahedral (O_h) and dodecahedral (T_h) are shown. For both cases, the order is learned at rank 4, and each block (pixel) is again identified by the spin color indices $[\alpha_1\alpha_2\alpha_3\alpha_4; \alpha'_1\alpha'_2\alpha'_3\alpha'_4]$. The coordinates of the dominant blocks feature four identical color indices (O_h) and two mutually exclusive pairs of identical color indices (T_h), respectively. Correspondingly, their interpretations give rise to the ordering tensors [84],

$$\mathbb{O}^{(O_h)} = \mathbf{T}^{\mathrm{llll}} + \mathbf{T}^{\mathrm{mmmm}} + \mathbf{T}^{\mathrm{nnnn}} \tag{6.13}$$

and

$$\mathbb{O}^{(T_h)} = \mathbf{T}^{\mathrm{llmm}} + \mathbf{T}^{\mathrm{mmnn}} + \mathbf{T}^{\mathrm{nnll}}. \tag{6.14}$$

In particular, $\mathbb{O}^{(T_h)}$ is a partially symmetric tensor and has six equivalent definitions generated by permuting its color indices. Interestingly, SVM captures all these variants exhaustively. Moreover, the subdominant blocks in Fig. 6.8 effectively remove the trace of $\mathbb{O}^{(O_h)}$ and $\mathbb{O}^{(T_h)}$, which does not change the decision function but is desirable in terms of SVM's optimization objective. Such blocks do not occur in Fig. 6.7(a) in the T_d case as $\mathbb{O}^{(T_d)}$ is traceless.

6.3.3 Rank 6: Icosahedral (I_h) order

Arguably the most complicated multipolar order breaking the O(3) symmetry is the icosahedral (I_h) order. Its minimal ordering tensor was only found recently [84] and has rank 6. Slightly cryptically, it can be written as

$$\begin{aligned}\mathbb{O}^{(I_h)} &= \sum_{\text{cyc}}\left[\mathrm{S}^{\mathrm{l}\otimes 6} + \sum_{\{+,-\}}\left(\frac{1}{2}\mathrm{S}^{\mathrm{l}} \pm \frac{\varphi}{2}\mathrm{S}^{\mathrm{m}} \pm \frac{1}{2\varphi}\mathrm{S}^{\mathrm{n}}\right)^{\otimes 6}\right] - \frac{1}{7}\sum_{\text{comb}}\delta_{\alpha_1\alpha_2}\delta_{\alpha_3\alpha_4}\delta_{\alpha_5\alpha_6}\mathrm{S}^{\alpha_1}\otimes\cdots\otimes\mathrm{S}^{\alpha_6}\\ &= \tfrac{7\varphi-1}{112}\left(\tfrac{5}{7\varphi-1}\,\mathrm{S}^{\mathrm{l}\otimes 6} - \mathrm{S}^{\mathrm{l}\otimes 4}\mathrm{S}^{\mathrm{m}\otimes 2} + \tfrac{7\varphi-6}{7\varphi-1}\,\mathrm{S}^{\mathrm{l}\otimes 4}\mathrm{S}^{\mathrm{n}\otimes 2} + \tfrac{5}{7\varphi-1}\,\mathrm{S}^{\mathrm{l}\otimes 2}\mathrm{S}^{\mathrm{m}\otimes 2}\mathrm{S}^{\mathrm{n}\otimes 2} + \ldots\right),\end{aligned} \tag{6.15}$$

where $\varphi = \frac{\sqrt{5}+1}{2}$ is the golden ratio and $\sum_{\text{cyc}}$ sums over cyclic permutations of $\{\mathrm{S}^{\mathrm{l}}, \mathrm{S}^{\mathrm{m}}, \mathrm{S}^{\mathrm{n}}\}$. The second term in the first line of the above equation is introduced to make $\mathbb{O}^{(I_h)}$ traceless, and $\sum_{\text{comb}}$ runs over all nonequivalent combinations of the color indices.

The icosahedral (I_h) order is captured by TK-SVM with a rank-6 tensorial kernel, and one thus extracts a coefficient matrix whose elements are denoted by $C_{\mu\nu} = C^{\boldsymbol{\alpha\beta}}_{\mathbf{ab}} = C^{\alpha_1\ldots\alpha_6,\beta_1\ldots\beta_6}_{a_1\ldots a_6,b_1\ldots b_6}$. The coefficient matrix is divided into 729-by-729 blocks, identified by their color indices $[\boldsymbol{\alpha}, \boldsymbol{\beta}]$. At ranks as high as this, the interpretation of the full coefficient matrix becomes rather tedious. Fortunately, it is again sufficient to rely on the block structure alone and infer the relevant terms of the ordering tensor from the appearance of these blocks and their relative weight.

In this way, the "coordinates" of the icosahedral ordering tensor can be found; the first few terms read:

$$\begin{aligned}\mathbb{O}^{(I_h)}_{\text{SVM}} = 0.48657\,\mathrm{S}^{\mathrm{l}\otimes 6} - \mathrm{S}^{\mathrm{l}\otimes 4}\mathrm{S}^{\mathrm{m}\otimes 2} + 0.51608\,\mathrm{S}^{\mathrm{l}\otimes 4}\mathrm{S}^{\mathrm{n}\otimes 2}\\ + 0.48450\,\mathrm{S}^{\mathrm{l}\otimes 2}\mathrm{S}^{\mathrm{m}\otimes 2}\mathrm{S}^{\mathrm{n}\otimes 2} + \ldots.\end{aligned} \tag{6.16}$$

The coefficients of these terms are normalized against the $\mathrm{S}^{\mathrm{l}\otimes 4}\mathrm{S}^{\mathrm{m}\otimes 2}$ term, but this choice is arbitrary. All in all, 183 nonvanisching terms are seen to contribute. The full coordinates have been published in the supplemental materials to Ref. [2]. This result for $\mathbb{O}^{(I_h)}_{\text{SVM}}$ is consistent with the theoretical expectation, Eq. (6.15). As a proof of principle, the golden ratio can be infered numerically by fitting all those coordinates in which it is expected to appear analytically to Eq. (6.16). The resulting value of 1.61784 confirms the quantitative accuracy of the method.

6.4 Quantifying quality of learning

After having demonstrated the analytical accessibility of the classifier learned by TK-SVM, this section will scrutinize the impact of both the regularization parameter and the setup of the classification problem.

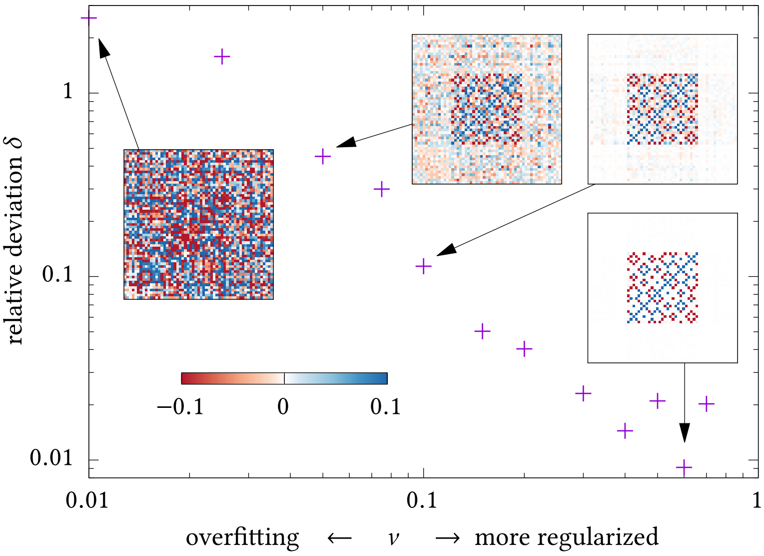

Figure 6.9: Deviation δ for the tetrahedral order, computed with different levels of regularization ν.

The usual procedure employed in the context of machine learning in this regard would involve testing the learned classifier on an additional set of labeled data and using the success rate of the prediction as a metric for its quality. Owing to the strong interpretability of TK-SVM, a more holistic approach can be taken by comparing the extracted coefficient matrix, $C_{\mu\nu}$, to the theoretically expected one, $\tilde{C}_{\mu\nu}$, and defining a relative deviation in terms of the elementwise discrepancy as expressed by the Frobenius norm,

$$\delta := \frac{\|\mathrm{C} - \tilde{\mathrm{C}}\|_F}{\|\tilde{\mathrm{C}}\|_F} = \sqrt{\left(\sum_{\mu\nu}(C_{\mu\nu} - \tilde{C}_{\mu\nu})^2\right)\left(\sum_{\mu\nu}(\tilde{C}_{\mu\nu})^2\right)^{-1}}. \tag{6.17}$$

6.4.1 Regularization parameter

In Sec. 4.1.1, the optimization problem that underlies SVMs, Eq. (4.4), has been introduced and the role of the regularization parameter was motivated. As discussed therein, the ν-SVM scheme [164] gives rise to an alternative regularization parameter, $\nu \in [0, 1)$ which is more convenient to use in practice. ν roughly corresponds to the fraction of training samples that are invoked as support vectors. A larger value of ν will thus “soften” the SVM margin, corresponding to a stronger regularization of the problem, while a small ν will place too much emphasis on individual samples, giving rise to overfitting.

For the present work, a stronger regularization in terms of ν was found to systematically improve the quality of the learned order parameter as demonstrated in Fig. 6.9 for the tetrahedral order.

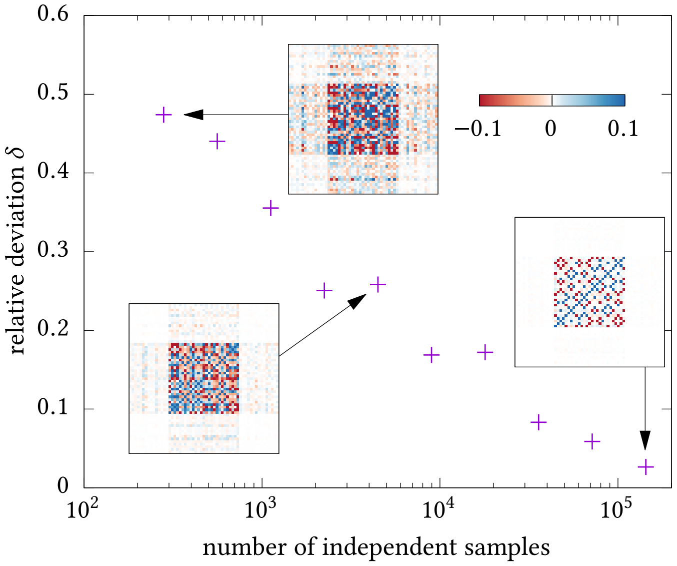

Figure 6.10: Deviation δ for the tetrahedral order as a function of the number of training samples used to calculate the SVM model which is doubled from point to point, all the while keeping the number of Monte Carlo steps between adjacent samples constant. The insets show excerpts of the coefficient matrix for selected points.

Thus, throughout this thesis, rather large values of ν between 0.4 and 0.6 have been chosen whenever the coefficient matrix was to be extracted. In situations were the presence of a meaningful distinction between the data, either in the form of a phase transition or a crossover, remained unclear, a lower regularization of $\nu = 0.1$ was adopted.

Tabs. 6.1 and 6.3 give results for both levels of regularization; it can be seen that a stronger regularization also results in a bias which is closer to its ideal value of $|\rho| = 1$ when a phase transition is indeed captured.

6.4.2 Size of the training dataset

Next, the dependence of the deviation δ on the number of training samples is demonstrated over several orders of magnitude. Again, the tetrahedral order is taken as a reasonably complicated example, but the general features are also valid for the other aforementioned orders.

Unsurprisingly, the deviation δ is seen in Fig. 6.10 to decline almost monotonously with the number of training samples, suggesting a systematic improvement. As can be seen from the insets, the pattern in the coefficient matrix becomes successively more clear. Interestingly, the expected block structure of $C_{\mu\nu}$ has already emerged at as little as 300 samples, which is sufficient to infer the underlying order parameter. One should note that δ is a rather sensitive deviation metric. Empirically, with a deviation $\delta \approx 0.5$, the measured decision function $d(\mathbf{x})$ remains in decent agreement with the true order parameter curve (see Fig. 6.6).

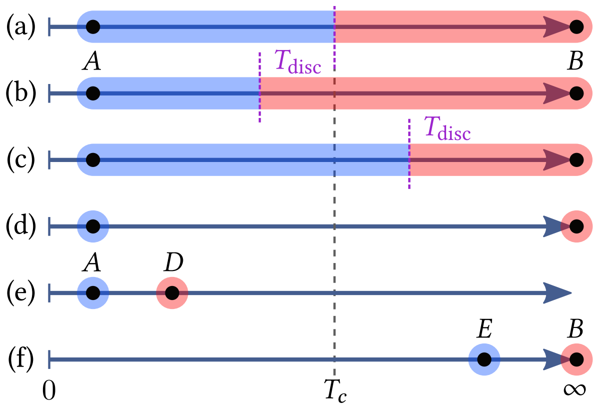

Figure 6.11: Graphical representation of different training schemes. Samples are taken from temperatures corresponding to the shaded regions and labeled as "ordered" (blue) or "disordered" (red). The first three schemes use a continuous distribution of temperatures from $T_A \ll T_c$ to $T_B = \infty$ and differ by the discriminatory temperature T_{disc} used to assign the labels, where $T_{\text{disc}} = T_c = 0.52$ (a), $T_{\text{disc}} = 0.4 < T_c$ (b), and $T_{\text{disc}} = 0.64 > T_c$ (c) have been chosen, respectively. The concrete temperatures read as $T_A = 0.2$, $T_B = \infty$, $T_D = 0.25$, $T_E = 2$.

6.4.3 Comparison of training schemes

Several different schemes to generate training data for the SVM are conceivable. These are illustrated in Fig. 6.11 and labeled (a) through (f). This subsection will elucidate the impact of this choice on the SVM result. This is not only relevant because it can give an indication as to the resilience towards unintentionally misclassified training samples, but will be seen to lay the groundwork for the further exploitation of the bias criterion in the next chapter. For this purpose, the example of a single quadrupolar order from the beginning of this chapter, Sec. 6.1, will be revisited.

One can either use samples generated from a uniform distribution of temperatures crossing the phase transition, (a) through (c), or at two discrete temperatures deep inside each phase, as shown in Fig. 6.11 (d). When adopting the first approach, one has to set a discriminatory temperature, T_{disc}, to label samples taken at temperatures below and above T_{disc}. Ideally, it should coincide with the critical temperature, $T_{\text{disc}} = T_c$, which is the case in scheme (a), whereas $T_{\text{disc}} \neq T_c$ is deliberately chosen in schemes (b) and (c) to study the effect of misclassified samples. If the temperature distribution is discrete, the notion (and choice) of a discriminatory temperature is not necessary. Schemes (e) and (f) are discussed at the end of this subsection.

Continuous vs. discrete training set

In all cases, the decision function is measured and the $C_{\mu\nu}$ matrix is examined as before. As anticipated, the coefficient matrix exhibits the same pattern as shown in Fig. 6.1 for continuous (a) and discrete (d) temperature distributions, meaning the physical order parameter is captured regardless.

		$\nu = 0.1$		$\nu = 0.4$	
	T_{disc}	$\lvert\rho\rvert$	δ	$\lvert\rho\rvert$	δ
(a)	0.52	1.012	0.14	1.001	0.063
(b)	0.4	6.83	1.97	1.003	0.042
(c)	0.64	2.32	0.14	1.0012	0.087
(d)	n/a	1.0012	0.0014	1.0007	0.0013
(e)	n/a	33.9	0.0090	25.2	0.0048
(f)	n/a	0.15	1.78	6.1	0.41

Table 6.3: The SVM bias parameter $|\rho|$ and the deviation δ from the true uniaxial nematic order parameter are given for 28K samples generated according to the training schemes (a)–(f) and for weak ($\nu = 0.1$) and strong ($\nu = 0.4$) regularization. $|\rho| \approx 1$ indicates a phase transition was captured.

Table 6.3 shows results for the various training schemes and for weak ($\nu = 0.1$) and strong ($\nu = 0.4$) regularization. Aside from the aforementioned deviation metric δ, also the bias $|\rho|$ is tabulated which is accessible as part of the optimization result and expected to attain a value of 1 if the SVM learned a physical order parameter for reasons laid out in Sec. 5.3.

First, observe that the order parameters extracted using strong regularization are always better than those obtained using weaker regularization. This is consistent with the previous findings of Sec. 6.4.1. Also observe that training set (d) in fact yields the best results, even compared to set (a) where the accurate critical temperature was used to discriminate the phases. Thus, SVM seems to work best if the training data exhibit the characteristics of the ordered phase most pronounced. It does not benefit from training data in the vicinity of the critical point.

However the continuous training sets (a) through (c) allow for a validation of the tentative phase diagram. Whereas in (a) the correct order parameter is learned for both degrees of regularization, the misclassification of the samples with temperatures between T_{disc} and T_c in sets (b) and (c) induces significant deviations from the true order parameter at weak regularization which is compensated for at stronger regularization. If continuous training is used in this way to verify the existence of a transition at T_{disc}, a relatively weak regularization may be desired.

However, even at the stronger regularization, the quality of the coefficient matrix continues to depend on the amount of misclassified samples, albeit rather weakly. Figure 6.12 shows δ against the discrepancy of the assumed T_{disc} from the real T_c. Note the relatively small deviation even for an estimate of the critical point that is off by as much as $|\tau| \sim 40\%$, where $\tau = \frac{T_{\text{disc}} - T_c}{T_c}$. This robustness of the SVM facilitates applications where the locus of the phase transition is not known *a priori*. Moreover, a crude $C_{\mu\nu}$ learned with large $|\tau|$ can in turn guide a better estimate of T_c, as a well behaved $d(\mathbf{x})$ is still obtained, somewhat reminiscent of the learning-by-confusion scheme [132]. Additionally, as seen from Fig. 6.10, a crude $C_{\mu\nu}$ may already suffice for an appropriate inference of the potential order parameter by which one could further

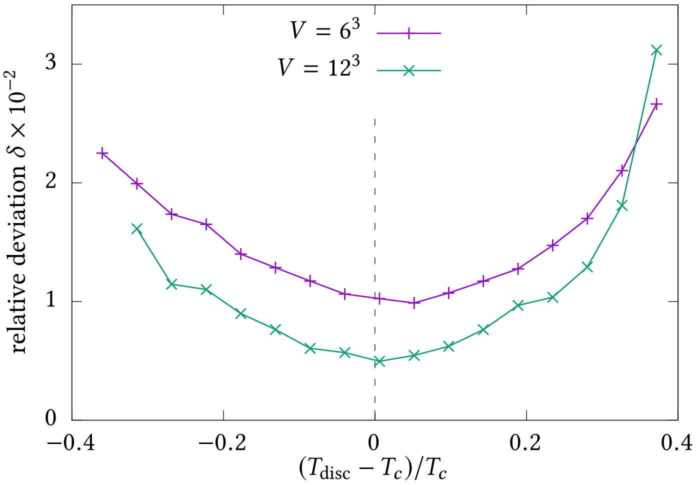

Figure 6.12: Deviation δ for the tetrahedral order against different discriminatory temperatures T_{disc} used to classify training samples. A relatively strong regularization of $\nu = 0.4$ was used.

derive more sensitive measurements of a phase transition, such as the susceptibility and Binder cumulant.

Further, note the correlation between a small deviation δ and a bias $|\rho|$ close to one in all cases for (a) through (d) in Tab. 6.3. This is consistent with the expectation of $|\rho| = 1$ for a physical order parameter and enables one to use the bias to gauge the quality of the learned order parameter without examining its analytical structure. In case (b), samples from the ordered phase are wrongly labeled as disordered and push the SVM margin boundary away from the manifold of truly disordered samples which both induces a bias $|\rho| \gg 1$ and deforms the decision boundary, resulting in a faulty order parameter, $\delta \gg 0$. Likewise, in the opposite case (c), which falsely classifies disordered samples as ordered ones, the margin is forcibly kept very narrow which makes it prone to overfitting.

In the left panel of Fig. 6.13, the "raw" decision functions without any rescaling are shown. Note that the constant value attained in the disordered phase corresponds to $-\rho$. The absolute scale of the decision function is related to the inverse width of the SVM margin. For the continuous sampling schemes, the margin is more narrow as it is constrained by samples close to the transition. In the discrete scheme (d), the decision function gives values between −1 and 1, corresponding to the extreme temperatures it was trained at. Furthermore, the zero crossing of the raw decision function, which determines the label of a testing sample, approximately reproduces the discriminatory temperatures used in the continuous training schemes (a) and (b), whereas the discrete scheme (d) is not trained to classify samples close to the transition.

While these features of the "raw" decision function can provide a deeper understanding of the workings of the SVM, they are physically irrelevant and the decision functions may therefore be shifted by ρ to obtain a value of zero in the disordered phase and rescaled to match the true nematicity. As can be seen from the right panel in Fig. 6.13, the result is very close in all three cases, even for scheme (b).

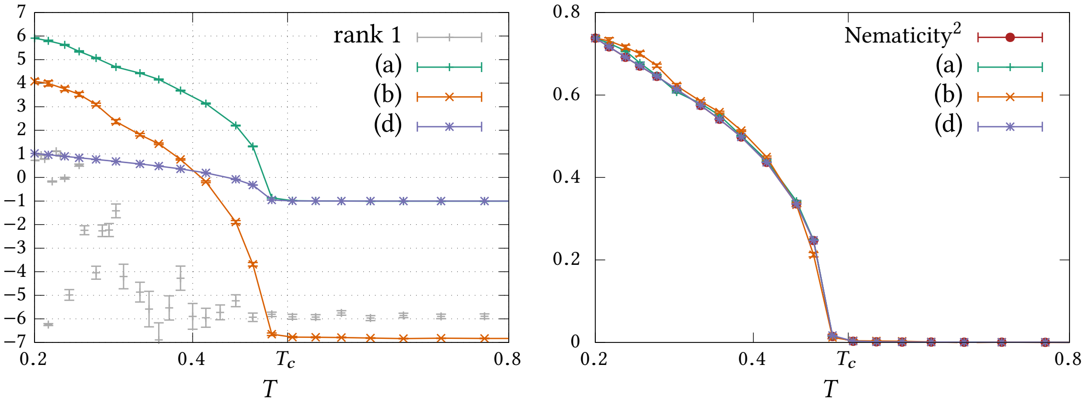

(a) raw decision functions

(b) rescaled

Figure 6.13: The decision function, obtained from the earlier training with regularization $\nu = 0.1$, is measured as an observable in Monte Carlo simulations at temperatures spanning the phase transition. The left panel shows the numerical values of the decision functions as obtained from SVM. When training the SVM with the rank-1 kernel (shown in gray), the quadrupolar order cannot be captured, resulting in an erratic decision function. The curves (a), (b), and (d) are trained with the rank-2 kernel and correspond to the eponymous training schemes (*cf.* Fig. 6.11). The zero crossing of the decision functions marks the decision boundary, whereas the constant value for $T > T_c$ is given by $-\rho$ (*cf.* Tab. 6.3). The right panel shows the same curves, but shifted up by ρ, and are seen to match the square of the uniaxial nematicity after being rescaled.

Training in the same phase

Finally, two more training schemes where the samples are taken at two discrete temperatures which are both in the ordered phase (e) or disordered phase (f) are examined. This serves to assess the capability to distinguish these cases where no phase transition takes place from those where it does, (a)–(d). This can be physically relevant in situations where the phase boundary is not known, source data is limited, or when multiple order parameters are involved, while not all of them experience a phase transition.

Interestingly, when both training temperatures lie within the ordered phase (e), the SVM still manages to learn the order parameter, as is apparent from the very small deviations δ in Tab. 6.3. This can be explained by the fact that the magnitude of the true order parameter is not constant within the ordered phase, but increases in value as one moves deeper inside the phase. The true order parameter is still the best decision function the SVM can learn in this situation to distinguish samples from the two temperatures. Note that this enables us to measure the decision function at a range of temperatures which can even exceed the training temperatures and read off the factual transition point from the decision function.

Despite the excellent δ in scenario (e), the corresponding biases ρ are far away from unity. This is no surprise as the argument put forth in Sec. 5.3 relied on the properties of disordered samples. Thus, the bias enables us to distinguish this situation from case (d) where a transition takes place between the training temperatures.

A different picture is obtained when one attempts to train the SVM with samples from two temperatures in the disordered phase (f). The magnitude of the true tensor order parameter is constant (zero) throughout the disordered phase which makes it unsuitable to distinguish samples from the two temperatures. Thus, SVM does not learn the correct order parameter, as is manifest from the large value of δ in Table 6.3, but instead overfits the training data in an attempt to construct a better decision function. As a further indication of overfitting, the decision function is not reproducible. Likewise, also the bias ρ is fluctuating and in general will not be close to one.

7

Mapping the topology of the phase diagram

Chapter 4 introduced support vector machines as an instance of supervised machine learning. In the preceding chapter, it was used as such in the context of phase classification by labeling the training data according to the tentative phases. It was also demonstrated that the bias parameter ρ can in fact be used to ascertain whether or not the labeling of the training samples is consistent with the presence of a phase transition between different phases. This ability has previously been rationalized by the argument put forth in Sec. 5.3 and the resulting criterion was summarized in Eq. (5.17).

Motivated by this, one can embrace this bias criterion as the central element of a learning scheme that relegates the supervision aspect to its weakest possible sense. Consider a spin system involving a set of physical parameters like temperature or interactions. One assigns the same labels to all spin configurations which were sampled at the same points in parameter space, while any two spin configurations sampled at different points in the parameter space are given distinct labels. Using the bias criterion, those points exhibiting the same physics—that is to say, those in the same phase—can be identified. In Sec. 6.2.1, this was the case between labels ② und ③. By considering a multitude of different points simultaneously, one can trace out the phase boundaries and infer an emergent labeling corresponding to genuine phases. In this way, TK-SVM becomes functionally unsupervised.

7.1 Graph construction

To attain the topology of the phase diagram more systematically, one can sample spin configurations from, say, M different points covering the parameter space uniformly and assign them distinct labels. This constitutes M classes of training samples to which TK-SVM multi-classification is applied. As a result, for each scrutinized rank n and spin cluster, one obtains $M(M-1)/2$ decision functions, each yielding a separate bias parameter, corresponding to the binary classifiers between any two labels.

One then has to make a decision whether or not each pair of labels is to be considered to originate from the same phase, based on the bias criterion. Exactly how this is decided will be expanded on below in Sec. 7.3. Ideally, already $\mathcal{O}(M)$ such equivalence decisions are sufficient to establish equivalence classes among the labels through transitivity. Hence, for reasonably large M, the $\mathcal{O}(M^2)$-many equivalence relations will exhibit a large amount of redundancy. This is just as well, since the bias rules [Eq. (5.17)] are not hard-and-fast and some of the derived equivalence relations are likely to contradict themselves.

In order to efficiently represent the entirety of the equivalence relations and to reconcile any inconsistencies, it is useful to encode them in a simple, undirected graph. To this end, one considers the M labels as vertices and introduces edges connecting two vertices whenever their labels have been deemed equivalent. As an example, let us revisit the phase diagram for the D_{2h} gauge symmetry of Sec. 6.2.1. The graph resulting from the above procedure on a 10×10 ($M = 100$) grid at rank 2 is shown in Fig. 7.1. Visual inspection of the graph immediately reveals three regions which are densely intraconnected while being sparsely interconnected, corresponding to the three phases of the phase diagram (*cf.* Fig. 6.2).

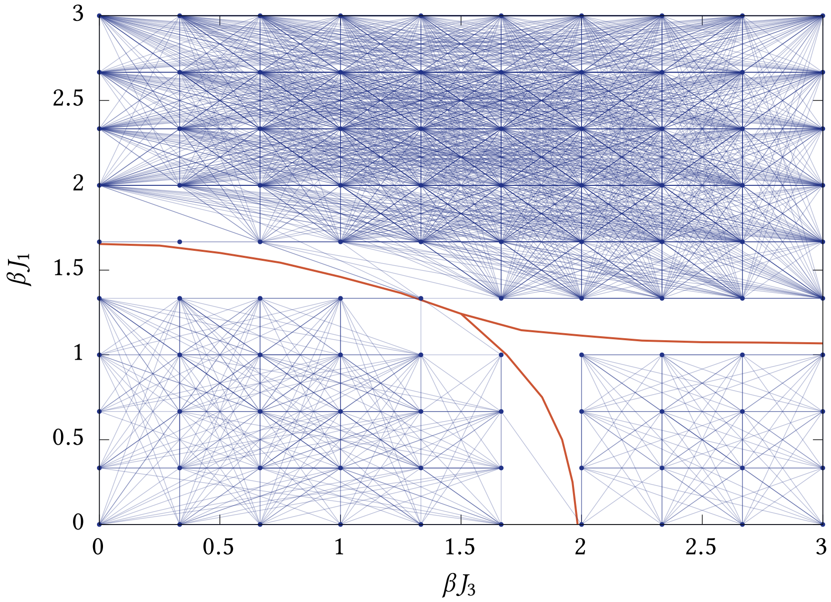

Figure 7.1: Graph representation of the relation between points on a 10×10 grid as inferred from the bias ρ of the corresponding SVM classifiers (regularization $\nu = 0.1$). Any two vertices are connected by an edge if $\rho > 2.5$. (See Sec. 7.3 for details.) The phase diagram which has been found based on the peak susceptibilities (*cf.* Fig. 6.2) is shown in red for reference. The phase boundaries are intersected by only few graph edges and this happens mostly where grid points are very close to the phase transition.

7.2 Spectral graph partitioning

This graph can subsequently be partitioned by a spectral clustering analysis to identify the phases in an objective fashion. To that end, one constructs the graph's Laplacian matrix $L = D - A \in \mathbb{R}^{M \times M}$. Here, A is the adjacency matrix, the $M \times M$ matrix having ones on the off-diagonal elements where vertices are connected by an edge; and D is the degree matrix, the diagonal matrix where the diagonal elements count the number of edges incident on each vertex.

As a consequence, the elements of the rows and columns of L sum to zero. By definition, L is symmetric positive definite. When calculating the eigenvalues and eigenvectors of L, the smallest eigenvalue is therefore exactly zero and $(1)^{\otimes M}$ is a corresponding eigenvector. In case that the graph consists of multiple disconnected components, the Laplacian is block-diagonal (up to a permutation) and the eigenvalue zero is thus degenerate with an algebraic multiplicity corresponding to the number of connected subgraphs. The eigenspace to eigenvalue zero is then spanned by vectors whose entries (corresponding to graph vertices) are constant on one of the connected subgraphs each and zero elsewhere.

In case the graph obtained through the bias criterion perfectly reflects the phase diagram, one could hence identify the phases through the eigenvectors to eigenvalue zero; though, the

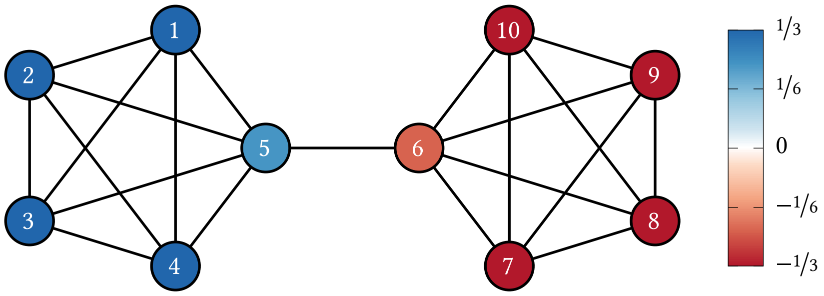

Figure 7.2: A graph with ten vertices which consists of two fully-connected subgraphs (vertices 1–5, 6–10) which are connected by a single edge. The eigenvalue zero of its Laplacian matrix is thus nondegenrate. The second-largest eigenvalue, the algebraic connectivity, equals approximately 0.3. The corresponding Fiedler vector elements are color-coded at the respective vertices.

task at hand is trivial in this case anyway. However, as alluded to in the previous section, the graph will in practice exhibit a few erroneous edges crossing the alledged phase boundaries. It is then beneficial to turn to the second-smallest[1] eigenvalue, dubbed Fiedler value or *algebraic connectivity*, and its corresponding eigenvector, the so-called *Fiedler vector*. The algebraic connectivity is upper-bounded by the traditional edge connectivity [182], *i.e.* the minimum number of edges one has to cut for the graph to become disconnected. For a connected graph, the elements of the Fiedler vector can be used to partition the graph: vertices with a positive entry in the corresponding position of the Fiedler vector are assigned to one subgraph, those with a negative corresponding entry to the other subgraph. This partition approximates the sparsest cut[2] [183]. This is illustrated for a small graph in Fig. 7.2. Partitioning the graph based on the sign of the Fiedler vector elements would cut the edge between vertices 5 and 6 which is indeed the sparsest cut of the graph.

One may thus use the Fiedler vector to partition the graph in Fig. 7.1. The entries of the Fiedler vector are shown in Fig. 7.3 for an even larger graph based on $M = 23 \times 23 = 529$ grid points. At that grid resolution, the graph itself becomes hard to visualize and is therefore omitted. A bipartition based on the sign would correctly split the graph into points originating from the D_{2h} phase on the one hand and the remaining points from the O(3) and $D_{\infty h}$ phases on the other hand. A subsequent bipartition of the latter would in fact run along the phase boundary between the O(3) and $D_{\infty h}$ phases. The algebraic connectivity of the resulting subgraphs may be used as an indicator to decide if any given subgraph admits further partitioning by a sparse cut or if it is “atomic” in the sense that the subgraph already encompasses a single phase. Such a recursive bipartition scheme is known as hierarchical clustering.

---

[1] This assumes that a degenerate eigenvalue zero is counted according to its algebraic multiplicity; *i.e.* the algebraic connectivity of a disconnected graph is zero. Note, however, that the first few nonzero eigenvalues are indeed the algebraic connectivities of the connected subgraphs.

[2] The sparsest cut of a graph of M vertices cuts through E_s edges to bipartition the graph into subgraphs of M_1 and M_2 vertices, $M = M_1 + M_2$, in such a way that minimizes the ratio $E_s / \min\{M_1, M_2\}$. It thus compromises between minimizing the number of edges in need of cutting and the balance of the resulting bipartition. Finding the sparsest cut is an NP-hard problem.

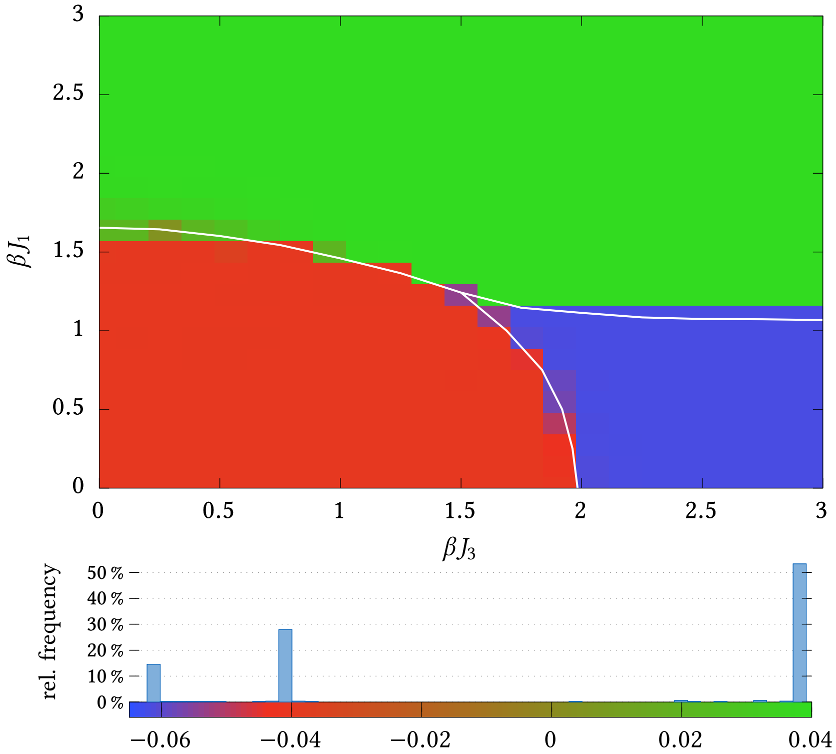

Figure 7.3: Upper panel: elements of the Fiedler vector corresponding to the graph obtained for a 23×23 grid by including edges for which $\rho > 12$. Each element is rendered as a pixel at the location of its corresponding grid point in parameter space and color-coded according to its value. The correct phase diagram (*cf.* Fig. 6.2) is shown in white for reference. Lower panel: a histogram of the elements' values is shown next to the color scale used to encode them in the upper panel.

An elaborate hierarchical clustering is however not necessary in case of Fig. 7.3. Indeed, the Fiedler vector entries are seen to firmly fall into one of three bins in the histogram in the lower panel of Fig. 7.3, *i.e.* they attain almost-constant values within each of the three phases. Only those few points in the vicinity of the phase boundaries exhibit intermediate values. Rendering the Fiedler vector entries as pixels in parameter space at the location, at which the corresponding data were sampled from, thus reproduces the phase diagram, Fig. 6.2, perfectly within the resolution dictated by the grid.

The D_{2h} model considered in this chapter as an example only exhibits symmetry-breaking (first-order) transitions. In the case studies of frustrated magnetism which are investigated in the next two chapters, additionally crossovers will be seen to play a key role in characterizing the phase diagram. In light of this, interpreting the depiction of the Fiedler vector directly as the phase diagram has another advantage aside from avoiding the introduction of another heuristic to guide hierarchical clustering: any phase boundary drawn by a bipartition based on the Fiedler vector entries between phases which are separated by a crossover would by definition be arbitrary. In those situations, the Fiedler vector entries will be seen to gradually change between phases as the crossover takes place; this is not a fault of the method, but rather protrays the physics accurately and can even give an indication as to the nature of a transition or the scale over which an ostensible crossover takes place. This will be demonstrated in Ch. 8.

One should note that the graph analysis outlined above does not rely on monitoring single phase transitions or tuning parameters individually. The topology of the phase diagram is in fact resolved by direct observation of the entire parameter region of interest while simultaneously scrutinizing various potential orders. Thus, it can be particularly useful when phase diagrams are multidimensional and complex in structure.

To conclude this section, it can be remarked that in the above example using the D_{2h} model, only about 10^3 samples per grid point were used. This is sufficient to obtain a reasonably indicative value for ρ. Thus, the total number of samples N_s is comparable to what was typically used in the binary multiclassifications of Ch. 6. The complexity of the SVM optimization, $\mathcal{O}((N_s/M)^{2.2}M^2)$, is close to that of an equivalent binary classification problem $\mathcal{O}(N_s^{2.2})$ (*cf.* Sec. 4.1.1). Once the topology of the phase diagram has been extracted, the same samples may be relabeled according to their phase to obtain clean order parameters without the need for resampling.

7.3 Graph edge weighting

In the construction of the graph, Sec. 7.1, each tentative edge is included in the graph based on the bias of the corresponding classifier. The simplest scheme to do so compares the deviation of the (unoriented) bias $|\rho|$ from unity and imposes a hard threshold ρ_c: for biases with $||\rho| - 1| > \rho_c$ the corresponding edge is included in the graph, while biases whose distance from unity is smaller than ρ_c are considered to capture a phase transition or crossover and therefore no edge is included. Larger values of ρ_c will result in graphs with less false-positive edges at the cost of more false-negative (missing) edges. Since all pairings of points in parameter space are considered, the graph contains a lot of redundant information, so false-negatives are more easily compensated for.

This leads to the inevitable question how one is to determine the threshold ρ_c. A useful approach which was adopted in Figs. 7.1 and 7.3 uses the degeneracy of eigenvalue zero of the resulting Laplacian to guide the choice of the threshold bias ρ_c. One calculates the spectrum of the Laplacian for an assortment of different values for ρ_c and selects the largest value for which the eigenvalue zero remains nondegenerate. Thus, one tweaks ρ_c such that the resulting graph is *just* connected with the understanding that the tentative phase boundary will intersect only few edges. Generically, a higher resolution of the grid will result in more redundant information and the graph will remain connected up to larger values of ρ_c. Even larger values of ρ_c would produce disconnected graphs with increasing numbers of connected subgraphs. As alluded to in Sec. 7.2, these could be interpreted as phases directly but the “desired” number of phases may not be known *a priori*, so it is preferrable to analyze the Fiedler vector of a (barely) connected graph.

While this approach works well enough when the phase diagram is composed of a few symmetry-breaking phases, it does discard information on the strength of the connection and different transitions or crossovers may become apparent at different values of ρ_c. Rather than using a fixed threshold to construct an unweighted graph, one may instead opt to use the bias value of each edge to determine its weight, resulting in a weighted graph. The spectral analysis described in the previous section retains its applicability for weighted graphs[3].

Using the biases (or their deviation from unity) directly as weights for the edges does not yield useful results, as it overrepresents the importance of large biases. Instead, the weight of each edge is given by $w(\rho)$, for a suitably chosen weighting function $w : \mathbb{R} \to [0, 1]$. Thus, the hard threshold employed previously amounts to choosing the weighting function $w(\rho) = \Theta(||\rho| - 1| - \rho_c)$ instead, resulting in weights zero and one exclusively.

In the case studies in Chs. 8 and 9, a Lorentzian weighting function is employed instead,

$$w(\rho) = 1 - \frac{\rho_c^2}{(|\rho| - 1)^2 + \rho_c^2}, \tag{7.1}$$

where ρ_c again gives a characteristic scale up to which edges do not contribute significantly, replacing the hard threshold by a soft one. Choosing a continuous weighting function retains more of the information provided by the biases and also simplifies the spectral analysis by ensuring that the graph never exhibits any truly disconnected components as these would lead to a degenerate eigenvalue zero of the Laplacian matrix. This is of particular practical relevance in identifying the crossovers (where vertices have few and weak connections to their neighbors) correctly as such; using a hard threshold, these vertices are at risk of being completely disconnected from the surrounding phases.

This also allows for a larger latitude regarding the choice of ρ_c. In Ch. 8, it will be shown empirically that again a more restrictive criterion, corresponding to a larger value of ρ_c, generally leads to a better result, *i.e.* a less noisy Fiedler vector. However, consistent results are obtained for values of ρ_c over several orders of magnitude (*cf.* Fig. 8.4 for an example). Hence, the choice of ρ_c is not of practical concern. In a similar vein, the specific choice of the weighting function does not matter in practice beyond the fact that it is continuous. Both Eq. (7.1) with its algebraic falloff and a similarly scaled Gaussian with an exponential falloff yield consistent results.

In the D_{2h} example of the foregoing sections, all transitions are quadrupolar in nature. Thus, the phase diagram could entirely be obtained from the SVM biases at rank $n = 2$. In case different transitions occur at different ranks (as is the case for the D_{3h} model considered in Sec. 6.2.2), one has two possibilities to reconcile this situation: (i) by building a "phase diagram" with respect to each rank and then combining these to arrive at the complete phase diagram (This approach is taken in Sec. 8.1.), or (ii) by combining the graphs at different ranks in a way that (the weight of) each edge in the final graph is obtained from (the weights of) the corresponding edge in each of the graphs; the spectral analysis is then performed only once on the combined graph. In case of an unweighted graph, the natural operation to combine edges would be a logical OR; in the case of weighted graphs, the edge weights could possibly be multiplied. The same caveat applies when orders on different spin clusters are considered.

---

[3] To construct the Laplacian $L = D - A$ of a weighted graph, the degree of each vertex, *i.e.* the diagonal elements of D, is replaced by the sum over the weights of all edges incident on that vertex. Likewise, the adjacency matrix A has the edges' weights on the respective off-diagonal elements. Hence, the rows and columns of L still each sum to zero.

Part III

Case studies

8

Pyrochlore XXZ antiferromagnet

Having introduced the basic techniques leading up to TK-SVM in part I of this thesis and having seen how they are used to find order parameter tensors and phase diagrams in the context of the gauge model in part II, this final part is devoted to their application to frustrated spin systems.

In this first chapter, the focus will be on the classical limit of the XXZ model on a pyrochlore lattice, which is accessible to large-scale classical Monte Carlo simulation, and known to support a plethora of different spin liquids, one of which also possesses hidden spin-nematic order [87, 88]. It is therefore suitable for the purpose of demonstrating the capabilities of TK-SVM where special emphasis will be placed on the handling of crossovers between—and characterization of—classical spin liquid (CSL) phases.

An unbiased approach will be taken which does not assume prior knowledge of the phase diagram. In Sec. 8.1, the topology of the phase diagram will be inferred from scratch. The resulting phases will given anonymous labels thereafter, pending a detailed characterization in Sec. 8.2. Aside from symmetry-breaking phases which are captured by TK-SVM by learning their respective order parameter tensor (Sec. 8.2.2), the emergent local constraints will be seen to play a crucial role to distinguish between different kinds of spin liquids (Sec. 8.2.3). Finally, the thermodynamics of the learned quantities are further scrutinzied in Sec. 8.3. The discussion is intended to provide general guidance on the use of TK-SVM and is transferable to other frustrated spin models. Indeed, the analysis of the Heisenberg antiferromagnet on the kagome lattice in Ch. 9 will follow much along the same lines and hearken back to this chapter many times.

The spin configurations used as input to the SVM are obtained from classical Monte Carlo simulations of the Hamiltonian H_{XXZ} [Eq. (2.13)], courtesy of Ludovic D. C. Jaubert. These simulations were carried out for a system of $N = 16L^3$ spins, where L^3 is the number of cubic unit cells. The results presented in this chapter used a system of size $L = 8$. A heat-bath algorithm for single-spin-flip updates (see Sec. 3.2.2) was combined with overrelaxation (see Sec. 3.3.2) and parallel tempering (see Sec. 3.4). Preliminary thermalization is carried out in two steps: first a slow annealing from high temperature to the temperature of measurement T during t_e Monte Carlo steps (MCs) followed by t_e MCs at temperature T. After thermalization, measurements are done every 10 MCs during $t_m = 10t_e$ MCs. Typical Monte Carlo times range from $t_m = 10^6$ to 3×10^7 Monte Carlo sweeps.

8.1 Topology of the phase diagram

In this section, the tools developed in Ch. 7 will be applied to the XXZ model on the pyrochlore lattice. Spin configuration samples were taken on a grid of parameter points $(J_\pm, T)$, covering a region of interest in parameter space uniformly. To be concrete, 29 equidistant values of $J_\pm$ between -1 and 0.4, as well as 17 logarithmically-spaced temperatures between 0.001 and 10 span a rectilinear grid. At each of the resulting $M = 29 \times 17 = 493$ parameter points, a mere 500 statistically independent spin configurations have been sampled. These constitute the training data. Assigning distinct labels to the samples from each of these parameter points, results in a massive multiclassification problem. Solving this using the tensorial kernel for a given rank and spin cluster yields 121 278 decision functions, each trying to distinguish between two parameter points. Here, spin clusters consisting of the four spins on the tetrahedra that form the pyrochlore lattice (*cf.* Fig. 1.1) will be used. Ranks 1–4 will be investigated.

8.1.1 Graph analysis

To begin with, the data are subjected to an analysis using the rank-1 tensorial kernel, to scrutinize potential dipolar orders. The graph resulting from the corresponding biases is shown in Fig. 8.1(a). It is apparent that the graph decomposes into two subgraph components. Both subgraphs appear to be uniformly intraconnected and do not exhibit any further structure. This means that, in terms of dipolar orders which are defined on tetrahedral spin clusters, the phase diagram appears split in two. However, as one cannot foresee or exclude the presence of more complicated orders, it is prudent to analyze both subgraphs further with higher-rank kernels. In principle, one should also explore the possibility of orders which are defined on larger clusters which is omitted here.

In fact, the smaller graph does not exhibit any further structure at ranks 2, 3, or 4 either and is therefore ignored for the remainder of this section.

Hence, the larger subgraph will be analyzed with the rank-2 tensorial kernel next, which detects quadrupolar orders as well as local constraints that can be expressed by terms which are quadratic in the spin components. The resulting graph is displayed in Fig. 8.1(b) and exhibits several regions which are strongly intraconnected, corresponding to regimes of congruent nature. However these regions appear less well separated compared to Fig. 7.1, rendering the graph less accessible to direct visual interpretation. On the one hand, one observes instances of regions which—while being less densely interconnected than—still exhibit a nonnegligible amount of edges connecting them, more so than what is observed for the symmetry-breaking transitions considered in Ch. 7. On the other hand, other areas of the graph feature almost no connections to their surroundings. At ranks 3 and 4, no further subdivisions become apparent, indicating that all the relevant phases can be described in terms of quadrupolar order parameters or quadratic constraints.

In order to obtain a more readable phase diagram from the graph in Fig. 8.1(b), one proceeds to apply the spectral clustering analysis which was introduced in Sec. 7.2. The resulting Fiedler vector can again be interpreted as the phase diagram by color-coding each pixel in parameter space according to the value of its corresponding Fiedler vector element, as depicted in Fig. 8.2. One observes that its entries attain distinct values within strongly intraconnected regions which are relatively constant throughout. In order to demonstrate the usage of TK-SVM in the absence of prior information, these regions are labeled anonymously by the roman numerals given in the figure for now. Their nature will become clear once they are characterized in the next section.

However, already at this point can one can note the remarkable agreement of this phase diagram with the phase transitions and crossovers found in Ref. 87 which are superimposed on Fig. 8.2 for reference. Also note that the boundary between regions III and IV is very sharp, whereas the distinction between some other regions is more gradual. It will be confirmed in Sec. 8.3, where the corresponding order parameters are examined, that the former represents a phase transition, while the latter mark the regions influenced by crossovers. Therefore, in

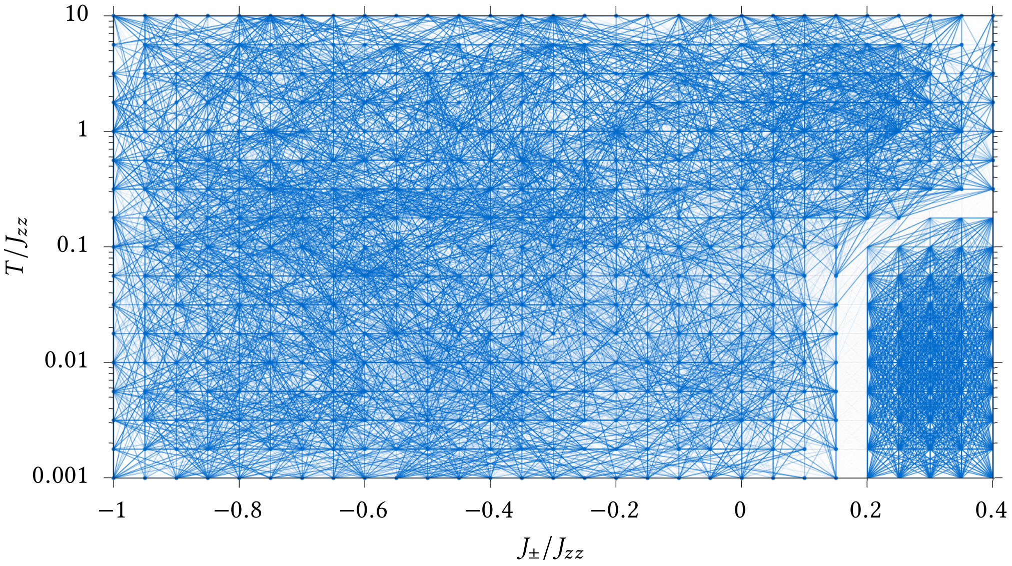

(a) Rank 1, $\rho_c = 2$

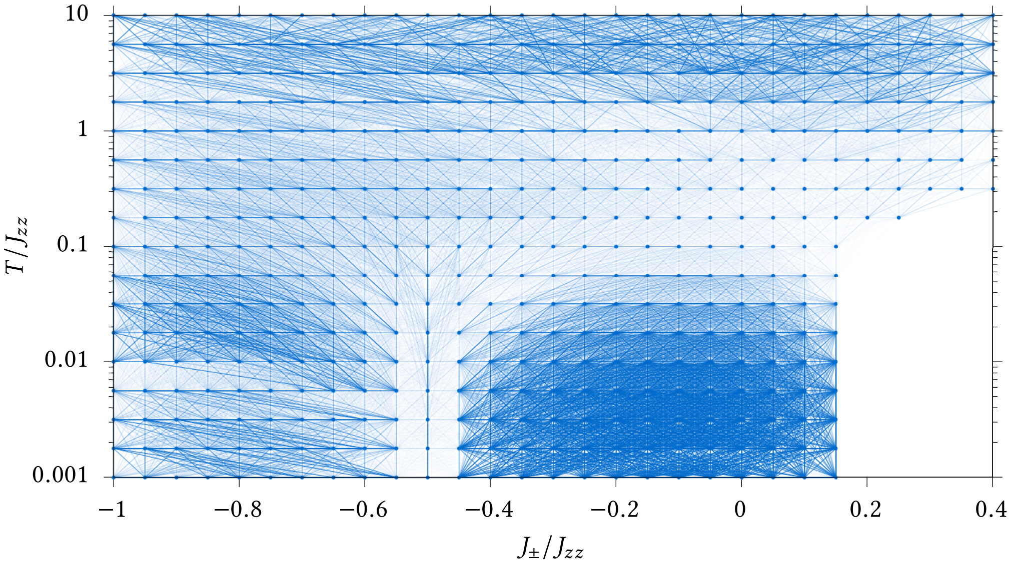

(b) Rank 2, $\rho_c = 25$, region I excluded

Figure 8.1: The graphs constructed from the biases between each pair of vertices using the tensorial kernel at rank 1 (a) and 2 (b). The opacity of each edge indicates its weight which is in both cases determined using a Lorentzian, Eq. (7.1), with characteristic scale ρ_c. Here, only edges between (at most) sixth-nearest neighboring grid points are considered, *i.e.* long-range edges have been excluded, merely to reduce the visual density of the figure; the subsequent analysis includes long-range edges as well.

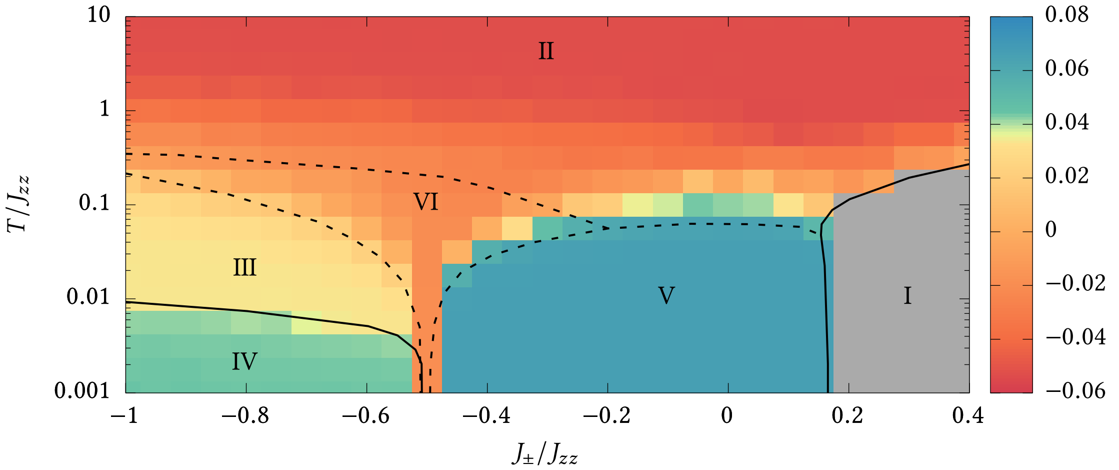

Figure 8.2: The phase diagram is obtained by color-coding the location of each vertices in parameter space according to the corresponding Fiedler vector entry. The underlying weighted graph has been constructed from the rank-2 TK-SVM biases using a Lorentzian weighting function with characteristic bias of $\rho_c = 50$ (*cf.* Sec. 8.1.2). The gray area labeled I dropped out from the rank-1 analysis and is excluded from the graph here. For comparison, the phase boundaries found in Ref. 87 are included. Solid (dashed) lines indicate phase transitions (crossovers).

addition to learning the topology of the phase diagram, the graph analysis can also distinguish crossovers from phase transitions.

8.1.2 Choice of the weighting function

The construction of the graphs in Fig. 8.1 employed the weighted scheme proposed in Sec. 7.3. It was already hinted therein that the choice of the weighting function—both in terms of its functional dependence and its characteristic scale, ρ_c—does not significantly impact the resulting Fiedler vector. Before proceeding with the analysis, this section will demonstrate this point explicitly for the case of the rank-2 subgraph, Fig. 8.1(b), and its resulting Fiedler vector, Fig. 8.2.

The biases of all the potential edges span many orders of magnitude as can be seen from their histogram in Fig. 8.3(a). Besides the pronounced peak at $|\rho| = 1$ corresponding to the edges spanning across phases, the remaining biases are following a fat-tailed distribution which becomes apparent from the log-log version of the same histogram in the inset Fig. 8.3(b). Panel 8.3(c) meanwhile shows the resulting distribution after mapping the biases through the Lorentzian weighting function, Eq. (7.1) with $\rho_c = 50$, which was used to obtain the Fiedler vector in Fig. 8.2.

Fig. 8.4 shows the Fiedler vector along with the distribution of the biases and their corresponding weights for different values of ρ_c spanning six orders of magnitude. Even in the most inclusive approach in panel (a), the topology of the phase diagram can be recognized, even

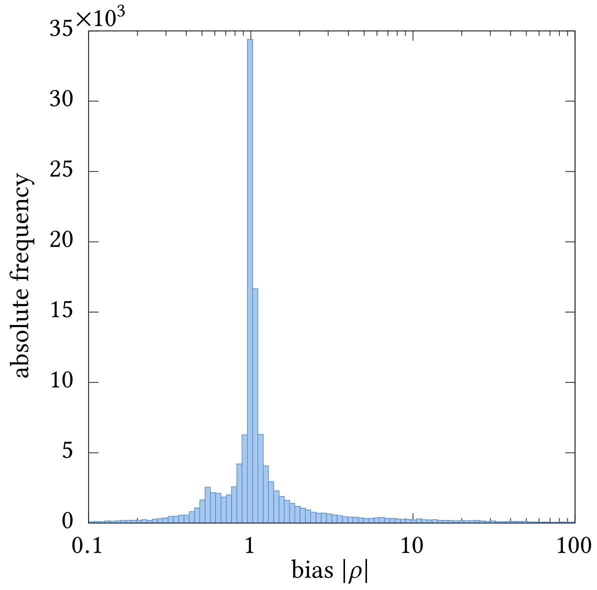

(a) Frequency plotted on a linear scale

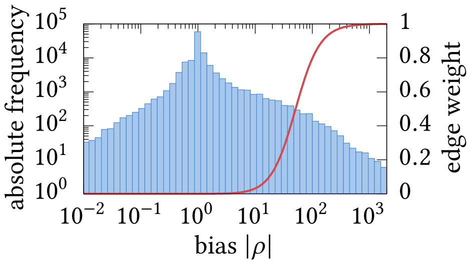

(b) Frequency plotted on a logarithmic scale

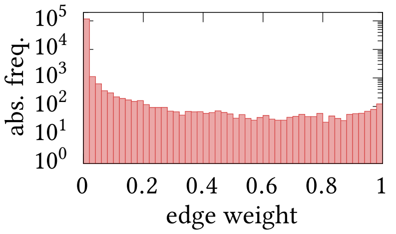

(c) Histogram of the resulting edge weight distribution

Figure 8.3: Histogram of the (unoriented) biases obtained from TK-SVM among the 493 points in parameter space. The bin width is proportional to the bias values. The red curve in panel (b) is the Lorentzian weighting function, Eq. (7.1) with characteristic scale $\rho_c = 50$, used to map biases to graph edge weights.

though the result is generally more noisy and the phase boundary of the spin nematic phase appears blurred. As successively more edges are discarded, these shortcomings are gradually rectified. The resulting Fiedler vectors for $\rho_c = 10^2$ [panel (d)], 10^3, 10^4, and 10^5 [panel (e)] are virtually indistinguishable, even though in the latter case, only the largest of biases contribute to the graph appreciably. Beyond $\rho_c = 10^6$, the analysis is limited by the numerical accuracy of the weights. Considering that this last choice exceeds the maximum bias that was found, it is unnatural.

One may conclude that (at least in the present case) the choice of the weighting function is not of practical concern. This reaffirmes the previous statement that it is generally beneficial to be more exclusive when deciding which biases to include in the graph. Using a continuous weighting function is, however, crucial to ensure that the graph stays (weakly) connected.

8.1.3 Reduced multiclassification problem

The partition of the parameter space obtained by means of the spectral graph analysis is also reflected by the histogram of the Fiedler vector entries which is presented in Fig. 8.5. The regions labeled II, III, IV, and V manifest themselves as distinct peaks in the histogram. In particular, regions III and IV lie closely together, but can be distinguished quite clearly which justifies our choice of a color scale with a large gradient in the vicinity. On the other hand, the

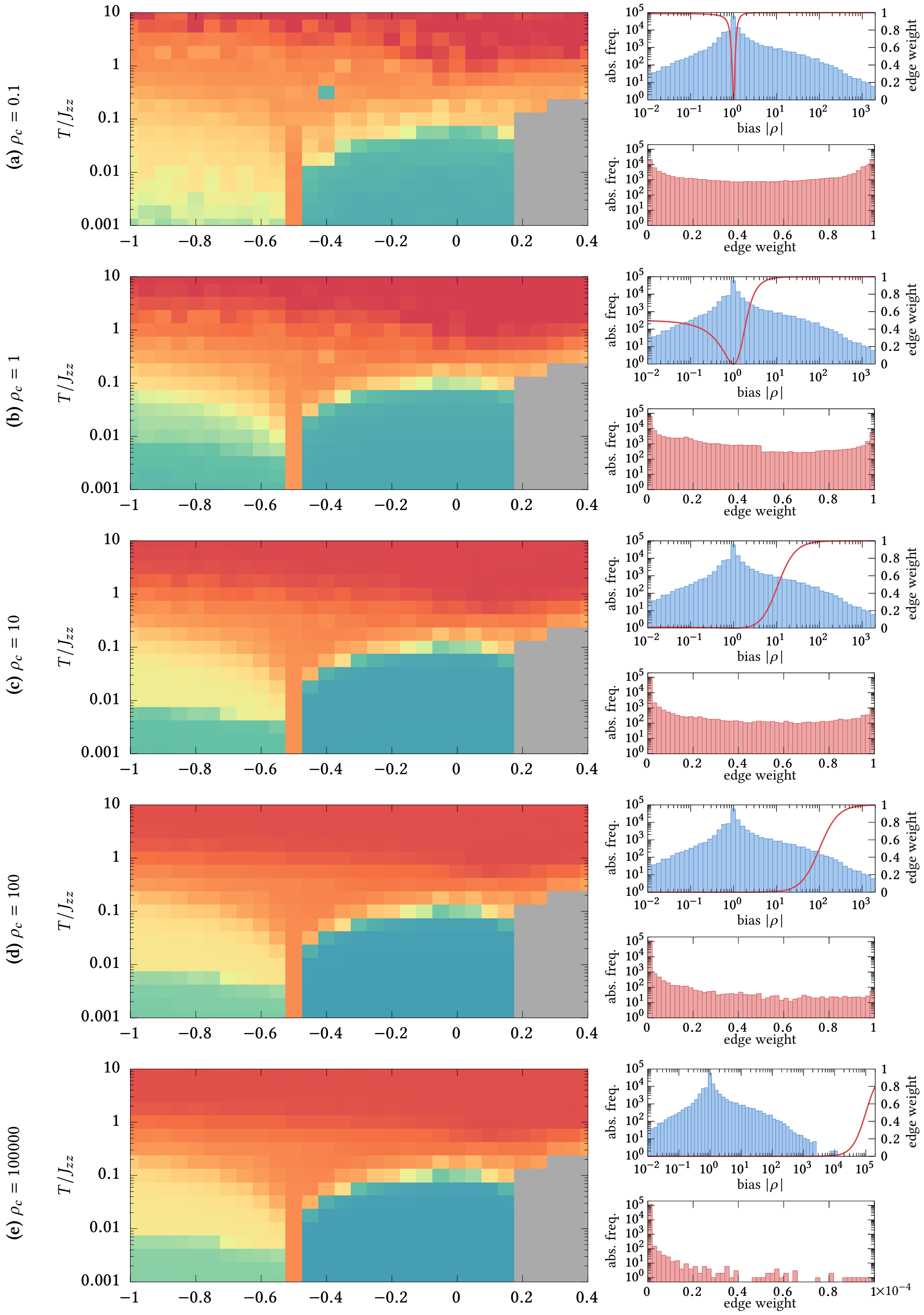

Figure 8.4: The Fiedler vector, representing the extracted phase diagram, is shown along with histograms of the biases and corresponding edge weights for a variety of different choices of the characteristic scale ρ_c of the weighting function. The weighting functions are superimposed on the bias histograms in each case. The color scale used for the Fiedler vector is identical to that used in Fig. 8.2.

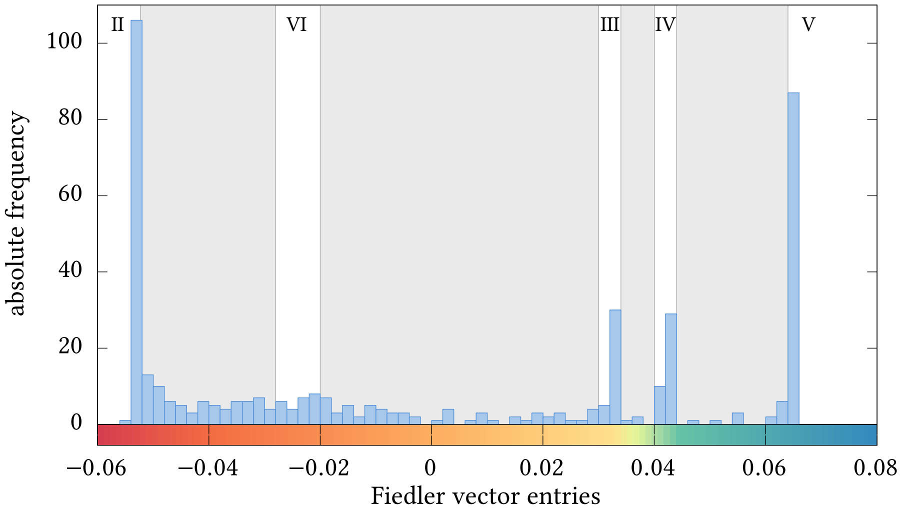

Figure 8.5: Histogram of the entries of the Fiedler vector shown in Fig. 8.2, alongside the color scale that was used therein. The four regions II, III, IV, and V can be readily identified as distinct peaks in the histogram. Region VI is less well-defined, owing to crossovers into other regions. The shaded areas in the background indicate which intervals of Fiedler vector entries were used to guide the setup of the reduced multiclassification problem.

region labeled VI is less well-defined. This may be attributed to the fact that it corresponds to an intermediate regime, both in coupling $J_\pm$ and temperature T, connected via crossovers to the surrounding regions with drastically different entries in the Fiedler vector.

In order to proceed with the detailed analysis of the physics governing each of the regions, a reduced multiclassification problem is set up which relabels the training data according to the region from which they originate. To that end, the corresponding intervals of the entries of the Fiedler vector have been identified and are indicate in Fig. 8.5. Their choice was guided by the by the location of the peaks in the histogram in the case of regions II–V. Since region VI does not exhibit a pronounced peak, its corresponding interval has been centered on the value attained in the Heisenberg limit ($J_\pm = -J_{zz}/2, T \to 0$).

The entries which do not fall into either of these intervals can be attributed to crossovers in between. The corresponding training data cannot be labeled unambiguously and are therefore not included in the merged dataset. The final partitioning of the phase diagram is presented in Fig. 8.6[1]. After relabeling, the SVM is trained with 24 000 (I), 49 500 (II), 16 500 (III), 18 000 (IV), 43 500 (V), and 13 500 (VI) spin configurations, respectively, while 81 500 samples have been excluded.

---

[1] Note that the partion depicted in Fig. 8.6 deviates slightly from the strict interval-based partitioning by manually excluding a handful of points on the boundary of region V (which are intermediate crossover points, but might otherwise have been labeled III or IV, purely based on their Fiedler vector entry).

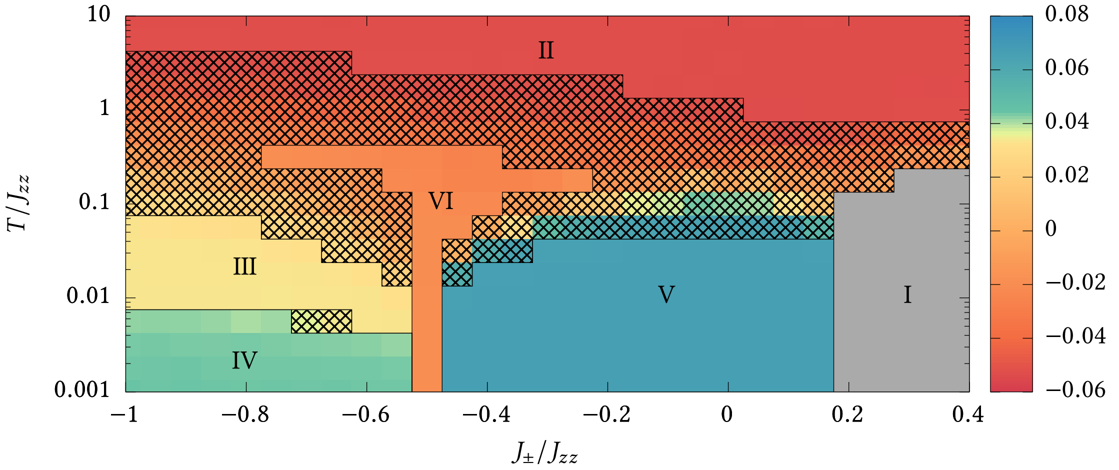

Figure 8.6: The partitioning of the phase diagram is superimposed on the Fiedler vector (*cf.* Fig. 8.2). Regions which can be unambiguously assigned to one of the phases, labeled by roman numerals I–VI, are separated by solid lines. For the hatched regions, this is not possible unambiguously and the corresponding data are excluded from the ensuing analysis.

In addition, the training data are supplemented with 50 000 fictitious configurations, consisting of random spins which are independently and isotropically sampled from the unit sphere. These fictitious configurations mimic states at infinite temperature and serve as a control group which turns out to be useful for interpreting both the coefficient matrices and the behavior of the bias parameters. They are labeled "T_∞" in the following discussion.

This sets up the reduced multiclassification problem. For each kernel of rank n, the solution leads to $q_n(q_n + 1)/2$ binary classifiers, where q_n denotes the number of phases identified at any given rank (here, $q_1 = 2$, $q_2 = 5$). The first q_n of the classifiers involve the control group and encode the characteristics distinguishing each phase from featureless T_∞-states. As will be seen in this section, the interpretation of these q_n classifiers will give sufficient information for understanding the phase diagram. The remaining $q_n(q_n - 1)/2$ classifiers emphasize the distinction between any two phases in the real data, hence providing a straightforward way to identify quantities that are responsible for phase transitions or crossovers.

8.2 Characterizing the phases

After the topology of the phase diagram has been established and a corresponding reduced multiclassification problem has been obtained, the next step is to attain an understanding of the nature of the phases and their phase transitions and crossovers.

In this section, this will be done in several steps. First, the biases of the reduced classification will be used to establish a hierarchical relation between phases (Sec. 8.2.1). Following that, one can go beyond the mere interpretation of the bias parameters and analyze the coefficient

	ρ	
	I	II–VI
T_∞	1.0006	1.4874
I		−1.0004

(a) Phase I is compared with the remainder of the parameter space and the control group using the rank-1 kernel.

	ρ				
	II	III	IV	V	VI
T_∞	4.586	1.012	1.009	1.004	1.025
II		1.026	1.016	1.012	1.097
III			1.336	0.534	−1.220
IV				0.383	−1.134
V					−1.028

(b) Phases II–VI are compared amongst each other and with the control group using the rank-2 kernel.

Table 8.1: Biases $\rho(A\,|\,B)$ of decision functions at different ranks between the data which are labeled according to the phase diagram partitioning obtained in Sec. 8.1. In both cases, a fictitious dataset of independently distributed isotropic spin configurations, referred to as "T_∞", is included as a control group. In the convention adopted in Ch. 5, A is the row label, while B is the column label. These biases are to be interpreted according to the rules laid out in Sec. 5.3 and summarized by Eq. (5.17).

matrices of the classifiers distinguishing between select phases. At first, this will follow the recipe of Ch. 6 to extract the order parameters of the symmetry-breaking phases (Sec. 8.2.2). At rank 2, this analysis can further be made systematic by decomposing the coefficient matrices into several quadrupolar ordering components. Even in correlated paramagnetic phases (*i.e.* classical spin liquids), these ordering components can be used to infer the local constraint (Sec. 8.2.3).

8.2.1 The hierarchy of disorder

In Ch. 5, it has been pointed out that the bias parameter ρ is oriented. During the construction of the phase diagram Fig. 8.2, only the magnitude of ρ was used. Here, the orientation of the biases in the reduced multiclassification will also be taken into account, and the mutual relations between the phases are analyzed.

Note that the set of all biases correspond to the 2-combination of the phases which does not rely on the topology of the phase diagram or the microscopics of the model. Therefore, one can infer a global hierarchy between the phases from them, going beyond the phase transitions and crossovers reflected in the phase diagram. This introduces the notion of a "hierarchy of disorder" which addresses order-to-disorder transitions and crossovers on an equal footing. A trivial paramagnet has the most disorder; symmetry-breaking phases, where spins align along common directions, are in the opposite limit; phases of constrained dynamics that do not break any symmetries reside in the middle.

The bias values resulting from the reduced multiclassification problems are tabulated in Tab. 8.1. According to the rules set out in Eq. (5.17), one can infer that phase I is the most ordered as the corresponding bias $\rho(\mathrm{I}\,|\,\mathrm{II}\text{–}\mathrm{VI})$ is approximately equal to -1. In contrast, phase II is entirely disordered and can be identified as the paramagnetic phase. Phase VI is the second most disordered phase, as only $\rho((T_\infty, \mathrm{II})\,|\,\mathrm{VI}) \approx +1$. Also note that both phases III and IV do not directly compare to phase V, as indicated by their biases in $(-1, 1)$.

With a little further analysis, the Table 8.1 can be summarized by the following hierarchy,

$$\begin{tikzcd} & & \mathrm{III} \arrow[rr] & & \mathrm{IV} \arrow[dr] & \\ (T_\infty, \mathrm{II}) \arrow[r] & \mathrm{VI} \arrow[ur] \arrow[drr] & & & & \mathrm{I}. \\ & & & \mathrm{V} \arrow[urr] & & \end{tikzcd} \tag{8.1}$$

These relations will confirmed by the analytical characterizations of the phases in forthcoming subsections. It will seen that phase VI is a classical O(3) spin liquid characterized by an isotropic local constraint. Phases III and V feature constraints in the easy-plane and easy-axis, respectively, and therefore experience less disorder. In addition, phases I and IV, which are not adjacent in the phase diagram, are two spontaneously symmetry-breaking phases, while the former breaks more symmetry and, hence, comes last in the hierarchy.

8.2.2 Identification of broken symmetries

One may now extract the analytical characterization of the phases from the coefficient matrices, $C_{\mu\nu}$ in Eq. (4.7). The focus of this subsection will be on the local orders in phases I and IV, and the discussion of the emergent constraints is deferred to the next subsection.

Rank-1 order

Let us first focus on results learned with the rank-1 decision function. At this rank, the graph in Fig. 8.1(a) contains only two disconnected components. Moreover, the $C_{\mu\nu}$ matrix learned to distinguish the two subgraphs appears identical to $C_{\mu\nu}(\mathrm{I}\,|\,T_\infty)$, suggesting one dipolar order is detected in phase I.

The corresponding 12×12 matrix $C_{\mu\nu}$ is shown in Fig. 8.7. Following the definition in Eq. (5.7), it is expanded by rank-1 basis functions S^α_a, where $\alpha = 1, 2, 3, 4$ and $a = x, y, z$. The nonvanishing entries identify which of these contribute to the underlying order parameter.

Furthermore, Fig. 8.7 shows a periodic structure of 3×3 blocks. This indicates that $C_{\mu\nu}(\mathrm{I}\,|\,T_\infty)$ learned with the four-spin tetrahedral cluster is reducible, because the order parameter can be inferred from a single block. According to their spin indices, one can assign a coordinate $[\alpha, \alpha']$ to each block, and express them by submatrices $\mathcal{B}^{\alpha\alpha'}(\mathrm{I}\,|\,T_\infty)$,

$$\mathcal{B}^{\alpha\alpha'}_{aa'}(\mathrm{I}\,|\,T_\infty) = \begin{array}{c|ccc|} \cline{2-4} z & & & \\ y & & \blacksquare & \\ x & \blacksquare & & \\ \cline{2-4} & x & y & z \end{array} = \delta_{aa'}(1 - \delta_{a,z}), \tag{8.2}$$

where only $a, a' = x, y$ components are relevant.

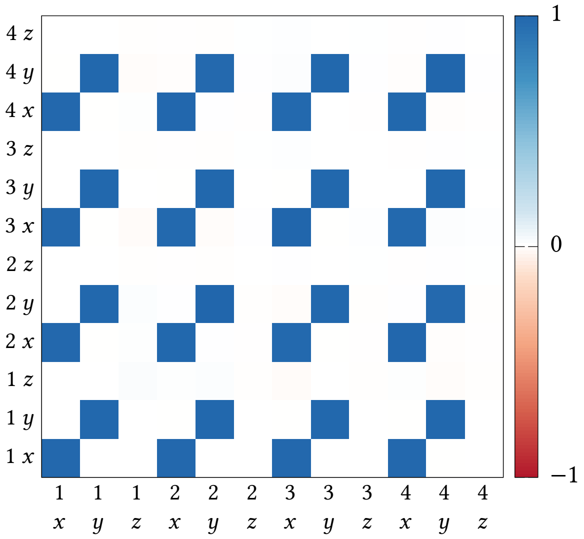

Figure 8.7: The coefficient matrix $C_{\mu\nu}(\mathrm{I}\,|\,T_\infty)$, characterizing phase I against the control group, obtained from TK-SVM at rank 1. The axes are labeled according to sublattice index, $\alpha = 1, 2, 3, 4$, and spatial component, $a = x, y, z$, in lexicographical order. The repeating 3×3 motif, *cf.* Eq. (8.2), reveals phase I as an easy-plane antiferromagnet.

Substituting $C_{\mu\nu}(\mathrm{I}\,|\,T_\infty) = \{\mathcal{B}^{\alpha\alpha'}\}$ back into the decision function, Eq. (4.7), one obtains

$$d(\mathbf{x}) \sim \frac{1}{N^2} \sum_i \left\langle (S_{i,x})^2 + (S_{i,y})^2 \right\rangle_{\mathrm{cl}} = \left\langle \|\mathbf{M}_\perp\|^2 \right\rangle_{\mathrm{cl}} . \tag{8.3}$$

One realizes that the interpretation of coefficient matrix here leads to nothing but easy-plane magnetization $\mathbf{M}_\perp = \frac{1}{N} \sum_i (S_x, S_y, 0)^T$. In addition, since the spins are defined by sublattice coordinates, it can be concluded that phase I is an easy-plane antiferromagnetic (AFM) phase.

Rank-2 orders

The coefficient matrices learned with higher-rank kernels are interpreted in the same spirit as in the rank-1 case. Namely, one identifies important basis functions in $\phi(\mathbf{x})$ and their weights entering $C_{\mu\nu}$. Again, $C_{\mu\nu}$ can be divided into smaller blocks, and it is often sufficient to examine a subset of those blocks and their global structure. At rank 2, $C_{\mu\nu}$ is expanded by $S^\alpha_a S^\beta_b$ and $S^{\alpha'}_{a'} S^{\beta'}_{b'}$, and the small blocks are again identified by the spin indices $[\alpha\beta, \alpha'\beta']$.

One observes that the coefficient matrix $C_{\mu\nu}(\mathrm{II}\,|\,T_\infty)$, which is supposed to learn a quantity to distinguish phase II from the fictitious T_∞ data, exhibits only noise. This reflects the result that phase II is a trivial paramagnet (PM) which is consistent with the result obtained through the bias criterion. In contrast, the coefficient matrices $C_{\mu\nu}(\mathrm{III}\,|\,T_\infty)$ and $C_{\mu\nu}(\mathrm{IV}\,|\,T_\infty)$ show a regular and robust pattern, indicating that nontrivial features have been detected.

The pattern of $C_{\mu\nu}(\mathrm{IV}\,|\,T_\infty)$ is given in Fig. 8.8(a). Indeed, one notices a structure of blocks of 9×9 elements. Furthermore, these blocks can be classified into three types: 16 “on-site” blocks

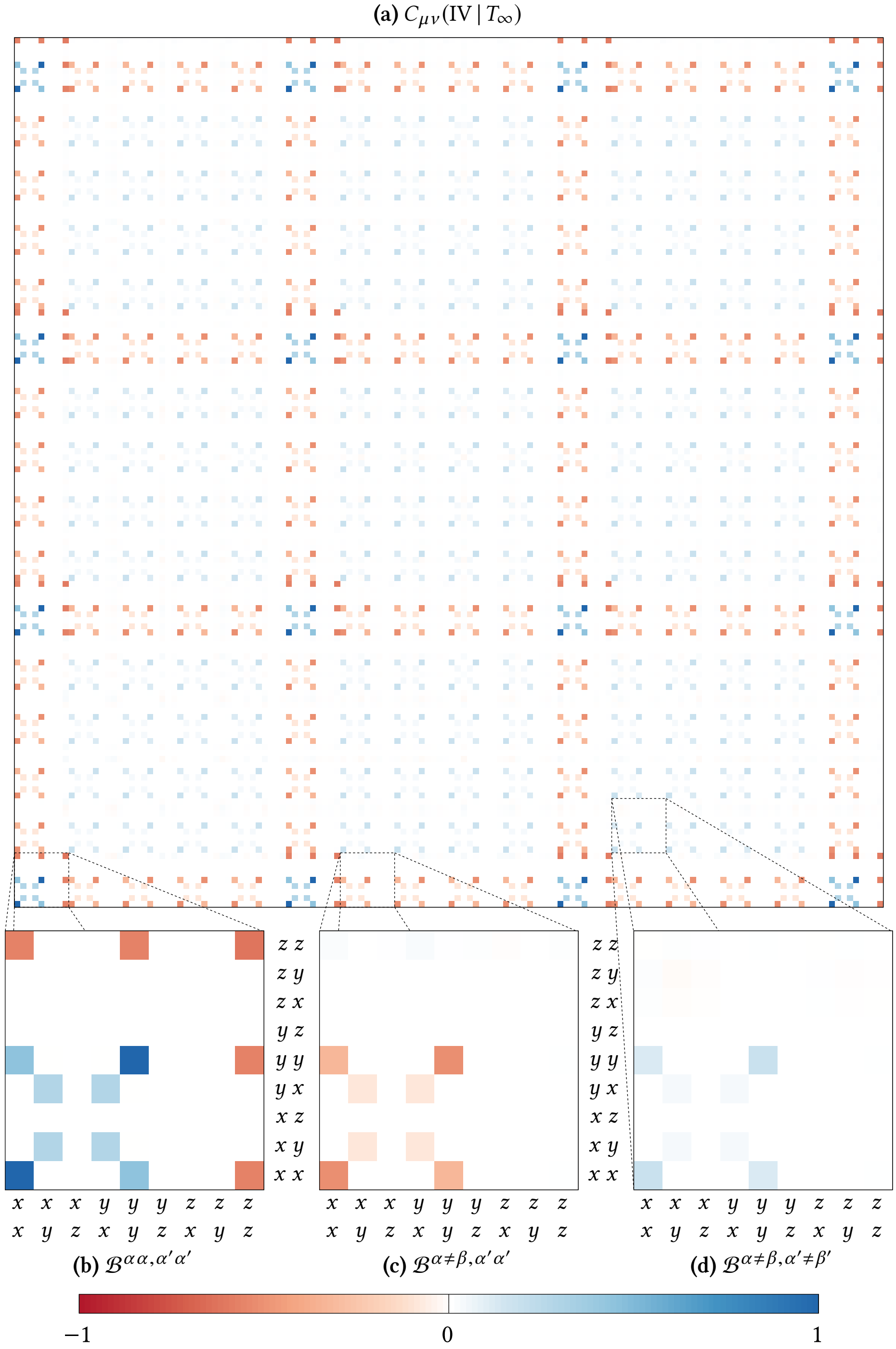

Figure 8.8: (a) The 144 × 144 coefficient matrix $C_{\mu\nu}(\mathrm{IV}\,|\,T_\infty)$ obtained from TK-SVM at rank 2. The axes iterate over sublattice indices α, β and spatial components a, b such that tuples (α, β, a, b) are lexicographically sorted. Panels (b) through (d) zoom in to various types of 9×9 blocks of fixed sublattice indices: (b) “on-site”, (c) “cross”, and (d) “bond”. The blocks exhibit similar patterns; (c) and (d) differ only by an overall factor and relate to the C_{2h} order parameter; the on-site block (b) additionally contains an equivalent contribution due to the spin normalization. Phase IV is thus an unconventional biaxial spin nematic.

($[\alpha\alpha, \alpha'\alpha']$), 96 site-bond "cross" blocks ($[\alpha\alpha, \alpha' \neq \beta']$ or $[\alpha \neq \beta, \alpha'\alpha']$), and 144 "bond" blocks ($[\alpha \neq \beta, \alpha' \neq \beta']$), respectively. Instances of each type are magnified in panels (b) through (d) of Fig. 8.8.

The structure of these blocks is encompassed by the following submatrix,

$$\mathcal{B}^{\alpha\beta,\alpha'\beta'} = \begin{bmatrix} A & 0 & 0 & 0 & A & 0 & 0 & 0 & B \\ 0 & 0 & 0 & 0 & 0 & F & 0 & F & 0 \\ 0 & 0 & G & 0 & 0 & 0 & G & 0 & 0 \\ 0 & 0 & 0 & 0 & 0 & F & 0 & F & 0 \\ D & 0 & 0 & 0 & C & 0 & 0 & 0 & A \\ 0 & E & 0 & E & 0 & 0 & 0 & 0 & 0 \\ 0 & 0 & G & 0 & 0 & 0 & G & 0 & 0 \\ 0 & E & 0 & E & 0 & 0 & 0 & 0 & 0 \\ C & 0 & 0 & 0 & D & 0 & 0 & 0 & A \end{bmatrix} \tag{8.4}$$

where vanishing entries are omitted, and the values of variables A through G can be read off from the patterns. Moreover, it turns out that it is sufficient to infer local orders in the phase VI (and also the phase III) by examining a single block, while the relative strength of different blocks encode an emergent constraint which will be discussed in Sec. 8.2.3.

From the general structure of the blocks $\mathcal{B}$ in the coefficient matrix, Eq. (8.4), one identifies seven constituent patterns:

$$\mathcal{A}[Q_{x^2+y^2+z^2}] = \begin{bmatrix} 1 & 0 & 0 & 0 & 1 & 0 & 0 & 0 & 1 \\ 0 & 0 & 0 & 0 & 0 & 0 & 0 & 0 & 0 \\ 0 & 0 & 0 & 0 & 0 & 0 & 0 & 0 & 0 \\ 0 & 0 & 0 & 0 & 0 & 0 & 0 & 0 & 0 \\ 1 & 0 & 0 & 0 & 1 & 0 & 0 & 0 & 1 \\ 0 & 0 & 0 & 0 & 0 & 0 & 0 & 0 & 0 \\ 0 & 0 & 0 & 0 & 0 & 0 & 0 & 0 & 0 \\ 0 & 0 & 0 & 0 & 0 & 0 & 0 & 0 & 0 \\ 1 & 0 & 0 & 0 & 1 & 0 & 0 & 0 & 1 \end{bmatrix}, \tag{8.5}$$

$$\mathcal{A}[Q_{z^2}] = \begin{bmatrix} 0 & 0 & 0 & 0 & 0 & 0 & 0 & 0 & 1 \\ 0 & 0 & 0 & 0 & 0 & 0 & 0 & 0 & 0 \\ 0 & 0 & 0 & 0 & 0 & 0 & 0 & 0 & 0 \\ 0 & 0 & 0 & 0 & 0 & 0 & 0 & 0 & 0 \\ 0 & 0 & 0 & 0 & 0 & 0 & 0 & 0 & 0 \\ 0 & 0 & 0 & 0 & 0 & 0 & 0 & 0 & 0 \\ 0 & 0 & 0 & 0 & 0 & 0 & 0 & 0 & 0 \\ 0 & 0 & 0 & 0 & 0 & 0 & 0 & 0 & 0 \\ 0 & 0 & 0 & 0 & 0 & 0 & 0 & 0 & 0 \end{bmatrix}, \qquad \mathcal{A}[Q_{x^2+y^2}] = \begin{bmatrix} 0 & 0 & 0 & 0 & 0 & 0 & 0 & 0 & 0 \\ 0 & 0 & 0 & 0 & 0 & 0 & 0 & 0 & 0 \\ 0 & 0 & 0 & 0 & 0 & 0 & 0 & 0 & 0 \\ 0 & 0 & 0 & 0 & 0 & 0 & 0 & 0 & 0 \\ 1 & 0 & 0 & 0 & 1 & 0 & 0 & 0 & 0 \\ 0 & 0 & 0 & 0 & 0 & 0 & 0 & 0 & 0 \\ 0 & 0 & 0 & 0 & 0 & 0 & 0 & 0 & 0 \\ 0 & 0 & 0 & 0 & 0 & 0 & 0 & 0 & 0 \\ 1 & 0 & 0 & 0 & 1 & 0 & 0 & 0 & 0 \end{bmatrix}, \tag{8.6}$$

$$\mathcal{A}[Q_{x^2-y^2}] = \begin{bmatrix} 0 & 0 & 0 & 0 & 0 & 0 & 0 & 0 & 0 \\ 0 & 0 & 0 & 0 & 0 & 0 & 0 & 0 & 0 \\ 0 & 0 & 0 & 0 & 0 & 0 & 0 & 0 & 0 \\ 0 & 0 & 0 & 0 & 0 & 0 & 0 & 0 & 0 \\ -1 & 0 & 0 & 0 & 1 & 0 & 0 & 0 & 0 \\ 0 & 0 & 0 & 0 & 0 & 0 & 0 & 0 & 0 \\ 0 & 0 & 0 & 0 & 0 & 0 & 0 & 0 & 0 \\ 0 & 0 & 0 & 0 & 0 & 0 & 0 & 0 & 0 \\ 1 & 0 & 0 & 0 & -1 & 0 & 0 & 0 & 0 \end{bmatrix}, \qquad \mathcal{A}[Q_{xy+yx}] = \begin{bmatrix} 0 & 0 & 0 & 0 & 0 & 0 & 0 & 0 & 0 \\ 0 & 0 & 0 & 0 & 0 & 0 & 0 & 0 & 0 \\ 0 & 0 & 0 & 0 & 0 & 0 & 0 & 0 & 0 \\ 0 & 0 & 0 & 0 & 0 & 0 & 0 & 0 & 0 \\ 0 & 0 & 0 & 0 & 0 & 0 & 0 & 0 & 0 \\ 0 & 1 & 0 & 1 & 0 & 0 & 0 & 0 & 0 \\ 0 & 0 & 0 & 0 & 0 & 0 & 0 & 0 & 0 \\ 0 & 1 & 0 & 1 & 0 & 0 & 0 & 0 & 0 \\ 0 & 0 & 0 & 0 & 0 & 0 & 0 & 0 & 0 \end{bmatrix}, \tag{8.7}$$

$$\mathcal{A}[Q_{yz+zy}] = \begin{bmatrix} 0&0&0&0&0&0&0&0&0 \\ 0&0&0&0&0&1&0&1&0 \\ 0&0&0&0&0&0&0&0&0 \\ 0&0&0&0&0&1&0&1&0 \\ 0&0&0&0&0&0&0&0&0 \\ 0&0&0&0&0&0&0&0&0 \\ 0&0&0&0&0&0&0&0&0 \\ 0&0&0&0&0&0&0&0&0 \\ 0&0&0&0&0&0&0&0&0 \end{bmatrix}, \quad \mathcal{A}[Q_{zx+xz}] = \begin{bmatrix} 0&0&0&0&0&0&0&0&0 \\ 0&0&0&0&0&0&0&0&0 \\ 0&0&1&0&0&0&1&0&0 \\ 0&0&0&0&0&0&0&0&0 \\ 0&0&0&0&0&0&0&0&0 \\ 0&0&0&0&0&0&0&0&0 \\ 0&0&1&0&0&0&1&0&0 \\ 0&0&0&0&0&0&0&0&0 \\ 0&0&0&0&0&0&0&0&0 \end{bmatrix}. \tag{8.8}$$

Each of these patterns contributes a quadrupolar ordering component $Q_\bullet$ to the decision function, which is related to the corresponding pattern $\mathcal{A}[Q_\bullet]$ through the relation $\left(Q_\bullet^{\alpha\beta}\right)^2 = \operatorname{Tr}\left[\mathcal{A}[Q_\bullet]\,(\mathrm{S}^\alpha \otimes \mathrm{S}^\beta)^{\otimes 2}\right]$:

$$\begin{aligned} Q^{\alpha\beta}_{x^2+y^2+z^2} &= S^\alpha_x S^\beta_x + S^\alpha_y S^\beta_y + S^\alpha_z S^\beta_z, && (8.9) \\ Q^{\alpha\beta}_{z^2} &= S^\alpha_z S^\beta_z, && (8.10) \\ Q^{\alpha\beta}_{x^2+y^2} &= S^\alpha_x S^\beta_x + S^\alpha_y S^\beta_y, && (8.11) \\ Q^{\alpha\beta}_{x^2-y^2} &= S^\alpha_x S^\beta_x - S^\alpha_y S^\beta_y, && (8.12) \\ Q^{\alpha\beta}_{xy+yx} &= S^\alpha_x S^\beta_y + S^\alpha_y S^\beta_x, && (8.13) \\ Q^{\alpha\beta}_{yz+zy} &= S^\alpha_y S^\beta_z + S^\alpha_z S^\beta_y, && (8.14) \\ Q^{\alpha\beta}_{zx+xz} &= S^\alpha_z S^\beta_x + S^\alpha_x S^\beta_z, && (8.15) \end{aligned}$$

where the first line corresponds to the intrinsic normalization constraint,

$$Q^{\alpha\alpha}_{x^2+y^2+z^2} := (S^\alpha_x)^2 + (S^\alpha_y)^2 + (S^\alpha_z)^2 \equiv 1 \tag{8.16}$$

in case of “on-site” ($\alpha = \beta$) blocks. Its appearance is physically irrelevant; examples of such a “self-contraction” have previously been discussed in Ch. 6.

The weights $p[Q_\bullet]$ of the ordering components are thus given by decomposing $\mathcal{B}$ in terms of $\mathcal{A}[Q_\bullet]$, *i.e.* by solving the linear equations $\boldsymbol{\mathcal{A}}\boldsymbol{p} = \mathcal{B}$, where $\boldsymbol{\mathcal{A}} = (\mathcal{A}[Q_{x^2+y^2+z^2}], \dots, \mathcal{A}[Q_{xy+yx}])$ and $\boldsymbol{p} = (p[Q_{x^2+y^2+z^2}], \dots, p[Q_{xy+yx}])^T$. In case the form of Eq. (8.4) was followed exactly, this would result in seven independent equations. When $\mathcal{B}$ is rather obtained through the SVM coefficient matrix and, hence, noisy, the linear system is overdetermined and the optimal choice of the component weights can be found by a least-squares fit, *i.e.* by minimizing $\|\boldsymbol{\mathcal{A}}\boldsymbol{p} - \mathcal{B}\|^2$. In fact, since blocks of each type (“on-site”, “cross”, and “bond” type) occur in the full coefficient matrix $C_{\mu\nu}$ many times over, all of these instances can be included in the least-squares fit to obtain common weights for each of the three block types.

The results are tabulated in Tab. 8.2 for the various cases discussed in this chapter and will be referred back to a few times during the subsequent discussions. As expected, the pattern (8.5) contributes significantly only in on-site blocks[2] where it corresponds to a constant and is, thus, physically irrelevant.

---

[2] The exception being phase VI where it is the only pattern to occur and does so in cross and bond blocks. Hence, it does contribute nontrivially to the decision function. Its effect will be studied in Secs. 8.2.3 and 9.2.

		$p[Q_{x^2+y^2+z^2}]$	$p[Q_{z^2}]$	$p[Q_{x^2+y^2}]$	$p[Q_{x^2-y^2}]$	$p[Q_{xy+yx}]$	$p[Q_{yz+zy}]$	$p[Q_{zx+xz}]$
IV | T_∞	on-site	−0.564	−0.021	**1.274**	**0.278**	**0.280**	0.000	0.000
	cross	−0.007	0.006	**−0.425**	**−0.093**	**−0.093**	0.000	0.000
	bond	0.003	−0.002	**0.142**	**0.031**	**0.031**	0.000	0.000
III | T_∞	on-site	0.717	0.281	**−1.681**	−0.001	−0.001	0.000	0.000
	cross	0.097	−0.081	**0.555**	0.000	0.000	0.000	0.000
	bond	−0.028	0.024	**−0.184**	0.000	0.000	0.000	0.000
III | IV	on-site	−0.088	0.082	0.146	**0.933**	**0.941**	0.000	0.000
	cross	0.022	−0.021	−0.052	**−0.311**	**−0.314**	0.000	0.000
	bond	−0.005	0.005	0.019	**0.104**	**0.105**	0.000	0.000
V | T_∞	on-site	−0.086	**1.068**	−0.073	0.000	0.000	0.000	0.000
	cross	−0.018	**−0.364**	0.016	0.000	0.000	0.000	0.000
	bond	0.003	**0.124**	−0.003	0.000	0.000	0.000	0.000
VI | T_∞	on-site	−0.001	0.001	0.000	0.000	0.000	0.000	0.000
	cross	**−0.997**	0.000	0.000	0.000	0.000	0.000	0.000
	bond	**0.313**	0.000	0.000	0.000	0.000	0.000	0.000

Table 8.2: The weights of the tentative quadrupolar ordering components, $p[Q_\bullet]$, are tabulated for five classifiers which are analyzed in this chapter (Figs. 8.8, 8.9, 8.10). These weights were obtained through a least-squares fit based on all blocks in the full coefficient matrix of each of the site-site ("on-site"), site-bond ("cross"), and bond-bond ("bond") types, as discussed in Sec. 8.2.3. For each classifier, weights corresponding to components which contribute significantly (and are of physical relevance) are set in bold type. The ratios between these weights for the three block types are given in Tab. 8.3.

For the case of $C_{\mu\nu}(\text{IV} \,|\, T_\infty)$, Fig. 8.8, one notices that three ordering components contribute appreciably (set in bold font in Tab. 8.2) and their physical meaning is transparent. $Q_{x^2+y^2}$ reflects the anisotropic interaction in the XXZ Hamiltonian Eq. (2.13). Additionally, Q_{xy+yx} and $Q_{x^2-y^2}$ form the hidden order recently discovered in Ref. 87. One observes that these two occur with equal weight, $p[Q_{xy+yx}] = p[Q_{x^2-y^2}]$. This is consistent with the fact that—given the presence of $Q_{x^2+y^2}$—the components Q_{xy+yx} and $Q_{x^2-y^2}$ define the C_{2h} group polynomial [84, 179].

Therefore, in addition to confirming the findings of Ref. 87, the present results also suggest that phase IV possesses a C_{2h} order. Its characterization consists of two fluctuating fields, a biaxial one

$$\mathrm{Q}^{\mathrm{B}}_{C_{2h}} = \left\langle \begin{pmatrix} Q_{xy+yx} \\ Q_{x^2-y^2} \end{pmatrix} \right\rangle_{\mathrm{cl}}, \tag{8.17}$$

where the components are subject to the relation

$$Q^{\alpha\alpha}_{x^2+y^2} Q^{\beta\beta}_{x^2+y^2} = (Q^{\alpha\beta}_{xy+yx})^2 + (Q^{\alpha\beta}_{x^2-y^2})^2, \tag{8.18}$$

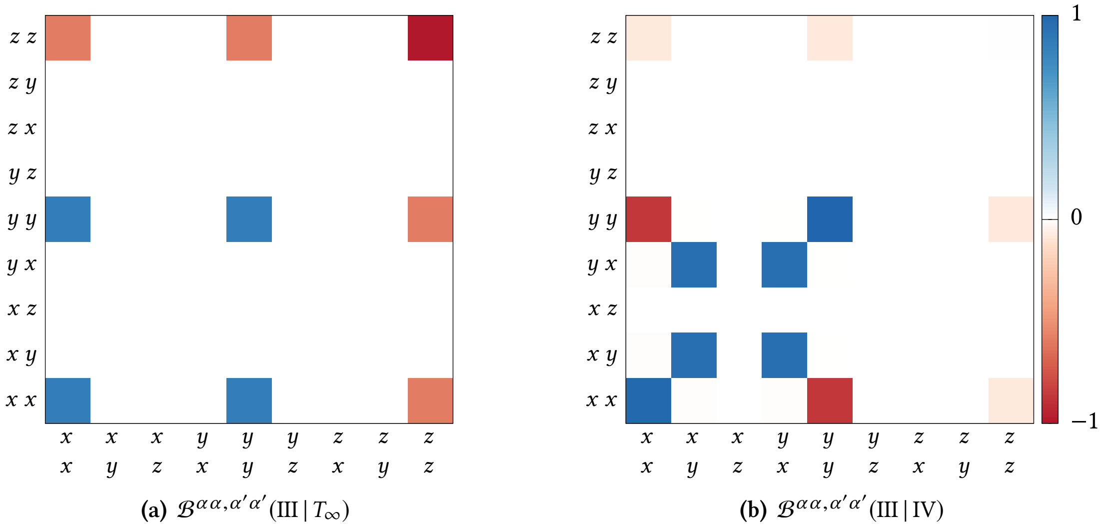

(a) $\mathcal{B}^{\alpha\alpha,\alpha'\alpha'}(\mathrm{III}\,|\,T_\infty)$ (b) $\mathcal{B}^{\alpha\alpha,\alpha'\alpha'}(\mathrm{III}\,|\,\mathrm{IV})$

Figure 8.9: The on-site 9×9 block of the coefficient matrix discerning phase III from the T_∞ control group (a) and from phase IV (b), respectively, as obtained from the TK-SVM at rank 2. The axes iterate over component indices a, b in lexicographical order. Both on-site block exhibit a redundant contribution due to the spin normalization. Apart from that, (a) corresponds to the $Q_{x^2+y^2}$ ordering component, revealing phase III as a uniaxial nematic (without spontaneous symmetry breaking); pattern (b) corresponds to the Q_{xy+yx} and $Q_{x^2-y^2}$ components, consistent with the fact that phase IV additionally spontaneously breaks the uniaxial symmetry down to a biaxial one.

and a uniaxial one $Q^{\mathrm{U}}_{C_{2h}} = \langle Q_{x^2+y^2}\rangle_{\mathrm{cl}}$. The former defines a spontaneously symmetry-breaking order in the easy-plane, while the latter distinguishes it from a C_2 phase which hosts the same biaxial order [84, 179].

Following the terminology of liquid crystal physics [180], phase IV may be called a biaxial spin nematic (BSN) phase. However, in contrast to the well known D_{2h} biaxial phase, which breaks only rotational symmetries, this C_{2h} phase also spontaneously breaks mirror symmetries σ_{xz} and σ_{yz} of the XXZ Hamiltonian Eq. (2.13), hence it is an unconventional biaxial nematic.

Phase III is another phase that possesses nonvanishing quadrupolar moments. The coefficient matrix $C_{\mu\nu}(\mathrm{III}\,|\,T_\infty)$ displays a similar global structure as $C_{\mu\nu}(\mathrm{IV}\,|\,T_\infty)$, but a more simple pattern within the small blocks. A representative block, $\mathcal{B}^{\alpha\alpha,\alpha'\alpha'}(\mathrm{III}\,|\,T_\infty)$, is provided in Fig. 8.9(a). From Tab. 8.2, one finds that $Q_{x^2-y^2}$ and Q_{xy+yx} no longer contribute, while $Q_{x^2+y^2}$ remains relevant. Phase III hence exhibits uniaxial physics. However, note that the appearance of $Q_{x^2+y^2}$ does not indicate the spontaneous breaking of a symmetry since the XXZ Hamiltonian explicitly breaks the spin O(3) symmetry down to the infinite dihedral group $D_{\infty h}$.

Moreover, it is clear that the biaxial order parameter $\mathbf{Q}^{\mathrm{B}}_{C_{2h}}$ is responsible for the transition between phases III and IV. One expects that they will be stressed in the coefficient matrix $C_{\mu\nu}(\mathrm{III}\,|\,\mathrm{IV})$. Indeed, as shown in Fig. 8.9(b), these components dominate the block

$\mathcal{B}^{\alpha\alpha,\alpha'\alpha'}(\mathrm{III}\,|\,\mathrm{IV})$, in comparison to $\mathcal{B}^{\alpha\alpha,\alpha'\alpha'}(\mathrm{IV}\,|\,T_\infty)$ in Fig. 8.8(b). This is also apparent from the corresponding weights given in Tab. 8.2.

8.2.3 Identification of emergent constraints

The example of spin ice in the introduction demonstrates that an emergent constraint can dramatically influence correlations and dynamics in the system. In fact many interesting phases in frustrated systems feature emergent constraints.

Their identification can be far from trivial in the absence of generic tools as they are not obvious from the Hamiltonian. In special cases, such as the pyrochlore lattice [87, 106, 184, 185], water ice [186], or the kagome lattice [187], obtaining them relies on systematic calculations using group theory (decomposition in terms of irreducible representations). These calculations are specific to corner-sharing geometries.

In this subsection, the procedure for deriving emergent constraints from the coefficient matrices is demonstrated. Both situations in which a phase is defined exclusively by an emergent constraint, and those in which a constraint coexists with symmetry-breaking orders, will be encountered.

Ice rule

The analysis begins with phase V, the most idiomatic case of a constraint. The procedure is similar to that for analyzing local order in the preceding subsection, but here also the relative weights of different blocks are taken into account.

To emphasize those weights, in Fig. 8.10(a) a reduced form of the coefficient matrix $C_{\mu\nu}(\mathrm{V}\,|\,T_\infty)$ is shown. Each pixel of this reduced matrix now corresponds to a 9×9 block in the full $C_{\mu\nu}$ matrix, while the value of the pixel is given by the weight of the Q_{z^2} ordering component. One notices that there are three different weights, corresponding to the site-site ($\mathcal{B}^{\alpha\alpha,\alpha'\alpha'}$), site-bond cross ($\mathcal{B}^{\alpha\alpha,\alpha'\neq\beta'}$, $\mathcal{B}^{\alpha\neq\beta,\alpha'\alpha'}$) and bond-bond ($\mathcal{B}^{\alpha\neq\beta,\alpha'\neq\beta'}$) blocks in the full $C_{\mu\nu}$, respectively. Details of these blocks are also provided in panels (b)–(d).

The site-site block in Fig. 8.10(b) can be expressed as

$$\begin{aligned}
\mathcal{B}^{\alpha\alpha,\alpha'\alpha'} &= p[Q_{x^2+y^2+z^2}]\begin{bmatrix} 1&0&0&0&1&0&0&0&1\\ 0&0&0&0&0&0&0&0&0\\ 0&0&0&0&0&0&0&0&0\\ 0&0&0&0&0&0&0&0&0\\ 1&0&0&0&1&0&0&0&1\\ 0&0&0&0&0&0&0&0&0\\ 0&0&0&0&0&0&0&0&0\\ 0&0&0&0&0&0&0&0&0\\ 1&0&0&0&1&0&0&0&1 \end{bmatrix} + p[Q_{z^2}]\begin{bmatrix} 0&0&0&0&0&0&0&0&1\\ 0&0&0&0&0&0&0&0&0\\ 0&0&0&0&0&0&0&0&0\\ 0&0&0&0&0&0&0&0&0\\ 0&0&0&0&0&0&0&0&0\\ 0&0&0&0&0&0&0&0&0\\ 0&0&0&0&0&0&0&0&0\\ 0&0&0&0&0&0&0&0&0\\ 0&0&0&0&0&0&0&0&0 \end{bmatrix}\\
\mathcal{B}^{\alpha\alpha,\alpha'\alpha'}_{ab,a'b'} &= p_{\mathrm{site}}[Q_{x^2+y^2+z^2}]\,\delta_{ab}\delta_{a'b'} + p_{\mathrm{site}}[Q_{z^2}]\,\delta_{z,a}\delta_{z,b}\delta_{z,a'}\delta_{z,b'}. \qquad (8.19)
\end{aligned}$$

When substituting $\mathcal{B}^{\alpha\alpha,\alpha'\alpha'}$ back into the decision function, one finds that the first term in Eq. (8.19) just leads to the normalization of a spin $\mathbf{S}^\alpha$. The second term, defining the product $(S_z^\alpha)^2(S_z^{\alpha'})^2$, nevertheless relates to a nontrivial constraint when compared to the cross and

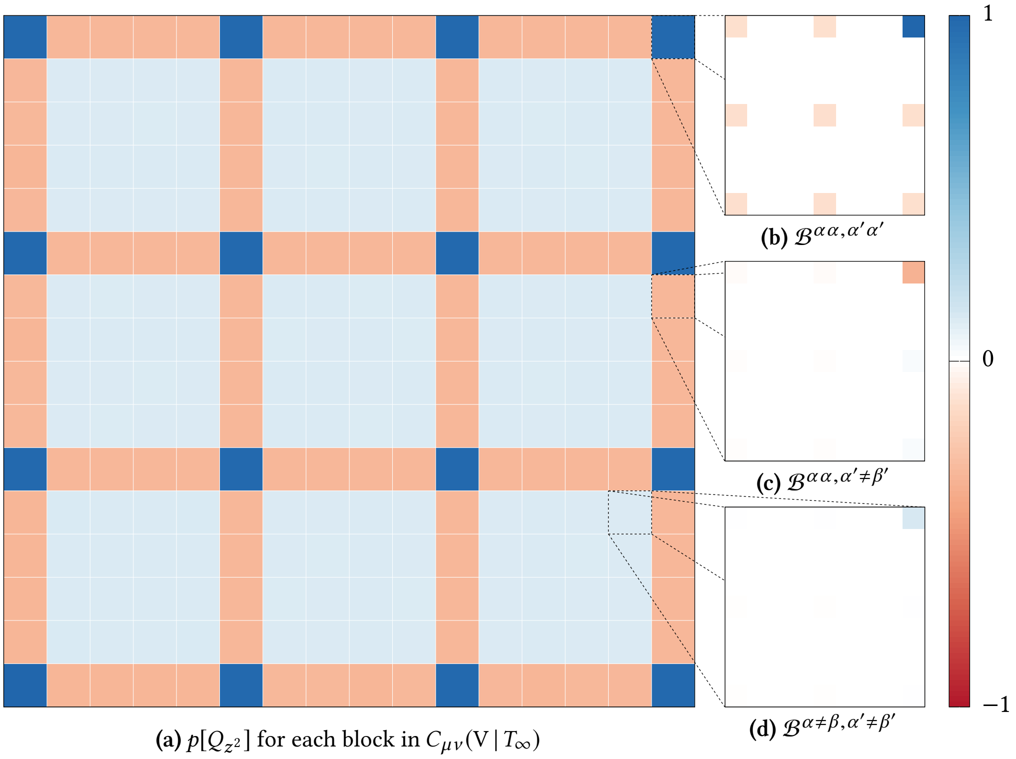

(a) $p[Q_{z^2}]$ for each block in $C_{\mu\nu}(\mathrm{V}\,|\,T_\infty)$

(b) $\mathcal{B}^{\alpha\alpha,\alpha'\alpha'}$

(c) $\mathcal{B}^{\alpha\alpha,\alpha'\neq\beta'}$

(d) $\mathcal{B}^{\alpha\neq\beta,\alpha'\neq\beta'}$

Figure 8.10: (a) The 16 × 16 reduced coefficient matrix where each 9 × 9 block in $C_{\mu\nu}(\mathrm{V}\,|\,T_\infty)$ is replaced by the weight of the Q_{z^2} ordering component, as obtained from the TK-SVM coefficient matrix at rank 2, *cf.* Tab. 8.2. The axes iterate over sublattice indices α, β in lexicographical order. Panels (b) through (d) zoom in to various types of 9 × 9 blocks of fixed sublattice indices: (b) “on-site”, (c) “cross”, and (d) “bond”. From the relative strength of the Q_{z^2} components in each type of block, one can infer the ice rule.

bond-bond block in Fig. 8.10(c) and (d), which can be expressed as

$$\mathcal{B}^{\alpha\alpha,\alpha'\neq\beta'}_{aa'} = p_{\mathrm{cross}}[Q_{z^2}]\,\delta_{z,a}\delta_{z,b}\delta_{z,a'}\delta_{z,b'}, \tag{8.20}$$

$$\mathcal{B}^{\alpha\neq\beta,\alpha'\neq\beta'}_{aa'} = p_{\mathrm{bond}}[Q_{z^2}]\,\delta_{z,a}\delta_{z,b}\delta_{z,a'}\delta_{z,b'}. \tag{8.21}$$

Note that the $p[Q_{x^2+y^2+z^2}]$ term does not appear here, because bond and cross terms do not obey an intrinsic constraint, unlike spin normalization in on-site terms.

One observes that these weights satisfy the relation,

$$\gamma_{z^2} := \frac{p_{\mathrm{bond}}[Q_{z^2}]}{p_{\mathrm{cross}}[Q_{z^2}]} = \frac{p_{\mathrm{cross}}[Q_{z^2}]}{p_{\mathrm{site}}[Q_{z^2}]} = \frac{\left\langle S_z^\alpha S_z^\beta \right\rangle}{\langle S_z^\alpha S_z^\alpha \rangle} \approx -\frac{1}{3}, \tag{8.22}$$

for $\alpha \neq \beta$ up to numerical accuracy (see Table 8.3). Summing over all sublattice indices (α, β), γ_{z^2} is absorbed by the ratio between on-site ($\alpha = \beta$; 4) and bond terms ($\alpha \neq \beta$; 12). As a

		$\gamma_{x^2+y^2+z^2}$	γ_{z^2}	$\gamma_{x^2+y^2}$	$\gamma_{x^2-y^2}$	γ_{xy+yx}
IV	T_∞			-0.334	-0.333	-0.333
III	T_∞			-0.331		
III	IV				-0.334	-0.334
V	T_∞		-0.341			
VI	T_∞	-0.314				

Table 8.3: Ratios of the relevant bond and on-site quadrupolar moments, $\gamma_\bullet := \left\langle Q_\bullet^{\alpha\beta} \right\rangle / \langle Q_\bullet^{\alpha\alpha} \rangle$. These are calculated by taking the ratio between the weights of the relevant component with respect to "bond" and "cross" blocks, or "cross" and "on-site" blocks (*cf.* Eqs. (8.22), (8.25), and (8.28)). Both ways yield consistent results in all cases (varying at most in the final digit). The weights of the ordering components themselves were calculated through a least-squares fit to the coefficient matrix and are given in Tab. 8.2.

consequence, Eq. (8.22) in turn gives rise to the relation

$$\sum_\alpha \langle S_z^\alpha S_z^\alpha \rangle_{\mathrm{cl}} + \sum_{\alpha \neq \beta} \left\langle S_z^\alpha S_z^\beta \right\rangle_{\mathrm{cl}} = \left\langle \left(\sum_\alpha S_z^\alpha \right)^2 \right\rangle_{\mathrm{cl}} = 0, \tag{8.23}$$

where $\langle \dots \rangle_{\mathrm{cl}}$ averages over all tetrahedral clusters.

As $(\dots)^2$ is semi-positive definite, the constraint

$$S_z^{(1)} + S_z^{(2)} + S_z^{(3)} + S_z^{(4)} = 0 \tag{8.24}$$

has to be fulfilled for each tetrahedron individually. Contrary to the spin normalization relation, which is an intrinsic constraint, this constraint emerges from the cooperative behavior of spins. It defines the 2-*in*-2-*out* rule of spin ice.

Spin ice is known as an example of classical spin liquids. It does not possess any long-range order, but features topological characteristics such as extensive ground state degeneracy (exGSD) and an effective $U(1)$ gauge-theoretical description [41]. These topological features actually are underpinned by the ice rule, Eq. (8.24). Therefore, the TK-SVM is able to identify spin ice by means of the characteristic ice rule.

Constraint in the easy-plane

We continue the analysis of emergent constraints in other regions of the phase diagram Fig. 8.2. This involves the phases III, IV, and VI.

In Sec. 8.2.2 the ordering components in the phases III and IV have been discussed already. It was seen that phase III has a planar quadrupolar component $Q_{x^2+y^2} = S_x^\alpha S_x^\beta + S_y^\alpha S_y^\beta$ which can be defined either by a single spin ($\alpha = \beta$) or on a bond connecting two spins ($\alpha \neq \beta$).

One finds that the weights with which the site and bond terms manifest themselves also fulfill a relation

$$\gamma_{x^2+y^2} := \frac{p_{\text{bond}}[Q_{x^2+y^2}]}{p_{\text{cross}}[Q_{x^2+y^2}]} = \frac{p_{\text{cross}}[Q_{x^2+y^2}]}{p_{\text{site}}[Q_{x^2+y^2}]} \approx -\frac{1}{3}. \tag{8.25}$$

(See Tabs. 8.2 and 8.3 for details.) Similar to the case of spin ice, the relation (8.25) in turn leads to a cooperation of spins

$$\left\langle \left(\sum_\alpha S_x^\alpha \right)^2 \right\rangle_{\text{cl}} = \left\langle \left(\sum_\alpha S_y^\alpha \right)^2 \right\rangle_{\text{cl}} = 0, \tag{8.26}$$

and, consequently, a vectorial constraint on the S_x and S_y components,

$$\begin{bmatrix} S_x^{(1)} + S_x^{(2)} + S_x^{(3)} + S_x^{(4)} \\ S_y^{(1)} + S_y^{(2)} + S_y^{(3)} + S_y^{(4)} \end{bmatrix} = \begin{bmatrix} 0 \\ 0 \end{bmatrix}. \tag{8.27}$$

Therefore, phase III is not just an explicitly symmetry-breaking phase, but also subject to constrained dynamics. This constraint is equivalent to that obtained by an irreducible-representation decomposition, Eq. (5) in Ref. 87, from which one can derive pinch points in the spin structure factor.

The constraint in Eq. (8.25) is also observed in phase IV (BSN phase), and is reflected by the weights of the biaxial orders, $p[Q_{x^2-y^2}]$ and $p[Q_{xy+yx}]$ corresponding to the quadrupolar components defined in Eqs. (8.12) and (8.13). One observes that both components occur with approximately the same weight for each type of block (see Tab. 8.2), as well as ratios of $\gamma_{x^2-y^2} = \gamma_{xy+yx} = -1/3$ (see Tab. 8.3) among them. Therefore, phase IV is a constrained biaxial phase where a local order and an emergent constraint coexist. As the latter signals an underlying gauge symmetry [87], it also represents an instance where symmetry-breaking order coexists with an emergent gauge theory.

This coexistence also indicates a crucial difference between emergent spin nematic orders and intrinsic nematic orders in the context of liquid crystals. In the latter case, nematic order parameters are considered as fundamental degrees of freedom (after coarse graining), whereas dipolar fields are typically trivial by construction. In an emergent spin nematic phase on the other hand, even in the absence of a long-range dipolar order, ordinary spins may remain strongly constrained and exhibit nontrivial correlations.

Isotropic constraint

Lastly, the phase VI too exhibits constrained dynamics. The coefficient matrix $C_{\mu\nu}(\mathrm{VI}\,|\,T_\infty)$ contrasting it to the decorrelated control group is shown in Fig. 8.11. Even though no local order is detected by the four-spin cluster up to rank 4, one observes the occurrence of isotropic ordering components $Q^{\alpha\beta}_{x^2+y^2+z^2}$, Eq. (8.9), in the bond and cross terms with a ratio

$$\gamma_{x^2+y^2+z^2} := \frac{p_{\text{bond}}[Q_{x^2+y^2+z^2}]}{p_{\text{cross}}[Q_{x^2+y^2+z^2}]} = -0.31, \tag{8.28}$$

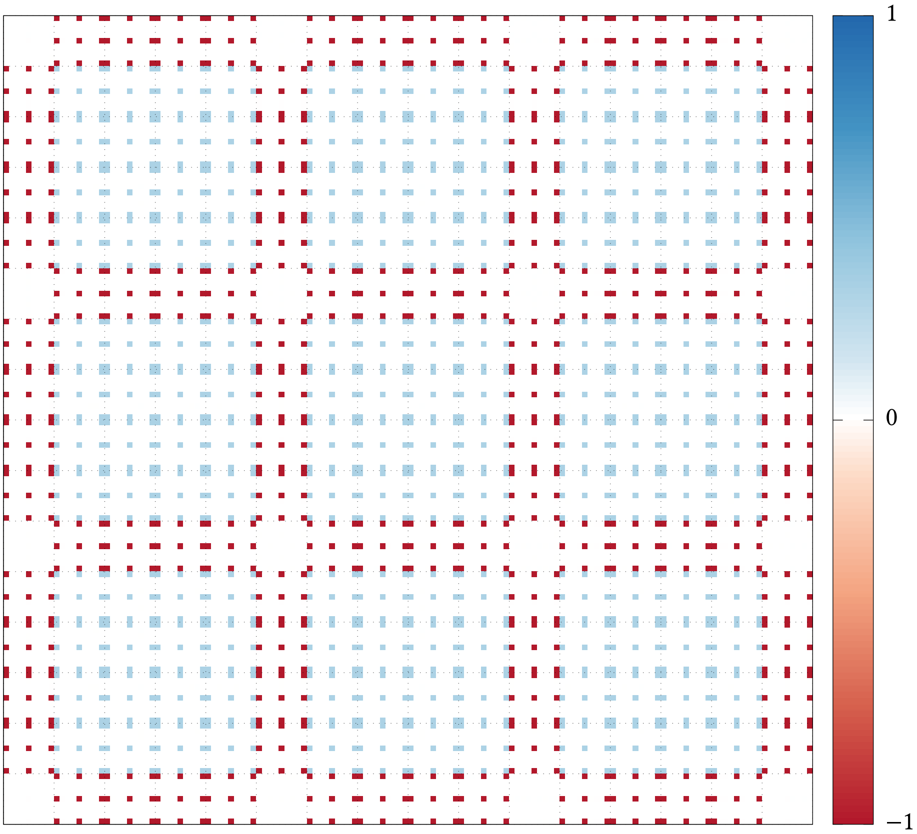

Figure 8.11: The 144 × 144 coefficient matrix $C_{\mu\nu}(\mathrm{VI}\,|\,T_\infty)$ obtained from TK-SVM at rank 2. The axes iterate over sublattice indices α, β and spatial components a, b such that tuples (α, β, a, b) are lexicographically sorted. The pattern (8.5) corresponding to the isotropic component, Eq. (8.9), appears in "cross" and "bond" type blocks, but is absent from the "on-site" blocks where it is canceled by the intrinsic spin normalization constraint. It manifests the isotropic constraint, Eq. (8.29). *Cf.* also the similar pattern in Fig. (9.3) and its detailed analysis in Sec. 9.2.

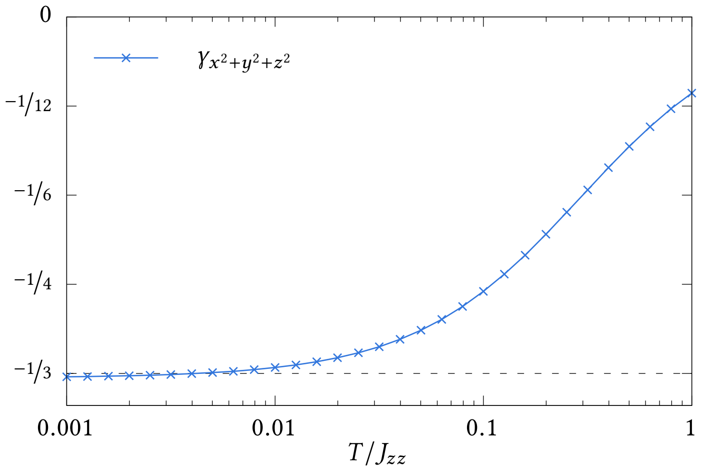

Figure 8.12: The ratio of the bond and on-site isotropic ordering components is plotted along the $J_\pm = -0.5J_{zz}$ line as a function of the temperature of the training samples. For $\gamma_{x^2+y^2+z^2} = -1/3$, the constraint $\mathbf{S}^{(1)} + \mathbf{S}^{(2)} + \mathbf{S}^{(3)} + \mathbf{S}^{(4)} = 0$ for the four spins in each tetrahedron is perfectly fulfilled; for $\gamma_{x^2+y^2+z^2} = 0$ the spins are entirely independent. Indeed, $\gamma_{x^2+y^2+z^2}$ is seen to approach $-1/3$ as $T \longrightarrow 0$. Hence, the curve shows the crossover from a trivial paramagnet at high temperature to a cooperative paramagnet at low temperature.

whereas a similar ratio cannot be inferred from the on-site blocks where it is canceled by spin normalization. However, contrary to Eq. (8.22) and Eq. (8.25), here $\gamma_{x^2+y^2+z^2}$ is noticeably different from $-1/3$ and shows a dependence on training samples. Such behavior seems to imply that the characterization of phase VI is emerging but not yet sharply defined in the training samples.

To verify this conjecture and quantify the variation of $\gamma_{x^2+y^2+z^2}$, the TK-SVM was trained separately on each of 17 parameter points along $J_\pm = -0.5J_{zz}$, which are apparently most representative of the phase, which are contrasted against fictitious isotropic configurations. The ratio $\gamma_{x^2+y^2+z^2}$ has been extracted from the resultant coefficient matrices and are plotted in Fig. 8.12 against the temperature of the respective training data. It becomes apparent that the ratio approaches $-1/3$ as $T \longrightarrow 0$.

As a result, one may interpret the relation (8.28) as a constraint that isotropically affects all of the three spin components,

$$\begin{bmatrix} S_x^{(1)} + S_x^{(2)} + S_x^{(3)} + S_x^{(4)} \\ S_y^{(1)} + S_y^{(2)} + S_y^{(3)} + S_y^{(4)} \\ S_z^{(1)} + S_z^{(2)} + S_z^{(3)} + S_z^{(4)} \end{bmatrix} = \begin{bmatrix} 0 \\ 0 \\ 0 \end{bmatrix}. \tag{8.29}$$

However, this constraint is only obeyed in the ground state. At finite temperature, it will be softened by thermal fluctuations and, consequently, a finite portion of spins will be released from the ground state configuration.

This is reminiscent of gapless excitations. Indeed, at $J_\pm = -0.5J_{zz}$, the XXZ Hamiltonian Eq. (2.13) becomes a pyrochlore Heisenberg model in local coordinates. It is analog to the pyrochlore Heisenberg antiferromagnet (HAF) which is an example for gapless classical spin liquids (or cooperative paramagnets) [69, 95]. Moreover, the fluctuation-induced deviation of γ from the ground state value $-1/3$ is also consistent with the finding that this phase has blurred pinch points at intermediate temperatures in the spin structure factor in Ref. 87.

Finally, the extracted order parameters and constraints confirm the hierarchy of the phases in Eq. (8.1) inferred from the bias criterion. Phase VI is O(3) symmetric, not breaking symmetry. Nevertheless, owing to the constraint Eq. (8.29), it does not explore the entire configuration space, thus appears less disordered than the trivial paramagnet. Phase III and V feature constrained dynamics in easy-plane and easy-axis, respectively; both have the $D_{\infty h}$ symmetry. Phase IV breaks the symmetry of phase III and develops a C_{2h} coplanar order. Furthermore, the bias criterion respects the distinct constraint in phase IV and V, so does not assign them a rank, though the latter is more symmetric. The magnetization $\mathbf{M}_\perp$ of phase I has the C_{1h} point-group symmetry and breaks the in-plane O(2) symmetry entirely. Thereby, one can express the disorder hierarchy by the nature of the phases,

$$\begin{tikzcd}
 & & \underset{\substack{\text{easy}\\\text{plane}}}{D_{\infty h}} \arrow[r] & \underset{\text{biaxial}}{C_{2h}} \arrow[dr] & \\
\underset{\text{trival}}{\mathrm{O}(3)} \arrow[r] & \underset{\text{constrained}}{\mathrm{O}(3)} \arrow[ur] \arrow[dr] & & & \underset{\text{magnetic}}{C_{1h}}\ . \\
 & & \underset{\substack{\text{easy}\\\text{axis}}}{D_{\infty h}} \arrow[urr] & &
\end{tikzcd} \tag{8.30}$$

8.3 Thermodynamics of constraints

When learning the phase diagram, Fig. 8.2, it was pointed out that gradual change of Fiedler vector entries at phase boundaries is indicative of a crossover. Thereby, aside from the topology of the phase diagram, the graph analysis also provides an intuitive way to recognize crossovers and the regions where they take place. In this section, this interpretation will be confirmed by examining the analytical order parameters and constraints extracted from the coefficient matrices. Moreover, possible advantages of those quantities regarding the identification of phase transitions and crossovers, as compared to the use of conventional quantities such as heat capacity or magnetic susceptibility, will be discussed.

8.3.1 Single crossover

Again, the crossover between the spin ice (phase V) and the trivial paramagnet (phase II) will mark the starting point of the discussion. It is well understood in terms of the Schottky anomaly in the specific heat which may serve as a reference point for the quantity learned by TK-SVM.

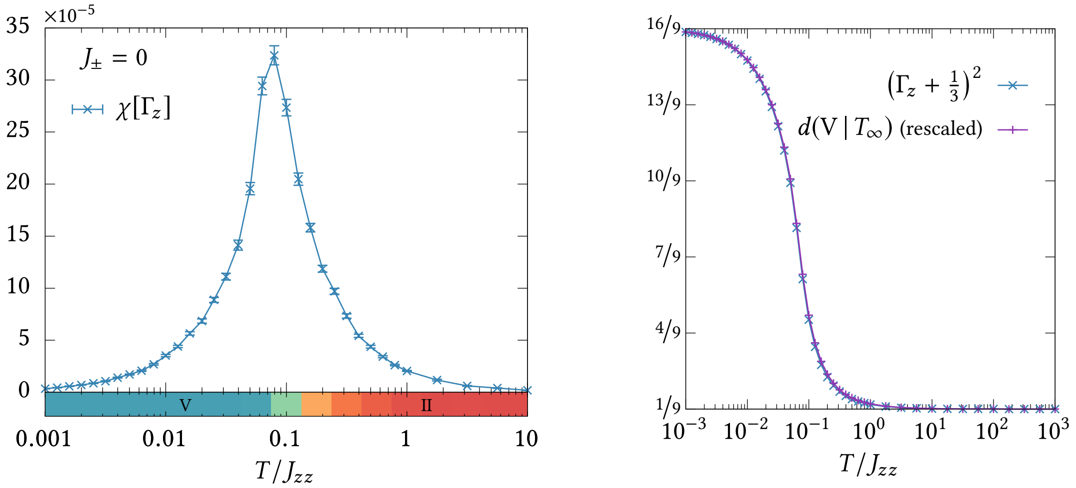

(a) The susceptibility of the spin ice constraint Γ_z [Eq. (8.31)] is measured along the $J_{zz} = 0$ line. The colored bar below the abscissa shows the corresponding slice of the phase diagram, Fig. 8.2, for comparison. The peak of the susceptibility is seen to coincide with the locus of the crossover between the spin ice phase (blue) and the paramagnet (red).

(b) The agreement of the decision function with $(\Gamma_z + 1/3)^2$, the expression that was inferred from its coefficient matrix, is confirmed, given suitable affine rescaling of the former.

Figure 8.13: The measurement of the spin ice "order parameter" Γ_z which the TK-SVM decision function learns and its corresponding susceptibility indicates that it can be used to locate the crossover.

The analytical quantity extracted from $C_{\mu\nu}(\mathrm{V}\,|\,T_\infty)$, Eqs. (8.19)-(8.22), may be expressed as

$$\Gamma_z := \left\langle \frac{1}{4} \sum_\alpha (S_z^\alpha)^2 - \frac{1}{12} \sum_{\alpha\neq\beta} S_z^\alpha S_z^\beta - \frac{1}{3} \right\rangle_{\mathrm{cl}} \tag{8.31}$$

$$= \left\langle \frac{1}{3} \sum_\alpha (S_z^\alpha)^2 - \frac{1}{12} \Big(\sum_\alpha S_z^\alpha \Big)^2 - \frac{1}{3} \right\rangle_{\mathrm{cl}}. \tag{8.32}$$

It measures the fulfillment of the ice-rule Eq. (8.24) and may be regarded as an order parameter, where $\Gamma_z = 1$ if the ice-rule is fully satisfied, while $\Gamma_z = 0$ for uncorrelated spins. Γ_z is normalized to satisfy these limiting cases.

One may define a susceptibility to quantify the fluctuation of Γ_z,

$$\chi[\Gamma_z] := \frac{1}{T} \left(\langle \Gamma_z^2 \rangle - \langle \Gamma_z \rangle^2 \right), \tag{8.33}$$

expecting that $\chi[\Gamma_z]$ is smooth at crossovers, but exhibits discontinuity or divergence when experiencing phase transitions.

In Fig. 8.13, Γ_z and $\chi[\Gamma_z]$ are measured along the $J_\pm = 0$ line. One indeed observes that $(\Gamma_z + 1/3)^2$ collapses onto the decision function[3], verifying the interpretation of the coefficient

---

[3] Note that the constant $-1/3$ in the definition (8.31) is not included in the TK-SVM decision function, *i.e.* $d(\mathrm{V}\,|\,T_\infty) \propto (\Gamma_z + 1/3)^2 + \mathrm{const.}$

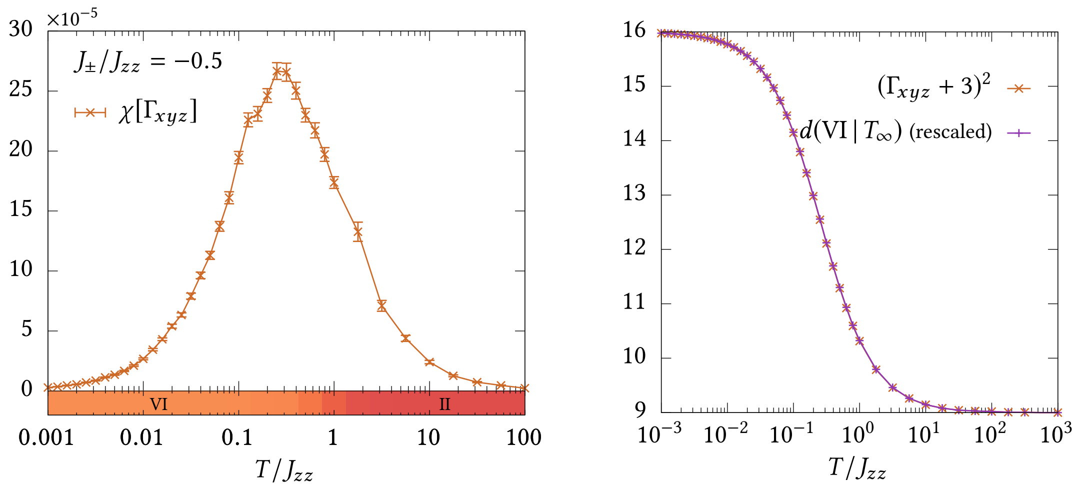

(a) The susceptibility of the isotropic constraint Γ_{xyz} [Eq. (8.34)] is measured along the $J_{zz} = -0.5 J_{zz}$ line (Heisenberg limit). The colored bar below the abscissa shows the corresponding slice of the phase diagram, Fig. 8.2, for comparison. The broad peak of the susceptibility is seen to coincide with the locus of the crossover between the cooperative (orange) and the trivial (red) paramagnet.

(b) The agreement of the decision function with $(\Gamma_{xyz} + 3)^2$, the expression that was inferred from its coefficient matrix, is confirmed, given suitable affine rescaling of the former.

Figure 8.14: The measurement of the "order parameter" encoding the isotropic constraint, Γ_{xyz}, which the TK-SVM decision function learns and its corresponding susceptibility indicates that it can be used to locate the crossover.

matrix $C_{\mu\nu}(\mathrm{V}\,|\,T_\infty)$. Moreover, $\chi[\Gamma_z]$ shows a broad peak at the boundary between the two phases, indicating a crossover driven by thermal violation of the ice rule. As expected, the characteristic temperature of this peak agrees with that inferred from the Schottky anomaly (the dashed line between phases II and V in Fig. 8.2) [87].

The above example confirms our approach which is consequently applied to the crossover between the cooperative (VI) and the trivial (II) paramagnet, whose characterization is less clear. The (normalized) order parameter corresponding to the relation (8.28) and the isotropic constraint, Eq. (8.29), is given by

$$\Gamma_{xyz} := 3 \sum_a \Gamma_a = 1 - \frac{1}{4} \left\langle \left\| \sum_\alpha \mathbf{S}^\alpha \right\|^2 \right\rangle_{\mathrm{cl}}, \tag{8.34}$$

where

$$\Gamma_a := \left\langle \frac{1}{3} \sum_\alpha (S_a^\alpha)^2 - \frac{1}{12} \left(\sum_\alpha S_a^\alpha \right)^2 - \frac{1}{3} \right\rangle_{\mathrm{cl}}, \tag{8.35}$$

and $a = x, y, z$. Accordingly, one may define its susceptibility $\chi[\Gamma_{xyz}] = \left(\langle \Gamma_{xyz}^2 \rangle - \langle \Gamma_{xyz} \rangle^2 \right) / T$.

Γ_{xyz} and $\chi[\Gamma_{xyz}]$ are measured along the $J_\pm = -0.5J_{zz}$, *i.e.* in the Heisenberg limit, in Fig. 8.14. One observes a bump over approximately three orders of magnitude in temperature. The location of its maximum is in agreement with that inferred on the basis of the magnetic susceptibility [87], its profile nevertheless marks a much larger area influenced by the crossover. Note that this region has in fact been hinted at by the slow variance of the Fiedler vector entries between the two phases.

In addition, the behavior of $\chi[\Gamma_{xyz}]$ is also consistent with that of the ratio γ in Fig. 8.12. Hence, this spin liquid is only well defined in the regime where $\gamma \approx -1/3$ at $T \lesssim 0.01$. Thereafter, the crossover starts to take hold, until very high temperature.

Here, the discussion relied on the susceptibilities of the analytical order parameters which were previously extracted from the coefficient matrices learned by TK-SVM. This has the advantage that they are immediately relatable to physical quantities. One may also choose to rely on the decision function directly and define a susceptibility for it instead. The resulting quantity cannot immediately be converted into the susceptibilities of the order parameter, whereas the reverse is true (the analytical order parameter can be squared and compared to the decision function as is the case in the insets of Figs. 8.13 and 8.14). Nonetheless, the susceptibilities of the decision functions exhibit peaks at approximately the same positions. Thus, this approach is entirely feasible to get a first impression of the behavior, without the effort of dissecting the coefficient matrices first.

8.3.2 Sequence of phase transitions and crossovers

The quantities learned by the TK-SVM are optimized to distinguish two given phases. This specialization can lead to a higher sensitivity of identifying phase transitions and crossovers, in particular when the system involves multiple fluctuating fields.

This is exemplified by the phase transition and crossovers relating to phases III and IV. In Sec. 8.2, phase IV was seen to be characterized by the quadrupolar fields $Q^{\mathrm{U}}_{C_{2h}}$ and $\mathbf{Q}^{\mathrm{B}}_{C_{2h}}$, where the latter represents the symmetry-breaking order, and the constraint (8.27) on the S_x and S_y components. When entering phase III, the biaxial order parameter $\mathbf{Q}^{\mathrm{B}}_{C_{2h}}$ vanishes, but the constraint remains in place. This constraint can be defined by an order parameter

$$\Gamma_{xy} \coloneqq \frac{3}{2}(\Gamma_x + \Gamma_y), \tag{8.36}$$

which is distinct from that of the cooperative paramagnet (Γ_{xyz}) at higher temperature.

Therefore, by increasing temperature at $J_\pm < -0.5J_{zz}$ in the phase diagram Fig. 8.2, the system undergoes the upper branch of the sequence in Eq. (8.30) (excluding the C_{1h} phase). The order parameter fields $\mathbf{Q}^{\mathrm{B}}_{C_{2h}}, \Gamma_{xy}, and \Gamma_{xyz}$ are expected to respond to the corresponding phase transition and crossovers separately.

In Fig. 8.15, their corresponding susceptibilities, $\chi[||\mathbf{Q}^{\mathrm{B}}_{C_{2h}}||]$, $\chi[\Gamma_{xy}]$, and $\chi[\Gamma_{xyz}]$, are measured along the $J_\pm = -0.6J_{zz}$ line. Indeed, they exhibit individual peaks/bumps at the relevant transitions and crossovers. The pronounced peak in $\chi[||\mathbf{Q}^{\mathrm{B}}_{C_{2h}}||]$ identifies the generalized biaxial-uniaxial phase transition [110] between the constrained C_{2h} and $D_{\infty h}$ phase. The bumps in $\chi[\Gamma_{xy}]$ and $\chi[\Gamma_{xyz}]$ are responsible for the two subsequent crossovers.

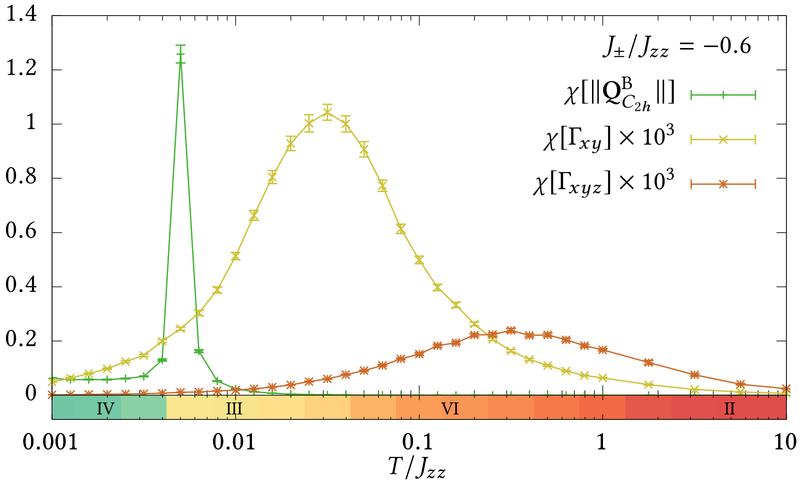

Figure 8.15: Various susceptibilities are measured along the $J_{zz} = -0.6J_{zz}$ line. The colored bar below the abscissa shows the corresponding slice of the phase diagram, Fig. 8.2, for comparison. The sharp peak in susceptibility of the biaxial order parameter $Q^{B}_{C_{2h}}$ [Eq. (8.17)] pinpoints the phase transition between the generalized biaxial (green) and uniaxial (yellow) phases; the broad peaks in the susceptibilities of the order parameters derived from the constraints, Γ_{xy} [Eq. (8.36)] and Γ_{xyz} [Eq. (8.34)], locate the crossovers into the cooperative (orange) and trivial (red) paramagnet, respectively. Note that the latter are exaggerated by a factor of 1000.

This ability to isolate phase transitions and crossovers is to be contrasted with the analysis of conventional thermodynamic quantities. For instance, the specific heat encodes thermal fluctuations of all order parameters at the same time; hence, not every phase transition or crossover may manifest itself noticeably. In particular, signals of crossovers are potentially drowned out by a phase transition or may not be distinguishable from other nearby crossovers. On the other hand, the magnetic susceptibility is sensitive to dipolar orders, nonetheless, it may not respond to the fluctuations of multipolar fields.

8.4 Kernel principal component analysis

This final section of the chapter on the pyrochlore XXZ antiferromagnet attempts to reproduce a subset of the finding that were obtained before using TK-SVM, by using the tensorial kernel in the context of kernel PCA (kPCA) as introduced in Sec. 4.1.2, dubbing the combination TK-PCA. To recap, the fundamental difference between SVM and PCA lies in the fact that the latter is unsupervised, meaning that no labeling of the training data has to be provided. For the sake of phase classification, this seems to put kPCA in an ideal position at first glance, as it eliminates the need for the prior graph analysis.

As discussed in Sec. 5.2, it is beneficial to carry out the mapping to monomial feature, $\boldsymbol{\phi}$, explicitly and rely on the kernel trick only with respect to the quadratic kernel. As mentioned in

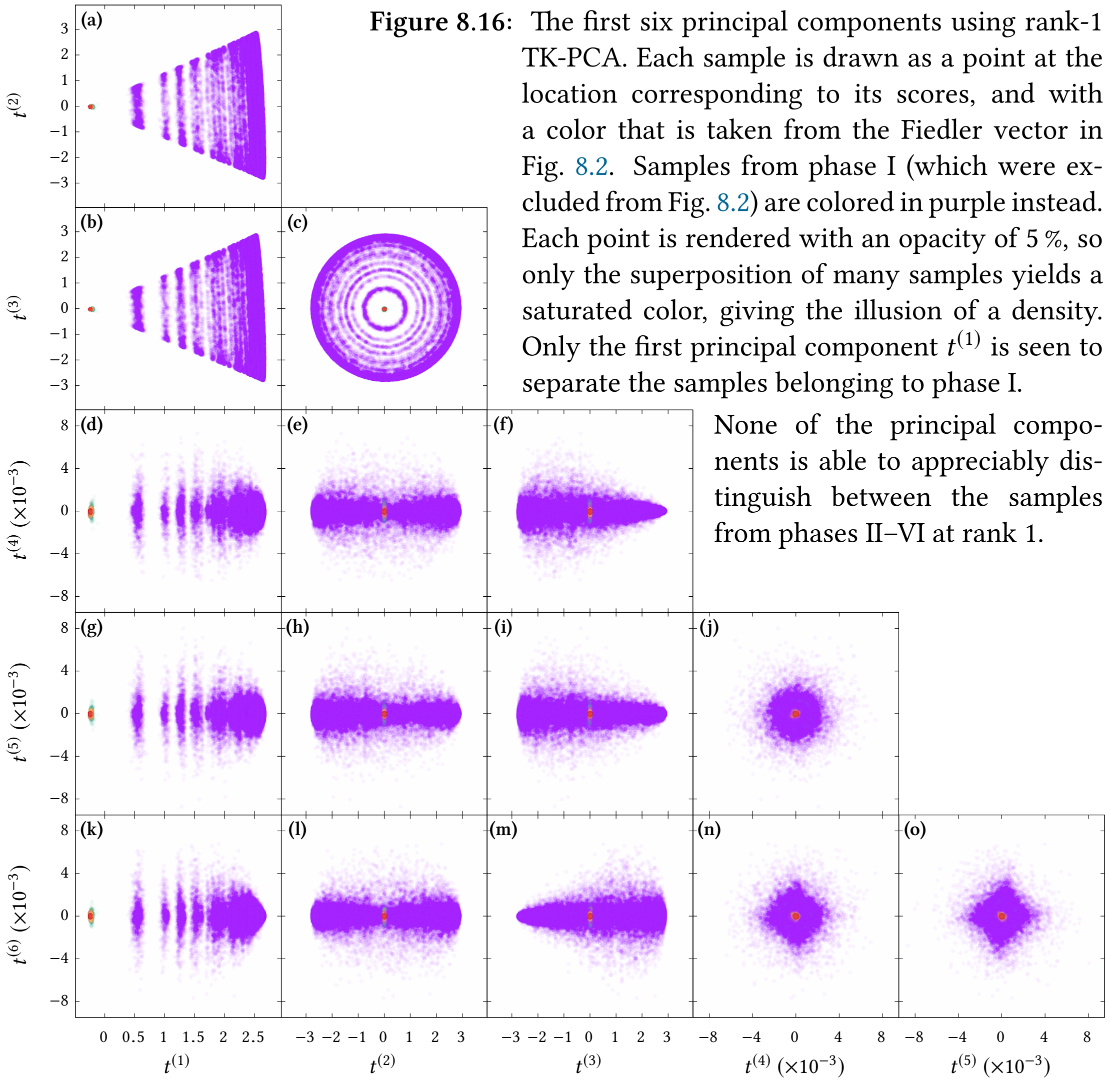

Figure 8.16: The first six principal components using rank-1 TK-PCA. Each sample is drawn as a point at the location corresponding to its scores, and with a color that is taken from the Fiedler vector in Fig. 8.2. Samples from phase I (which were excluded from Fig. 8.2) are colored in purple instead. Each point is rendered with an opacity of 5 %, so only the superposition of many samples yields a saturated color, giving the illusion of a density. Only the first principal component $t^{(1)}$ is seen to separate the samples belonging to phase I. None of the principal components is able to appreciably distinguish between the samples from phases II–VI at rank 1.

Sec. 4.1.2, kPCA requires the diagonalization of the $N_s \times N_s$ kernel matrix. For the $N_s = 246\,500$ training samples which were used from all over the parameter space, the kernel matrix would require almost 500 GB of memory. For this reason, only a subset of 5 % of all samples was used for training. One can then use the result to calculate the scores for all samples with respect to these principal components according to Eq. (4.28).

Once again, the natural starting point of the analysis is to apply the tensorial kernel at rank 1 on a tetrahedral spin cluster. In Fig. 8.16, the scores of the first six principal components are plotted between each pair. Each sample is color-coded according to the color that was assigned to the location in the phase diagram, Fig. 8.2, at which it was sampled from, based on the Fiedler vector obtained through the graph analysis in Sec. 8.1. The exception to the rule are the samples from phase I which are colored purple instead. Note that the purpose of this

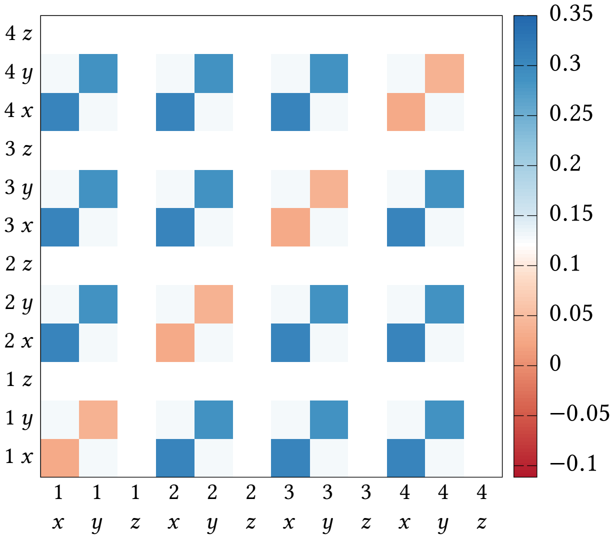

Figure 8.17: The coefficient matrix $C^{(1)}_{\alpha,a;\beta,b}$ corresponding to the first principal component obtained from the rank-1 TK-PCA treatment using a tetrahedral spin cluster.

color-coding is to compare the capabilities of TK-PCA with those of TK-SVM; in an unbiased study, this information would not be available *a priori*.

In agreement with the finds of TK-SVM, no distinction among the samples belonging to phases II–VI can be drawn at rank 1. Consequently, the scores of corresponding (nonpurple) samples collapse onto a single point in all panels of Fig. 8.16. Meanwhile, the samples from phase I are seen to scatter around the other ones with respect to all principal components but the first. Indeed, the first principal component does serve to distinguish the samples from phase I which consistently exhibit larger scores $t^{(1)}$. Thus, $t^{(1)}$ may be thought of as an order parameter with respect to phase I.

Note that the panels in Fig. 8.16 which involve the first three principal components exhibit stripy patterns and concentric circles. This can be attributed to the fact that the samples originate from a regular grid in the parameter space of the phase diagram. For the purpose of identifying phases based on the formation of clusters in the principal components, it would therefore have been advisable to sample the parameter space from a uniform random distribution to avoid such artifacts.

Since the tensorial kernel is based on a quadratic kernel, the scores admit to interpretation by rewriting them in a quadratic form with respect to the monomial features, *cf.* Eq. (4.29). The coefficient matrix may then be extracted according to Eq. (4.33). Doing so for the first principal component using rank-1 TK-PCA, yield Fig. 8.17. A striking resemblance to Fig. 8.7 is immediately apparent. Note that the color scale is however shifted, such that white is offset from the zero position. This discrepancy between Figs. 8.7 and 8.17 can be attributed to the centralization of the kernel, *cf.* Eq. (4.25), (and hence implicitly the features) and does neither bear any further physical relevance, nor does it impede one's ability to infer the analytic expression from the coefficient matrix.

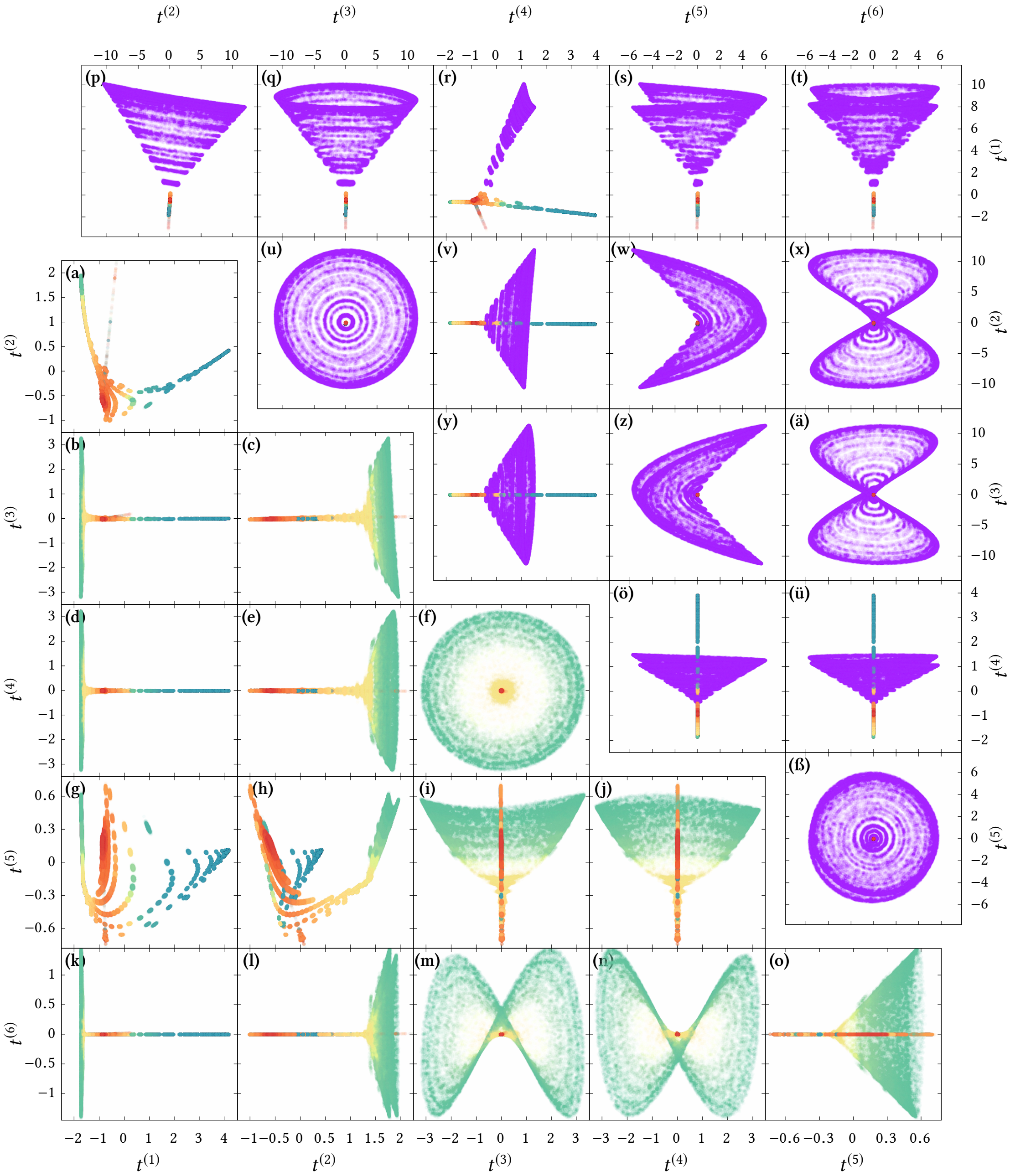

Figure 8.18: The first six principal components using rank-2 TK-PCA. The same color coding as in Fig. 8.16 is used. In the upper triangle, panels (a)–(o), all samples are taken into account and the covariance among those from phase I is seen to dominate. The latter are excluded from the analysis in the lower triangle, panels (p)–(ß), where the principal components are seen to capture some of the characteristics of the other phases. In particular, $t^{(1)}$ is sensitive towards the spin ice phase (V; blue) and $t^{(2)}$ towards the biaxial nematic phase (IV; green).

Moving on, one may subject the data to a similar analysis at rank 2. The scatter plots of the scores with respect to the most important principal components are shown in Figs. 8.18(p)–(ß). Once again, the samples from phase I (drawn in purple) seem to dominate, which was also the case in the TK-SVM treatment at rank 2. However, at least the principal components $t^{(1)}$ and $t^{(4)}$ seem capable of discerning between some of the samples from phases II–VI, while the other ones again map those samples to the same score.

As was the case in the TK-SVM treatment, the overwhelming presence of the samples from phase I may be combated by identifying them based on the (relatively unambiguous) rank-1 analysis and explicitly excluding them from the further analysis at rank 2. The resulting PCA can thus focus on the distinction between the remaining samples which was previously impossible at rank 1. It is shown in Figs. 8.18(a)–(o).

Somewhat strikingly, the samples from the biaxial nematic phase (BSN, a.k.a. phase IV, rendered in green) are seen to be predominantly (but not exclusively) singled out. Intuitively, this makes sense as it represents the only symmetry-breaking phase other than the easy-axis antiferromagnet (phase I). Indeed, in panel 8.18(f), the principal components $t^{(3)}$ and $t^{(4)}$ are seen to separate the point cloud belonging to the BSN phase from all the other points, including the uniaxial spin liquid (USL, a.k.a. phase III, yellow points), with a gap in-between, marking a jump (or sharp rise) in the associated quantity. However, neither $t^{(3)}$, nor $t^{(4)}$ distinguish the BSN samples on their own; rather, they form a circle. Hence, the quantities that distinguishes the BSN phase is given by the radius $\sqrt{(t^{(3)})^2 + (t^{(4)})^2}$. In contrast, in panel 8.18(a), $t^{(2)}$ can be seen to map the samples from the BSN (and to a lesser extent those from the USL phase) to larger values than most of the remaining samples. $t^{(1)}$ does the same with respect to the samples from the spin ice phase (SI, a.k.a. phase V, blue points).

To corroborate these observations, one again turns to the corresponding coefficient matrices. Fig. 8.19 shows part of the coefficient matrices of the two most relevant principal components. In $C^{(1)}_{\mu\nu}$, panel (a), the Q_{z^2} component is seen to constitute the dominant contribution in each block. The coefficient matrix is reminiscent of that obtained for the TK-SVM decision function distinguishing the spin ice phase from the trivial paramagnet, *cf.* Fig. 8.10. Likewise, the coefficient matrix corresponding to the second principal component, Fig. 8.19(b), bears resemblance to the coefficient matrix $C_{\mu\nu}(\mathrm{IV} \mid T_\infty)$ depicted in Fig. 8.8. Both of these interpretations are consistent with the observations of the previous paragraph based on the scores.

Also the next couple of principal components admits interpretation: $t^{(3)}$ manifests the ordering component Q_{xy+yx} while $t^{(4)}$ yields $Q_{x^2-y^2}$. In light of this identification, the above observation that $\sqrt{(t^{(3)})^2 + (t^{(4)})^2}$ distinguishes the BSN samples from the USL ones is rationalized by noting that it equals the biaxial order parameter, $\left\|\mathbf{Q}^{\mathrm{B}}_{C_{2h}}\right\|$, *cf.* Eq. (8.17). The fact that Q_{xy+yx} and $Q_{x^2-y^2}$ occur here as independent components which are, however, not capable to single out samples from the BSN individually, but only in conjunction via the norm, further affirms the conclusion based on the TK-SVM analysis that the order parameter is given by $\mathbf{Q}^{\mathrm{B}}_{C_{2h}}$.

To conclude, this section has demonstrated that the tensorial kernel can also be combined with kPCA, resulting in an unsupervised scheme for the exploratory analysis of multipolar spin order and classical spin liquids. This allows one to forgo the additional step of the graph analysis. The principal components were seen to capture roughly the same quantities as their TK-SVM counterparts and the tensorial kernel admits the same level of interpretability. This

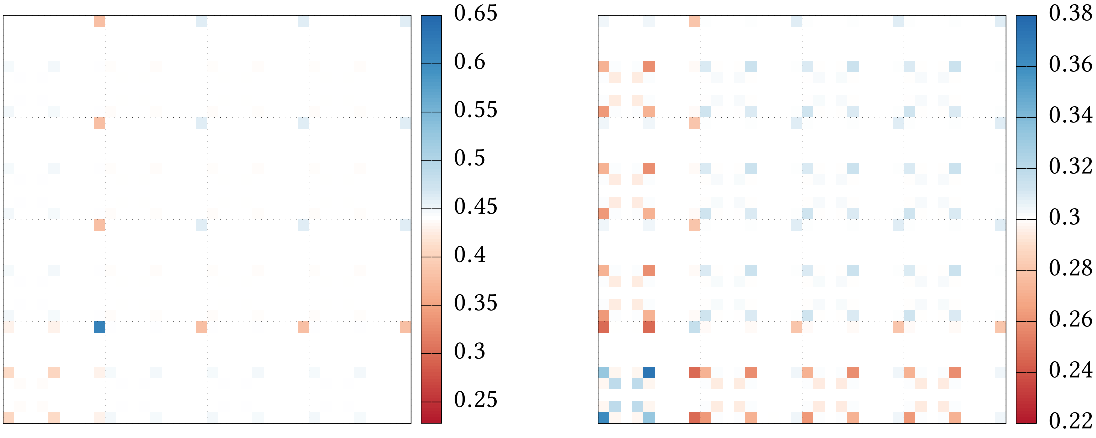

(a) first principal component, $C^{(1)}_{\mu\nu}$ **(b)** second principal component, $C^{(2)}_{\mu\nu}$

Figure 8.19: Coefficient matrices corresponding to the two most relevant principal components as obtained from rank-2 TK-PCA using a tetrahedral spin cluster and excluding samples from phase I. In both cases, only a representative cutout of 16 blocks is shown, including one on-site block, six "cross"-type blocks, and nine "bond"-type blocks. Note that the color scale is chosen in such a way that it is centered on the "background" elements. This shift from the zero position is an artifact of the centralization of the kernel matrix, *cf.* Eq. (4.25).

not only allows for the extraction of analytic order parameters, but also carries over to the identification of emergent constraints, as also the ratios between the different types of blocks are recovered. That being said, inferring the unknown phase diagram solely based on the clustering of the principal component scores would be a challenging endeavor. In fact, based on the results presented in this section, one would only be able to discern the BSN and the easy-plane antiferromagnet, while the samples from different regions of the phase diagram which are connected by crossovers unsurprisingly do not separate into recognizable clusters.

Before closing this section, some more results are given in relation to the frequently asked question whether or not a kernel other than $K_{\text{quad}} \circ (\boldsymbol{\phi}, \boldsymbol{\phi})$, *cf.* Eq. (5.5), might be better suited. It is beyond the scope of this thesis to perform an exhaustive analysis; instead, we consider as an example the composition of the monomial feature map with the RBF Kernel, Eq. (4.13) with $\varepsilon = 10$, which is the default choice for kernel methods in the machine learning community, $K_{\text{RBF}} \circ (\boldsymbol{\phi}, \boldsymbol{\phi})$.

Fig. 8.20 shows the resulting principal components. In almost all cases, the spin ice and uniaxial spin liquid phases as well as the cooperative and trivial paramagnet show up as distinct "tentacles". Conversely, the samples from the BSN phase collapse onto a narrowly confined region in all cases; in some, even to a single point. This is in stark contrast with the observations of Fig. 8.18 and no explanation of this is apparent.

Unlike the quadratic kernel, the RBF kernel does not admit to rewriting as a quadratic form, or a similarly accessible analytical expression. Indeed, the sum over the training samples

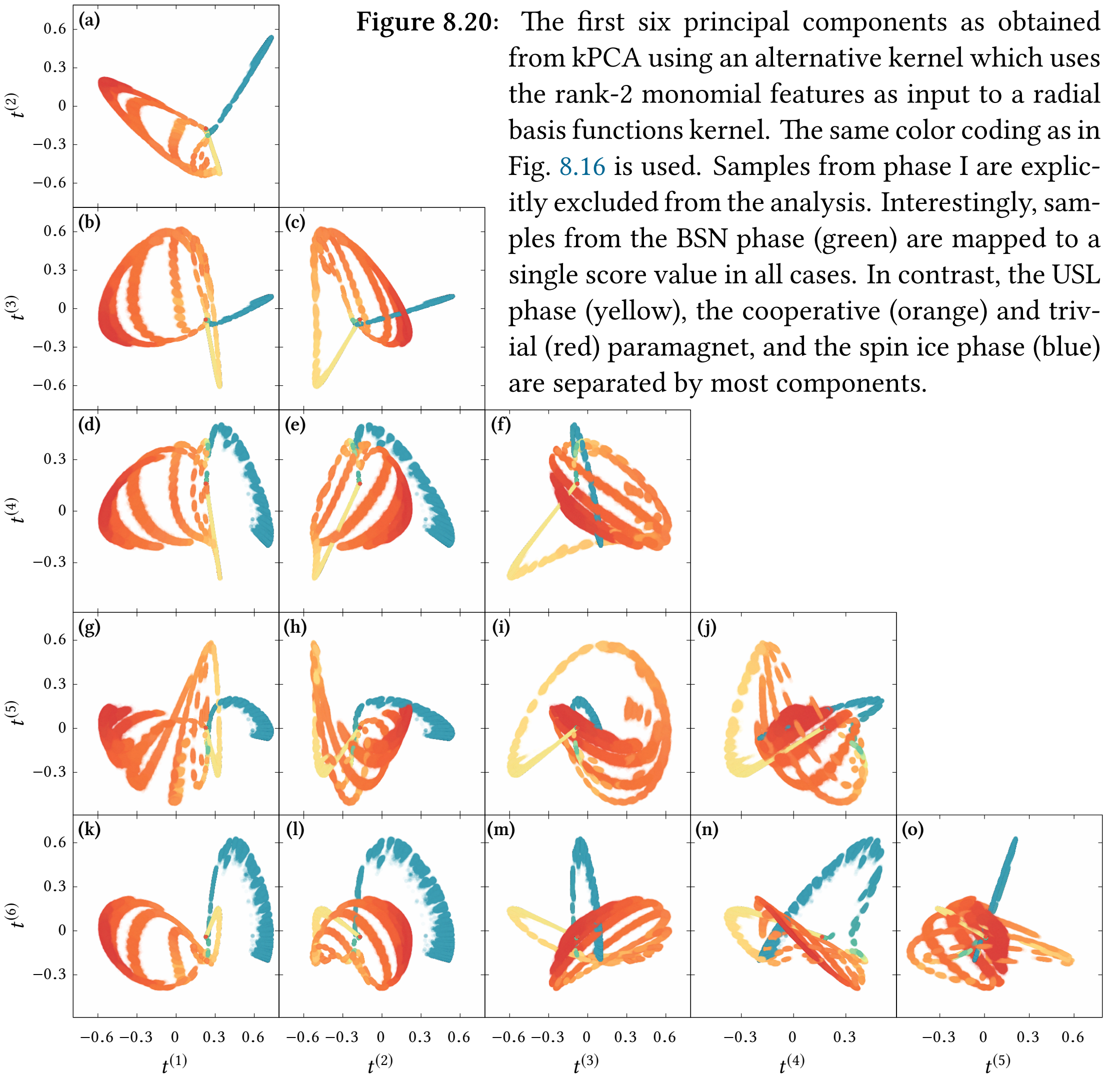

Figure 8.20: The first six principal components as obtained from kPCA using an alternative kernel which uses the rank-2 monomial features as input to a radial basis functions kernel. The same color coding as in Fig. 8.16 is used. Samples from phase I are explicitly excluded from the analysis. Interestingly, samples from the BSN phase (green) are mapped to a single score value in all cases. In contrast, the USL phase (yellow), the cooperative (orange) and trivial (red) paramagnet, and the spin ice phase (blue) are separated by most components.

in Eqs. (5.6) and (4.29) cannot be carried out before the argument of the decision function or component score is specified. Without the particular choice of the quadratic kernel, the method thus loses its interpretability; at the same time, the decision function or component score can no longer be expected to probe the linear space spanned by the basis tensors exhaustively. The remaining utility of the method would lie in identification of phases based on the kPCA scores alone. This would be difficult to pull off in a systematic way based on the plots in Fig. 8.20. Nonetheless, in the view of this author, the resulting plots are aesthetically pleasing and evocative of Jackson Pollock.

9

Kagome Heisenberg antiferromagnet

The second case study on the application of the TK-SVM method concerns itself with the antiferromagnetic Heisenberg model on the kagome lattice. The history of this model is of great relevance for the study of hidden order and was touched upon in Ch. 2. The reason for this lies in the simultaneous occurrence of hidden order at different ranks, a feature that is absent from the XXZ model on the pyrochlore model discussed in the previous chapter where the entirety of the phase diagram could be characterized by dipolar or quadrupolar order parameters.

The data for training and measurement of the TK-SVM decision functions is generated once more from classical Monte Carlo simulations. In order to reach extremely low temperatures of $T = 10^{-5}J$, a combination of the heat-bath algorithm, global O(3) rotoreflections, overrelaxation, and parallel tempering was used, all of which are described in Ch. 3. To facilitate parallel tempering acceptance, 64 temperatures, equidistant on a logarithmic scale between $T/J = 10^{-5}$ and 10, were simulated in parallel and 1000 independent spin configuration snapshots taken at each temperature. Another 21 temperatures between $T/J = 10$ and 1000 were simulated without the use of parallel tempering, resulting in a total number of configuration samples of 85 000. A lattice of 3072 spins (32×32 unit cells, each containing three spins) was used.

The remainder of this chapter follows the same methodology as the previous one. We will begin by inferring the phase diagram systematically. This will already expose certain distinctive features owing to the coexistence of order parameters of different ranks, as well as the presence of a constraint. Sec. 9.2 is devoted to the detailed analysis of said constraint. It will revisit some of the contents of Sec. 8.2.3 and give an elaborate derivation of the associated order parameter. The remaining two sections discuss the quadrupolar and octupolar order at low temperature, respectively.

9.1 Phase diagram

As before, the distillation of the phase diagram constitutes the first step of the analysis. Unlike in the previous cases where the parameter space was two dimensional, here only the temperature is tuned.

Both quadrupolar and octupolar orders are anticipated, so the TK-SVM is trained for ranks 2 and 3 separately. Additionally, two different choices of the spin cluster are considered: a single-spin cluster and a three-spin cluster corresponding to the unit cell of the kagome lattice, encompassing a triangular plaquette. The training data are labeled according to the 85 temperatures, resulting in a multiclassification problem.

Before performing the spectral clustering analysis, the statistics of the distribution of the biases of each of the 3570 resulting decision functions are inspected; *cf.* Tab. 9.1. As previously observed in Fig. 8.3, the distributions are extremely left-skewed and leptokurtic. Hence, median and interquartile range (IQR) characterize them more truthfully compared to median and standard deviation (root mean square, RMS). Strikingly, the case of the rank-2 treatment using the three-spin triangular cluster deviates from the other three cases in that the median is significantly off from the value one and the interquartile range is larger by a factor of around five. This anomaly already hints that this case is qualitatively different from the other three; the reason will become clear in the ensuing discussion.

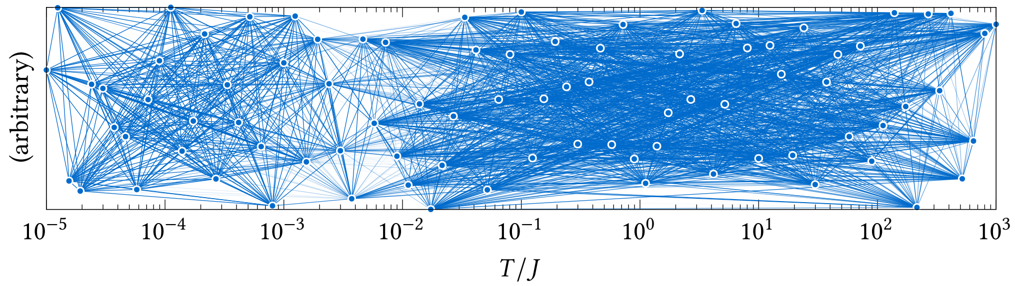

(a) single-spin cluster, rank-2

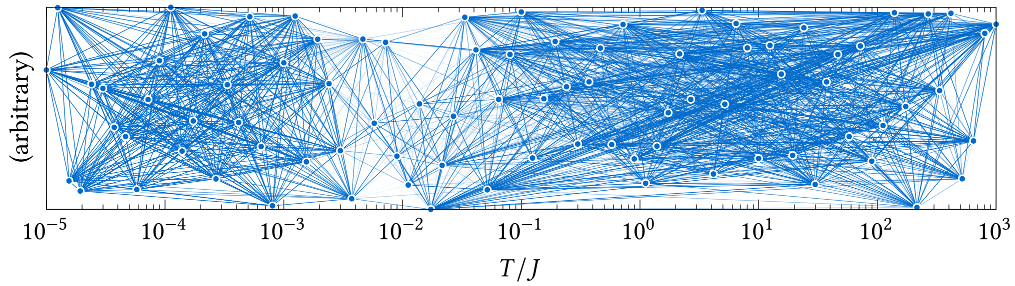

(b) single-spin cluster, rank-3

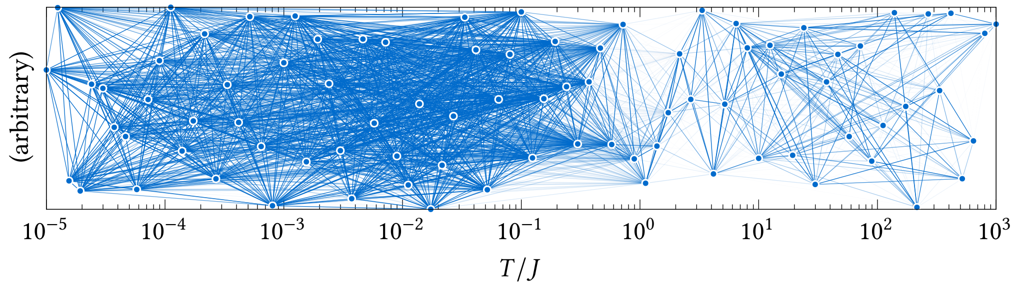

(c) three-spin triangular cluster, rank-2

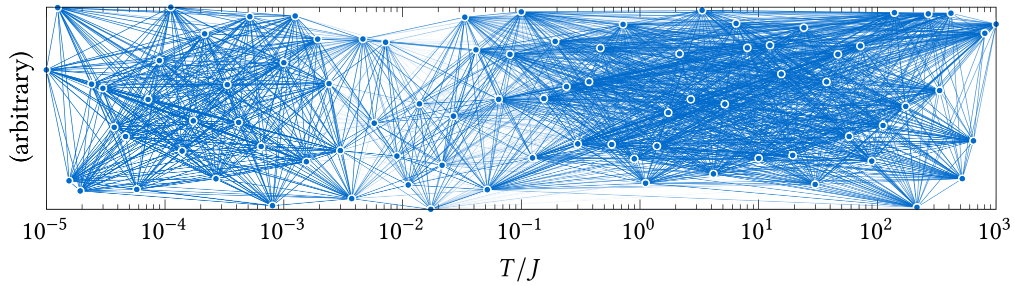

(d) three-spin triangular cluster, rank-3

Figure 9.1: The weighted graphs based on the biases resulting from the four multiclassifications considered (two cluster choices; ranks 2 and 3). Since the phase diagram is one-dimensional, each vertex is assigned a random second coordinate such that the graph does not collapse onto a single line.

Cluster	single spin		triangle	
Rank	2	3	2	3
Mean	9.44	17.9	199	10.6
Median	1.010	1.028	1.596	1.002
RMS	107	173	5811	183
IQR	0.611	0.782	3.25	0.548

Table 9.1: Statistics of the distribution of the SVM biases for four different sets of multiclassifications using a single-spin and triangular three-spin cluster, respectively, with TK-SVM at ranks two and three. The distributions are highly left-skewed and leptokurtic.

For each of the four multiclassification problems, the weighted graph is constructed from the biases in accordance with the general procedure laid out in Ch. 7. Again, the Lorentzian weighting function, Eq. (7.1), was used to map SVM biases to graph edge weights. The characteristic scale, ρ_c, has been chosen as half of the interquartile range of the respective distribution as given in Tab. 9.1.

The resulting graphs are depicted in Fig. 9.1. One observes that each graph features two temperature regimes where vertices are densely intraconnected, while the regimes are sparsely interconnected. However, the rank-2 treatment of the triangular cluster [panel (c)] again deviates from the other three cases in the location of the crossover between these regimes.

This becomes more visible from the Fiedler vector of these graphs. In Fig. 9.2, the elements of the Fiedler vector in all four cases are seen to follow a sigmoid curve, attaining relatively constant values at low and high temperature, respectively. The crossover in between is comparable in width in all four cases and extends over roughly one order of magnitude in temperature. The rank-3 treatment in fact produces the same curve for both the single-spin and triangular spin clusters, indicating that a rank-3 order parameter is present which can in turn be defined for a single spin and that its representation on the larger cluster is redundant. At rank 2, a qualitatively different behavior is observed: the single-spin cluster TK-SVM reveals the presence of a rank-2 order parameter which exhibits a crossover at roughly the same (or slightly lower) temperature as the rank-3 order parameter. In contrast, on the triangular cluster a crossover is observed at a much higher temperature between $T/J = 1$ and 10.

In the next section, it will become apparent that rank-2 TK-SVM captures a constraint on the three spins in the triangular cluster which comes into force at relatively high temperatures. This explains why different behavior is observed when using the single-spin cluster which cannot realize such a constraint. Instead, it captures the quadrupolar order parameter. As will be seen in Sec. 9.3, that same quadrupolar order parameter is still learned when using the triangular cluster. Upon closer inspection, the Fiedler vector is in fact not perfectly constant throughout the temperature range from 10^{-5} to 10^{-1}, but exhibits a tiny secondary step in agreement with the quadrupolar transition. Hence, the order parameter capturing the

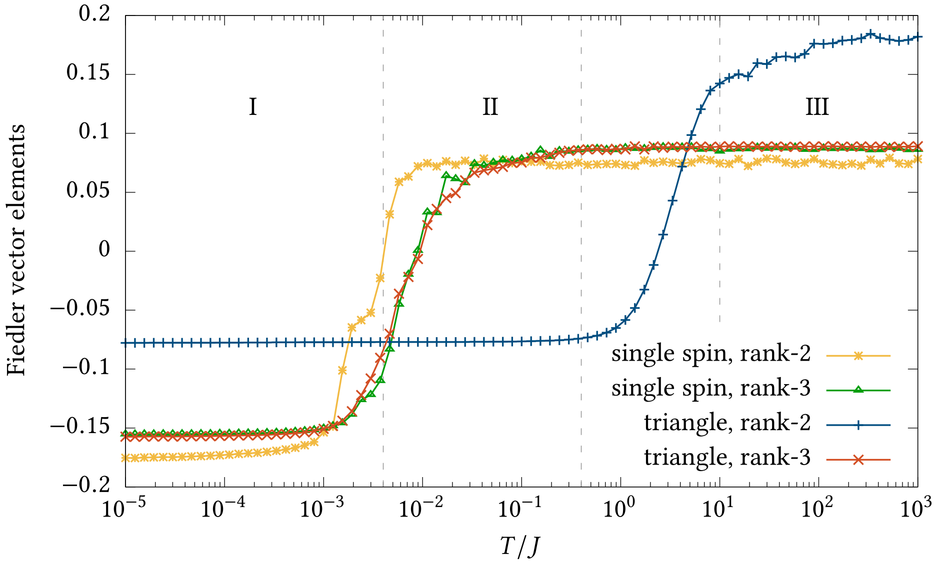

Figure 9.2: The entries of the Fiedler vector are plotted against their corresponding temperature for each of the four multiclassification problems considered. The rank-3 cases are seen to produce the same qualitative curve, independent of the choice of spin cluster. At rank 2, a similar curve is also obtained when using a single-spin cluster, manifesting the simultaneous occurrence of quadrupolar and octupolar order at the transition temperature $T_K = 0.004J$. When using the triangular spin cluster, a constraint among the spins on the triangle is captured. The associated crossover into the regime of constraint dynamics roughly takes place between temperatures 0.4 and 10. The dashed lines indicate the boundaries of these regimes which are labeled by roman numerals.

constraint is apparently overpowering the signature of the quadrupolar order for the purposes of the spectral graph partitioning.

Regardless, the combined results allow for a suitable partition of the phase diagram. Since both the quadrupolar and octupolar order are seen to appear at a temperature that is consistent with the value of $T_K = 0.004J$ proclaimed by Zhitomirsky [82], this value will be used to distinguish the regimes labeled I and II. The subsequent measurement of the order parameters in Secs. 9.3 and 9.4 will confirm the validity of this choice. Regime II extends up until the onset of the crossover is observed. The samples in the interim of the crossover between temperatures 0.4 and 10 are discarded from the subsequent analysis, similar to the procedure in Sec. 8.1.3. Finally, the temperatures above 10 are designated regime III. This sets up a reduced multiclassification problem which relabels the training data according to regimes I (28 000 samples), II (21 000 samples), and III (21 000 samples). Additionally, 25 000 fictitious independent isotropic spin configurations corresponding to infinite temperature ("T_∞") are included as a control group.

The SVM biases resulting from the reduced multiclassification problems are given in Tab. 9.2. Not at all surprisingly, the high-temperature regime III yields qualitatively the same behavior

Cluster	single spin		triangle	
Rank	2	3	2	3
I | II	−1.0131	−1.0131	−3.286	−1.0145
I | III	−1.0121	−1.0041	−1.0035	−1.0026
I | T_∞	−1.0129	−1.0044	−0.9928	−1.0028
II | III	10.63	−0.9592	−1.0260	−1.0691
II | T_∞	4.218	−1.0598	−1.0103	−1.0805
III | T_∞	2.158	−1285	−20.54	−1.9802

Table 9.2: TK-SVM biases obtained from the reduced multiclassification problems among the temperature regimes I ($T/J = 10^{-5} \ldots 0.004$), II ($0.004 \ldots 0.4$), and III ($10 \ldots 1000$), as well as the fictitious control group, T_∞.

as the control group (T_∞) and is not readily distinguishable therefrom. When probing the regimes I and II, *i.e.* across the transition temperature T_K, only the triangular cluster at rank 2 gives a bias that is significantly different from one, in line with the fact that the bias argument (*cf.* Sec. 5.3) is invalidated by the simultaneous presence of a constraint. Conversely, the triangular cluster allows for the distinction of regimes II and III by realizing the constraint which is not possible when using the single-spin cluster at rank 2. Perhaps surprisingly, at rank 3 the single-spin cluster does seem capable of distinguishing II and III. This can be attributed to finite-size effects: a residual finite magnetization (in itself a vector quantity) is detectable at odd ranks while it cancels for even ranks. This becomes apparent from the corresponding decision function curve which has a small, finite slope throughout the crossover regime, but lacks any distinct feature therein.

9.2 Emergent constraint

We will now focus on the constraint whose signature is manifest in rank-2 TK-SVM using the triangular spin cluster. The corresponding coefficient matrix of the decision function distinguishing regime II from random spins (T_∞) is shown in Fig. 9.3. It is immediately apparent that this pattern bears resemblance to the one depicted in Fig. 8.11 in the previous chapter which was found to encode the isotropic constraint in the Heisenberg limit. Hence, one may already conclude that a crossover into a cooperative paramagnet, defined by the analogous constraint $\mathbf{S}^{(1)}+\mathbf{S}^{(2)}+\mathbf{S}^{(3)} = \mathbf{0}$ for the three spins on the corners of each triangular plaquette, takes place. In contrast to the four spins on the tetrahedra of the pyrochlore lattice, three spins can only sum to zero if they lie in the same plane. The constraint thereby imposes a 120° state (*cf.* Sec. 2.1.1).

Rather than leaving it at that, the coefficient matrix will be decoded explicitly and it will be shown that the decision function is indeed related to the order parameter defined for the

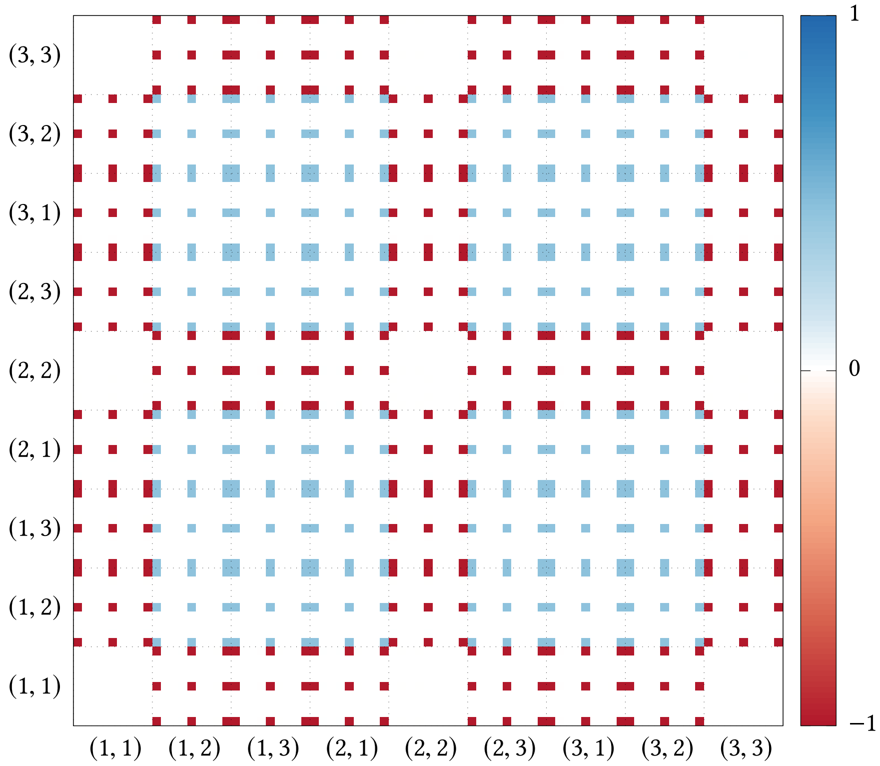

Figure 9.3: Coefficient matrix $C_{\mu\nu}(\mathrm{II}\,|\,T_\infty)$ learned from rank-2 TK-SVM on a three-spin triangular cluster. The dotted lines demarcate 9×9 blocks corresponding to identical sublattice indices $(\alpha, \beta), (\alpha', \beta')$; while the contents of each 9×9 block are enumerated in a similar way by component indices $(a, b), (a', b')$. On-site blocks $(\alpha = \beta, \alpha' = \beta')$ are seen to be empty, while "cross" and "bond" blocks exhibit a nonvanishing $\delta_{ab}\delta_{a'b'}$ pattern with relative weights of -1 and $-\gamma = 0.446$, respectively.

isotropic constraint,

$$\Gamma_{xyz} := 1 - \frac{1}{N_b} \left\langle \left\| \sum_\alpha \mathbf{S}^\alpha \right\|^2 \right\rangle_{\mathrm{cl}}, \tag{9.1}$$

where $N_b = 3$ designates the number of spins in the crystallographic basis (*cf.* Eq. 8.34 where $N_b = 4$ for the pyrochlore lattice).

The coefficient matrix is composed of 9×9 blocks which can be enumerated by sublattice indices $[\alpha, \beta; \alpha'\beta']$. It is once again useful to distinguish three types of blocks which appear in Fig. 9.3: "on-site" blocks for which $\alpha = \beta$ and $\alpha' = \beta'$, "bond" blocks ($\alpha \neq \beta$, $\alpha' \neq \beta'$), and the mixed "cross" blocks. Each of the nonvanishing blocks exhibits the same pattern of nine elements in the locations satisfying $a = b$ and $a' = b'$. These are the exact elements which

		$p[Q_{x^2+y^2+z^2}]$	$p[Q_{z^2}]$	$p[Q_{x^2+y^2}]$	$p[Q_{x^2-y^2}]$	$p[Q_{xy+yx}]$	$p[Q_{yz+zy}]$	$p[Q_{zx+xz}]$
I | II	on-site	−0.487	1.460	0.731	0.732	0.733	0.727	0.735
	cross	0.081	−0.730	−0.366	−0.366	−0.367	−0.363	−0.367
	bond	0.038	0.365	0.183	0.183	0.183	0.182	0.184
I | T_∞	on-site	0.059	−0.176	−0.088	−0.088	−0.088	−0.088	−0.088
	cross	0.910	0.089	0.044	0.044	0.044	0.044	0.044
	bond	−0.462	−0.044	−0.022	−0.022	−0.022	−0.022	−0.022
II | T_∞	on-site	0.000	0.000	0.000	0.000	0.000	0.000	0.000
	cross	−0.998	−0.001	0.000	0.000	0.000	0.000	0.000
	bond	0.445	−0.001	0.000	0.000	0.000	0.000	0.000

Table 9.3: The weights of the tentative quadrupolar ordering components, $p[Q_\bullet]$, are tabulated for the three classifiers distinguishing between regimes I, II, and III (here, the perfectly decorrelated control group is used instead). These weights were obtained through a least-squares fit based on all blocks in the full coefficient matrix of each of the site-site ("on-site"), site-bond ("cross"), and bond-bond ("bond") types. The ratios between these weights for the three block types are given in Tab. 9.4.

produce the intrinsic spin normalization constraint in on-site blocks which leads to them being exactly canceled by self-contractions there. Meanwhile, the weight of the contributions in bond blocks differs from that in cross blocks by a factor of $\gamma < 0$. Hence, one may express the weight of block $[\alpha\beta, \alpha'\beta']$ by $(\gamma + \bar{\gamma}\delta_{\alpha\beta})(\gamma + \bar{\gamma}\delta_{\alpha'\beta'}) - \delta_{\alpha\beta}\delta_{\alpha'\beta'}$ where $\bar{\gamma} := 1 - \gamma$. Plugging this into the decision function, Eq. (5.6), yields (up to an affine rescaling, denoted by the tilde):

$$d(\{\mathrm{S}_i\}) \sim \sum_{\substack{\alpha,\beta\\ \alpha',\beta'}} \sum_{\substack{a,b\\ a',b'}} \left[(\gamma + \bar{\gamma}\delta_{\alpha\beta})(\gamma + \bar{\gamma}\delta_{\alpha'\beta'}) - \delta_{\alpha\beta}\delta_{\alpha'\beta'}\right] \delta_{ab}\delta_{a'b'} \left\langle S_a^\alpha S_b^\beta \right\rangle \left\langle S_{a'}^{\alpha'} S_{b'}^{\beta'} \right\rangle \tag{9.2}$$

$$= \left(\sum_{\alpha\beta} \sum_a (\gamma + \bar{\gamma}\delta_{\alpha\beta}) \left\langle S_a^\alpha S_a^\beta \right\rangle \right)^2 - \left(\sum_\alpha \sum_a \left\langle S_a^\alpha S_a^\alpha \right\rangle \right)^2 \tag{9.3}$$

$$= \left(\gamma \left\langle \sum_a \left(\sum_\alpha S_a^\alpha \right)^2 \right\rangle + \bar{\gamma} \sum_\alpha \left\langle \sum_a \|\mathrm{S}^\alpha\|^2 \right\rangle \right)^2 - \left(\sum_\alpha \left\langle \|\mathrm{S}^\alpha\|^2 \right\rangle \right)^2 \tag{9.4}$$

$$= \gamma^2 \left(\left\langle \left\| \sum_\alpha \mathrm{S}^\alpha \right\|^2 \right\rangle + N_b \frac{\bar{\gamma}}{\gamma} \right)^2 - N_b^2 \tag{9.5}$$

$$= N_b^2 \left[\gamma^2 \left(\Gamma_{xyz} - \frac{1}{\gamma} \right)^2 - 1 \right], \tag{9.6}$$

where the definition of the isotropic constraint, Eq. (9.1), has been substituted in the last line. Hence, the decision function is seen to realize a quadratic function of the constraint order parameter, $d \sim (\Gamma_{xyz} - 1/\gamma)^2$.

		$\gamma_{x^2+y^2+z^2}$	γ_{z^2}	$\gamma_{x^2+y^2}$	$\gamma_{x^2-y^2}$	γ_{xy+yx}	γ_{yz+zy}	γ_{zx+xz}
I | II	c ÷ s	−0.166	−0.500	−0.500	−0.500	−0.500	−0.500	−0.500
	b ÷ c	0.471	−0.500	−0.500	−0.500	−0.500	−0.500	−0.500
I | T_∞	c ÷ s		−0.504	−0.499	−0.502	−0.502	−0.502	−0.502
	b ÷ c	−0.508	−0.492	−0.495	−0.493	−0.493	−0.493	−0.493
II | T_∞	b ÷ c	−0.446						

Table 9.4: Ratios of the quadrupolar moments, $\gamma_\bullet := \left\langle Q_\bullet^{\alpha\beta}\right\rangle / \langle Q_\bullet^{\alpha\alpha}\rangle$. These can be calculated by taking the ratio between the weights of the relevant component with respect to "cross" and "on-site" blocks (c ÷ s), or "bond" and "cross" blocks (b ÷ c). The weights of the ordering components themselves were calculated through a least-squares fit to the coefficient matrix and given in Tab. 9.3.

To systematically find the value of γ in the kagome system, one follows the same approach as in Sec. 8.2.2 for the pyrochlore model by least-squares-fitting the isotropic ordering component $Q_{x^2+y^2+z^2}$, Eq. (8.9), as represented by the pattern $\mathscr{A}[Q_{x^2+y^2+z^2}]$, Eq. (8.5), to each of the blocks. The thus found corresponding component weights are tabulated in Tab. 9.3. The ratio between the isotropic components in cross and bond terms yields a value of $\gamma_{x^2+y^2+z^2} = -0.446$, see Tab. 9.4. This value was extracted from $C_{\mu\nu}(\mathrm{II}\,|\,T_\infty)$ and does not include data at temperatures below T_K. When attempting to include the latter, in addition to the pure constraint, contributions to the other ordering components due to the presence of quadrupolar order appear which need to be accounted for in the least-squares fit. In this way, one finds a value of $\gamma_{x^2+y^2+z^2} = -0.508$.

Despite the slight mismatch in the above values, one may comfortably conclude that the ideal value in case of a fully realized constraint would in fact be $\gamma = -1/2$. As previously argued in Sec. 8.2.3, the constraint requires that N_b site terms, $\langle Q^{\alpha\alpha}_{x^2+y^2+z^2}\rangle$, and $N_b(N_b-1)$ bond terms, $\langle Q^{\alpha\neq\beta}_{x^2+y^2+z^2}\rangle$, cancel. Given that their ratio is γ, one finds $\gamma = -1/(N_b-1)$, *i.e.* $-1/2$ on the kagome lattice and $-1/3$ on the pyrochlore lattice.

As shall be seen in the forthcoming sections, γ can also be computed from the ratios of the other ordering components once such an order occurs below T_K. As can be read in Tab. 9.4 for the classifier distinguishing regimes I and II, the estimate of γ obtained from any of them matches the expected value to three significant digits. To explain the superior precision in this case, recall that the decision function without additional order, Eq. (9.6), involves Γ_{xyz} regardless of the particular value of γ; thus, a small deviation in γ will not significantly impact the performance of the decision function. In contrast, when the constraint "piggybacks" on a symmetry-breaking order, γ will be seen to enter the resulting order parameter tensor, giving TK-SVM less leeway in determining the relative weight of the blocks.

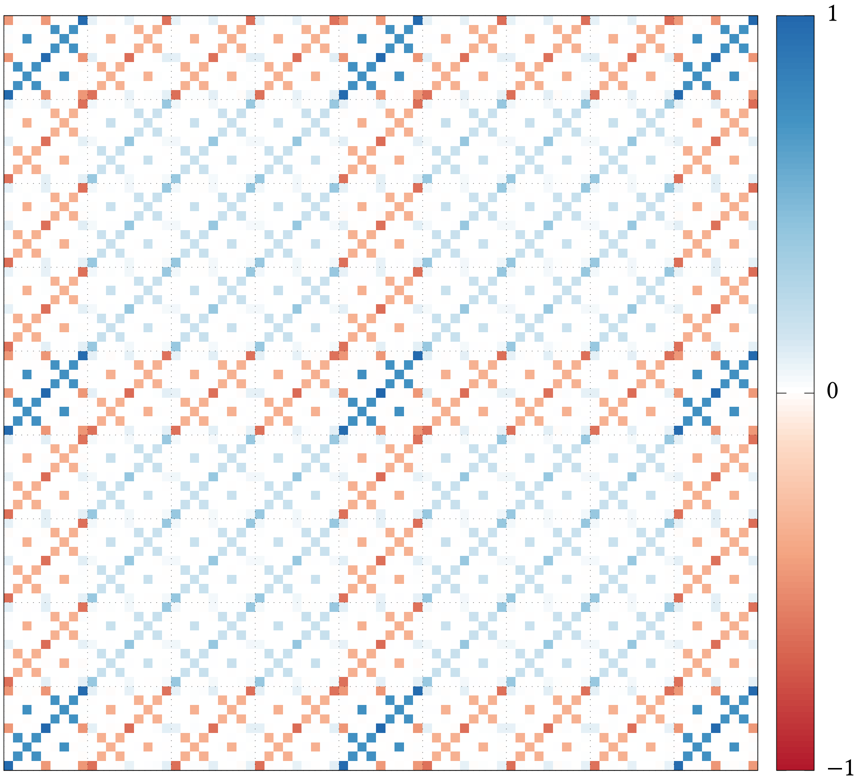

Figure 9.4: Coefficient matrix $C_{\mu\nu}(\mathrm{I}\,|\,\mathrm{II})$ learned from rank-2 TK-SVM on a three-spin triangular cluster. The dotted lines demarcate 9×9 blocks corresponding to identical sublattice indices. The same motif repeats in each block, but multiplied by a factor of $\gamma = -1/2$ on cross-type blocks and γ^2 on bond-type blocks, as compared to on-site blocks, *cf.* Tab. 9.4. This modulation encodes the constraint, in addition to the quadrupolar order parameter that is seen using a single-spin cluster.

9.3 Quadrupolar order

Whereas the Fiedler vector of the rank-2 TK-SVM using the triangular cluster predominantly signifies the onset of the emergent constraint, the analogous treatment using the single spin cluster exhibits a quadrupolar transition at the temperature T_K, as seen in Sec. 9.1.

It is therefore prudent to start the analysis of the latter by studying the single-spin coefficient matrix $C_{ab,a'b'}(\mathrm{I}\,|\,\mathrm{II})$. It is virtually indistinguishable from the one depicted in Fig. 6.1. Therefore, it is immediately clear that the corresponding quadrupolar order parameter is given by $\langle \mathbf{S} \otimes \mathbf{S} \rangle$ (where the angle brackets denote the lattice average over all spins), which is exactly the single-spin form put forth by Zhitomirsky [82], *cf.* Eq. (2.11).

Given that the quadrupolar order can be defined on a single-spin cluster, it has to manifest itself also when considering the larger, three-spin cluster, despite the ostensible absence of a signature in the graph analysis based on the biases alone. Fig. 9.4 indeed shows a highly structured coefficient matrix for the classifier distinguishing the low-temperature regimes I and II.

The same pattern as for the single-spin cluster appears in the on-site blocks. Additionally, the same motif (sans self-contractions) repeats also in cross and bond blocks, up to a factor. Resorting once again to the decomposition of the coefficient matrix in terms of the contributions of the individual quadrupolar ordering components, one finds from Tab. 9.3 that all of them occur simultaneously with coupled weights,

$$\frac{1}{2}\,p[Q_{z^2}] = p[Q_{x^2+y^2}] = p[Q_{x^2-y^2}] = p[Q_{xy+yx}] = p[Q_{yz+zy}] = p[Q_{zx+xz}], \tag{9.7}$$

$$= -\frac{3}{2}\,p[Q_{x^2+y^2+z^2}], \tag{9.8}$$

with the exception that the last equality only holds in on-site blocks where the isotropic component produces a constant due to spin normalization, whereas it is absent from cross and bond blocks[1].

Indeed, the weighted superposition of the ordering components in Eq. (9.7),

$$2\left\langle Q^{\alpha\beta}_{z^2}\right\rangle^2 + \left\langle Q^{\alpha\beta}_{x^2+y^2}\right\rangle^2 + \left\langle Q^{\alpha\beta}_{x^2-y^2}\right\rangle^2 + \left\langle Q^{\alpha\beta}_{xy+yx}\right\rangle^2 + \left\langle Q^{\alpha\beta}_{yz+zy}\right\rangle^2 + \left\langle Q^{\alpha\beta}_{zx+xz}\right\rangle^2 \tag{9.9}$$

$$= 2\sum_{a}\left\langle S^\alpha_a S^\beta_a\right\rangle^2 + \sum_{a\neq b}\left\langle S^\alpha_a S^\beta_b\right\rangle^2 + \sum_{a\neq b}\left\langle S^\alpha_a S^\beta_b\right\rangle\left\langle S^\alpha_b S^\beta_a\right\rangle \tag{9.10}$$

$$= \sum_{a,b}\left(\left\langle S^\alpha_a S^\beta_b\right\rangle\left\langle S^\alpha_b S^\beta_a\right\rangle + \left\langle S^\alpha_a S^\beta_b\right\rangle\left\langle S^\alpha_a S^\beta_b\right\rangle\right) = \mathrm{Tr}\left[XX + XX^\top\right], \tag{9.11}$$

yields a symmetric contraction over the matrix $X := \left\langle \mathrm{S}^\alpha \otimes \mathrm{S}^\beta \right\rangle$ which reduces to the familiar quadrupolar order parameter tensor on-site ($\alpha = \beta$) where both contractions become equivalent.

As mentioned already in the end of the previous section, all of the above ordering components do in fact respect the ratio $\gamma = -1/2$ between bond and cross blocks, as well as cross and on-site blocks, to high accuracy (Tab. 9.4). Adopting the shorthand $\bar{\gamma} := 1 - \gamma$ once again, the relative weight of the $[\alpha\beta, \alpha'\beta']$ block can be expressed as $(\bar{\gamma}\delta_{\alpha\beta} + \gamma)(\bar{\gamma}\delta_{\alpha'\beta'} + \gamma)$. In total, one

---

[1] As can be seen from Tab. 9.3, $p[Q_{x^2+y^2+z^2}]$ is not quite zero in cross and bond blocks of $C_{\mu\nu}(\mathrm{I}\,|\,\mathrm{II})$, but significantly less than what it would be if Eq. (9.8) were to apply. For the purpose of decoding the quadrupolar order parameter tensor in this section, it will be treated as zero. The reason for the residual weight lies in the fact that $C_{\mu\nu}(\mathrm{I}\,|\,\mathrm{II})$ (Fig. 9.4) is not pristine, but rather mixes in a small contribution due to the constraint, as represented by $C_{\mu\nu}(\mathrm{II}\,|\,T_\infty)$ (Fig. 9.3). Indeed, the same is true for $C_{\mu\nu}(\mathrm{I}\,|\,T_\infty)$ (*cf.* Tab. 9.3) which manifests a mixture of the other two cases as well.

can rewrite the decision function,

$$d(\{\mathbf{S}_i\}) \sim \frac{1}{2} \sum_{\substack{\alpha,\beta \\ \alpha',\beta'}} \sum_{\substack{a,b \\ a',b'}} (\gamma + \bar{\gamma}\delta_{\alpha\beta})(\gamma + \bar{\gamma}\delta_{\alpha'\beta'}) \left(\delta_{aa'}\delta_{bb'} + \delta_{ab'}\delta_{ba'}\right) \left\langle S_a^{\alpha} S_b^{\beta} \right\rangle \left\langle S_{a'}^{\alpha'} S_{b'}^{\beta'} \right\rangle \tag{9.12}$$

$$= \sum_{\substack{\alpha,\beta \\ \alpha',\beta'}} \sum_{a,b} (\gamma + \bar{\gamma}\delta_{\alpha\beta})(\gamma + \bar{\gamma}\delta_{\alpha'\beta'}) \left\langle S_a^{\alpha} S_b^{\beta} \right\rangle \left\langle S_a^{\alpha'} S_b^{\beta'} \right\rangle \tag{9.13}$$

$$= \sum_{a,b} \left(\sum_{\alpha,\beta} (\gamma + \bar{\gamma}\delta_{\alpha\beta}) \left\langle S_a^{\alpha} S_b^{\beta} \right\rangle \right)^2 \tag{9.14}$$

$$= \sum_{a,b} \left\langle \bar{\gamma} \sum_{\alpha} S_a^{\alpha} S_b^{\beta} + \gamma \left(\sum_{\alpha} S_a^{\alpha} \right) \left(\sum_{\beta} S_b^{\beta} \right) \right\rangle^2 \propto \mathrm{Tr}\left[\mathbb{O}_{\mathrm{quad}}^2 \right], \tag{9.15}$$

as the trace over the square of a (symmetric) order parameter matrix,

$$\mathbb{O}_{\mathrm{quad}} = \left\langle \frac{1}{3} \sum_{\alpha} \mathbf{S}^{\alpha} \otimes \mathbf{S}^{\alpha} - \left(\frac{1}{3} \sum_{\alpha} \mathbf{S}^{\alpha} \right)^{\otimes 2} \right\rangle_{\mathrm{cl}}. \tag{9.16}$$

While the first term corresponds to the single-spin quadrupolar order parameter tensor $\langle \mathbf{S} \otimes \mathbf{S} \rangle$ which is explicitly averaged over the three spins within the triangular cluster, the second term expresses the constraint as a quadrupolar tensor with respect to the total spin within the triangular plaquette.

9.4 Octupolar order

In this final section, the octupolar order parameter tensor is extracted from the coefficient matrix of the rank-3 TK-SVM decision function distinguishing between regimes I and II. As in the case of the quadrupolar order parameter, the natural starting point is once again the single-spin cluster. The resulting 27 × 27 coefficient matrix is virtually identical to Fig. 6.7(b), a block in the coefficient matrix representing the rank-3 order parameter of the T_d-symmetric gauge model, Eq. (6.12). One is thus led to conclude that in the present case, the order parameter is given by the lattice-averaged tensor product $\langle \mathbf{S} \otimes \mathbf{S} \otimes \mathbf{S} \rangle$. Indeed, this is essentially[2] the triatic order parameter given by Zhitomirsky [82], *cf.* Eq. (2.12).

Again, by choosing a larger spin cluster, one can confirm if this single-spin octupolar order parameter persists or whether a more fundamental order parameter is found. In analogy to the rank-2 case, the coefficient matrix can be partitioned into blocks which are enumerated by sublattice indices $[\alpha\beta\gamma, \alpha'\beta'\gamma']$. As was the case in the previous section, the rank-3 single-spin coefficient matrix is found to repeat within each block, but modulated with a factor. Unlike in the quadrupolar case, where the spin-normalization gave rise to the isotropic ordering component in on-site blocks only, no such discrepancy is present at rank 3, so one can forgo a composition into individual octupolar ordering components and infer the relative weights of the blocks, *e.g.* by calculating their Frobenius norm.

---

[2] The additional terms in Eq. (2.12), involving one spin component each, are merely included to render T_{abc} traceless and bear no physical relevance.

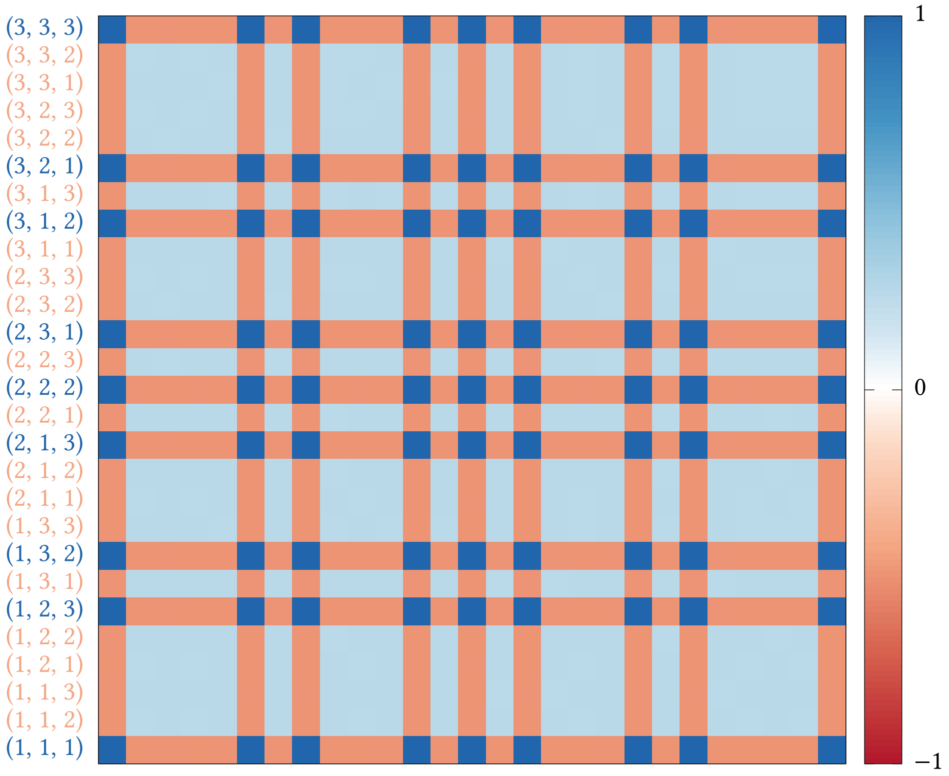

Figure 9.5: The block structure of the coefficient matrix obtained from rank-3 TK-SVM on a triangular cluster. Each of the blocks of the full coefficient matrix follows the form depicted in Fig. 6.7(b), multiplied by the block weights indicated here. Basis tensors $S^\alpha \otimes S^\beta \otimes S^\gamma$ with $\alpha = \beta = \gamma$ and $\alpha \neq \beta \neq \gamma$ are seen to contribute equally, whereas all others are diminished by by a factor of $\gamma = -1/2$.

The resulting block structure is shown in Fig. 9.5; the full coefficient matrix is not shown as it does not add further information. Similar to the ratio γ between on-site ($\alpha = \beta$) and bond terms ($\alpha \neq \beta$) in the quadrupolar order parameter, here one observes a similar situation were the same weight is observed in on-site terms ($\alpha = \beta = \gamma$) and those defined on all three spins in the cluster ($\alpha \neq \beta \neq \gamma$), but a different weight is observed for terms involving only two distinct spins (*e.g.* $\alpha = \beta \neq \gamma$). The ratio between these types of blocks is again $\gamma = -1/2$. As will become apparent, it is again expressing the isotropic constraint. Indeed, since there are $3 + 6 = 9$ terms of the former type, but 18 terms of the latter type, a ratio of $\gamma = -1/2$ between them will ensure that the sums over all of them cancels, and, thus,

$$0 = \sum_{\alpha,\beta,\gamma} \left\langle S^\alpha \otimes S^\beta \otimes S^\gamma \right\rangle = \left(\sum_\alpha S^\alpha \right)^{\otimes 3}. \tag{9.17}$$

By a similar calculation to the one in Eqs. (9.12)-(9.16), one arrives at the following octupolar order parameter tensor:

$$\mathbb{O}_{\mathrm{oct}} = \frac{2}{27} \sum_{\alpha,\beta,\gamma} \left[\frac{3}{2}(\delta_{\alpha\beta\gamma} + |\varepsilon_{\alpha\beta\gamma}|) - \frac{1}{2} \right] \left\langle \mathrm{S}^{\alpha} \otimes \mathrm{S}^{\beta} \otimes \mathrm{S}^{\gamma} \right\rangle_{\mathrm{cl}} \tag{9.18}$$

$$= \left\langle \frac{1}{9} \left[\sum_{\alpha} (\mathrm{S}^{\alpha})^{\otimes 3} + \sum_{\alpha \neq \beta \neq \gamma} \mathrm{S}^{\alpha} \otimes \mathrm{S}^{\beta} \otimes \mathrm{S}^{\gamma} \right] - \left(\frac{1}{3} \sum_{\alpha} \mathrm{S}^{\alpha} \right)^{\otimes 3} \right\rangle_{\mathrm{cl}}. \tag{9.19}$$

It is seen to again include a term which expresses the constraint as an additional octupolar tensor with respect to the total spin on the triangular plaquette. Meanwhile the first term corresponds to the on-site order parameter that was found already using the single-site cluster. Additionally, the second term corresponds to the order parameter that was previously found for the gauge model of T_d-symmetric mesogens, Eq. (6.12). Here, it is seen to contribute equally to the total order parameter. By measuring these three terms individually, it becomes apparent that the first two terms are indeed equivalent. This is in line with the observation made throughout the preceding chapters that TK-SVM will learn all equivalent manifestations of an order parameter simultaneously in a way that minimizes the Frobenius norm of the full coefficient matrix. In cases where these are nonoverlapping, such as the present one, this implies a realization with equal weights.

10

Conclusion

In this thesis, a machine-learning framework for phase classification in classical magnetic systems was introduced which is based on tensorial kernel methods. The center stage is taken by the tensorial kernel (TK) function [Eq. (5.5)] which involves a mapping [Eq. (5.3)] to monomials of spin components, corresponding to the elements of product tensors between spin vectors. Its design allows it to capture the order parameter tensors of multipolar spin orders at any given rank.

At the same time, the TK is highly interpretable which admitted the development of powerful analytical tools in part II of the thesis. Their interpretability may be considered a major advantage of tensorial kernel methods over neural networks. This led to a usage scenario which is rather uncharacteristic of machine learning methods: After training the machine to accomplish the successful classification of phases, rather than simply classifying further samples accordingly, the classifier is instead deconstructed to infer the physical quantity that distinguishes between phases: the order parameter.

The focus on multipolar order is motivated primarily by its prevalence in classical frustrated magnets. Frustration can give rise to many interesting phenomena, chief among which is the formation of classical spin liquids (CSLs) which do not break any symmetries but exhibit strong, algebraically decaying correlations nonetheless. However, at low temperatures, symmetry-breaking orders may still emerge, in some cases driven by the order-by-disorder phenomenon (*cf.* Ch. 1). These are then typically spin nematics with a multipolar nature and are thus invisible to conventional numeric probes: “hidden orders”. Historically, these tend to be missed in tentative CSL candidates, the prime example of which is the Heisenberg model on the kagome lattice (see Sec. 2.1.1) which was studied in Ch. 9.

The applicability of the TK is not limited to any particular kernel method but it has been used in conjunction with support vector machines (TK-SVM) for the majority of this thesis. It has also been applied to kernel principal component analysis (TK-PCA) in Sec. 8.4 as a proof of concept but does not lend itself to an unbiased interpretation in quite the same way as TK-SVM does for the reasons discussed therein.

By example of a gauge model of generalized nematics, several different multipolar orders, each breaking O(3) down to a different symmetry, have been scrutinized by TK-SVM. For each, the order parameter tensor was reconstructed, covering cases ranging from vector order parameters to the sixth-rank order parameter tensor of an icosahedral nematic. Several training scenarios which deviate from a standard binary classification, distinguishing between an ordered phase and a disordered phase, have been considered: (i) several orders may coexist in which case they can still be isolated individually; (ii) one may attempt to train the machine on samples which exclusively originate from either the disordered or (iii) the ordered phase. In the last case, TK-SVM still identifies the correct order parameter (which varies in strength within the phase).

The examination of these cases upheaved two quintessential virtues of TK-SVM which go beyond its original conception. First, the bias parameter of the TK-SVM decision function admits an interpretation in the context of phase classification which is summarized in Eq. (5.17). It gives an indication as to whether two sets of samples do indeed display different physics and, hence, originate from different phases. This bias criterion was brought to full fruition in obtaining the phase diagram from a spectral analysis of the graph that is constructed based on the biases (see Ch. 7). Under this scheme, TK-SVM is used in a semantically unsupervised way by labeling the training data trivially by the parameters of the simulation from which they were harvested. This is in spite of the fact that SVM is technically a supervised learning scheme.

Second, the TK proved capable of distinguishing CSL regimes from both trivially paramagnetic ones and symmetry-breaking phases. This came as a surprise as the TK was constructed with tensorial order parameters in mind and these are absent in spin liquids. However, the space of functions which the TK-SVM decision functions (or the TK-PCA score functions) encompass is not limited to those. As laid out in Chs. 8 and 9 to varying degrees of detail, the TK then distinguishes CSLs by their associated local constraints. The resulting decision function acts as an "order parameter" for CSLs and one can even derive generalized susceptibilities from them to quantify the location and width of their associated crossover regimes.

In part III of the thesis, TK-SVM has been applied to two frustrated spin models with some success: In the aforementioned Heisenberg model on the kagome lattice, the hidden ordered phase was found and the correct tensorial description of its triatic symmetry in terms of both a quadrupolar and an octupolar order parameter was uncovered, consistent with the one obtained by Zhitomirsky [82]. Additionally, the local constraint describing the CSL regime above the ordering temperature could be inferred and the crossover to the trivial paramagnet was observed as a function of temperature. The other system which was considered is the XXZ model on the pyrochlore lattice. Its intricate phase diagram—featuring two symmetry-breaking phases (one of them a spin nematic) and three distinct types of spin liquids—could be obtained in near perfect agreement to the one previously proposed by Taillefumier *et al.* based on a careful manual analysis [87].

Given these encouraging results, which limitations do tensorial kernel methods face? First, by design, the TK is limited to quasi-local phenomena, *i.e.* those which manifest themselves within the spin cluster the kernel is defined on. This precludes topological quantities such as the one governing the vortex-unbinding transition in the XY model. However, this is something that other machine-learning methods have struggled with anyway without extensive feature engineering (*cf.* Sec. 4.2). That being said, evidence of topologically nontrivial phases may still be picked up by the TK. The constraints characteristic of CSLs are an example of that: They manifest themselves in local quantities, yet they provide the basis for fractionalized excitations such as magnetic monopoles which are inherently topologically nontrivial.

Second, in its current form, the TK relies on the full microscopic spin configuration (or spin cluster average thereof). While the method is not intrinsically restricted to a combination with Monte Carlo methods to harvest the training data, this information is usually not readily available from experiments. Conversely, the order parameters or constraints found by TK-SVM on model systems may provide valuable input to the experimental identification of hidden orders and CSLs in materials.

Third, this reliance on vector-valued spin information also accounts for its current limitation to (semi-)classical spin systems. As of now, the generalization to genuine quantum systems remains an open question. However, simulations of frustrated spin systems by means of quantum Monte Carlo are notoriously limited by the sign problem anyway, while tensor network methods are restricted to small system sizes. Fortunately, many frustrated systems already show nontrivial phenomena at the classical level, which also provide useful insight into their quantum counterparts, and many of those are pending a thorough investigation of their phase diagram.

One class of such systems are the Kitaev materials [188, 189], including spin liquid candidates Li_2IrO_3, Na_2IrO_3 [190, 191], Sr_2IrO_4 [192] and α-$RuCl_3$ [193, 194]. These materials involve various competing interactions, such as the Heisenberg, Kitaev, and off-diagonal Gamma interactions and also show a strong dependence on external magnetic fields [189, 195, 196]. Even when varying only a subset of the interaction parameters, their (classical) phase diagrams exhibit multiple exotic orders competing with the desired spin liquids [197, 198], whereas order parameters of those phases are not yet clear and significant parts of the phase diagram remain unexplored. Following the framework provided by TK-SVM to compute the phase diagram, one does not have to scan each physical parameter individually; phase transitions and crossovers in the entire parameter space of interest can instead be identified in one fell swoop. Independent of the number of physical parameters, the analysis will result in a univariate histogram (*cf.* Figs. 7.3 and 8.5), whose peaks imply distinct phases. One can thereby obtain a comprehensive phase diagram more efficiently.

The ability to construct a high-dimensional phase diagram in turn allows to systematically classify which interactions favor hidden order or spin liquids. This may accelerate the pace at which theoreticians can scrutinize material-inspired model Hamiltonians and might open the door towards the engineering of unconventional phases in the future.

Source code and data availability

The source codes for the SVM framework, including the Monte Carlo simulation of the gauge model and the Heisenberg model on the kagome lattice have been made available under a free software license [199]. The code used to simulate the XXZ model on the pyrochlore lattice was written by Ludovic D. C. Jaubert and is not openly available. The raw data supporting the findings of Ch. 6 are available as part of the supplementary materials of Ref. 2. The data relating to Chs. 8 and 9 will be made available through other means. Links may be found in the README files accompanying the source codes.

Bibliography

[1] Ke Liu, Jonas Greitemann, and Lode Pollet. *Generic first-order phase transitions between isotropic and orientational phases with polyhedral symmetries.* Phys. Rev. E **97**, 012706 (2018).

[2] Jonas Greitemann, Ke Liu, and Lode Pollet. *Probing hidden spin order with interpretable machine learning.* Phys. Rev. B **99**, 060404 (2019).

[3] Ke Liu, Jonas Greitemann, and Lode Pollet. *Learning multiple order parameters with interpretable machines.* Phys. Rev. B **99**, 104410 (2019).

[4] Jonas Greitemann, Ke Liu, Ludovic D. C. Jaubert, Han Yan, Nic Shannon, and Lode Pollet. *Identification of hidden order and emergent constraints in frustrated magnets using tensorial kernel methods.* ArXiv preprint (2019), arXiv:1907.12322.

[5] BBC News Online. *Google's AI wins final Go challenge.* 15 March 2016, retrieved 8 June 2019. URL `https://www.bbc.com/news/technology-35810133`.

[6] David Silver, Aja Huang, Chris J. Maddison, Arthur Guez, Laurent Sifre, George van den Driessche, Julian Schrittwieser, Ioannis Antonoglou, Veda Panneershelvam, Marc Lanctot, Sander Dieleman, Dominik Grewe, John Nham, Nal Kalchbrenner, Ilya Sutskever, Timothy Lillicrap, Madeleine Leach, Koray Kavukcuoglu, Thore Graepel, and Demis Hassabis. *Mastering the game of Go with deep neural networks and tree search.* Nature **529**, 484–489 (2016).

[7] David Silver, Thomas Hubert, Julian Schrittwieser, Ioannis Antonoglou, Matthew Lai, Arthur Guez, Marc Lanctot, Laurent Sifre, Dharshan Kumaran, Thore Graepel, Timothy Lillicrap, Karen Simonyan, and Demis Hassabis. *A general reinforcement learning algorithm that masters chess, shogi, and Go through self-play.* Science **362**, 1140–1144 (2018).

[8] Warren S. McCulloch and Walter Pitts. *A logical calculus of the ideas immanent in nervous activity.* Bull. Math. Biophys. **5**, 115–133 (1943).

[9] Frank Rosenblatt. *The perceptron: A probabilistic model for information storage and organization in the brain.* Psychol. Rev. **65**, 386 (1958).

[10] Mikel Olazaran. *A Sociological Study of the Official History of the Perceptrons Controversy.* Soc. Stud. Sci. **26**, 611–659 (1996).

[11] Paul J. Werbos. *Beyond Regression: New Tools for Prediction and Analysis in the Behavioral Sciences.* PhD thesis, Harvard University (1975).

[12] David E. Rumelhart, Geoffrey E. Hinton, and Ronald J. Williams. *Learning representations by back-propagating errors.* Nature **323**, 533–536 (1986).

[13] Wei Zhang, Kazuyoshi Itoh, Jun Tanida, and Yoshiki Ichioka. *Parallel distributed processing model with local space-invariant interconnections and its optical architecture.* Appl. Opt. **29**, 4790–4797 (1990).

[14] Corinna Cortes and Vladimir Vapnik. *Support-vector networks.* Mach. Learn. **20**, 273–297 (1995).

[15] Bernhard Schölkopf, Alexander Smola, and Klaus-Robert Müller. *Nonlinear Component Analysis as a Kernel Eigenvalue Problem.* Neural Comput. **10**, 1299–1319 (1998).

[16] Yann LeCun, Corinna Cortes, and Christopher J. C. Burges. *The MNIST database of handwritten digits.* Retrieved 10 June 2019. URL `http://yann.lecun.com/exdb/mnist/`.

[17] Yann LeCun, Léon Bottou, Yoshua Bengio, and Patrick Haffner. *Gradient-based learning applied to document recognition.* Proc. IEEE **86**, 2278–2324 (1998).

[18] Tin Kam Ho. *Random decision forests.* In *Proceedings of 3rd International Conference on Document Analysis and Recognition*, volume 1, pages 278–282 (1995). doi: 10.1109/ICDAR.1995.598994.

[19] Alex Krizhevsky, Ilya Sutskever, and Geoffrey E. Hinton. *ImageNet Classification with Deep Convolutional Neural Networks.* Commun. ACM **60**, 84–90 (2017).

[20] Yann LeCun, Yoshua Bengio, and Geoffrey Hinton. *Deep learning.* Nature **521**, 436–444 (2015).

[21] Henry W. Lin, Max Tegmark, and David Rolnick. *Why Does Deep and Cheap Learning Work So Well?* J. Stat. Phys. **168**, 1223–1247 (2017).

[22] Zi Cai and Jinguo Liu. *Approximating quantum many-body wave functions using artificial neural networks.* Phys. Rev. B **97**, 035116 (2018).

[23] Philippe Suchsland and Stefan Wessel. *Parameter diagnostics of phases and phase transition learning by neural networks.* Phys. Rev. B **97**, 174435 (2018).

[24] Giuseppe Carleo and Matthias Troyer. *Solving the quantum many-body problem with artificial neural networks.* Science **355**, 602–606 (2017).

[25] Xun Gao and Lu-Ming Duan. *Efficient representation of quantum many-body states with deep neural networks.* Nat. Commun. **8**, 662 (2017).

[26] Pedro Ponte and Roger G. Melko. *Kernel methods for interpretable machine learning of order parameters.* Phys. Rev. B **96**, 205146 (2017).

[27] Sandro Sorella and Luca Capriotti. *Green function Monte Carlo with stochastic reconfiguration: An effective remedy for the sign problem.* Phys. Rev. B **61**, 2599–2612 (2000).

[28] Sandro Sorella. *Generalized Lanczos algorithm for variational quantum Monte Carlo.* Phys. Rev. B **64**, 024512 (2001).

[29] Ivan Glasser, Nicola Pancotti, Moritz August, Ivan D. Rodriguez, and J. Ignacio Cirac. *Neural-Network Quantum States, String-Bond States, and Chiral Topological States.* Phys. Rev. X **8**, 011006 (2018).

[30] Jing Chen, Song Cheng, Haidong Xie, Lei Wang, and Tao Xiang. *Equivalence of restricted Boltzmann machines and tensor network states.* Phys. Rev. B **97**, 085104 (2018).

[31] Matthew B. Hastings. *An area law for one-dimensional quantum systems.* J. Stat. Mech.: Theory Exp. **2007**, P08024–P08024 (2007).

[32] J. D. Bernal and R. H. Fowler. *A Theory of Water and Ionic Solution, with Particular Reference to Hydrogen and Hydroxyl Ions.* J. Chem. Phys. **1**, 515–548 (1933).

[33] M. J. Harris, S. T. Bramwell, D. F. McMorrow, T. Zeiske, and K. W. Godfrey. *Geometrical Frustration in the Ferromagnetic Pyrochlore* $Ho_2Ti_2O_7$. Phys. Rev. Lett. **79**, 2554–2557 (1997).

[34] Steven T. Bramwell and Michel J. P. Gingras. *Spin Ice State in Frustrated Magnetic Pyrochlore Materials.* Science **294**, 1495–1501 (2001).

[35] Linus Pauling. *The Structure and Entropy of Ice and of Other Crystals with Some Randomness of Atomic Arrangement.* J. Am. Chem. Soc. **57**, 2680–2684 (1935).

[36] Jason S. Gardner, Michel J. P. Gingras, and John E. Greedan. *Magnetic pyrochlore oxides.* Rev. Mod. Phys. **82**, 53–107 (2010).

[37] A. P. Ramirez, A. Hayashi, R. J. Cava, R. Siddharthan, and B. S. Shastry. *Zero-point entropy in 'spin ice'.* Nature **399**, 333–335 (1999).

[38] Claudio Castelnovo, Roderich Moessner, and Shivaji L. Sondhi. *Magnetic monopoles in spin ice.* Nature **451**, 42–45 (2008).

[39] John T. Chalker. *Geometrically Frustrated Antiferromagnets: Statistical Mechanics and Dynamics.* In Claudine Lacroix, Philippe Mendels, and Frédéric Mila, editors, *Introduction to Frustrated Magnetism*, chapter 1. Springer Berlin Heidelberg (2011). ISBN 978-3-642-10588-3.

[40] C. L. Henley. *Power-law spin correlations in pyrochlore antiferromagnets.* Phys. Rev. B **71**, 014424 (2005).

[41] Christopher L. Henley. *The "Coulomb Phase" in Frustrated Systems.* Annu. Rev. Condens. Matter Phys. **1**, 179–210 (2010).

[42] T. Fennell, P. P. Deen, A. R. Wildes, K. Schmalzl, D. Prabhakaran, A. T. Boothroyd, R. J. Aldus, D. F. McMorrow, and S. T. Bramwell. *Magnetic Coulomb Phase in the Spin Ice* $Ho_2Ti_2O_7$. Science **326**, 415–417 (2009).

[43] Ivan A. Ryzhkin. *Magnetic relaxation in rare-earth oxide pyrochlores.* J. Exp. Theor. Phys. **101**, 481–486 (2005).

[44] Claudio Castelnovo, Roderich Moessner, and Shivaji L. Sondhi. *Spin Ice, Fractionalization, and Topological Order.* Annu. Rev. Condens. Matter Phys. **3**, 35–55 (2012).

[45] Ludovic D. C. Jaubert and Peter C. W. Holdsworth. *Signature of magnetic monopole and Dirac string dynamics in spin ice.* Nat. Phys. **5**, 258–261 (2009).

[46] D. J. P. Morris, D. A. Tennant, S. A. Grigera, B. Klemke, C. Castelnovo, R. Moessner, C. Czternasty, M. Meissner, K. C. Rule, J.-U. Hoffmann, K. Kiefer, S. Gerischer, D. Slobinsky, and R. S. Perry. *Dirac Strings and Magnetic Monopoles in the Spin Ice* $Dy_2Ti_2O_7$. Science **326**, 411–414 (2009).

[47] Sean R. Giblin, Steven T. Bramwell, Peter C. W. Holdsworth, Dharmalingam Prabhakaran, and Ian Terry. *Creation and measurement of long-lived magnetic monopole currents in spin ice.* Nat. Phys. **7**, 252–258 (2011).

[48] Bruno Tomasello, Claudio Castelnovo, Roderich Moessner, and Jorge Quintanilla. *Correlated Quantum Tunneling of Monopoles in Spin Ice.* Phys. Rev. Lett. **123**, 067204 (2019).

[49] Yann Perrin, Benjamin Canals, and Nicolas Rougemaille. *Extensive degeneracy, Coulomb phase and magnetic monopoles in artificial square ice.* Nature **540**, 410–413 (2016).

[50] H. Fukazawa, R. G. Melko, R. Higashinaka, Y. Maeno, and M. J. P. Gingras. *Magnetic anisotropy of the spin-ice compound* $Dy_2Ti_2O_7$. Phys. Rev. B **65**, 054410 (2002).

[51] Leon Balents. *Spin liquids in frustrated magnets.* Nature **464**, 199–208 (2010).

[52] G. Baskaran, Z. Zou, and P. W. Anderson. *The resonating valence bond state and high-*T_c *superconductivity — A mean field theory.* Solid State Commun. **63**, 973–976 (1987).

[53] P. W. Anderson, G. Baskaran, Z. Zou, and T. Hsu. *Resonating-valence-bond theory of phase transitions and superconductivity in* La_2CuO_4*-based compounds.* Phys. Rev. Lett. **58**, 2790–2793 (1987).

[54] G. Baskaran and P. W. Anderson. *Gauge theory of high-temperature superconductors and strongly correlated Fermi systems.* Phys. Rev. B **37**, 580–583 (1988).

[55] Lucile Savary and Leon Balents. *Quantum spin liquids: a review.* Rep. Prog. Phys. **80**, 016502 (2017).

[56] Alexei Yu. Kitaev. *Fault-tolerant quantum computation by anyons.* Ann. Phys. (N. Y.) **303**, 2–30 (2003).

[57] Alexei Kitaev and Chris Laumann. *Topological quantum phases and quantum computation.* In Jesper Jacobsen, Stephane Ouvry, Vincent Pasquier, Didina Serban, and Leticia Cugliandolo, editors, *Exact Methods in Low-dimensional Statistical Physics and Quantum Computing*, volume 89 of *Lecture Notes of the Les Houches Summer School*, chapter 4. Oxford University Press, Oxford, U.K. (2008), arXiv:0904.2771.

[58] Yi Zhou, Kazushi Kanoda, and Tai-Kai Ng. *Quantum spin liquid states.* Rev. Mod. Phys. **89**, 025003 (2017).

[59] Nic Shannon, Tsutomu Momoi, and Philippe Sindzingre. *Nematic Order in Square Lattice Frustrated Ferromagnets.* Phys. Rev. Lett. **96**, 027213 (2006).

[60] John A. Mydosh and Peter M. Oppeneer. Colloquium*: Hidden order, superconductivity, and magnetism: The unsolved case of* URu_2Si_2. Rev. Mod. Phys. **83**, 1301–1322 (2011).

[61] Joseph A. M. Paddison, Henrik Jacobsen, Oleg A. Petrenko, Maria Teresa Fernández-Díaz, Pascale P. Deen, and Andrew L. Goodwin. *Hidden order in spin-liquid* $Gd_3Ga_5O_{12}$. Science **350**, 179–181 (2015).

[62] Yao-Dong Li, Xiaoqun Wang, and Gang Chen. *Hidden multipolar orders of dipole-octupole doublets on a triangular lattice.* Phys. Rev. B **94**, 201114 (2016).

[63] H. Takatsu, S. Onoda, S. Kittaka, A. Kasahara, Y. Kono, T. Sakakibara, Y. Kato, B. Fåk, J. Ollivier, J. W. Lynn, T. Taniguchi, M. Wakita, and H. Kadowaki. *Quadrupole Order in the Frustrated Pyrochlore* $Tb_{2+x}Ti_{2-x}O_{7+y}$. Phys. Rev. Lett. **116**, 217201 (2016).

[64] Qiang Luo, Shijie Hu, Bin Xi, Jize Zhao, and Xiaoqun Wang. *Ground-state phase diagram of an anisotropic spin-*$\frac{1}{2}$ *model on the triangular lattice.* Phys. Rev. B **95**, 165110 (2017).

[65] A. F. Andreev and I. A. Grishchuk. *Spin Nematics.* J. Exp. Theor. Phys. **87**, 467–475 (1984).

[66] Andrey V. Chubukov. *Fluctuations in spin nematics.* J. Phys.: Condens. Matter **2**, 1593 (1990).

[67] Tsutomu Momoi, Philippe Sindzingre, and Nic Shannon. *Octupolar Order in the Multiple Spin Exchange Model on a Triangular Lattice.* Phys. Rev. Lett. **97**, 257204 (2006).

[68] Tsutomu Momoi, Philippe Sindzingre, and Kenn Kubo. *Spin Nematic Order in Multiple-Spin Exchange Models on the Triangular Lattice.* Phys. Rev. Lett. **108**, 057206 (2012).

[69] Roderich Moessner and John T. Chalker. *Low-temperature properties of classical geometrically frustrated antiferromagnets.* Phys. Rev. B **58**, 12049–12062 (1998).

[70] Andreas Läuchli, Frédéric Mila, and Karlo Penc. *Quadrupolar Phases of the* $S = 1$ *Bilinear-Biquadratic Heisenberg Model on the Triangular Lattice.* Phys. Rev. Lett. **97**, 087205 (2006).

[71] Congjun Wu. *Orbital Ordering and Frustration of p-Band Mott Insulators.* Phys. Rev. Lett. **100**, 200406 (2008).

[72] J. Yamaura, K. Ohgushi, H. Ohsumi, T. Hasegawa, I. Yamauchi, K. Sugimoto, S. Takeshita, A. Tokuda, M. Takata, M. Udagawa, M. Takigawa, H. Harima, T. Arima, and Z. Hiroi. *Tetrahedral Magnetic Order and the Metal-Insulator Transition in the Pyrochlore Lattice of* $Cd_2Os_2O_7$. Phys. Rev. Lett. **108**, 247205 (2012).

[73] M. Mourigal, M. Enderle, B. Fåk, R. K. Kremer, J. M. Law, A. Schneidewind, A. Hiess, and A. Prokofiev. *Evidence of a Bond-Nematic Phase in* $LiCuVO_4$. Phys. Rev. Lett. **109**, 027203 (2012).

[74] O. Janson, J. Richter, P. Sindzingre, and H. Rosner. *Coupled frustrated quantum spin-*$\frac{1}{2}$ *chains with orbital order in volborthite* $Cu_3V_2O_7(OH)_2 \cdot 2H_2O$. Phys. Rev. B **82**, 104434 (2010).

[75] R. Wawrzyńczak, Y. Tanaka, M. Yoshida, Y. Okamoto, P. Manuel, N. Casati, Z. Hiroi, M. Takigawa, and G. J. Nilsen. *Classical Spin Nematic Transition in* $LiGa_{0.95}In_{0.05}Cr_4O_8$. Phys. Rev. Lett. **119**, 087201 (2017).

[76] A. Orlova, E. L. Green, J. M. Law, D. I. Gorbunov, G. Chanda, S. Krämer, M. Horvatić, R. K. Kremer, J. Wosnitza, and G. L. J. A. Rikken. *Nuclear Magnetic Resonance Signature of the Spin-Nematic Phase in* $LiCuVO_4$ *at High Magnetic Fields.* Phys. Rev. Lett. **118**, 247201 (2017).

[77] Jacques Villain, R. Bidaux, J.-P. Carton, and R. Conte. *Order as an effect of disorder.* J. Phys. France **41**, 1263–1272 (1980).

[78] Doron Bergman, Jason Alicea, Emanuel Gull, Simon Trebst, and Leon Balents. *Order-by-disorder and spiral spin-liquid in frustrated diamond-lattice antiferromagnets.* Nat. Phys. **3**, 487–491 (2007).

[79] John T. Chalker, Peter C. W. Holdsworth, and E. F. Shender. *Hidden order in a frustrated system: Properties of the Heisenberg Kagomé antiferromagnet.* Phys. Rev. Lett. **68**, 855–858 (1992).

[80] I. Ritchey, P. Chandra, and P. Coleman. *Spin folding in the two-dimensional Heisenberg kagomé antiferromagnet.* Phys. Rev. B **47**, 15342–15345 (1993).

[81] Michael E. Zhitomirsky. *Field-Induced Transitions in a Kagomé Antiferromagnet.* Phys. Rev. Lett. **88**, 057204 (2002).

[82] Michael E. Zhitomirsky. *Octupolar ordering of classical kagome antiferromagnets in two and three dimensions.* Phys. Rev. B **78**, 094423 (2008).

[83] Ke Liu, Jaakko Nissinen, Robert-Jan Slager, Kai Wu, and Jan Zaanen. *Generalized Liquid Crystals: Giant Fluctuations and the Vestigial Chiral Order of* I*,* O*, and* T *Matter.* Phys. Rev. X **6**, 041025 (2016).

[84] Jaakko Nissinen, Ke Liu, Robert-Jan Slager, Kai Wu, and Jan Zaanen. *Classification of point-group-symmetric orientational ordering tensors.* Phys. Rev. E **94**, 022701 (2016).

[85] John D. Bernal and Isidor Fankuchen. *X-ray and crystallographic studies of plant virus preparations.* J. Gen. Physiol. **25**, 111–146 (1941).

[86] John Lydon. *Virus Particle-Based Liquid Crystals.* In *Handbook of Liquid Crystals*, chapter 7. American Cancer Society (2014). ISBN 978-3-527-67140-3.

[87] Mathieu Taillefumier, Owen Benton, Han Yan, L. D. C. Jaubert, and Nic Shannon. *Competing Spin Liquids and Hidden Spin-Nematic Order in Spin Ice with Frustrated Transverse Exchange.* Phys. Rev. X 7, 041057 (2017).

[88] Owen Benton, Ludovic D. C. Jaubert, Rajiv R. P. Singh, Jaan Oitmaa, and Nic Shannon. *Quantum Spin Ice with Frustrated Transverse Exchange: From a π-Flux Phase to a Nematic Quantum Spin Liquid.* Phys. Rev. Lett. **121**, 067201 (2018).

[89] John Hubbard and Brian Hilton Flowers. *Electron correlations in narrow energy bands.* Proc. R. Soc. Lond. A **276**, 238–257 (1963).

[90] Assa Auerbach. *Interacting Electrons and Quantum Magnetism.* Graduate Texts in Contemporary Physics. Springer, New York, NY, U.S.A. (1994). ISBN 978-0-387-94286-5.

[91] P. W. Anderson. *Ordering and Antiferromagnetism in Ferrites.* Phys. Rev. **102**, 1008–1013 (1956).

[92] A. P. Ramirez. *Strongly Geometrically Frustrated Magnets.* Annu. Rev. Mater. Sci. **24**, 453–480 (1994).

[93] G. H. Wannier. *Antiferromagnetism. The Triangular Ising Net.* Phys. Rev. **79**, 357–364 (1950).

[94] James C. Maxwell. Philos. Mag. **27**, 294–299 (1864).

[95] Roderich Moessner and John T. Chalker. *Properties of a Classical Spin Liquid: The Heisenberg Pyrochlore Antiferromagnet.* Phys. Rev. Lett. **80**, 2929–2932 (1998).

[96] N. D. Mermin and H. Wagner. *Absence of Ferromagnetism or Antiferromagnetism in One- or Two-Dimensional Isotropic Heisenberg Models.* Phys. Rev. Lett. **17**, 1133–1136 (1966).

[97] David A. Huse and Andrew D. Rutenberg. *Classical antiferromagnets on the Kagomé lattice.* Phys. Rev. B **45**, 7536–7539 (1992).

[98] Jan N. Reimers and A. J. Berlinsky. *Order by disorder in the classical Heisenberg kagomé antiferromagnet.* Phys. Rev. B **48**, 9539–9554 (1993).

[99] X. Obradors, A. Labarta, A. Isalgué, J. Tejada, J. Rodriguez, and M. Pernet. *Magnetic frustration and lattice dimensionality in* $\mathrm{SrCr_8Ga_4O_19}$. Solid State Commun. **65**, 189–192 (1988).

[100] A. P. Ramirez, G. P. Espinosa, and A. S. Cooper. *Strong frustration and dilution-enhanced order in a quasi-2D spin glass.* Phys. Rev. Lett. **64**, 2070–2073 (1990).

[101] Yan V. Fyodorov and E. F. Shender. *Random-field effects in antiferromagnets with classically degenerate ground states.* J. Phys.: Condens. Matter **3**, 9123–9128 (1991).

[102] A. P. Ramirez, G. P. Espinosa, and A. S. Cooper. *Elementary excitations in a diluted antiferromagnetic Kagomé lattice.* Phys. Rev. B **45**, 2505–2508 (1992).

[103] E. F. Shender, V. B. Cherepanov, P. C. W. Holdsworth, and A. J. Berlinsky. *Kagomé antiferromagnet with defects: Satisfaction, frustration, and spin folding in a random spin system.* Phys. Rev. Lett. **70**, 3812–3815 (1993).

[104] W. Schweika, M. Valldor, and P. Lemmens. *Approaching the Ground State of the Kagomé Antiferromagnet.* Phys. Rev. Lett. **98**, 067201 (2007).

[105] B. Fåk, F. C. Coomer, A. Harrison, D. Visser, and M. E. Zhitomirsky. *Spin-liquid behavior in a kagomé antiferromagnet: Deuteronium jarosite.* EPL **81**, 17006 (2007).

[106] Han Yan, Owen Benton, Ludovic Jaubert, and Nic Shannon. *Theory of multiple-phase competition in pyrochlore magnets with anisotropic exchange with application to* $Yb_2Ti_2O_7$, $Er_2Ti_2O_7$, *and* $Er_2Sn_2O_7$. Phys. Rev. B **95**, 094422 (2017).

[107] Igor Dzyaloshinsky. *A thermodynamic theory of "weak" ferromagnetism of antiferromagnetics.* J. Phys. Chem. Solids **4**, 241–255 (1958).

[108] Tôru Moriya. *Anisotropic Superexchange Interaction and Weak Ferromagnetism.* Phys. Rev. **120**, 91–98 (1960).

[109] S. Elitzur. *Impossibility of spontaneously breaking local symmetries.* Phys. Rev. D **12**, 3978–3982 (1975).

[110] Ke Liu, Jaakko Nissinen, Josko de Boer, Robert-Jan Slager, and Jan Zaanen. *Hierarchy of orientational phases and axial anisotropies in the gauge theoretical description of generalized nematic liquid crystals.* Phys. Rev. E **95**, 022704 (2017).

[111] P. A. Lebwohl and G. Lasher. *Nematic-Liquid-Crystal Order—A Monte Carlo Calculation.* Phys. Rev. A **6**, 426–429 (1972).

[112] Paul E. Lammert, Daniel S. Rokhsar, and John Toner. *Topology and nematic ordering.* Phys. Rev. Lett. **70**, 1650–1653 (1993).

[113] Leonid G. Fel. *Tetrahedral symmetry in nematic liquid crystals.* Phys. Rev. E **52**, 702–717 (1995).

[114] Amir Haji-Akbari and Sharon C. Glotzer. *Strong orientational coordinates and orientational order parameters for symmetric objects.* J. Phys. A: Math. Theor. **48**, 485201 (2015).

[115] Carl D. Meyer. *Matrix Analysis and Applied Linear Algebra.* Society for Industrial and Applied Mathematics, Philadelphia (2000). ISBN 978-0-89871-454-8.

[116] Bernd A. Berg. *Markov Chain Monte Carlo Simulations and Their Statistical Analysis.* World Scientific Publishing, Singapore (2004). ISBN 978-981-238-935-0.

[117] Robert H. Swendsen and Jian-Sheng Wang. *Nonuniversal critical dynamics in Monte Carlo simulations.* Phys. Rev. Lett. **58**, 86–88 (1987).

[118] Ulli Wolff. *Collective Monte Carlo Updating for Spin Systems.* Phys. Rev. Lett. **62**, 361–364 (1989).

[119] Peter Hitchcock, Erik S. Sörensen, and Fabien Alet. *Dual geometric worm algorithm for two-dimensional discrete classical lattice models.* Phys. Rev. E **70**, 016702 (2004).

[120] Yuan Wang, Hans De Sterck, and Roger G. Melko. *Generalized Monte Carlo loop algorithm for two-dimensional frustrated Ising models.* Phys. Rev. E **85**, 036704 (2012).

[121] Geet Rakala and Kedar Damle. *Cluster algorithms for frustrated two-dimensional Ising antiferromagnets via dual worm constructions.* Phys. Rev. E **96**, 023304 (2017).

[122] Nicholas Metropolis, Arianna W. Rosenbluth, Marshall N. Rosenbluth, Augusta H. Teller, and Edward Teller. *Equation of State Calculations by Fast Computing Machines.* J. Chem. Phys. **21**, 1087–1092 (1953).

[123] Michael Creutz. *Monte Carlo study of quantized SU(2) gauge theory.* Phys. Rev. D **21**, 2308–2315 (1980).

[124] David P. Landau and Kurt Binder. *A Guide to Monte Carlo Simulations in Statistical Physics.* Cambridge University Press, Cambridge, U.K., 4th edition (2014). ISBN 978-1-107-07402-6.

[125] Michael Creutz. *Overrelaxation and Monte Carlo simulation.* Phys. Rev. D **36**, 515–519 (1987).

[126] Frank R. Brown and Thomas J. Woch. *Overrelaxed heat-bath and Metropolis algorithms for accelerating pure gauge Monte Carlo calculations.* Phys. Rev. Lett. **58**, 2394–2396 (1987).

[127] Koji Hukushima and Koji Nemoto. *Exchange Monte Carlo Method and Application to Spin Glass Simulations.* J. Phys. Soc. Jpn. **65**, 1604–1608 (1996).

[128] Helmut G. Katzgraber, Simon Trebst, David A. Huse, and Matthias Troyer. *Feedback-optimized parallel tempering Monte Carlo.* J. Stat. Mech.: Theory Exp. **2006**, P03018 (2006).

[129] Juan Carrasquilla and Roger G. Melko. *Machine learning phases of matter.* Nat. Phys. **13**, 431–434 (2017).

[130] Sebastian J. Wetzel and Manuel Scherzer. *Machine learning of explicit order parameters: From the Ising model to SU(2) lattice gauge theory.* Phys. Rev. B **96**, 184410 (2017).

[131] Kelvin Ch'ng, Juan Carrasquilla, Roger G. Melko, and Ehsan Khatami. *Machine Learning Phases of Strongly Correlated Fermions.* Phys. Rev. X **7**, 031038 (2017).

[132] Evert P. L. van Nieuwenburg, Ye-Hua Liu, and Sebastian D. Huber. *Learning phase transitions by confusion.* Nat. Phys. **13**, 435–439 (2017).

[133] Frank Schindler, Nicolas Regnault, and Titus Neupert. *Probing many-body localization with neural networks.* Phys. Rev. B **95**, 245134 (2017).

[134] Peter Broecker, Juan Carrasquilla, Roger G. Melko, and Simon Trebst. *Machine learning quantum phases of matter beyond the fermion sign problem*. Sci. Rep. 7, 8823 (2017).

[135] Yi Zhang and Eun-Ah Kim. *Quantum Loop Topography for Machine Learning*. Phys. Rev. Lett. **118**, 216401 (2017).

[136] Yi Zhang, Roger G. Melko, and Eun-Ah Kim. *Machine learning $\mathbb{Z}_2$ quantum spin liquids with quasiparticle statistics*. Phys. Rev. B **96**, 245119 (2017).

[137] Tomoki Ohtsuki and Tomi Ohtsuki. *Deep Learning the Quantum Phase Transitions in Random Two-Dimensional Electron Systems*. J. Phys. Soc. Jpn. **85**, 123706 (2016).

[138] Pengfei Zhang, Huitao Shen, and Hui Zhai. *Machine Learning Topological Invariants with Neural Networks*. Phys. Rev. Lett. **120**, 066401 (2018).

[139] Ning Sun, Jinmin Yi, Pengfei Zhang, Huitao Shen, and Hui Zhai. *Deep learning topological invariants of band insulators*. Phys. Rev. B **98**, 085402 (2018).

[140] Giacomo Torlai, Guglielmo Mazzola, Juan Carrasquilla, Matthias Troyer, Roger Melko, and Giuseppe Carleo. *Neural-network quantum state tomography*. Nat. Phys. **14**, 447–450 (2018).

[141] Giacomo Torlai and Roger G. Melko. *Machine learning quantum states in the NISQ era*. ArXiv preprint (2019), arXiv:1905.04312.

[142] Benno S. Rem, Niklas Käming, Matthias Tarnowski, Luca Asteria, Nick Fläschner, Christoph Becker, Klaus Sengstock, and Christof Weitenberg. *Identifying quantum phase transitions using artificial neural networks on experimental data*. Nat. Phys. (2019).

[143] Dong-Ling Deng, Xiaopeng Li, and Sankar Das Sarma. *Machine learning topological states*. Phys. Rev. B **96**, 195145 (2017).

[144] Wenjian Hu, Rajiv R. P. Singh, and Richard T. Scalettar. *Discovering phases, phase transitions, and crossovers through unsupervised machine learning: A critical examination*. Phys. Rev. E **95**, 062122 (2017).

[145] Ce Wang and Hui Zhai. *Machine learning of frustrated classical spin models. I. Principal component analysis*. Phys. Rev. B **96**, 144432 (2017).

[146] Sebastian J. Wetzel. *Unsupervised learning of phase transitions: From principal component analysis to variational autoencoders*. Phys. Rev. E **96**, 022140 (2017).

[147] Ye-Hua Liu and Evert P. L. van Nieuwenburg. *Discriminative Cooperative Networks for Detecting Phase Transitions*. Phys. Rev. Lett. **120**, 176401 (2018).

[148] Matthew J. S. Beach, Anna Golubeva, and Roger G. Melko. *Machine learning vortices at the Kosterlitz-Thouless transition*. Phys. Rev. B **97**, 045207 (2018).

[149] Lei Wang. *Exploring cluster Monte Carlo updates with Boltzmann machines.* Phys. Rev. E **96**, 051301 (2017).

[150] Li Huang and Lei Wang. *Accelerated Monte Carlo simulations with restricted Boltzmann machines.* Phys. Rev. B **95**, 035105 (2017).

[151] Junwei Liu, Yang Qi, Zi Yang Meng, and Liang Fu. *Self-learning Monte Carlo method.* Phys. Rev. B **95**, 041101 (2017).

[152] Yuki Nagai, Huitao Shen, Yang Qi, Junwei Liu, and Liang Fu. *Self-learning Monte Carlo method: Continuous-time algorithm.* Phys. Rev. B **96**, 161102 (2017).

[153] Huitao Shen, Junwei Liu, and Liang Fu. *Self-learning Monte Carlo with deep neural networks.* Phys. Rev. B **97**, 205140 (2018).

[154] Xiao Yan Xu, Yang Qi, Junwei Liu, Liang Fu, and Zi Yang Meng. *Self-learning quantum Monte Carlo method in interacting fermion systems.* Phys. Rev. B **96**, 041119 (2017).

[155] Junwei Liu, Huitao Shen, Yang Qi, Zi Yang Meng, and Liang Fu. *Self-learning Monte Carlo method and cumulative update in fermion systems.* Phys. Rev. B **95**, 241104 (2017).

[156] Chuang Chen, Xiao Yan Xu, Junwei Liu, George Batrouni, Richard Scalettar, and Zi Yang Meng. *Symmetry-enforced self-learning Monte Carlo method applied to the Holstein model.* Phys. Rev. B **98**, 041102 (2018).

[157] Lukas Kades, Jan M. Pawlowski, Alexander Rothkopf, Manuel Scherzer, Julian M. Urban, Sebastian J. Wetzel, Nicolas Wink, and Felix Ziegler. *Spectral Reconstruction with Deep Neural Networks.* ArXiv preprint (2019), arXiv:1905.04305.

[158] Kai-Wen Zhao, Wen-Han Kao, Kai-Hsin Wu, and Ying-Jer Kao. *Generation of ice states through deep reinforcement learning.* Phys. Rev. E **99**, 062106 (2019).

[159] Dian Wu, Lei Wang, and Pan Zhang. *Solving Statistical Mechanics Using Variational Autoregressive Networks.* Phys. Rev. Lett. **122**, 080602 (2019).

[160] Ryan Sweke, Markus S. Kesselring, Evert P. L. van Nieuwenburg, and Jens Eisert. *Reinforcement Learning Decoders for Fault-Tolerant Quantum Computation.* ArXiv preprint (2018), arXiv:1810.07207.

[161] Philip Andreasson, Joel Johansson, Simon Liljestrand, and Mats Granath. *Quantum error correction for the toric code using deep reinforcement learning.* ArXiv preprint (2018), arXiv:1811.12338.

[162] Agnes Valenti, Evert van Nieuwenburg, Sebastian Huber, and Eliska Greplova. *Hamiltonian Learning for Quantum Error Correction.* ArXiv preprint (2019), arXiv:1907.02540.

[163] Stephen Boyd and Lieven Vandenberghe. *Convex Optimization.* Cambridge University Press, Cambridge, U.K. (2004). ISBN 978-0-521-83378-3.

[164] Bernhard Schölkopf, Alexander J. Smola, Robert C. Williamson, and Peter L Bartlett. *New support vector algorithms.* Neural Comput. **12**, 1207–1245 (2000).

[165] Chih-Chung Chang and Chih-Jen Lin. *Training ν-support vector classifiers: theory and algorithms.* Neural Comput. **13**, 2119–2147 (2001).

[166] John C. Platt. *Fast Training of Support Vector Machines Using Sequential Minimal Optimization.* In Bernhard Schölkopf, Christopher J. C. Burges, and Alexander J. Smola, editors, *Advances in Kernel Methods – Support Vector Learning*. MIT Press, Cambridge, MA (1998). ISBN 978-0-262-19416-7.

[167] Rong-En Fan, Pai-Hsuen Chen, and Chih-Jen Lin. *Working set selection using second order information for training support vector machines.* J. Mach. Learn. Res. **6**, 1889–1918 (2005).

[168] Bernhard Schölkopf, Alexander J. Smola, Francis Bach, et al. *Learning with kernels: support vector machines, regularization, optimization, and beyond.* MIT press, Cambridge, MA (2001). ISBN 978-0-262-19475-4.

[169] Chih-Wei Hsu and Chih-Jen Lin. *A comparison of methods for multiclass support vector machines.* IEEE Trans. Neural Netw. **13**, 415–425 (2002).

[170] Chih-Chung Chang and Chih-Jen Lin. *LIBSVM: A Library for Support Vector Machines.* ACM Trans. Intell. Syst. Technol. **2**, 27:1–27:27 (2011).

[171] Nicolas Le Roux and Yoshua Bengio. *Representational Power of Restricted Boltzmann Machines and Deep Belief Networks.* Neural Comput. **20**, 1631–1649 (2008).

[172] Kelvin Ch'ng, Nick Vazquez, and Ehsan Khatami. *Unsupervised machine learning account of magnetic transitions in the Hubbard model.* Phys. Rev. E **97**, 013306 (2018).

[173] V. V. Mazurenko A. Y. Deviatov, I. A. Iakovlev. *Recurrent network classifier for ultrafast skyrmion dynamics.* ArXiv preprint (2019), arXiv:1907.01814.

[174] Zewang Zhang, Shuo Yang, Chenxi Liu, Yimin Han, Ching Hua Lee, Zheng Sun, Guangjie Li, and Xiao Zhang. *Predicting quantum many-body dynamics with Long Short-Term Memory based neural networks.* ArXiv preprint (2019), arXiv:1905.09168.

[175] Kurt Hornik, Maxwell Stinchcombe, and Halbert White. *Multilayer feedforward networks are universal approximators.* Neural Netw. **2**, 359–366 (1989).

[176] Kurt Hornik. *Approximation capabilities of multilayer feedforward networks.* Neural Netw. **4**, 251–257 (1991).

[177] Joaquin F. Rodriguez-Nieva and Mathias S. Scheurer. *Identifying topological order through unsupervised machine learning.* Nat. Phys. **15**, 790–795 (2019).

[178] Grégoire Montavon, Wojciech Samek, and Klaus-Robert Müller. *Methods for interpreting and understanding deep neural networks.* Digit. Signal Proc. **73**, 1–15 (2018).

[179] Louis Michel and Boris I. Zhilinskií. *Symmetry, invariants, topology. Basic tools.* Phys. Rep. **341**, 11–84 (2001).

[180] Pierre-Gilles de Gennes and Jacques Prost. *The Physics of Liquid Crystals.* International Series of Monographs on Physics. Oxford University Press, New York City (1995). ISBN 978-0-19-851785-6.

[181] Joseph P. Straley. *Ordered phases of a liquid of biaxial particles.* Phys. Rev. A **10**, 1881–1887 (1974).

[182] Miroslav Fiedler. *Algebraic connectivity of graphs.* Czech. Math. J. **23**, 298–305 (1973).

[183] Bojan Mohar. *Isoperimetric numbers of graphs.* J. Comb. Theory, Series B **47**, 274–291 (1989).

[184] Owen Benton, L. D. C. Jaubert, Han Yan, and Nic Shannon. *A spin-liquid with pinch-line singularities on the pyrochlore lattice.* Nat. Commun. **7**, 11572 (2016).

[185] Han Yan, Owen Benton, Ludovic D. C. Jaubert, and Nic Shannon. *Rank-2* $U(1)$ *spin liquid on the breathing pyrochlore lattice.* ArXiV preprint (2019), arXiv:1902.10934.

[186] Owen Benton, Olga Sikora, and Nic Shannon. *Classical and quantum theories of proton disorder in hexagonal water ice.* Phys. Rev. B **93**, 125143 (2016).

[187] Karim Essafi, Owen Benton, and Ludovic D. C. Jaubert. *A kagome map of spin liquids from XXZ to Dzyaloshinskii–Moriya ferromagnet.* Nat. Commun. **7**, 10297 (2016).

[188] Simon Trebst. *Kitaev Materials.* In S. Blügel, Y. Mokrusov, T Schäpers, and Y. Ando, editors, *Topological Matter – Topological Insulators, Skyrmions and Majoranas, Lecture Notes of the 48th IFF Spring School 2017*, volume 139 of *Key Technologies.* Forschungszentrum Jülich, Jülich (2017), arXiv:1701.07056.

[189] Lukas Janssen and Matthias Vojta. *Heisenberg-Kitaev physics in magnetic fields.* J. Phys.: Condens. Matter **31**, 423002 (2019).

[190] Jiří Chaloupka, George Jackeli, and Giniyat Khaliullin. *Kitaev-Heisenberg Model on a Honeycomb Lattice: Possible Exotic Phases in Iridium Oxides* A_2IrO_3. Phys. Rev. Lett. **105**, 027204 (2010).

[191] Zohar Nussinov and Jeroen van den Brink. *Compass models: Theory and physical motivations.* Rev. Mod. Phys. **87**, 1–59 (2015).

[192] G. Jackeli and G. Khaliullin. *Mott Insulators in the Strong Spin-Orbit Coupling Limit: From Heisenberg to a Quantum Compass and Kitaev Models.* Phys. Rev. Lett. **102**, 017205 (2009).

[193] A. Banerjee, C. A. Bridges, J. Q. Yan, A. A. Aczel, L. Li, M. B. Stone, G. E. Granroth, M. D. Lumsden, Y. Yiu, J. Knolle, S. Bhattacharjee, D. L. Kovrizhin, R. Moessner, D. A. Tennant, D. G. Mandrus, and S. E. Nagler. *Proximate Kitaev quantum spin liquid behaviour in a honeycomb magnet.* Nat. Mater. **15**, 733–740 (2016).

[194] Heung-Sik Kim and Hae-Young Kee. *Crystal structure and magnetism in α-RuCl$_3$: An ab initio study*. Phys. Rev. B **93**, 155143 (2016).

[195] Jiacheng Zheng, Kejing Ran, Tianrun Li, Jinghui Wang, Pengshuai Wang, Bin Liu, Zheng-Xin Liu, B. Normand, Jinsheng Wen, and Weiqiang Yu. *Gapless Spin Excitations in the Field-Induced Quantum Spin Liquid Phase of α-RuCl$_3$*. Phys. Rev. Lett. **119**, 227208 (2017).

[196] A. U. B. Wolter, L. T. Corredor, L. Janssen, K. Nenkov, S. Schönecker, S.-H. Do, K.-Y. Choi, R. Albrecht, J. Hunger, T. Doert, M. Vojta, and B. Büchner. *Field-induced quantum criticality in the Kitaev system α-RuCl$_3$*. Phys. Rev. B **96**, 041405 (2017).

[197] Lukas Janssen, Eric C. Andrade, and Matthias Vojta. *Honeycomb-Lattice Heisenberg-Kitaev Model in a Magnetic Field: Spin Canting, Metamagnetism, and Vortex Crystals*. Phys. Rev. Lett. **117**, 277202 (2016).

[198] Li Ern Chern, Ryui Kaneko, Hyun-Yong Lee, and Yong Baek Kim. *Magnetic Field Induced Competing Phases in Spin-Orbital Entangled Kitaev Magnets*. ArXiv preprint (2019), arXiv:1905.11408.

[199] The C++ source codes for the TK-SVM framework and the Monte Carlo simulation of the gauge model and kagome-Heisenberg model are available through the GitLab instance of LMU's physics department:
`https://gitlab.physik.uni-muenchen.de/LDAP_ls-schollwoeck/svm-order-params`.

A mirrored repository is privately maintained at:
`https://github.com/jgreitemann/svm-order-params`.

These depend on a C++ library wrapper for LIBSVM which is separately maintained at:
`https://github.com/jgreitemann/svm`.

Unless otherwise specified, the terms of the GNU General Public License version 3 apply.